Modeling and Optimal Design of

Annular Array Based Ultrasound Pulse-Echo System

A Thesis submitted to the faculty

of

WORCESTER POLYTECHNIC INSTITUTE

in partial fulfillment of the requirements for

The Degree of Master of Science

in

Electrical and Computer Engineering

by

Li WAN

Li WAN

April 2001

APPROVED

Prof. Peder C. Pedersen, Major Advisor

Prof. Reinhold Ludwig, Committee Member

Prof. Nathaniel A. Whitmal, Committee Member

Abstract

The ability to numerically determine the received signal in an ultrasound pulse-echo system is very important for many ultrasound applications such as tissue characterization, complex object recognition, identification of surface topology, and etc. The relationship between, on one hand, the output signal from an ultrasound pulse-echo system, and, on the other hand, the specified ultrasound transducer and the geometry, orientation and location of the reflector, is very complex. Consequently, only by numerical modeling can the output signal for a given measurement configuration be predicted. Especially when it comes to optimizing the design of an ultrasound system to carry out such tasks as identifying objects of specified shapes, determining surface topology or alignment of surface, etc., numerical modeling is the only practical way. This thesis is concerned with the numerically modeling and optimal design of annular array based ultrasound pulse-echo system.

This thesis describes the implementation of two numerical modeling methods for calculating received signal from a transducer in a pulse-echo system. One method is the simple, but computationally demanding *Huygens Method*, based on the Huygens' Principle, and the other one is the computationally more efficient *Diffraction Response for Extended Area Method (DREAM)*. The DREAM method operates by dividing the

surface of the reflector into a relatively small number (say, a few hundred) of rectangular or triangular "tiles" and performing the spatial integration of the *diffraction response* over each tile by an equivalent low pass filtering. In this thesis, the DREAM method is implemented using both rectangular and triangular tiles. To determine the optimal tile size for the DREAM method for various combinations of transducers size, reflector location, etc, the results obtained by DREAM method are compared with the corresponding results obtained from the Huygens method as an accurate reference. Both graphical and numerical results are presented. The modeling concept is further extended to include ultrasound pulse-echo system using planar annular array transducers where the calculation for the individual array elements is based on calculation of the received signals from planar circular transducers.

The optimal design of the ultrasound pulse-echo system for object recognition is based on the annular array transducer that gives us the flexibility to create a wide variety of insonifying fields and receiver characteristics. These fields and receiver characteristics can be realized by assigning different delay and amplitude gain values to each array element in transmit and receive, respectively. As the first step towards solving the optimization problem for identifying a given type of reflector among many possible ones, the problem of optimally identifying one out of two specific reflectors is investigated. To solve this problem, we propose to find the set of transmit and receive delay values which will maximize the energy of the difference signal between array output signals from the two reflectors. Two optimization methods have been investigated for the optimal delay set, the *Global Search Method* and the *Waveform Alignment Method.* The Global Search Method operates by searching through all possible combinations of delay values, applied

to the individual transmitting elements and the receiving elements of the annular array transducer, then calculates the energy of the difference signal between received output signals from the two reflectors for each delay value combination. The set of delay values that produces the largest energy in difference signal is considered the optimal delay set. The Waveform Alignment Method operates by using a time shifted and amplitude scaled version of a specific waveform to represent the calculated waveform in the received signal matrix which contains the received signal for all combinations of transmitting and receiving array elements. Thus, each received signal in the received signal matrix can be represented by a delay value and amplitude scale factor. In this thesis, only the delay values are used to align these waveforms to get the optimal delay matrix. The results obtained by the Global Search Method and the Waveform Alignment Method are presented and compared to each other.

Acknowledgements

First of all, I would like to express my sincere gratefulness to my advisor Prof. Peder C. Pedersen for his tremendous efforts and time spent in teaching me, discussing with me and refining all my writings. Without his inspiration and guidance, finishing this thesis might have been impossible. All that I learned from him, including the patience, carefulness and persistence, benefited me and will benefit me greatly in the future.

I appreciate Prof. Reinhold Ludwig and Prof. Nathaniel A. Whitmal for their help and being my thesis committee members.

I would also like to thank Yurong Sun and Ruben Lara-Montalvo, who provided hearty help and happy hours.

Last but not least, my sincere thanks go to my family and my friends for their care and encouragement, especially to my husband, whose love is the source of my happiness and strength.

Table of Contents

List of Figures

flat reflector. The x-axis for all signals is in ms and the y-axis for all signals is in m^4/s^3.

List of Tables

transducer surface.

Chapter 1

Introduction

1.1 Ultrasound Pulse-Echo Modeling Techniques

The ability to numerically determine the received signal in an ultrasound pulse-echo system is very important for many ultrasound applications such as tissue characterization, complex object recognition, identification of surface topology, etc. There exists very complex relationship between, on one hand, the output signal from an ultrasound pulse-echo system, and, on the other hand, the specified ultrasound transducer and the geometry, orientation and location of the reflector. As a result, only by numerical modeling can the output signal for a given measurement configuration be predicted. Especially when it comes to optimizing the design of ultrasound system to carry out such tasks as identifying objects of specified shapes, determining surface topology or alignment of surface, etc., numerical modeling is the only practical way.

There are several techniques being applied to model the pulse-echo system, including analytical approaches, Finite-Element Method (FEM), Angular Spectrum Methods (ASM), and Spatial Impulse-Response Method (SIRM). As we will briefly discuss in this section, each technique has its own advantages and disadvantages.

Analytical approaches, as the name indicates, are based on the analytical solutions for the received signal in the pulse-echo system. This type of approaches was

investigated by Johnson and Davaney [1] for a planar circular piston transducer insonifying an elastic infinite planar reflecting surface strictly at normal incidence. When the analytical solutions for the received signals are available, the analytical approaches make the computer simulation of the system efficient and general. However, analytical formulations do not exist for general transducer and reflector geometries; in addition, the analytical approaches can not include such effects as attenuation, scattering and refraction; therefore, analytical approaches are not of much interest in general purpose modeling.

The FEM method, which is based on the solution of a complete set of fundamental differentiation equations with the restriction of linearity, is a well-established numerical technique for field computations in complex and heterogeneous media. Lerch applied the FEM in the computation of sound fields in fluids and gases [2]. His theoretical results was quantitatively verified by measurements of electrical impedances of a long parallelepiped piezoceramic bar, mechanical displacements of array transducers and the sound field of piezoelectric transducers immersed in water [2]. Based on the theoretical framework developed by Lerch, the FEM was also applied to model the pulse-echo behavior of ultrasound transducers by Lerch, Landes and Kaarmann [3]. In their work, a hybrid scheme was applied, i.e., the FEM is used to model the transducer and the reflector as well as their fluid environment to calculate the reflected acoustic pressure while the forward and backward wave propagation between the transducer and the reflector was calculated via Helmholtz integral. With the FEM, it is possible to model very complex, thus more realistic, situations at the price of long computation time due to the complex model. Another problem of FEM is that when the

source and reflector are far apart, a large number of propagation steps are needed to propagate the wavefield from the transducer to the reflector and from the reflector back to the transducer. Therefore, the error introduced for each propagation step could accumulate to a unacceptably large error.

The ASM method is based on a decomposition of the acoustic field into harmonic plane waves, and this method allows simple analysis of the propagation of scalar fields. Orofino and Pedersen discussed a practical angular spectrum decomposition method based on the 2-D FFT [4]. The angular spectrum decomposition was expressed as a 2-D spatial Fourier transform which, for a fixed temporal frequency, is a function of the spatial frequencies of the particle velocity distribution in the x- and y-directions. This method enables the decomposition of normal velocity and pressure fields radiated by transducers of arbitrary shape into component plane waves with amplitudes and propagation directions determined by the temporal frequency and spatial frequencies. The ASM based method was also extended to model the received ultrasound signals from finite planar targets by Pedersen and Orofino [5]. The propagation from source to reflector of a given plane wave component is directly achieved by a single phase term, therefore, ASM avoids the accumulative error problem encountered by the FEM. The ASM is very useful in some situations, particularly for modeling of reflections from planar reflectors of arbitrary size. However, the ASM is very computationally intensive when applied to pulse-echo modeling because the ASM is based on harmonic waves only. Hence, a temporal Fourier Transform is needed to decompose acoustic field into harmonic waves before the ASM can be applied. Another drawback of the ASM is that the determination of the spatial frequencies is very

complicated because the spatial frequencies are dependent on the geometry of transducer and reflector.

The SIRM method is currently used for calculation of pressure field from a variety of transducer types [5]; in a similar fashion, the pulse-echo responses from a given transducer due to a point-like scatterer can be found using this method. The SIRM can be further extended to the calculation of the received signals due to extended reflector surfaces in pulse-echo system. Most of the SIRM applications for the pulse-echo systems are based on the derivation by Weight and Hayman [6] of the received signal from a small reflector surface insonified by a transducer with short pulse excitation. Their derivation is based on Rayleigh integral and the principle of acoustic reciprocity. Using the results in [6], McLaren and Weight made detailed calculation of the received signals arising from solid targets of various size interrogated by short pulses of ultrasound propagating in a fluid medium [7]. They also investigated the effects of target size, field position and material on the amplitude and shape of the received signals. Later, Lhemery developed a model to predict the received signal from targets of complex geometry [8], with specific formulations for arbitrary shape targets with very high acoustic impedance, arbitrary acoustic impedance and near zero acoustic impedance. More details of SIRM will be presented in section 2.2.

1.2 Objectives of the Thesis

1.2.1   DREAM Method and Huygens Method

A fast impulse-response based numerical modeling tool, the *Diffraction Response from Extended Area Method* (DREAM), was developed by Jespersen,

Pedersen, and Wilhjelm [9]. The DREAM is a SIRM based method. The acoustic principle behind DREAM is the same as used in [6, 7, 8]. The DREAM is based on linearity and operates by dividing the surface of the reflector into a relatively small number (say, a few hundred) of rectangular or triangular "tiles". The spatial integration of the *diffraction response* over each tile is then performed by an equivalent low pass filtering. The DREAM method is able to efficiently calculate the received signal from a given ultrasound transducer due to a specified reflector at a specified location and orientation.

The DREAM method using rectangular tile was implemented as part of the PhD thesis of S.K. Jespersen at Technical University of Denmark [10]. In his work, he compared the simulation results obtained using DREAM method with the results obtained using other simulation techniques, such as the angular spectrum method. For all the simulations, the transmitting and receiving transducers are both circular planar transducer with radius of 12.7mm.

The DREAM method can also be implemented using triangular tiles. The use of triangular tiles solves two inherent problems with the implementation of rectangular tiles. First, it eliminates the small error introduced by the least squares approximation in the delay linearization for the rectangular tiles, as will be discussed in the next chapter. Second, the triangular tile can be used to tessellate a specific reflector surface more accurately than the rectangular tile. Therefore, one of the objectives of this thesis is to implement and evaluate the DREAM using triangular tiles. Furthermore, we would like to investigate the performance of the DREAM method over a wider range of simulation scenarios, that is, for more types of reflectors and for more different combination of

5

transmitting and receiving transducers. A simpler, but slower, method based on Huygens' principle, namely, Huygens method, is used as benchmark to evaluate the results obtained by the DREAM method. The Huygens method is based on the integration of the diffraction response from a very large number of micro-tiles which make up the surface of the entire reflector.

1.2.2 Optimal Design of Ultrasound System

The modeling concept of ultrasound pulse-echo system can be extended to array transducers. With the DREAM method as an efficient modeling tool, the received signal from any array element due to transmission with any array element can be readily calculated, based on the superposition of the received signal from planar circular transducers. With array transducers, a large number of different acoustic fields can be produced by varying the relative excitation delay and the amplitude scale factor for the individual transmitting elements. In a similar fashion, a large number of receiver characteristics can be achieved. By customizing the acoustic field and receiver characteristics of an ultrasound pulse-echo system with annular array, it may be possible to develop an acoustic system which can be optimized in the terms of identifying a given object or interface among a limited set of objects or interfaces. Therefore, another objective of the thesis is to investigate the optimal design of ultrasound system for such tasks as identifying objects of specified shapes, determining surface topology or alignment of surface.

1.3 Contributions of the Thesis

The original work of this thesis has made contributions in the following aspects:

- The Huygen method is implemented to model the output signal of a pulse-echo system and some important implementation issues are investigated.

- The DREAM method is implemented using both triangular and rectangular tiles. The segmentation and the delay interpolation, which are the two most important aspects in the practical implementation of DREAM, are improved relative to the implementation in [9] to generate more accurate results for more general simulation scenarios, especially, when the transmitting and the receiving transducers are of different size. The issue of finding the optimal tile size for DREAM method is investigated in details.

- The results obtained by DREAM method are evaluated, in terms of accuracy and computation time, by comparing to those obtained by Huygens method for a variety of simulation scenarios.

- Two methods, the *Global Search Method* and the *Waveform Alignment Method*, are implemented as the first step towards the optimal design of ultrasound system in terms of identifying a given object or interface among a limited set of objects or interfaces. The optimal delay matrix is obtained as a preliminary solution to differentiate between two specific interfaces by optimizing the delay values assigned to the elements in the array.

1.4 Outline of the Thesis

This section describes the overall content of the thesis. Chapter 2 and Chapter 3 provide background material including a description of the pulse-echo system, the modeling of pulse-echo system and the implementation aspects of such system. Chapter 4 and Chapter 5 present and evaluate the simulation results obtained by Huygens method and by the computationally efficient DREAM method, respectively. More results are included in Appendix A and Appendix B rather than in the individual chapters, in order to keep the main text concise. In Chapter 6, the modeling concept has been extended to annular array system. It is investigated how to optimally design an ultrasound system with respect to its ability to identify a given object or interface among a limited set of objects or interfaces. Chapter 7 presents the conclusion and future research work related to the work of this thesis. Each major chapter of this thesis is individually summarized below for the convenience:

Chapter 2:

The ultrasound pulse-echo system is briefly discussed. Definition of *Pulse-echo Diffraction Impulse Response* is presented to simplify the formulation of the received electrical signal in pulse-echo ultrasound systems. Then, the *multi-rate algorithm*, which is used to numerically compute the pulse-echo diffraction impulse response, is described. Two methods, which are used to calculate the received signal in pulse-echo systems from extended area reflectors, are introduced: *Huygens method* and *Diffraction Response for Extended Area Method* (DREAM). Finally, the modeling concepts are extended to calculate the received signal from individual array elements in annular array system.

Chapter 3:

The details about the implementation of ultrasound pulse-echo simulation system are discussed in this chapter. First, the velocity potential impulse response as well as the diffraction response for one single field point are derived. Then, the Huygens method to calculate the received signal from extended reflector is discussed. Next, the computational efficient DREAM method is described based on the concepts of segmentation and delay interpolation. Finally, the mechanism for the simulation coding is described in term of efficiency.

Chapter 4:

Different aspects of the Huygens method are discussed in this chapter. First, Huygens method based on the integration of the response of central point of the micro-tile is compared with Huygens method based on the integration of the response of corner point of the micro-tile. Next, the optimal micro-tile size which can be used by Huygens method to produce results with good accuracy is investigated.

Chapter 5:

The optimal tile-size, which can be used by DREAM method to produce results with good accuracy, is explored. The relationship between, on one hand, the *DREAM Error*, the *energy* of the received signal, and the *normalized DREAM Error* for a small reflector, and, on the other hand, such factors as the radial position of the reflector, the tilt angle of the reflector and the radii of the transducers are illustrated. Finally, the received signal from small flat reflectors, large tilted flat reflectors and large curved reflectors is calculated by the DREAM method (T-DREAM and/or R-DREAM), using optimal tile size. The results are calculated for different combinations of planar circular

transducers and evaluated by those obtained by Huygens method in terms of accuracy and computation time.

Chapter 6:

A brief introduction is given to the concept of the optimal design of ultrasound system, in the terms of identifying a given object or interface among a limited set of objects or interfaces. Two methods are introduced: the *Global Search Method* and the *Waveform Alignment Method*. Both methods are applied to find the best transmit and receive characteristics of the array transducer in the form of the optimal delay matrix, to most reliably differentiate between a tilted flat surface and a convex curved surface, based on a 3-ring annular array system. The *Waveform Alignment Method* is also applied based on a 6-ring annular array system. All the results are compared. In addition, the *Waveform Alignment Method* is applied to find the optimal delay matrix to most reliably differentiate between a tilted flat surface and a concave curved surface, as well as between a convex curved and a concave curved surface, based on both a 3-ring annular array system and 6-ring annular array system. All the results are compared.

Chapter 2

Modeling of Ultrasound Pulse-Echo System

The ultrasound pulse-echo system is the basis for most practical applications of ultrasound as images of local backscatter level (B-mode images) are readily generated using linear array transducers. The first section of this chapter begins with descriptions of an ultrasound pulse-echo system, introducing the operation of such a system, as well as the importance of numerical modeling of the system for quantitative analysis. In section 2.2, a term *Pulse-Echo Diffraction Impulse Response* is defined to simplify the formulation of the received electrical signal in pulse-echo ultrasound systems, followed by section 2.3 where a multi-rate algorithm, which is used to compute the pulse-echo diffraction impulse response, is described. Then the *Huygens method* and the *Diffraction Response for Extended Area Method* (DREAM), which are used to calculate the received signal in pulse-echo systems from extended area reflectors, are introduced in sections 2.4 and 2.5. Finally, in section 2.6, the modeling concept is expanded to calculate the received signals from individual elements in an annular array transducer.

2.1 Introduction

Sound is mechanical energy transmitted by pressure waves in a medium. Sound waves, whose frequency is greater than 20 KHz, are termed *ultrasound*. The word *transducer* denotes any device that is used to convert signals or energy from one energy form to another. In the context of this thesis, the term transducer refers to the *ultrasonic transducer* that converts acoustic signals to electrical signals and/or electrical signals to acoustic signals [11].
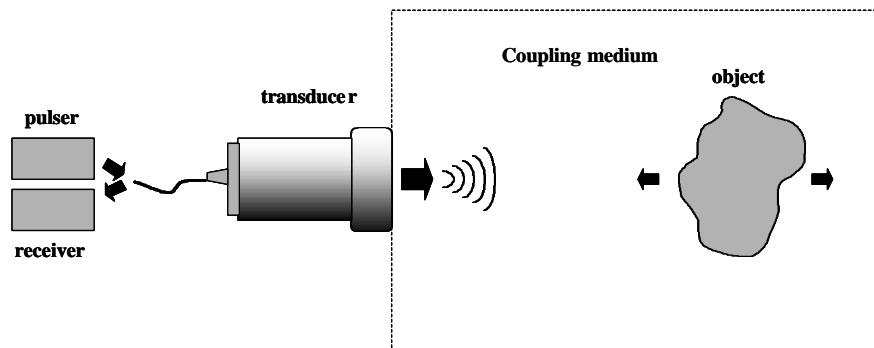
Figure 2.1: Illustration of an ultrasound pulse echo system.

When an ultrasonic transducer transmits short-duration acoustic pulses into a medium containing a reflecting object, the pulses undergo reflection at the surface of the object which gives rise to echo signals returning to the receive transducer [11]. Such a system is called ultrasound pulse-echo system and is illustrated in Figure 2.1 in which the same transducer is used in both transmission and reception. The ultrasound transducer is typically implemented by using a piezoelectric layer with electrodes on each side. A piezoelectric transducer is a resonant device which has bandpass filter

characteristics. The excitation signal from a pulser/receiver is typically a large voltage spike, which can be modeled by a delta function.

The ultrasound pulse-echo system is the basis for most practical applications of ultrasound as images of local backscatter level (B-mode images) are readily generated by using linear array transducers. In many situations, pulse-echo ultrasound is the only practical way that ultrasonic imaging, the most common qualitative ultrasound application, can be performed. Ultrasound imaging is carried out in both medical ultrasound and non-destructive testing. Proper development of quantitative ultrasound, on the other hand, often requires that the received signal in a pulse-echo system be determined. Quantitative ultrasound applications include tissue characterization, complex object recognition and identification of surface topology. Unfortunately, it is quite difficult to efficiently determine the received electrical signal in pulse-echo ultrasound systems because of the complexity of generation, propagation, backscattering and reception of the ultrasound fields in pulse-echo systems. Therefore, efficient computational tools for pulse-echo system are essential to the progress of the quantitative medical and industrial applications of ultrasound.

The relationship between the output signal from an ultrasound pulse-echo system on one hand and the excitation signal, the geometry, properties and location of the ultrasound transducers and size, geometry, location and orientation of the reflector on the other hand is very complex, so that only by numerical modeling can the output signal for a given measurement configuration be predicted. Especially when it comes to optimizing the design of ultrasound system to carry out such tasks as identifying objects of specified shapes, determining surface topology or alignment of surface, etc.,

13

numerical modeling is the only practical way. The factors that influence the received signal include: the excitation signal; the geometry, location, electro-acoustic transfer function of the transmit and receive transducers; the size, shape, surface geometry, interface orientation, location of the reflector; and the effect of attenuation, absorption, refraction and non-linearity of the coupling medium [9].

As described in section 1.1.1, there are several modeling techniques being applied to model the pulse-echo system: 1) analytical approaches; 2) Finite-Element Method (FEM); 3) Angular Spectrum Methods (ASM), and 4) Spatial Impulse-Response Method (SIRM). The *Diffraction Response for Extended Area Method* (DREAM method) which is the main topic of this thesis is based on the impulse-response based approach. DREAM modeling utilizes the *diffraction responses* derived from the velocity potential impulse responses of the transmitting and receiving transducers as will be discussed in section 2.2. The modeling concept has been extended to calculate the received signals from individual elements in an annular array transducer, described in section 2.6.

2.2 Diffraction Response Formulation

It is well known that a sound field from a baffled planar piston source in a fluid can be accurately described by the *Rayleigh integral*. For a source with a radiating surface S and a normal particle velocity function $u_n(\vec{r}_s, t)$, the *Rayleigh integral* for time-dependent velocity potential $\boldsymbol{f}(\vec{r}, t)$ is given by [12 – 14]

$$f(\vec{r},t) = \int_S \frac{u_n(\vec{r}_s, t - |\vec{r} - \vec{r}_s|/c)}{2p\,|\vec{r} - \vec{r}_s|}\,dS \tag{2.1}$$

where $\vec{r}_s$ represents points on the surface S and $\vec{r}$ represents the field point. The

parameter c is the sound speed in the homogeneous propagation medium. If all of the

points on the source vibrate with equal amplitude and in phase, i.e., the vibration of the

piston is uniform, then $u_n(\vec{r}_s, t) = u_n(t)$ on S and zero outside, and (2.1) can be

expressed as:

$$f(\vec{r},t) = \int_S \frac{u_n(t - |\vec{r} - \vec{r}_s|/c)}{2p\,|\vec{r} - \vec{r}_s|}\,dS = u_n(t) \otimes h(\vec{r},t) \tag{2.2}$$

where $\otimes$ is the convolution in time-domain, and $h(\vec{r},t)$ is the spatial impulse response

of the velocity potential and defined as [14]

$$h(\vec{r},t) = \int_S \frac{d(t - |\vec{r} - \vec{r}_s|/c)}{2p\,|\vec{r} - \vec{r}_s|}\,dS = \int \frac{d(t - r'/c)}{2pr'}\,dS \tag{2.3}$$

where $r' = |\vec{r} - \vec{r}_s|$. The pressure field at point $\vec{r}$, $p(\vec{r},t)$, can be obtained from $f(\vec{r},t)$
as [7, 15]

$$p(\vec{r},t) = r_0 \frac{\partial f(\vec{r},t)}{\partial t} = r_0 \frac{\partial [u_n(t) \otimes h(\vec{r},t)]}{\partial t} = r_0 u_n(t) \otimes \frac{\partial h(\vec{r},t)}{\partial t} \tag{2.4}$$

where r_0 is the density of the medium in front of the transducer. From (2.4), it is not

difficult to understand why the method discussed above is named the "Velocity

Potential Impulse Response Method" or just the "Impulse Response Method".

The impulse response method has also been applied to calculate the received

signal in a pulse-echo system. The *principle of acoustic reciprocity* [16, p. 172] is the

basis for the following derivation. One form of the principle states that if the locations

and orientations of a small source and a small receiver are interchanged, the received

15

signal will remain the same. For pulsed radiation, the principle is stated as [6]: "For a given transducer in reception, the output voltage waveform due to a pulse emitted at a point is identical to the pressure waveform at that point resulting from transmission of the same pulse by the transducer."
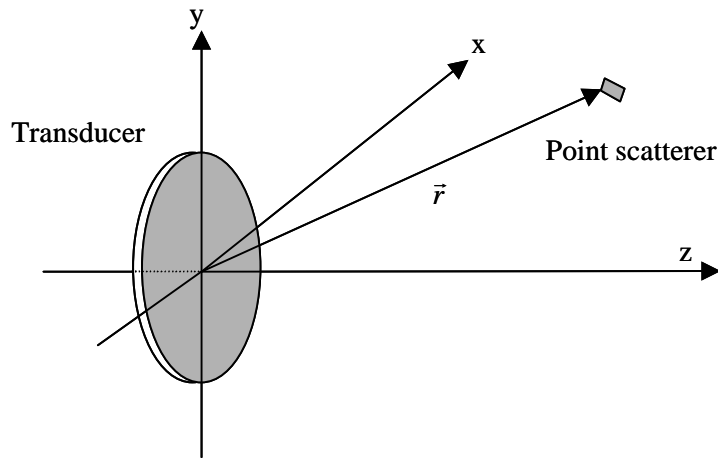
Figure 2.2 Illustration of the simplest pulse-echo system with point scatterer as reflector.

The first step towards determining the received signal in a pulse-echo system is to calculate the received signal due to small reflector surface with dimensions much smaller than a wavelength, i.e., *point scatterer*. The situation is illustrated in Figure 2.2. The point scatter is at point $\vec{r}$ and is subjected to the incident pressure field $p_i(\vec{r},t)$. Equation (2.4) gives the formulation for $p_i(\vec{r},t)$ at point $\vec{r}$. It can be assumed that the incident field is locally plane if it is observed over a very small region. It is also assumed that the impedance of the point scatterer is either zero or infinite; therefore, the reflected pressure magnitude at the surface of the point scatterer is equal to the incident pressure magnitude. According to the *principle of acoustic reciprocity*, the received signal for the receiving transducer can be calculated by assuming the point scatterer acts

as a point source. The point source is characterized by its surface velocity $u_s(\vec{r}, t)$, which is [16, p. 126]

$$u_s(\vec{r}, t) = -\frac{p_i(\vec{r}, t)}{\boldsymbol{r}_0 c} \tag{2.5}$$

and the surface velocity of the point source will create the reflected velocity potential over the surface of the receiver [17, p. 298-303],

$$\boldsymbol{f}(\vec{r}, t) = \frac{u_s(\vec{r}, t - r'/c)}{4\boldsymbol{p}r'} dA = -\frac{p_i(\vec{r}, t - r'/c)}{4\boldsymbol{p}r' \boldsymbol{r}_0 c} dA \tag{2.6}$$

where r' is the distance from the point scatterer to the observation point on the transducer surface and dA is the small surface area of the point scatterer. By combining (2.4) and (2.6), the reflected pressure on the transducer, $p_r(\vec{r}, t)$, can be found as:

$$p_r(\vec{r}, t) = \boldsymbol{r}_0 \cos[\boldsymbol{q}(\vec{r}, t)] \frac{\partial \boldsymbol{f}(\vec{r}, t)}{\partial t} = -\cos[\boldsymbol{q}(\vec{r}, t)] \frac{\partial p_i(\vec{r}, t - r'/c)}{\partial t} \frac{dA}{4\boldsymbol{p}r' c} \tag{2.7}$$

In equation (2.7), $\boldsymbol{q}(\vec{r}, t)$ is the angle between the unit normal vector of the reflector surface and the particle velocity vector at $\vec{r}$; Therefore, the output voltage, $dv_r(\vec{r}, t)$, due to the point scatterer is:

$$dv_r(\vec{r}, t) = E_r(t) \otimes \int_S p_r(\vec{r}, t) dS \tag{2.8}$$

where $E_r(t)$ is the acoustic-electrical impulse response of the receiving transducer. With several straightforward operations and applying equation (2.7), equation (2.8) can be rewritten as [6, 9]

$$dv_r(\bar{r},t) = -\frac{dA\boldsymbol{r}_0}{2c}\cos[\boldsymbol{q}(\bar{r},t)]E_r(t)\otimes u_n(t)\otimes\frac{\partial^2}{\partial t^2}[h_t(\bar{r},t)\otimes h_r(\bar{r},t)] \qquad (2.9)$$

where $u_n(t)$ is the uniform particle velocity on the surface of the transmitter and $h_t(\bar{r},t)$ and $h_r(\bar{r},t)$ are the velocity potential impulse response of the transmitter and receiver, respectively. Now, the received signal due to a small reflector surface with dimensions much smaller than a wavelength can be expressed as (2.10) by application of (2.9) (multiplied by two since the small reflector is now part of an extended, locally smooth reflector) [8, 9]:

$$dv_r(\bar{r},t) = \frac{\boldsymbol{r}_0}{c}\cos[\boldsymbol{q}(\bar{r},t)]E_r(t)\otimes u_n(t)\otimes\frac{\partial^2}{\partial t^2}[h_t(\bar{r},t)\otimes h_r(\bar{r},t)]dA \qquad (2.10)$$

If we express $u_n(t)$ as $u_n(t) = v_{exc}(t)\otimes E_t(t)$ and then define $E(t) = E_t(t)\otimes E_r(t)$ where $E_t(t)$ is the acoustic-electrical impulse response of the transmitting transducer and $v_{exc}(t)$ is the excitation voltage applied to the transmitting transducer, equation (2.10) can be rewritten as:

$$dv_r(\bar{r},t) = \frac{\boldsymbol{r}_0}{c}\cos[\boldsymbol{q}(\bar{r},t)]E(t)\otimes v_{exc}(t)\otimes\frac{\partial^2}{\partial t^2}[h_t(\bar{r},t)\otimes h_r(\bar{r},t)]dA \qquad (2.11)$$

This result, in a similar format, was originally derived by Weight and Hayman, and some measurement results were presented [6]. Those measured results, using short pulses and small targets, are consistent with the theoretical results based on the reciprocity between transmission and reception. Figure 2.3 illustrates one of the experimental results obtained in [6]. The transducer is 8*mm* radius disk of PZK backed with tungsten-epoxy composite and the target is 0.8*mm* diameter axial target at 20*mm* range. The predicted result in part (b) agrees well with the measured result in part (a),

apart from a low-frequency component, which according to the authors is due to "radial mode reverberation in the transducer" and "the limited dynamic range of the transducer (~ 55dB)" [6], as well as the limited bandwidth of the transducer.

(a)   (b)
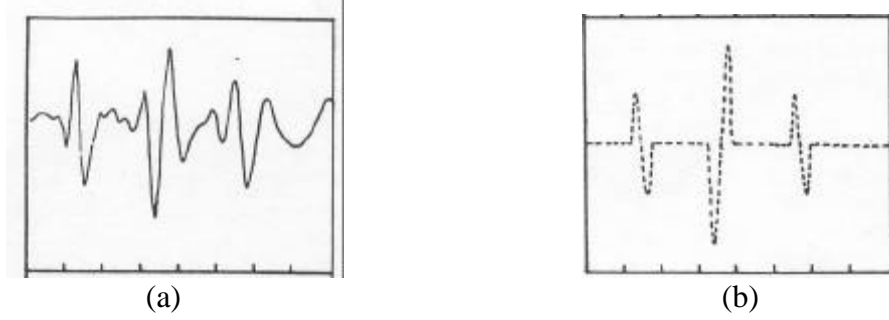
Figure 2.3 Comparison of the experimental output voltage (solid line in part a) and the theoretical prediction (broken line in part b) from 0.8*mm* diameter axial target at 20*mm* range. The transducer is 8*mm* radius disk of PZK backed with tungsten-epoxy composite [6].

To simplify the notation in (2.11), the *Pulse-Echo Diffraction Impulse Response* is defined as:

$$D(\vec{r},t) = \frac{\partial^2}{\partial t^2}[h_t(\vec{r},t) \otimes h_r(\vec{r},t)] \tag{2.12}$$

Further simplification of (2.11) is achieved by: i) assuming that $E(t) = \boldsymbol{d}(t)$ and $v_{exc}(t) = \boldsymbol{d}(t)$. Although these assumptions are not realistic, they do not limit the practical value of the approach because the realistic functions for $E(t)$ and $v_{exc}(t)$ can be convolved onto the calculated response at any time in the process; ii) approximating $\boldsymbol{q}(\vec{r},t)$ with $\boldsymbol{q}(\vec{r})$; and iii) defining $A_1 = \frac{\boldsymbol{r}_0}{c}$. Applying these approximations and the definition for $D(\vec{r},t)$ to equation (2.11), the resulting expression becomes:

$$dv_r(\vec{r},t) = A_1 \cos[\boldsymbol{q}(\vec{r})]D(\vec{r},t)dA \tag{2.13}$$

2.3 Computational Strategies for Calculating the Diffraction Response

From equations (2.13), it can be seen that it is will not be difficult to obtain the received signal in pulse-echo ultrasound system for a very small reflector surface as long as the diffraction response can be calculated. With the definition of diffraction response in equation (2.12), we know that the key to calculate the diffraction response is to obtain the velocity potential impulse response of the transducer. Analytic formulations of the velocity potential impulse response for a planar piston transducer will be presented in section 3.1.1. As will also be illustrated in section 3.1.1, the bandwidth of the velocity potential impulse response is quite large, especially when the field point is near the transducer axis. Therefore, high sampling rates such as 6.4Ghz, 3.2GHz, etc., are required to avoid aliasing effect. However, since the frequency of our interest is from near *dc* to 15.625MHz, such high sampling rates are excessive in the final results, and we can decrease the sampling rates of the velocity potential impulse response to save computational sources. Therefore, a *multi-rate digital signal processing algorithm* is used to calculate the velocity potential impulse response. The procedure of the algorithm is briefly described as following [15]:

1.   Analytical solutions to velocity potential impulse response have been found for a number of transducer geometries [9], such as a planar circular piston [18, 19], a rectangular planar piston [20], a spherically curved rectangular strip [21], a spherically focused circular piston [22] and a triangular piston [23]. These analytical solutions are the basis for further signal processing.

2.   The analytical solutions of the velocity potential impulse response must be sampled or discretized before further signal processing procedure can be carried out.

There are many types of sampling, including nonuniform sampling, uniform sampling, random sampling and multiple-function uniform sampling [24]. We have used uniform (periodic) sampling. The frequency f is the sampling rate and is a fundamental consideration in many signal processing techniques and applications. It often determines the convenience, efficiency and/or accuracy with which the signal processing can be performed. In some cases, it may be necessary to convert the sampling rates of the signals in the system from one rate to another. Such systems are referred as *multirate system* [24].

The first step to sample the analytical solution of the velocity potential impulse response is to specify the *minimum global sampling rates f_{sm}* based on different applications and the error level allowed. Next, the maximal duration of the velocity potential impulse response is determined. For a planar circular transducer of radius *a*, the duration of the velocity potential impulse response, Δt, is always less than the travel time of the wave across the transducer surface, $\Delta t_{max} = 2a/c$, where *c* is the sound speed as defined in equation (2.1). Based on the specified minimal global sampling frequency f_{sm} and the maximal duration of the velocity potential impulse response Δt_{max}, the *maximum sample sequence length N* for a specific transducer can be obtained as $N \geq \Delta t_{max} \times f_{sm}$, which guarantees the sampling rates for all observation points are higher than or equal to f_{sm}. Then the *local sampling frequency f_{sl}* for a specific field point is determined by the duration, Δt, of the velocity potential impulse response at that point and the *N*: $f_{sl} = N / \Delta t$. However, in order to achieve a more efficient down-sampling scheme by limiting the number of sampling rate values, the velocity

21

potential function is sampled at a *global sampling frequency* f_{sg}, which is defined to be

an even multiple of the predetermined *minimum global sampling rates f_{sm}*. The chosen

sampling rate for a given observation point is the largest global sampling rate less than

or equal to the local sampling frequency, f_{sl}, of that point [15]. More details and

quantitative analysis will be presented in Chapter 3 "Implementation for simulation

system".

  3. The global sampling rates used in step 2 are much higher than the range of

frequencies of interest. Therefore, the velocity potential function obtained in discrete

form in step 2 can be low-pass-filtered and decimated to decrease the sampling rate.

This results in a reduced number of samples, which saves significant amount of CPU

time and computer memory without decreasing the accuracy of the signal processing.

The digital process that converts the sampling rate of a signal from a given rate to a

lower rate [24] is referred to as *Decimation*. If it is necessary, this step can be repeated

with different down-sampling rates. The final sampling rate is the same for all

observation points and depends on the specific application. For the calculation of the

velocity potential function and the received signal, only a single lowpass digital filter

was designed with a given set of normalized design parameters. The passband and

stopband cutoff frequencies of such a filter vary with the sampling frequency of its

input sequence. Such implementation simplifies the design work, saves space when

storing the filter coefficients and creates a more efficient decimation calculation.

  For the DREAM algorithm, a Linear-Phase Digital Lowpass Filter was chosen

because of the phase-sensitivity of pulse-echo ultrasound system. After the LPF is

designed, the impulse response of the filter in time-domain as well as frequency-domain

response should be checked because the segmentation algorithm following the LPF and the decimator is sensitive to the amplitude characteristics of the time-domain response as it tries to find the peak values of the amplitude of the response.

After the velocity potential impulse responses are obtained for the transmitting and the receiving transducers, the two velocity potential impulse responses are convolved, then the results of the convolution is differentiated twice to obtain the diffraction response as in given (2.12). Because of the high final sampling rate used in multi-rate algorithm, specifically 400MHz, the straightforward digital differentiation method can be applied with acceptable error level. This will be discussed in Chapter 3. Therefore, the procedure to obtain the diffraction response from the velocity potential is very straightforward. Figure 2.4 illustrates the whole procedure to obtain the diffraction response. It is noted that step 1 and step 2 are carried out only once for a specific simulation scenario. Step 3 to step 7 are carried out for each field point.

Step1:	Decide the minimal global sampling rate f_{sm}, based on different applications and error allowed.

Analytical solution to velocity potential function for a specific field point.

Step2:	Calculate the maximal duration of the velocity potential impulse response, Δt_{max}, then determine the maximal sample sequence length N

Step3:	Calculate the duration of the velocity potential impulse response, Δt, then calculate the local sampling rate f_{sl} for the specific field point, then obtain the global sampling rate f_{sg}.

Step4:	Sample the analytical solution to velocity potential function, using the global sampling rate f_{sg} obtained in step 3.

Step5:	Low-pass-filter and decimate the sampled velocity potential function obtained in step 4 to decrease the final sampling rate.

Step6:	Convolve the velocity potential functions obtained in step 5 for the transmitter and receiver .

Step7:	Differentiate the convoluted result in step 6 twice to obtain the diffraction response .

Figure 2.4 Flow chart of the calculation of diffraction response.

2.4 Huygens Method

As discussed in section 2.2, the received signal from a point scatterer in a pulse-echo system is obtained using the velocity potential impulse response method. Such method can be expanded to calculate the received signal from an extended reflector. With the assumption of linearity, that is, all effects due to multiple scattering, angle dependent reflection coefficients, etc. are excluded, the received signal from an extended reflector is just the integration or summation of the responses obtained by equation (2.13) over the reflector surface, as shown in (2.14):

$$v_r(t) = A_1 \int_A \cos[\boldsymbol{q}(\vec{r})]D(\vec{r},t)dA = A_1 \sum \cos[\boldsymbol{q}(\vec{r})]D(\vec{r},t)\Delta A \qquad (2.14)$$

The most straightforward way to implement (2.14) is to divide the reflector surface into a large number of planar small surface elements, calculate the responses from each point and sum the responses. With this approach, it will be possible to obtain the received signal as long as the diffraction response is calculated. This method will be referred to as *Huygens method*.

Huygens' principle [25] states that, for a plane vibrating surface, every point may be considered the source of an outgoing spherical wavelet and that the field at an arbitrary point can be constructed from the superposition of these wavelets. As discussed in section 2.2, the calculation of the diffraction response is based on *Rayleigh integral* which is a special case of Huygens principle, in which the radiating source and boundary lie in a plane. Therefore, the method is named after *Huygens*.

25

2.5 DREAM Method

Huygens method described in last section is straightforward to implement. The disadvantage of it is that the size of the surface elements must be chosen very small to satisfy the assumption of point source behavior. Therefore, then the number of the integrated points is very large, and thus the computation time to obtain the received signal for the whole reflector is quite long.

A new approach to efficiently calculate the received signal due to an extended reflector of arbitrary geometry has been derived by Professor Pedersen at Worcester Polytechnic Institute [9]: the *Diffraction Response for Extended Area Method* (DREAM method). It is based on the velocity potential impulse response and the basic idea is: Divide the reflector surface into planar reflector elements (tiles) of moderate dimensions, such that the tessellated tiles are chosen to approximate the reflector surface well. Then calculate the received signal contribution from each tile and sum the received signals. This overall principle is identical to the Huygens method, but the DREAM allows for much larger tiles, thus much less computation time. The problem becomes how to obtain the received signal from a moderate size flat reflector tile based on the diffraction responses of points on the tile plane, specifically, the corners and the center of the tile. As will be shown in section 2.5.1 and section 2.5.2, the spatial integration formulation in equation (2.15) and (2.25) for obtaining the received signal from a moderate size of the tile is replaced by a time domain filtering of a single diffraction response, as in equation (2.22) and (2.30). The time-domain filters are determined by the delay difference of the responses from the corners of the tile. At

present, the DREAM is implemented for the pulse-echo system in which the transmitter and receiver are planar circular piston transducers. However this algorithm can be applied to transmitting and receiving transducers with different geometry.

The DREAM algorithm has been implemented with both rectangular and triangular tiles, as will be discussed in following subsections.

2.5.1 Rectangular-tile-based DREAM (R-DREAM)

Figure 2.5 illustrates the pulse-echo system with a reflector in the form of a single rectangular tile. The side lengths of the tile are U and V in the u-direction and v-direction, respectively. It is noted that the rectangular tile is drawn much larger than it should be for the purpose of clarity. By applying (2.14), the received signal due to the single rectangular tile is

$$v_{tile}(t) = A_1 \int_0^U \int_0^V \cos[\boldsymbol{q}(u,v)] D(u,v,t) dv du = A_1 \cos[\boldsymbol{q}(\vec{r})] \int_0^U \int_0^V D(u,v,t) dv du \qquad (2.15)$$

where $\boldsymbol{q}(u,v)$ is the angle between the unit normal vector of the tile surface and the particle velocity vector at the position of the tile. Because the tile surface is planar, the $\boldsymbol{q}(u,v)$ is approximated as

$$\boldsymbol{q}(u,v) \cong \boldsymbol{q}(\vec{r}) = \hat{z} \bullet \vec{n} \qquad (2.16)$$

where $\hat{z}$ is a unit vector in the z-direction and $\vec{n}$ is the unit normal vector of the reflector surface. The basis for this approximation is the fact that the plane waves which make up the actual field from the transducer propagate mainly in the z-direction as long as the aperture of the transducer, measured in wavelengths, is large.

27
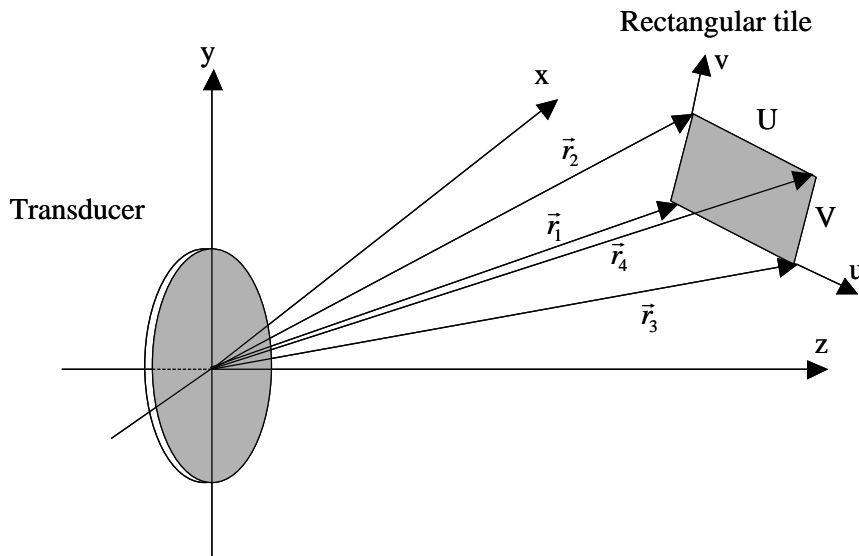
Figure 2.5 Illustration of the pulse-echo system with s single rectangular tile.

During the implementation of diffraction responses of the individual field points, it is found that, for points situated not too far away from each other, the responses are quite similar. The responses have similar shape or waveform, similar amplitude, except for different delays. (Detailed discussion and illustrations will be presented in section 3.2 "Implementation of DREAM", and an example of pulse-echo diffraction responses from four corners of a *1mm*1mm* tile will be presented in Figure 3.8). Therefore, the diffraction response of the center of the rectangular tile, with the propagation delay removed, can be used to approximate the diffraction response of the field points within the small rectangular area shown in Figure 2.5, apart from the roundtrip propagation delay associated with each field point. It is also possible to linearize the delay of the diffraction responses over the rectangular area, i.e., to find a delay linearization plane to represent the delay of individual diffraction response as a linear function of its coordinates *u* and *v*, based on the diffraction responses of the four

28

corners of the rectangular tile. For the delay linearization, the common propagation delay from transducer to tile and back is removed.
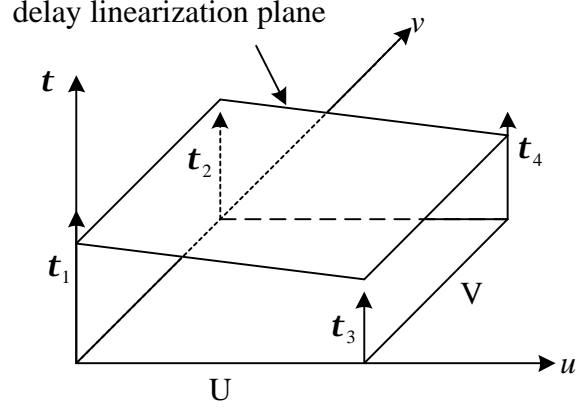
Figure 2.6 Delay linearization plane for the delays for the corners of a rectangular tile.

From planar geometry, we know that only three points are needed to specify a plane. Now there are four delay values available to specify the delay linearization plane, which means it is over-determined. A *Least Mean Square Error* (LMSE) method is applied to find an adaptive delay linearization plane which minimizes the mean square error of the four corners' delay values of the rectangular tile with respect to the delay linearization plane [9]. The plane is shown in Figure 2.6 and defined as

$$t(u,v) = t_1^c + \Gamma_u u + \Gamma_v v \tag{2.17}$$

where Γ_u and Γ_v are the delay slopes in the u and v-directions. Using LMSE method, we can derive that [10, section 3.1.2]:

$$\Gamma_u = \frac{1}{2U}(-t_1 + t_3 - t_2 + t_4)$$

$$\Gamma_v = \frac{1}{2V}(-t_1 - t_3 + t_2 + t_4)$$

and

$$t_1^c = \frac{1}{4}[3t_1 + t_2 + t_3 - t_4] \qquad (2.18)$$

The parameters t_1, t_2, t_3, t_4 are the delays for diffraction response of the four corners of the rectangular tile shown in Figure 2.5. With (2.17), the diffraction response for individual field points on the tile plane, $D(u,v,t)$, can be expressed as:

$$D(u,v,t) = D_0(\vec{r}_{center},t) \otimes d(t - t(u,v)) \qquad (2.19)$$

where $D_0(\vec{r}_{center},t)$ means the diffraction response of the individual field point at the center of the rectangular tile, with the propagation delay from the transducer and back removed. By means of (2.19), (2.15) becomes:

$$
\begin{aligned}
v_{tile}(t) &= A_1 \cos[q(\vec{r})]\int_0^U \int_0^V D(u,v,t)dvdu \\
&= A_1 \cos[q(\vec{r})]\int_0^U \int_0^V D_0(\vec{r}_{center},t) \otimes d(t - t(u,v))dvdu \qquad (2.20) \\
&= A_1 \cos[q(\vec{r})]D_0(\vec{r}_{center},t) \otimes \int_0^U \int_0^V d(t - t(u,v))dvdu
\end{aligned}
$$

It is easy to find, based on (2.17), that

$$d(t - t(u,v)) = d(t - t_1^c) \otimes d(t - \Gamma_u u) \otimes d(t - \Gamma_v v) \qquad (2.21)$$

With some straightforward operations on (2.20), the overall response from the rectangular tile can be found as:

$$v_{tile}(t) = A_1 \cos[q(\vec{r})]D_0(\vec{r}_{center},t) \otimes d(t - t_1^c) \otimes F(t) \qquad (2.22)$$

where $F(t)$ is the delay filter defined as:

$$F(t) = \int_0^U d(t - \Gamma_u u)du \otimes \int_0^V d(t - \Gamma_v v)dv = X_u(t) \otimes X_v(t) \qquad (2.23)$$

The functions $X_u(t)$ and $X_v(t)$ in (2.23) have been derived in [10] and are specified as follows:

$$X_u(t) = \int_0^U \boldsymbol{d}(t - \Gamma_u u) du = \begin{cases} 1/\Gamma_u, & 0 \le t < U\Gamma_u, & \Gamma_u > 0 \\ -1/\Gamma_u, & U\Gamma_u \le t < 0, & \Gamma_u < 0 \\ \boldsymbol{d}(t)U, & t = 0, & \Gamma_u = 0 \\ 0, & \text{otherwise} \end{cases}$$

$$X_v(t) = \int_0^V \boldsymbol{d}(t - \Gamma_v v) dv = \begin{cases} 1/\Gamma_v, & 0 \le t < V\Gamma_v, & \Gamma_v > 0 \\ -1/\Gamma_v, & V\Gamma_v \le t < 0, & \Gamma_v < 0 \\ \boldsymbol{d}(t)V, & t = 0, & \Gamma_v = 0 \\ 0, & \text{otherwise} \end{cases} \qquad (2.24)$$

In summary, by use of the delay interpolation method, we are able to calculate the delay slopes in the tile plane using the delays of tile corners, then formulate a delay filter which is used to filter the reference response, i.e., the diffraction response at the center of the rectangular tile, with the delay removed, This operation, with some scale factors added, produces the received signal for the given tile.

2.5.2 Triangular-tile-based DREAM (T-DREAM)

The pulse-echo system with a single triangular tile is shown in Figure 2.7, where the longest side of the triangular tile ABC is the side AC. It is noted that the triangular tile ABC is drawn much larger than it should be for the purpose of clarity. The *u-v* coordinate system is determined so that the *u*-axis is in the direction of the BC side and the origin is at the corner B, which is opposite to the longest side of the triangle.

31
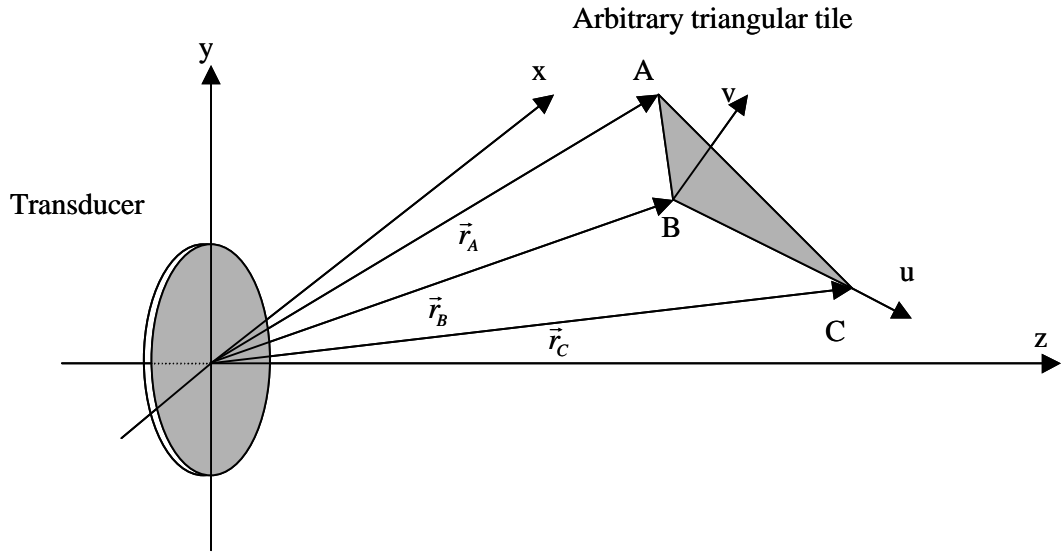
Figure 2.7 Illustration of the pulse-echo system with a single triangular tile.

By applying equation (2.14), the response due to the triangular tile is:

$$v_{tile}(t) = A_1 \cos[\boldsymbol{q}(\vec{r})] \iint_{\Delta} D(u,v,t)\,dv\,du \qquad (2.25)$$

In equation (2.25), Δ refers to the area of the triangular tile.
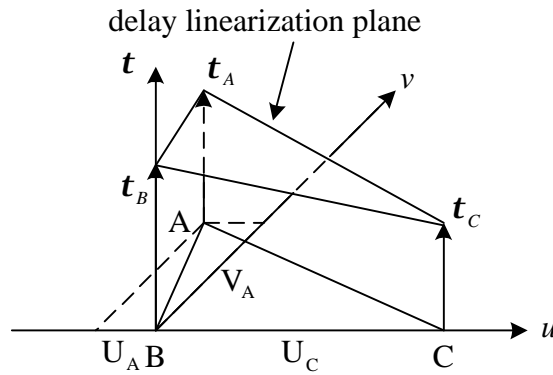
Figure 2.8 Delay linearization plane for the delays for the corners of a triangular tile.

Similar to the approach used for the rectangular-tile-based DREAM (R-DREAM), the spatial integration in equation (2.25) which is used to obtain the received signal from the triangular tile can be replaced by temporal filtering of a single

diffraction response. The delay filter is decided by the delay linearization plane, which is shown in Figure 2.8 and defined as:

$$t(u,v) = t_B + \Gamma_u u + \Gamma_v v \tag{2.26}$$

where Γ_u and Γ_v are the delay slopes in the u and v-directions. Based on equation (2.26), equation (2.25) becomes:

$$
\begin{aligned}
v_{tile}(t) &= A_1 \cos[\boldsymbol{q}(\vec{r})] \iint\limits_{\Delta} D_0(\vec{r}_{center}, t) \otimes \boldsymbol{d}(t - \boldsymbol{t}(u,v)) dv du \\
&= A_1 \cos[\boldsymbol{q}(\vec{r})] D_0(\vec{r}_{center}, t) \otimes \iint\limits_{\Delta} \boldsymbol{d}(t - \boldsymbol{t}_B - \Gamma_u u - \Gamma_v v) dv du
\end{aligned}
\tag{2.27}
$$

The delay filter function $F(t)$ is defined as:

$$F(t) = \iint\limits_{\Delta} \boldsymbol{d}(t - \boldsymbol{t}_B - \Gamma_u u - \Gamma_v v) dv du \tag{2.28}$$

and the delay filter function can be derived as [10, section 3.1.3]:

$$
F(t) = \begin{cases}
\dfrac{(t - \boldsymbol{t}_{min}) * 2\Delta}{(\boldsymbol{t}_{med} - \boldsymbol{t}_{min})(\boldsymbol{t}_{max} - \boldsymbol{t}_{min})}, & \boldsymbol{t}_{min} \leq t < \boldsymbol{t}_{med} \\[2ex]
\dfrac{(t - \boldsymbol{t}_{max}) * 2\Delta}{(\boldsymbol{t}_{max} - \boldsymbol{t}_{med})(\boldsymbol{t}_{min} - \boldsymbol{t}_{max})}, & \boldsymbol{t}_{med} \leq t < \boldsymbol{t}_{max} \\[2ex]
0, & \text{otherwise}
\end{cases}
\tag{2.29}
$$

where $\boldsymbol{t}_{min}$, $\boldsymbol{t}_{med}$, $\boldsymbol{t}_{max}$ are the smallest, middle, and largest of the delay values at the three corners of the triangular tile, respectively. The parameter Δ is the area of the triangular tile. The received signal from the triangular tile, $v_{tile}(t)$ can now be expressed as:

$$v_{tile}(t) = A_1 \cos[\boldsymbol{q}(\vec{r})] D_0(\vec{r}_{center}, t) \otimes F(t) \tag{2.30}$$

33

where $\boldsymbol{q}(\vec{r})$ is the angle defined in (2.16); and $D_0(\vec{r}_{center}, t)$ is the diffraction response (with the delay removed) of the center of the triangular tile.

It is readily seen that the delay linearization plane of T-DREAM is exactly determined by the delays of the three corners of the triangular element. For R-DREAM, the delay linearization plane is over-determined because of the availability of the delays of four corners; therefore, an approximated delay linearization plane is used. Another advantage of T-DREAM is that triangle provides a better tessellation and match to the surface of the reflectors, especially those with complicated shape. The triangular element is the standard element used in many finite element methods. Therefore, there are software packages for surface tessellation into triangular elements available [9] which makes the practical applications of T-DREAM much easier to implement. The advantage of R-DREAM is that the derivation of its delay linearization plane is much more straightforward than that of T-DREAM.

Now, based on the discussion in section 2.5.1 and 2.5.2, we observe that the calculation of the received signal for a flat tile of moderate size is carried out by calculating the diffraction responses at the corners and at the center of the tessellated tile, either rectangular or triangular, and finding the corresponding delay filter, followed by the convolution of the center response with the delay filter. The received signal from the entire reflector is finally found by applying (2.14):

$$v_{r,all}(t) = \sum_{all\ tiles} v_{tile}(t) \tag{2.31}$$

In summary, the data-processing procedure for DREAM method is as follows:

1) Tessellate the reflector into *M* tiles (rectangular or triangular), each of which are small enough to apply DREAM. Calculate the velocity potential impulse responses of the transmitter transducer and receiving transducers, using multi-rate digital signal processing algorithm with final sampling rate of 400MHz for the corners and the center of the tile: $h_t(\vec{r}, t)$ and $h_r(\vec{r}, t)$.

2) Calculate the diffraction response for the corners and the center:

$$D(\vec{r}, t) = \frac{\partial^2}{\partial t^2}[h_t(\vec{r}, t) \otimes h_r(\vec{r}, t)]$$

3) Determine delay filter based on the diffraction responses for the given tile.

4) Calculate the received signal from the tile using delay filtering: $v_{tile}(t)$.

5) Calculate overall received signal: $v_{all}(t) = \sum\limits_{all\,tiles}^{M} v_{tile}(t)$.

6) Calculate the spectra of received signal: $V_{all}(\boldsymbol{w}) = F[v_{all}(t)]$.

2.6 Modeling of Pulse-echo System with Annular Array Transducer

Now, the received signal of the pulse-echo system with planar circular transducers can be readily formulated, based on the discussion in sections 2.3, 2.4 and 2.5. The actual received signal from a reflector for a specific pair of transmitting and receiving transducers requires the analytic formulations of the velocity potential impulse response for a planar circular transducer which will be presented in section 3.1.1. The detailed implementation and results will be presented in following chapters.

The modeling concept can be extended for pulse-echo system with planar annular concentric array as well. Array transducers are of specific interest in this

research, as they allow a given transmitter field and a given receiver characteristics to be formulated for a specific measurement situation. The received signal from a given element in the array, due to transmission with any element in the same array, can be derived based on the superposition of the received signal from the planar circular transducer. Figure 2.9 indicates the geometry of an annular array transducer, which consists of N concentric rings.
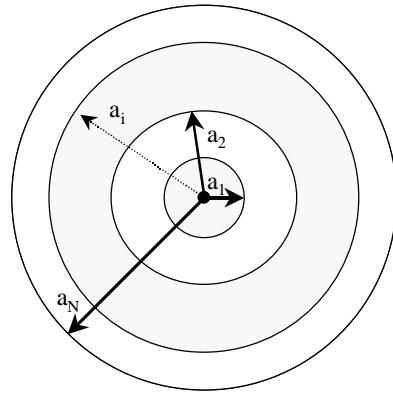
Figure 2.9 Geometry of an N-ring planar concentric annular array, indicating annulus outer radii a_i.

For a given reflector, an $N \times N$ signal matrix $\mathbf{V^{REFL}}(t)$ of the form shown in equation (2.32) can be generated in the pulse-echo system with N-ring annular array.

$$\mathbf{V^{REFL}}(t) = \begin{bmatrix} v_{1,1}^{REFL}(t) & . & . & v_{1,j}^{REFL}(t) & . & . & v_{1,N}^{REFL}(t) \\ . & . & . & . & . & . & . \\ v_{i,1}^{REFL}(t) & . & . & v_{i,j}^{REFL}(t) & . & . & v_{i,N}^{REFL}(t) \\ . & . & . & . & . & . & . \\ v_{N,1}^{REFL}(t) & . & . & v_{N,j}^{REFL}(t) & . & . & v_{N,N}^{REFL}(t) \end{bmatrix} \qquad (2.32)$$

The elements of the matrix are represented by $v_{i,j}^{REFL}(t)$, $i, j \in [1, N]$. $v_{i,j}^{REFL}(t)$ refers to the received signal from the entire reflector, produced with the ith ring as

transmitter and the jth ring as receiver. If the entire reflector is approximated by a number of small tiles, by applying equation (2.31), it is simple to get

$$v_{i,j}^{REFL}(t) = \sum_{all\ tiles} v_{i,j}(\vec{r},t) \tag{2.33}$$

where $v_{i,j}(\vec{r},t)$ is the receive signal from a single tile at location $\vec{r}$ on the reflector surface, produced with the ith ring as transmitter and the jth ring as receiver. In principle, $v_{i,j}(\vec{r},t)$ can be calculated using equation (2.14) and (2.12):

$$\begin{aligned} v_{i,j}(\vec{r},t) &= A_1 \int_A \cos[\boldsymbol{q}(\vec{r})]D(\vec{r},t)dA \\ &= A_1 \int_A \cos[\boldsymbol{q}(\vec{r})]\frac{\partial^2}{\partial t^2}[h_{i,i-1}(\vec{r},t) \otimes h_{j,j-1}(\vec{r},t)]dA \end{aligned} \tag{2.34}$$

where $h_{i,i-1}(\vec{r},t)$ and $h_{j,j-1}(\vec{r},t)$ are the velocity potential impulse responses at the field point for the ith ring as transmitter and the jth ring as receiver, respectively. Based on the assumption of linearity, we can write

$$\begin{aligned} \frac{\partial^2}{\partial t^2}[h_{i,i-1}(\vec{r},t) \otimes h_{j,j-1}(\vec{r},t)] &= \frac{\partial^2}{\partial t^2}\{[h_i(\vec{r},t) - h_{i-1}(\vec{r},t)] \otimes [h_j(\vec{r},t) - h_{j-1}(\vec{r},t)]\} \\ &= \frac{\partial^2}{\partial t^2}[h_i(\vec{r},t) \otimes h_j(\vec{r},t) - h_i(\vec{r},t) \otimes h_{j-1}(\vec{r},t) - h_{i-1}(\vec{r},t) \otimes h_j(\vec{r},t) + h_{i-1}(\vec{r},t) \otimes h_{j-1}(\vec{r},t)] \\ &= D_{i,j}(\vec{r},t) - D_{i,j-1}(\vec{r},t) - D_{i-1,j}(\vec{r},t) + D_{i-1,j-1}(\vec{r},t) \end{aligned} \tag{2.35}$$

In equation (2.35), $h_i(\vec{r},t)$ is the velocity potential impulse responses at the field point for the planar circular transducer with radius of a_i shown in Figure 2.9 and $D_{i,j}(\vec{r},t)$ is the diffraction impulse response at the field point for a pulse-echo system with a planar circular transmitter of radius a_i and a planar circular receiver of radius a_j. As can readily be seen, now, equation (2.34) can be expanded into four terms as in equation (2.36):

37

$$v_{i,j}(\vec{r},t) = A_1 \int_A \cos[\boldsymbol{q}(\vec{r})][D_{i,j}(\vec{r},t) - D_{i,j-1}(\vec{r},t) - D_{i-1,j}(\vec{r},t) + D_{i-1,j-1}(\vec{r},t)]dA$$
$$= A_1 \int_A \cos[\boldsymbol{q}(\vec{r})]D_{i,j}(\vec{r},t)dA - A_1 \int_A \cos[\boldsymbol{q}(\vec{r})]D_{i,j-1}(\vec{r},t)dA$$
$$- A_1 \int_A \cos[\boldsymbol{q}(\vec{r})]D_{i-1,j}(\vec{r},t)dA + A_1 \int_A \cos[\boldsymbol{q}(\vec{r})]D_{i-1,j-1}(\vec{r},t)dA$$

$$(2.36)$$

Each term in (2.36) represents the received signal from different combinations of planar circular transmitting and receiving transducers, and can be calculated using either equation (2.22) or (2.30), based on the shape of the tiles used to tessellate the entire reflector. Now, by combining equation (2.33) and (2.36), $v_{i,j}^{REFL}(t)$ can readily be calculated. And the summed output voltage from the entire annular array transducer can be calculated as

$$v_{total}(t) = \sum_{i=1}^{N}\sum_{j=1}^{N} A_i A_j' v_{i,j}^{REFL}(t) \otimes \boldsymbol{d}(t - (\boldsymbol{t}_i + \boldsymbol{t}_j')) \qquad (2.37)$$

where A_i is an amplitude scale factor, assigned to the ith element in the array in transmitting mode, $A_j \mathcal{C}$ is an amplitude scale factor, assigned to the jth element in the array in receiving mode, $\boldsymbol{t}_i$ is the (positive) delay assigned to the ith element in the array in transmitting mode, τ_j' is the (positive) delay assigned to the jth element in the array in receiving mode and $\otimes$ indicates convolution.

Chapter 3

Implementation of Simulation System

In this chapter, the details about the implementation of ultrasound pulse-echo simulation system are discussed. Two methods are implemented to calculate the received signal due to an extended reflector surface, namely Huygens method and DREAM method. In this chapter, all implementations are based on planar piston transducers. However, the approaches can also be applied to other transducer types. In section 3.1, we discuss the Huygens method. In section 3.2, the DREAM method is discussed. Finally, the mechanism for the simulation coding is described in term of efficiency.

3.1 Implementation of Huygens Method

Recall that the expression for the received signal due to an extended reflector was derived in (2.14) in section 2.4. Equation (2.14) is repeated below for convenience:

$$v_r(t) = A_1 \sum \cos[\boldsymbol{q}(\vec{r})] D(\vec{r}, t) \Delta A \tag{3.1}$$

In equation (3.1), A_1 is a system related constant as defined in section 2.2; $\boldsymbol{q}(\vec{r})$ is the

angle between the unit normal vector of the reflector surface and the particle velocity

vector at the field point $\vec{r}$; $D(\vec{r},t)$ is the diffraction response of one single field point

and ΔA is the area of a small planar reflecting surface, located at the field point.

Generally, $\boldsymbol{q}(\vec{r})$ is very computationally demanding to evaluate. As long as the field

point is not very close to the surface of the transducer, it is valid to approximate that

$$\boldsymbol{q}(\vec{r}) = \hat{z} \bullet \vec{n} \tag{3.2}$$

where $\hat{z}$ is a unit vector in the z-direction and $\vec{n}$ is the unit normal vector of the

reflector surface. Recall the definition of diffraction response in (2.12) in section 2.2, it

is restated here for convenience because it will be referred to quite often in the

following parts of the chapter:

$$D(\vec{r},t) = \frac{\partial^2}{\partial t^2}[h_t(\vec{r},t) \otimes h_r(\vec{r},t)] \tag{3.3}$$

3.1.1 Calculation of Velocity Potential Impulse Response for One Single Field Point

From (3.1) and (3.3), it is seen that the first step to calculate the diffraction

response is to calculate the velocity potential impulse response $h(\vec{r},t)$ for the baffled

transmitter and receiver. As described in section 2.3, the *multi-rate digital signal*

processing algorithm is used to calculate the velocity potential based on the analytical

solution to velocity potential impulse response. Figure 3.1 illustrates a specific

simulation scenario with a baffled planar circular transducer and two field points.
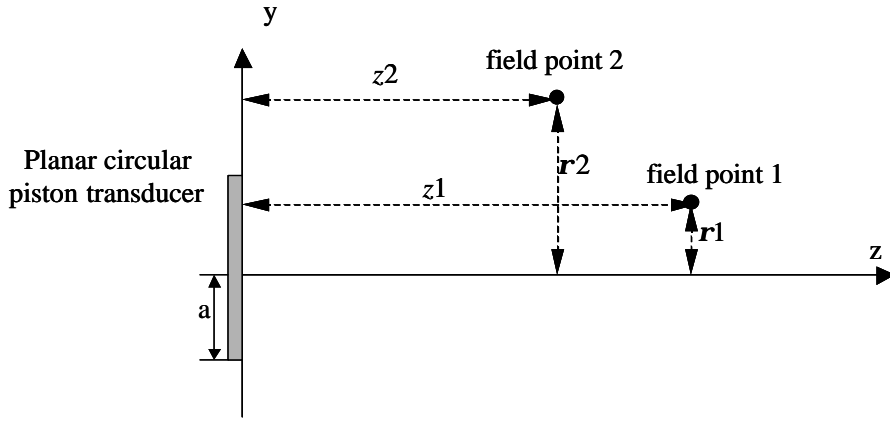
Figure 3.1: The side view of the geometry of the simulation scenario with a planar circular piston transducer and two field points. The radius of the transducer is *a=12.7mm*. The radial distance of the field point 1, *r*1, is less than *a*; the radial distance of the field point 2, *r*2, is larger than *a*.

The analytical solutions of $h(\vec{r},t)$ for this case was derived in [18]

$$h(\vec{r},t)=\begin{cases}\begin{matrix}0 & t<t_0\\c & t_0\leq t<t_1\\ \dfrac{c}{p}\Omega(\vec{r},t) & t_1\leq t<t_2\\0 & t_2\leq t\end{matrix}\end{cases}\quad r\leq a \qquad(3.4)$$

$$h(\vec{r},t)=\begin{cases}\begin{matrix}0 & t<t_1\\ \dfrac{c}{p}\Omega(\vec{r},t) & t_1\leq t<t_2\\0 & t_2\leq t\end{matrix}\end{cases}\quad r>a \qquad(3.5)$$

The variables t_0, t_1, t_2 and $\Omega(\vec{r},t)$ are given as:

$$t_0=z/c$$
$$t_1=\sqrt{(a-\mathbf{r})^2+z^2}/c$$
$$t_2=\sqrt{(a+\mathbf{r})^2+z^2}/c \qquad(3.6)$$

$$\Omega(\vec{r},t)=\arccos\left(\frac{c^2t^2+\mathbf{r}^2-z^2-a^2}{2\mathbf{r}\sqrt{c^2t^2-z^2}}\right) \qquad(3.7)$$

41

In equations (3.4) to (3.7), the parameter z is the axial distance from the plane of the transducer surface to the field point; $\boldsymbol{r}$ is the radial distance from the field point to the z axis; and a is the radius of the planar circular piston transducer. The distances z and $\boldsymbol{r}$ are illustrated in Figure 3.1.

Velocity potential responses for a planar piston a=12.7mm,z$_p$=50mm
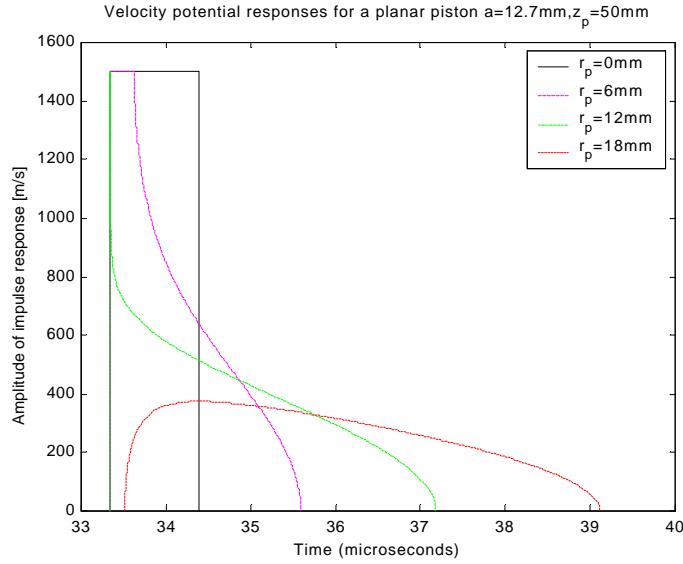
Figure 3.2 The velocity potential responses at different field points for a planar circular piston of radius a=12.7*mm*. The axial distance of the points is 50*mm*. The radial distance of the points are 0*mm*, 6*mm*, 12*mm*, 18*mm* respectively.

Figure 3.2 illustrates the velocity potential impulse responses $h(\vec{r}, t)$ for four different radial distances from a planar circular piston, which are obtained from the analytical solutions given in (3.4) and (3.5). The analytical solutions to $h(\vec{r}, t)$ needs to be discretized before we can make use of them to calculate the diffraction response. The sampling rate to discretize $h(\vec{r}, t)$ must be high enough to make aliasing effects negligible. As can be found from the shapes of the response in Figure 3.2, the bandwidth of the velocity potential impulse response increases as the field point moves closer to the transducer axis, namely, the z-axis. When it moves onto the z-axis, the

bandwidth of the velocity potential impulse response reaches the maximum and the $h(\vec{r},t)$ has the form of a rectangular function. The thin solid line in Figure 3.3 illustrates the envelope of the spectrum of the on-axis $h(\vec{r},t)$, which is a *sinc* function and denoted $\tilde{H}(f)$.
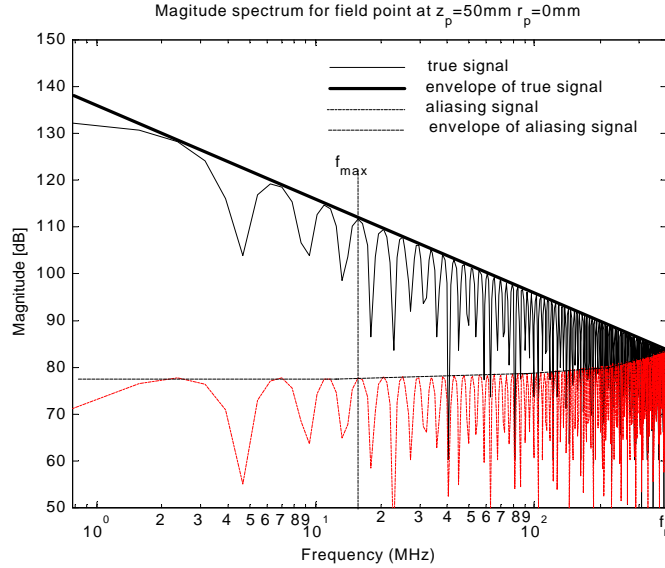
Figure 3.3 Magnitude spectrum of velocity potential function of on-axis field point, illustrating how to determine approximate aliasing error due to its discrete representation.

If the sampling rate is f_s and $f_n = f_s/2$ is the corresponding Nyquist frequency, the dominating contribution to aliasing signal at a given frequency is approximately equal to $\tilde{H}(f_s - f)$ and the dash dot line in Figure 3.3 illustrates the aliasing signal. We can determine the approximate aliasing error using the envelopes of the true and aliasing signal. The envelope of $\tilde{H}(f)$ is denoted $\tilde{E}(f)$ and can be deduced to be [15]:

$$\tilde{E}(f) = c/\pi f \qquad (3.8)$$

Similarly, the envelope of the aliasing signal is:

43

$$\tilde{E}(f_s - f) = c / [\boldsymbol{p}(f_s - f)] \tag{3.9}$$

If *Err* is defined as the ratio of the aliasing signal frequency magnitude and the true signal frequency magnitude, it can be approximated as [15]:

$$Err = \frac{\tilde{E}(f_s - f)}{\tilde{E}(f)} = \frac{c / [\boldsymbol{p}(f_s - f)]}{c / [\boldsymbol{p}f]} = \frac{f}{f_s - f} \tag{3.10}$$

Therefore, the minimal sampling rate f_s which satisfies the aliasing error requirement is:

$$f_s \geq f_{\max}(1 + 1 / Err) \tag{3.11}$$

where f_{max} is the highest frequency of interest, i.e., f_{max} = 15.625MHz in our case. For Err = 0.3%, i.e., the aliasing signal frequency magnitude is at least 50 dB below the true signal frequency magnitude at frequency f, we can easily derive that $f_s \geq 5.3\,\text{GHz}$. When the field points moves away from the axis, the duration of the velocity potential increases. Meanwhile, the spectrum of the velocity potentials becomes more narrow, so that much lower sampling rates can be used to keep the level of aliasing error acceptable low. One example is given in Figure 3.4 and Figure 3.5. The sampling rate is 800MHz. Within the frequency range that we are interested in, i.e., the frequency less than 15.625Mhz, for the on-axis field point, the aliasing signal is only about 30 dB below the true signal at some frequency points, which corresponds to about 3% aliasing error. While for the field point with 18*mm* radial distance, the aliasing signals are almost 50 dB below the true signal, which corresponds to 0.3% aliasing error. So the minimal sampling frequency, f_{sm}, which is used to sample the long temporal velocity potential of field points far from the source, may be set equal to 800MHz with

acceptable aliasing error. When the field point moves closer to the *z*-axis, the duration of the velocity potential decreases which allows higher sampling rate if the sample sequence length is the same for all field points. One thing to keep in mind is that the minimal global sampling frequency is dependent on different applications and the maximal aliasing error allowed.
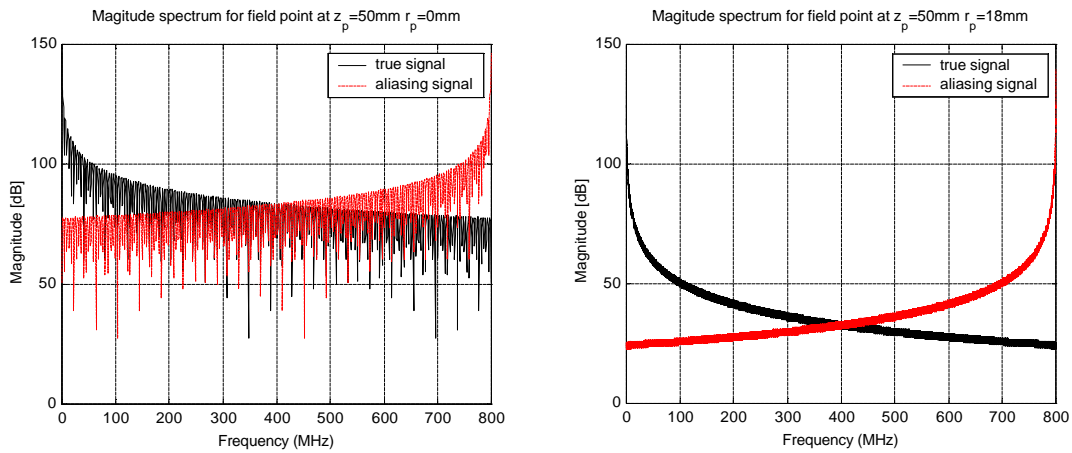
Figure 3.4 Illustration of the magnitude spectrum with the aliasing signal for two different field points for a planar circular piston of radius a=12.7*mm*. The sampling rate is 800MHz. The axial distance of the points is 50*mm*. The radial distance of the points are 0*mm*, 18*mm* respectively.
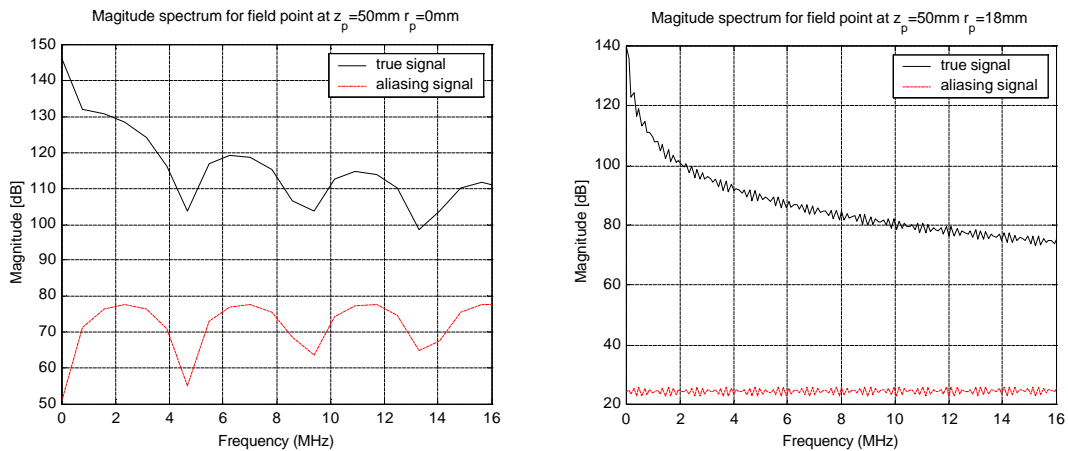
Figure 3.5 Enlarged version of Figure 3.4 to highlight the frequency range of interest, i.e. 0-15.625MHz.

For a planar circular transducer of radius a, the duration of the velocity potential impulse response, Δt, is always less than the travel time of the wave across the transducer surface, which is [15]:

$$\Delta t_{max} = 2a/c \tag{3.12}$$

In equation (3.12), the parameter c is the sound speed. Based on the specified minimal global sampling frequency f_{sm} and the maximal duration of the velocity potential impulse response Δt_{max}, the *maximum sample sequence length N* for a specific transducer can be obtained as $N \geq \Delta t_{max} \times f_{sm}$, which guarantees the sampling rates for all observation points are valid, i.e., all sampling rates are higher than or equal to the minimal global sampling rate f_{sm} as shown in equation (3.13)

$$f_{min} = N / \Delta t_{max} \geq f_{sm} \tag{3.13}$$

Thus, from (3.12) and (3.13), it can be derived that if

$$N \geq 2 * a * f_{sm} / c \tag{3.14}$$

there exists no invalid sampling regions. In our case, with transducer radius 12.7*mm* and 800MHz minimal sampling rate, N should be larger or equal to *13547*. For the convenience of following calculation, N is set to *16384*, i.e., 2^{14}.

Based on the maximum sample sequence length N, the sampling rate at any field point can be calculated by

$$f_{sl} = N / \Delta t \tag{3.15}$$

where Δt is the duration of the velocity potential at that field point. f_{sl} is called *local sampling rate* because it is specified for each individual field point. The actual sampling is carried out using *global sampling rate* for efficient calculation. The global sampling

rate is defined to be an even multiple of the predetermined minimum global sampling rate f_{sm}. As discussed above, f_{sm} is 800Mhz for our application, therefore, the global sampling rates can take on a limited number of specific values, 6.4GHz, 3.2GHz, 1.6GHz, etc. The chosen sampling rate for a given observation point is the largest global sampling rate less than or equal to the local sampling frequency, f_{sl}, of that point [15]. The conversion from local sampling rate to global sampling rates is illustrated in the first two rows in Table 3.1.

Table 3.1: Local to global sampling rate translation and down-sampling ratio used in DREAM.

Local sampling rate: f_{sl} (GHz)	f_{sl} >=6.4	f_{sl} <=6.4 f_{sl} >=3.2	f_{sl} <=3.2 f_{sl} >=1.6	f_{sl} <=1.6 f_{sl} >=0.8	f_{sl} <=0.8
Global sampling rate: f_{sg} (GHz)	6.4	3.2	1.6	0.8	Invalid
Down-sampling ratio, M:	16	8	4	2	
Final sampling rate (MHz):	400 MHz				

The frequency range that we are interested in is from *dc* component to 15.625MHz. If the high sampling rates, such as 6.4GHz, 3.2GHz, etc., were to be kept in the following calculation, a lot of resources, such as the computer memory, CPU time would be wasted. In addition, when the sampling rate is too high, too few frequency-domain samples are left in the relatively narrow frequency range of interest. Hence, the discretized velocity potential has to be down-sampled to lower sampling rate for further calculation. For our purpose, i.e., to calculate the diffraction response by twice differentiation of the convolution of velocity potentials, the sampling rate of 400MHz is necessary for the direct digital differentiation to be carried out with negligible error [9], as will be discussed in detail in section 3.1.2. Therefore, the final

down-sampling rate is set to be 400MHz and the third row of Table 3.1 indicates the down-sampling ratio corresponding to different global sampling rate. For other applications, such as mapping of pressure fields, it is convenient to use a second stage of low-pass-filtering and decimation to decrease the final sampling rate to a much smaller value.

In order to down-sample the high frequency velocity potential while minimizing the signal aliasing, the velocity potential must be processed by a low-pass filter prior to the decimation operation. A Linear-Phase Digital Filter is chosen to low-pass-filter the high frequency velocity potential because of the phase-sensitivity of pulse-echo ultrasound system. In order to simplify the design work, save space when storing the filter coefficients and create a more efficient decimation calculation, only one single lowpass digital filter was designed with a given set of normalized design parameters in our implementation. The absolute passband and stopband cutoff frequencies of such a filter vary with the sampling frequency of its input sequence. The absolute passband cutoff frequency must be larger than the desired baseband before the decimation, which is the multiplication of the down-sampling ratio M and the maximum frequency of our interest, i.e., f_{max}=15.625MHz. Therefore, the normalized passband cutoff frequency $\boldsymbol{w}_{pb}$ can be decided by [15]:

$$\boldsymbol{w}_{pb} > \frac{f_{max} M_{max}}{f_{sg\,max}} \tag{3.16}$$

In equations (3.16), the parameter M_{max} is the largest down-sampling ratio, i.e., 16 in Table 3.1 and f_{sgmax} is the largest input global sampling rate, i.e., 6.4GHz in Table 3.1. To prevent aliasing of the decimated output, the stopband cutoff frequency must be less

than the Nyquist frequency of the subsequent decimation stage, which is $f_{sg}/M/2$. But because the frequency of our interest is in the range from dc to f_{max}=15.625MHz, there is no aliasing introduced in the frequency range of our interest as long as the stopband cutoff frequency is less than $f_{sg}/M - f_{max}$. Therefore, the normalized stopband cutoff frequency $\boldsymbol{w}_{sb}$ can be decided by [15]:

$$\boldsymbol{w}_{sb} < \frac{1}{M_{max}} - \frac{f_{max}}{f_{sg\,max}} \tag{3.17}$$

For maximum computational efficiency, $\boldsymbol{w}_{pb}$ is chosen to be as small as possible, and $\boldsymbol{w}_{sb}$ is chosen to be as large as possible as long as they satisfy (3.16) and (3.17). The Matlab function "*REMEZ*" is used to obtain the coefficients of the low-pass-filter based on the parameters decided by (3.16) and (3.17).

During the actual implementation, the low-pass-filtering and decimation are implemented at the same time, which means that the filter operates on the decimated signal directly instead of decimating the low-pass-filtered signal. Therefore, the computation is more efficient.

3.1.2   Calculation of Diffraction Response for One Single Field Point

In section 3.1.1, the discretized velocity potential at any field point is obtained with same final sampling rate 400MHz for all field points. Now (3.3) is applied to calculate the diffraction response in two steps.

1) Convolution of the velocity potential for the transmitter with the velocity potential for the receiver: $h_t(\vec{r},t)$ and $h_r(\vec{r},t)$. This step is implemented with Matlab

command "*CONV*". Figure 3.7 part (a) illustrates the convolution signals for a pulse-echo system using the same planar circular piston as the transmitter and receiver.

2) Double differentiation of the convolution result with respect to time to obtain diffraction response. The differentiation is implemented using a simplified direct digital differentiation method, which is based on:

$$\frac{\partial f}{\partial t}\Big|_{t=(t_0+t_1)/2} \approx \frac{f(t_1) - f(t_0)}{t_1 - t_0} \tag{3.18}$$

The transfer function of (3.18) is

$$H(f) = j2f_s \sin(\mathbf{p}f / f_s) \tag{3.19}$$

As well known, the transfer function of an ideal differentiator is:

$$H_{ideal}(f) = j2\mathbf{p}f \tag{3.20}$$

By comparing (3.19) and (3.20), we can find there is no phase difference between the ideal differentiator and the simple differentiator because both expressions are purely imaginary. The magnitude error of the simple differentiator is:

$$\frac{|H_{ideal}(f)| - |H(f)|}{|H_{ideal}(f)|} = \frac{2\mathbf{p}f - 2f_s \sin(\mathbf{p}f / f_s)}{2\mathbf{p}f} = 1 - \sin(\mathbf{p}f / f_s)/(\mathbf{p}f / f_x) \tag{3.21}$$

And Figure 3.6 illustrates the relative magnitude error derived in (3.21) as a function of normalized frequency f/f_s:
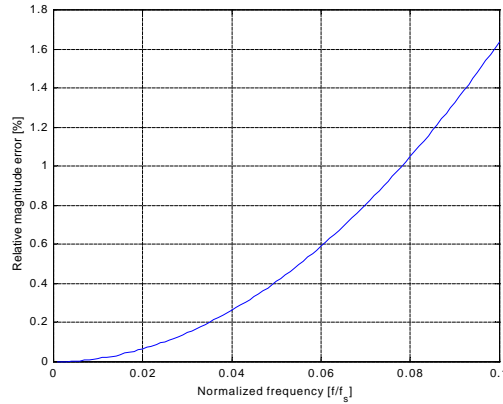
Figure 3.6 The relative magnitude error of the transfer functions for the simple differentiator.

From Figure 3.6, it can be seen that the error magnitude increases dramatically when the normalized frequency f/f_s increases. For the maximal frequency of interest, i.e., $f_{max} = 15.625$MHz, if the sampling rate is $f_s = 400$MHz, then $f_{max}/f_s = 0.0391$ and the magnitude error is around 0.25% as can be observed in Figure 3.6 or be calculated by equation (3.21). This magnitude error is small enough to be negligible.

Figure 3.7 part (b) and (c) illustrate the first and second differentiation result respectively. Because the signal, resulting from second differentiation, for the field point with radial distance 18mm is much smaller than others, it is not shown in part (c). Figure 3.7 part (d) is the enlarged version of part (c) to shown more details for field points with large radial distance.
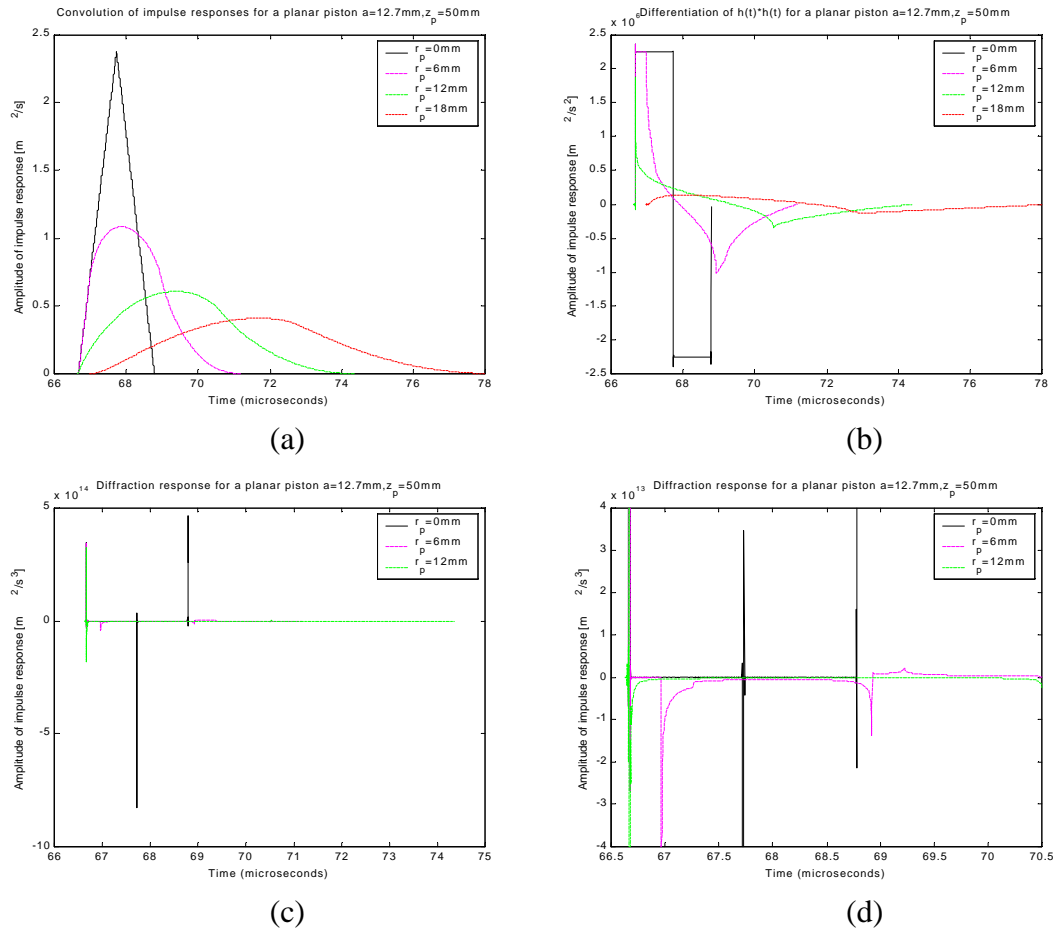
Figure 3.7 Illustration of the steps involved in the calculation of diffraction responses. A planar circular piston with radius a=12.7 *mm* acts as both transmitter and receiver. The axial distance is 50 *mm* and the radial distance is 0 *mm*, 6 *mm*, 12 *mm*, 18 *mm* respectively. a) The convolution of the velocity potential of transmitter and receiver. b) The first differentiation of the convolution results. c) The second differentiation of the convolution results. d) Enlarged version of c)

3.1.3 Huygens Method for the Received Signal from Extended Reflector

After the extended reflector is tessellated into "microtiles" and the diffraction responses from individual field point are obtained, (3.1) can be applied to obtain the diffraction response from the entire extended reflector by the integration of the individual response over the reflector surface. In this context, a "microtile" is a small rectangular planar surface whose dimension must be small relative to the wavelength at

52

the highest frequency considered. The data-processing procedures of the Huygens method is summarized as follows:

1). Tessellate the reflector into N tiles which are small enough to be treated as simple sources. A simple source means a reflector with dimensions much smaller than a wavelength.

2). Calculate the velocity potential impulse response, use the multi-rate digital signal processing algorithm with final sampling rate of 400MHz, for each point: $h(\vec{r},t)$

3). Calculate the diffraction response for each point: $D(\vec{r},t) = \dfrac{\partial^2}{\partial t^2}[h(\vec{r},t) \otimes h(\vec{r},t)]$

4). Calculate received signal from the extended reflector using equation (3.1):

$$v_r(t) = A_1 \sum_{all\ tiles}^{N} \cos[\boldsymbol{q}(\vec{r})]D(\vec{r},t)\Delta A$$

During the implementation of Huygens method, there are two things to keep in mind:

1) If the response of central point of rectangle is used for the integration instead of that of one corner point of the rectangle, the accuracy of the result may be quite different for some cases.

2) The largest size of the microtile, which can be chosen to obtain acceptable accuracy for the linear assumption, is quite dependent on geometry and the tilt angle of the surface.

Different implementation results for Huygens method will be shown and discussed in Chapter 4 "Evaluation of Huygens method".

3.2 Implementation of DREAM Method

Figure 3.8 illustrates the pulse-echo diffraction responses from four corners of a $1mm*1mm$ rectangular planar reflector surface with its center at $(x,y,z)=(3,3,50)mm$ and tilted $10°$ in the y-direction. In this case, a planar circular piston with radius $a=12.7mm$ acts as both the transmitter and receiver. For the purpose of clarity, the first positively going impulses have been truncated at $5*10^{13} m^2/s^3$, while they actually extend to about $3.7*10^{14} m^2/s^3$. By examining the diffraction responses at the four corners of the tile with moderate dimension in Figure 3.8, we can find that the shape of the waveforms from the four corner points are very similar, while the time shift of the waveforms are quite different. It can also be found that the diffraction responses consist of several short "impulsive" segments, separated by regions of very low amplitude and different segments exhibit different amount of time shift. Another observation is that the number of segments for the four corners is the same. To compensate for the different time shift of different segments, i.e., the time compression/expansion of the diffraction response, a segmentation method is used to divide the responses into several segments. Then the equivalence between spatial integration and delay filtering, which is discussed in section 2.5, is applied to segments to obtain the corresponding contribution by individual segments for the entire tile. The overall response from the entire tile is the sum of the responses of the individual segments as in (3.22):

$$v_{tile}(t) = A_1 * \cos(\boldsymbol{q}(\vec{r}_r)) * \sum_{i=1}^{n\_seg} [\boldsymbol{d}(t-\boldsymbol{t}_{r,i}) \otimes seg_{r,i}(\vec{r}_r,t) \otimes F_i(t)] \qquad (3.22)$$

where *n_seg* is the number of segments; $t_{r,i}$ is the delay of the *i*th segment of the diffraction response of the reference point; $seg_{r,i}$ is the responses of the *i*th segment of the diffraction response of the reference point, with associated propagation delay removed; $F_i(t)$ is the delay filter obtained for the *i*th segment.
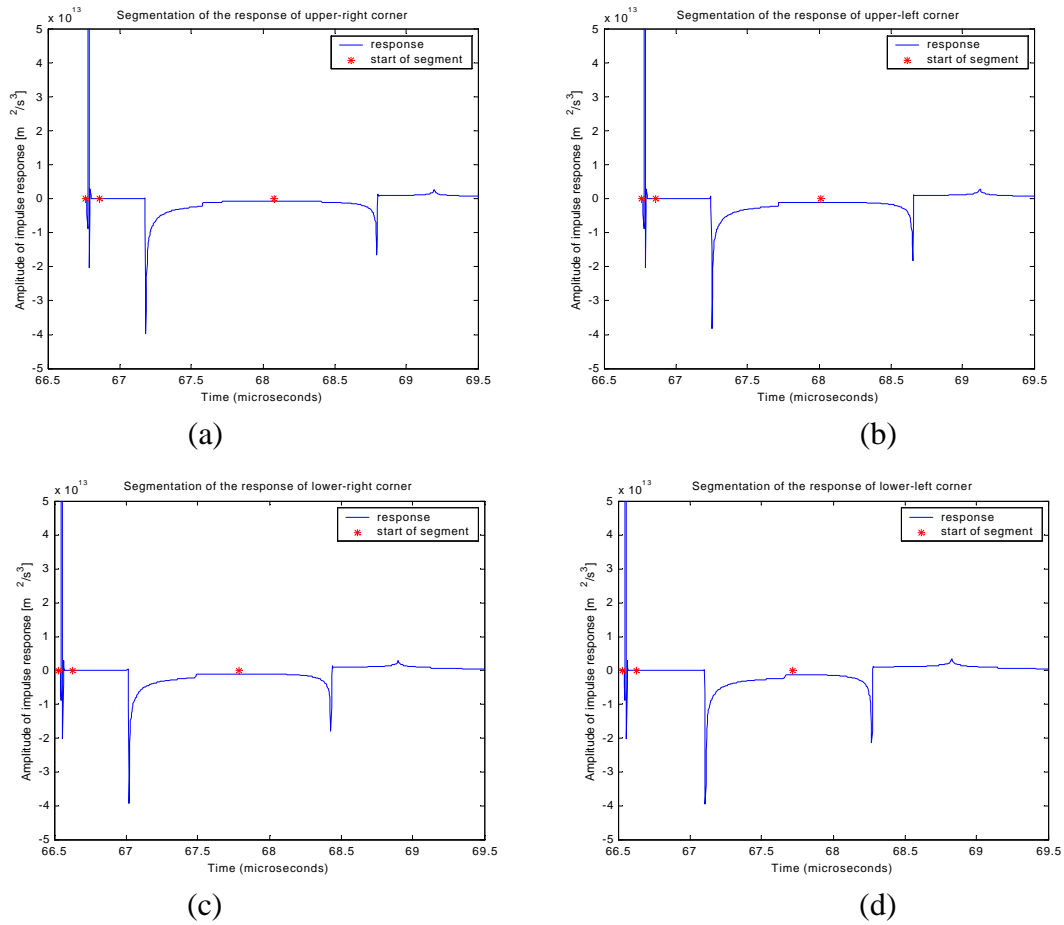
Figure 3.8: Example of pulse-echo diffraction responses from four corners of a *1mm*1mm* tile as well as the segmentation (3 segments) of the diffraction responses. A planar circular piston with radius a=12.7*mm* acts as both transmitter and receiver. The tile centers at (*x,y,z*)=(3,3,50)*mm* and tilted 10° in the *y*-direction.

It is important to note that the similarity of the diffraction responses from the corners of the tile (either rectangular tile or triangular tile) is the basis for the DREAM method, or, specifically, the delay filtering approximation of the spatial integration. For

some cases, for example, when the radius of the transmitter is 12.7mm and the radius of the receiver is 3mm, smaller tile size must be chosen so that the diffraction responses from the corners of the tile do not differ too much. This issue will be discussed in details from section 5.1 to 5.5 in chapter 5.

3.2.1 Segmentation

As shown in Figure 3.8, the diffraction responses can generally be divided into a limited number of segments such that the signal level around each segment boundary is almost zero. In addition, different segments exhibit different time shift, therefore, it is necessary to perform a separate delay filtering for each of these segments. The procedure of the segmentation of a single response is as follows:

1) Find the peak points of the overall diffraction response: Find the maximal amplitude among the peak points of the response first and call it "the largest response amplitude". Then identify all the extremes; if the amplitude of one extreme is larger than a specified fraction of "the largest response amplitude", it can be considered as peak point of the diffraction response. For our application, the fractional value is set to 20%.

2) Segment the signal with one peak point per segment and set the segment boundaries to occur at the time instance between the peak points where the amplitude is closest to zero.

3) Check the boundaries between segments. If the amplitude at a given boundary is above a specified fraction, i.e., 20% of the smaller amplitude of peak points, the two segments separated by that boundary are merged into one segment.

The stars "*" in Figure 3.8 illustrate the segmentation of the diffraction responses for the four corners of the tile described above.

3.2.2 Delay Interpolation

As discussed in section 2.5, a delay filter is used to filter the response of one reference point to obtain the overall response of the entire tile. The delay filter is based on the delay slopes in the tile plane which is calculated by delay interpolation method. Therefore, it is meaningful to check the delay interpolation method first. Now the delay interpolation method is used to estimate the diffraction response of the field point c in Figure 3.9, based on the diffraction responses of other field points on the same plane as it. Point c is the central point of the rectangle $ABCD$. The length of the rectangle is U and the width is V. For the convenience of formulation, it is supposed that there are three segments of the diffraction response. The formulation of the time delay interpolation is similar for Rectangular-tile-based DREAM (R-DREAM) and Triangular-tile-based DREAM (T-DREAM), while not exactly the same. We discuss the two DREAM methods separately.

(a)   (b)
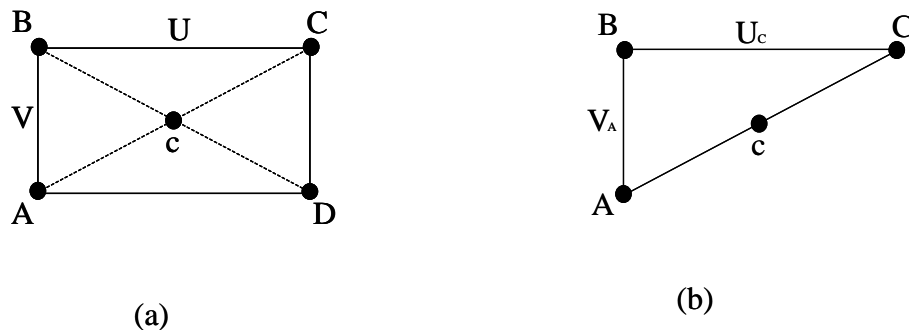
Figure 3.9 The simulation scenario for the delay interpolation method.

As a test of the validity of the delay interpolation method, we will first try to estimate the diffraction response of point c based on the diffraction responses of point A, B, C, D which corresponds to the R-DREAM. The response of one corner (e.g. the upper-right corner B) is chosen to be the reference response. The three segments of the response of this corner are time shifted by individual delays calculated by the delay interpolation method and then added to form the total estimated response at the center of the tile. Mathematically, $seg_{B,1}(\vec{r},t)$, $seg_{B,2}(\vec{r},t)$, $seg_{B,3}(\vec{r},t)$ are defined as the responses of each segment of the diffraction response at the point B, with the associated propagation delay $t_{B,1}(\vec{r})$, $t_{B,2}(\vec{r})$, $t_{B,3}(\vec{r})$ *removed*. $t_{i,j}(\vec{r})$ is defined as the delay of the jth segment of the response for the ith corner. Using delay interpolation method [9], we are able to estimate the delay of the three segments of the center point: $t_{c,1}(\vec{r})$, $t_{c,2}(\vec{r})$ and $t_{c,3}(\vec{r})$, given $t_{i,j}(\vec{r})$ (i=A,B,C,D and j=1,2,3) and the length U and width V of the tile:

$$t_{c,j}(\vec{r}) = t_{B,j}^{c} + \Gamma_{u,j} * \frac{U}{2} + \Gamma_{v,j} * \frac{V}{2} \qquad (3.23)$$

where

$$t_{B,j}^{c} = \frac{1}{4}[3t_{B,j}(\vec{r}) + t_{C,j}(\vec{r}) + t_{A,j}(\vec{r}) - t_{D,j}(\vec{r})];$$

$$\Gamma_{u,j} = \frac{1}{2U}(-t_{B,j} + t_{A,j} - t_{C,j} + t_{D,j});$$

$$\Gamma_{v,j} = \frac{1}{2V}(-t_{B,j} - t_{A,j} + t_{C,j} + t_{D,j});$$

Then the estimated diffraction response of the center of the tile is given by:

$$\sum_{j=1}^{3} seg_{B,j}(\vec{r}_B,t) \otimes d(t - t_{c,j}) \tag{3.24}$$

Similarly, we tried to estimate the diffraction response of point c based on the diffraction responses of point A, B, C which corresponds to the T-DREAM. The triangle is redrawn in Figure 3.9 part (b) for purpose of clarity. The response of corner B was chosen to be the reference response. As discussed in section 2.5.2, by applying equation (2.26), we are able to estimate the delay of the three segments of the center point: $t_{c,1}(\vec{r})$, $t_{c,2}(\vec{r})$ and $t_{c,3}(\vec{r})$, given $t_{i,j}(\vec{r})$ ($i = A, B, C$ and $j=1,2,3$) as:

$$t_{c,j}(\vec{r}) = t_{B,j} + \Gamma_{u,j} * \frac{U_C}{2} + \Gamma_{v,j} * \frac{V_A}{2} \tag{3.25}$$

In equation (3.25), U_C is the length of side BC; V_A is the v-direction component of side BA, but because in this case, the triangle ABC has been chosen to be a right triangle, V_A is the length of side BA; $\Gamma_{u,j}$ and $\Gamma_{v,j}$ are the delay slopes in the u- and v- directions, respectively, for the jth segment of the diffraction response. By plugging the delay values of the point C and A into equation (3.25), it is easy to find $\Gamma_{u,j}$ and $\Gamma_{v,j}$ as

$$\Gamma_{u,j} = (t_{C,j} - t_{B,j})/U_C$$

$$\Gamma_{v,j} = (t_{A,j} - t_{B,j})/V_A \tag{3.26}$$

Then the estimated diffraction response of point c is readily obtained by equation (3.24).

Figure 3.10 shows the results for diffraction response of the central point of specific rectangular tile discussed in section 3.2.1. Also for the purpose of clarity, the

59

positively going impulse for the first segments has been truncated at $5*10^{13} m^2/s^3$, while it actually extends to about $3.7*10^{14} m^2/s^3$.
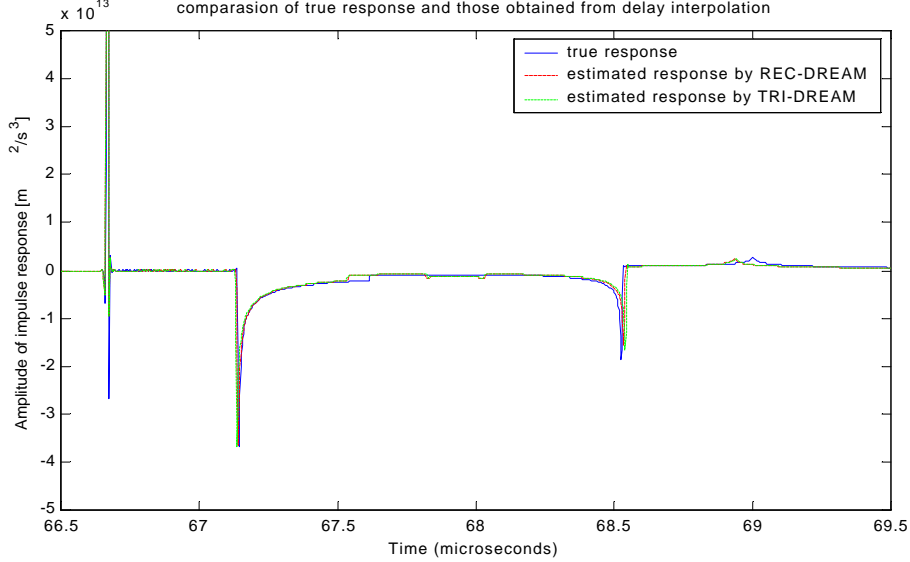
Figure 3.10: Example of how well the estimated pulse-echo diffraction responses obtained by R-DREAM and T-DREAM delay interpolation method compares to the true response at the center of $1mm*1mm$ planar rectangular tile. The tile centers at $(x,y,z)=(3,3,50)mm$ and tilted 10° in the y-direction.

It can be found that the results of the time delay interpolation model based on rectangular tile and triangular tile closely approximate the true response. The good match between the real response and the estimated responses obtained by the delay interpolation method verifies that the delay linearization plane can be used to linearize the diffraction responses on the planar tile area, either rectangular or triangular tile.

3.2.3   DREAM Method

Based on the discussion in section 2.5, section 3.2.1 and section 3.2.2, the data-processing procedures of the DREAM method is summarized as following:

1). Tessellate the reflector into M tiles (rectangular or triangular), which are small enough to apply DREAM. Normally, $M << N$ where N is the number of tiles tessellated by Hugyens method.

2). Calculate the velocity potential impulse responses of the transmitter transducer and receiving transducers, using multi-rate digital signal processing algorithm with final sampling rate of 400MHz for the corners and the center of the tile: $h_t(\bar{r},t)$ and $h_r(\bar{r},t)$.

3). Calculate the diffraction response for the corners and the center of the tile:

$$D(\bar{r},t) = \frac{\partial^2}{\partial t^2}[h_t(\bar{r},t) \otimes h_r(\bar{r},t)]$$

4) Segment the diffraction responses from the corners and the center.

5). Determine delay filters for each segment of the responses of the tile.

6). Calculate the received signal from each tile using segmentation and delay filtering: $v_{tile}(t)$.

7) Calculate overall received signal from the entire reflector: $v_{all}(t) = \sum_{all\ tiles}^{M} v_{tile}(t)$.

Different implementation results for DREAM method will be shown and discussed in Chapter 5 "Evaluation of DREAM method".

3.3 Mechanism for Coding

One of the most important issues we concern about on the modeling methods is the computational time of the algorithms. One factor effecting the execution time is the language used for coding.

Currently, Matlab and C are widely used for scientific and engineering numeric computation. Matlab is an interactive, matrix-based system and its strength lies in the fact that a solution to the complex numerical problems can be developed easily and in a fraction of the time required with C. Matlab can also be easily extended to create new commands and functions. In the terms of signal processing, there are a lot of well-developed functions in Matlab, such as Fast Fourier transform (FFT), inverse FFT, functions for filter analysis, implementation and design, etc., not to mention such basic operations as correlation, convolution and so on. It is also very convenient to visualize the results obtained in Matlab. The drawback of Matlab is that the execution time is much larger for some mathematics operations than C codes, especially for "for-loop" operations. In order to take advantage of both Matlab and C, we decided the mechanism for the coding as follows: The overall code should be controlled from Matlab, with the computationally intensive parts written in C. The C subroutines are compiled into MEX-file routines. After MEX files are generated, there is no need for a C compiler and the MEX-file routines are callable directly from Matlab as other Matlab functions.

To have an idea about how well our coding mechanism works, the computational time using two implementation methods are compared for the task of calculating acoustic pressure field, one is pure Matlab, and the other is C embedded Matlab. It is found that if all the multi-rate algorithm was implemented in Matlab, it would take about 71 minutes to calculate the complex pressure field of one frequency points over a 50*50 grid of spatial observation points and 76 minutes for all 2048 frequencies (from 0Hz to 62.5MHz with a resolution of roughly 30.52KHz). However if we calculate the impulse velocity potential functions and implement the low-pass-filter

and decimator in C, it takes only 59 seconds (compared with 70 minutes) and 74 seconds (compared with 76 minutes) to produce the exactly same results as we obtained before. The computation time used to calculate the received signal from pulse-echo system will be presented in chapter 5, together with description of the specific simulation scenarios and other parameters.

Chapter 4

Evaluation of Huygens Method

In section 2.4 and section 3.1, we discussed the principle and implementation of Huygens method. In this chapter, Huygens method will be used for calculating the received signals in ultrasound pulse-echo systems for different parameter values, such as tile dimension, and different simulation scenarios. Huygens method is based on the integration of the response from a very large number of micro-tiles which form the surface of the entire reflector. The dimension of these micro-tiles must be much smaller than the wavelength at the highest frequency of interest, and they can be viewed as rectangular or square tiles with a finite small area.

First, in section 4.1, the different results are compared for two implementation methods: (1) The received signal from the entire reflector is obtained based on the diffraction response at central point of the micro-tile. (2) The received signal from the entire reflector is obtained based on the diffraction response at one corner point of the micro-tile. It is found that the first method produces a higher accuracy. Therefore, the Huygens method, based on the response of central point of the micro-tile, is used throughout the following sections in this thesis. In section 4.2, the accuracy of the spectra of the received signal obtained with different tile size is investigated for

different simulation scenarios. In using Huygens method, it is preferable for the micro-tile size to be as large as possible to reduce computation time. However, the larger the tiles are, the larger is also the error. Considering the trade-off between the computational time and accuracy, we need to find the *optimal tile size,* which is the size of the micro-tiles we use to tessellate the entire reflector. It is found that the accuracy of the spectra of the received signal obtained with a given tile size is dependent on the parameters of the specific simulation scenario such as the tilt angle of the reflector surface, the radial location relative to the radius of the transducer, shape and size of reflector, etc. Therefore, the "optimal micro-tile size" is found empirically by "trial and error" method, and the optimal size is dependent on specific simulation scenario.

4.1 Center Summation versus Corner Summation Huygens Methods

Recall that the expression for the received signal due to an extended reflector was derived in (2.13) in section 2.4. Equation (2.13) is repeated below for convenience:

$$v_r(t) = A_1 \sum \cos[\boldsymbol{q}(\vec{r})] D(\vec{r}, t) \Delta A \tag{4.1}$$

The extended reflector is tessellated into micro-tiles which are small enough to be treated as simple sources (reflectors with dimensions much smaller than a wavelength). These micro-tiles can be viewed as square or rectangular tiles with finite small area, and the diffraction response can be calculated at any *real point* inside the rectangle. The "real point" means an abstract point with infinite small dimension. In practice, either the corner or the center of the rectangle is used for convenience. Thus, the received signal from the extended reflector can be calculated either by the summation of the

response of the corners of the tessellated micro-tiles or by the summation of the response of the centers of the tessellated micro-tiles. Because the center is normally considered a good approximation for all points within the area of the micro-tile, intuitively, we think that summation using the diffraction response at the center should produce better result than summation using the diffraction response at the corner, if the choice of the diffraction response really makes difference. Now both ways are evaluated and compared for calculating the received signal due to a $1mm*1mm$ square reflector. The reflector is centered at $(r, z) = (7.07, 50)$ mm and is tilted $10°$ relative to the transducer surface. The parameter r is the radial distance of the center of the square reflector from the z-axis and z is the axial distance from the transducer. Two planar circular piston transducers of radius $3mm$ and $6mm$ are used as transmitter and receiver, respectively. This simulation scenario is chosen as a representative scenario. Square tessellation tiles with different side lengths are used for the summation: $500mm$, $200mm$, $100mm$, $50mm$, $20mm$, $10mm$, $5mm$. Because the spectrum of the received signal is used for the error analyses, the following discussion takes place in the frequency domain. The accuracy of the spectrum of the integrated diffraction responses are compared using the *Mean Square Error* (MSE) method, and the MSE is calculated as:

$$\text{MSE} = \frac{\int_0^{15MHz} (|V_r(f)| - |V_{ref}(f)|)^2 \, df}{\int_0^{15MHz} |V_{ref}(f)|^2 \, df} * 100\% \tag{4.2}$$

In equation (4.2), $V_r(f)$ is the frequency spectrum of $v_r(t)$, the signal whose accuracy is to be evaluated. $V_{ref}(f)$ is the frequency spectrum of the *reference signal* $v_{ref}(t)$ (the reference signal is to be explained shortly). In our calculation, a discrete approximation

of the integral in (4.2) is used with a frequency interval Df = 400MHz/8192 = 48.8KHz, which is the frequency resolution of discrete Fourier Transform. The MSE is calculated only for the frequency range of our interest: [0-15MHz]. The smallest tile size to be considered is 5mm which is much smaller than the smallest wavelength in the frequency range of interest, i.e. l_{min}=1500/(15×10^6) [m] = 100mm. The difference between the results obtained by the summation of the diffraction responses at the center and corner of the 5mm tile is just 0.0002% using (4.2), which means they are very close indeed. Thus, it is reasonable to use the result obtained by summation of the diffraction responses at the center of 5mm tile as a reference signal, $V_{ref}(f)$, when evaluating the accuracy of the center summation method for different tile sizes. Similarly, the result obtained by summation of the diffraction responses at the corner of 5mm tile is considered a reference signal when evaluating the accuracy of the corner summation method for different tile sizes. Table 4.1 illustrates the accuracy obtained by two methods with different tile sizes. As can be found from Table 4.1, when "center summation" method is used, the results obtained with 10mm and 20mm tile size are the same as that obtained with 5mm tile size. In contrast, for "corner summation" method, there still exists some difference between the results obtained with 10mm and 5mm tile sizes, although very little. Also can be found from Table 4.1, when the tile size increases to 50mm, 100mm and larger, the "corner summation" method produces much larger error compared with "center summation" method. Based on this, we are confident in saying that the "center summation" method produces higher accuracy than "corner summation" method, especially when the tile size is relatively large. Therefore, center

summation Huygens method will be used as a reference for the remaining part of the thesis.

Table 4.1: Mean Square Error of the spectra of the received signals obtained by center and corner summation methods and with different tile size. The reflector is a 1*mm**1*mm* square reflector and centers at (*r, z*) = (7.07, 50) *mm* and tilted 10° relative to the transducer surface. Two planar circular piston transducers of radius 3*mm* and 6*mm* are used as transmitter and receiver, respectively. The results obtained by the summation of the diffraction responses of the 5*mm* tiles are used as reference signal for each method, respectively. The unit of MSE is "%".

	5*mm*	10*mm*	20*mm*	50*mm*	100*mm*	200*mm*	500*mm*
center summation	0	0	0	0.0003	0.0047	0.1879	21.8272
corner summation	0	0.0002	0.0021	0.0208	0.1083	0.7905	48.1841

Figure 4.1 illustrates the spectra of the received signals obtained by center summation Huygens method using different tile size from the 1*mm**1*mm* square reflector described above. For the purpose of clarity, the spectra obtained with 10*mm* and 20*mm* tile size are not shown because they are too close to the spectrum obtained with 5*mm* tile size. In using Huygens method, the micro-tile size should preferably be as large as possible to reduce the computational time. From Figure 4.1, we can observe that the result obtained with 50*mm* tile size is also quite close to that obtained with 5*mm* tile size, while the result obtained with 100*mm* tile size has relatively larger difference. As a result, considering the trade-off between the computation time and accuracy, we choose the micro-tile size of 50*mm* to be the *optimal micro-tile size* for this specific simulation scenario.
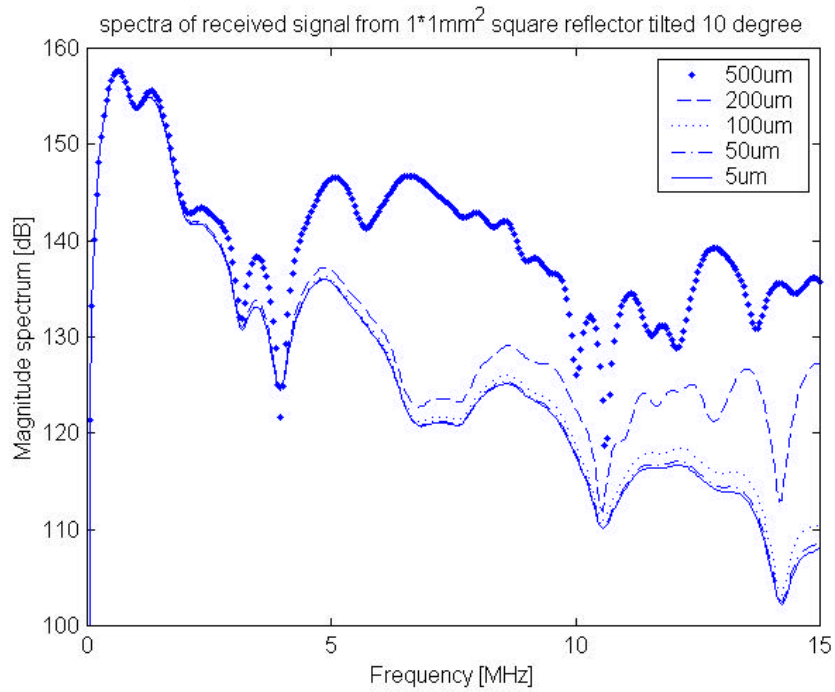
Figure 4.1 Spectra of received signal from a 1*mm**1*mm* square reflector to show the different results obtained by center summation Huygens method using different tile size. The reflector centers at (*r, z*) = (7.07, 50) *mm* and tilted 10° relative to the transducer surface. Two planar circular piston transducers of radius 3*mm* and 6*mm* are used as transmitter and receiver, respectively.

4.2 Optimal Tile Size for Huygens Method

In the previous section, we checked the different results obtained by the center summation and corner summation Huygens method and found that the center summation method produces more accurate results. It is also found in previous section that the optimal micro-tile size is 50*mm* which is the largest tile size that can be used to obtain the received signal with high accuracy. It should be emphasized that the optimal micro-tile size is very dependent on tilt angle of the reflector surface, the location, shape and size of reflector, the size of the transducers, etc.

69

Table 4.2 illustrates the accuracy of the results obtained with different tile sizes for different simulation scenarios. The reflector and the transducers are the same as those in section 4.1 except that the reflector is tilted 2° and 20°, respectively, relative to the transducer surface. To make the comparison convenient, the results obtained when the reflector is tilted 10° are repeated in Table 4.2. It can be found that the different tilt angle really makes a difference.

Table 4.2: Mean Square Error of the spectra of the received signals obtained by center summation Huygens method with different tile size and tilt angle of reflector. The reflector is a 1*mm**1*mm* square reflector and centers at (*r, z*) = (7.07, 50)*mm*. The reflector is tilted 2°, 10°, 20° relative to the transducer surface, respectively. Two planar circular piston transducers of radius 3*mm* and 6*mm* are used as transmitter and receiver, respectively. The results obtained by the summation of the diffraction responses of the 5*mm* tiles are used as reference signal for each case. The unit of MSE is "%".

	5*mm*	10*mm*	20*mm*	50*mm*	100*mm*	200*mm*	500*mm*
Tilted 2°	0	0	0	0	0.0004	0.0075	0.9266
Tilted 10°	0	0	0	0.0003	0.0047	0.1879	21.8272
Tilted 20°	0	0	0.0001	0.0017	0.0436	8.0159	73.8032

Figure 4.2 and Figure 4.3 illustrate the spectra of the received signals obtained for a 2° tilted reflector and a 20° tilted reflector, respectively. For the purpose of clarity, the spectra obtained with 10*mm* and 20*mm* tile size are not shown in Figure 4.2 because they are too close to that obtained with the 5*mm* tile size. From Figure 4.2, we can observe that the result obtained with 100*mm* tile size is quite close to that obtained with 5*mm* tile size, while the results obtained with 200*mm* tile size has an observable difference. As a result, we may choose the tile size of 100*mm* to be the optimal tile size when the reflector is tilted 2°. However, when the reflector is tilted 20°, as shown in Figure 4.3, we find that the received signal obtained with 100*mm* tile size is quite

different from that obtained with 5*mm*. Even the result obtained with 50*mm* tile size is

not close to that obtained with 5*mm*. Therefore, we choose the tile size of 20*mm* to be the

optimal tile size for this specific simulation scenario. In Figure 4.3, for the purpose of

clarity, the received signal obtained with 10*mm* and 500*mm* tile size are not shown

because the former is too close to that obtained with 5*mm* tile size, while the latter is too

different from that obtained with 5*mm* tile size.
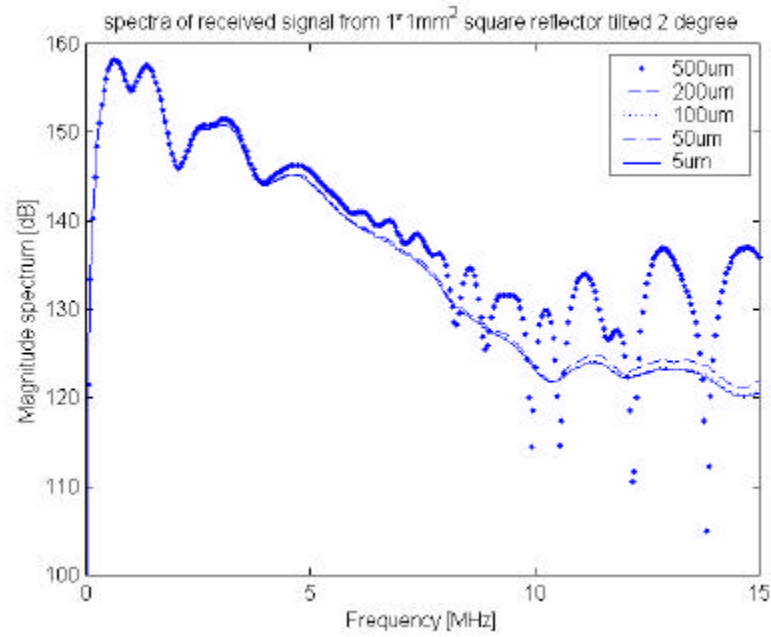
Figure 4.2 Spectra of received signal from a 1*mm**1*mm* square reflector to show the different results obtained by center summation Huygens method using different tile size. The reflector centers at (*r*, *z*) = (7.07, 50) *mm* and tilted 2° relative to the transducer surface. Two planar circular piston transducers of radius 3*mm* and 6*mm* are used as transmitter and receiver, respectively.
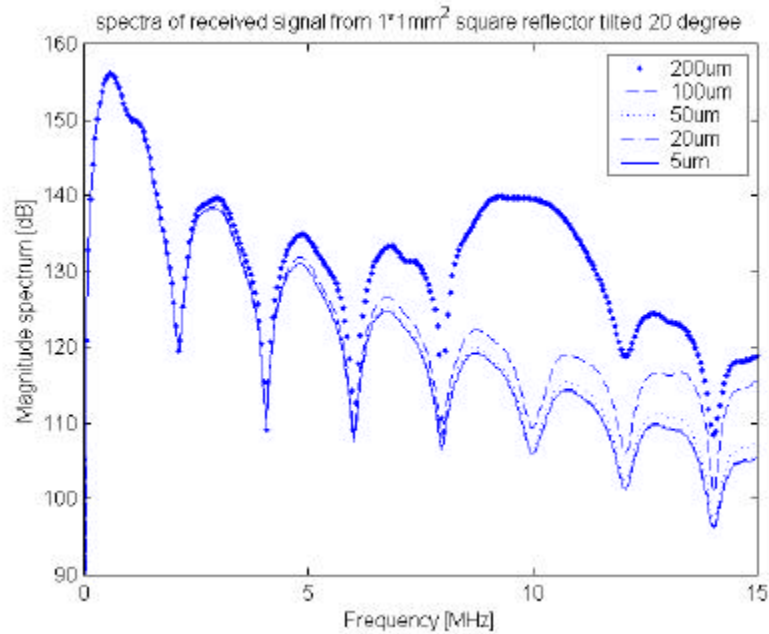
Figure 4.3 Spectra of received signal from a 1*mm**1*mm* square reflector to show the different results obtained by center summation Huygens method using different tile size. The reflector centers at (*r, z*) = (7.07, 50) *mm* and tilted 20° relative to the transducer surface. Two planar circular piston transducers of radius 3*mm* and 6*mm* are used as transmitter and receiver, respectively.

From Table 4.2 and from the comparison between Figure 4.1, Figure 4.2 and Figure 4.3, we have found that the accuracy of the results obtained with certain tile sizes is dependent on the tilt angle of the reflector surface. It is also found that the accuracy of the results obtained with certain tile size is dependent on many other factors, such as the location, shape and size of the reflector, and the transducer size. We will now present several different simulation scenarios to give a general illustration of this issue. Case 1: The reflector is a 1*mm**1*mm* square flat reflector, tilted 10° relative to the transducer surface and centered at (*r, z*) = (0.707, 50) *mm.* Two planar circular piston transducers of radius 3*mm* and 6*mm* are used as transmitter and receiver, respectively; Case 2: The simulation parameters are the same as those in case 1, except that the reflector is centered at (*r, z*) = (7.07, 50) *mm*; Case 3: The simulation parameters are the

same as those in case 1, except that the reflector is centered at (r, z) = (14.14, 50) *mm*;

Case 4, 5 and 6: The simulation parameters are the same as those in case 1, 2 and 3, respectively, except that a planar circular piston transducer of radius 12.7*mm* is used as both the transmitter and receiver; Case 7: The simulation parameters are the same as those in case 2, except that the reflector is a curved one. It is a 60° arc of a cylinder with radius = 1*mm* and length = 1*mm*, with the arc centered at (r, z) = (7.07, 50) *mm*. Table 4.3 summarizes the different parameters for the seven different simulation scenarios described above. Table 4.4 presents the accuracy of the results obtained for those seven cases. In the same way as in Table 4.1 and Table 4.2, the results obtained with the 5***mm*** tiles are used as reference signal for each case. We observe that the accuracy of the received signals obtained with certain tile size is quite dependent on the situation of the specific simulation scenario. To give a graphical comparison between the simulation scenarios considered, we have included Figure 4.4 to illustrate the spectra of the received signals for "case 1" to "case 6". In Figure 4.5, the spectra of the received signals for "case 2" and "case 7" are presented to make comparison between the received signals of flat and curved reflectors.

Table 4.3 Summary of the parameters used for different simulation scenarios discussed above.

	reflector center position	transmitter radius	receiver radius	reflector shape
case 1	(0.707, 50) *mm*	$a_t = 3$ *mm*	$a_r = 6$ *mm*	flat
case 2	(7.07, 50) *mm*	$a_t = 3$ *mm*	$a_r = 6$ *mm*	flat
case 3	(14.14, 50) *mm*	$a_t = 3$ *mm*	$a_r = 6$ *mm*	flat
case 4	(0.707, 50) *mm*	$a_t = 12.7$ *mm*	$a_r = 12.7$ *mm*	flat
case 5	(7.07, 50) *mm*	$a_t = 12.7$ *mm*	$a_r = 12.7$ *mm*	flat
case 6	(14.14, 50) *mm*	$a_t = 12.7$ *mm*	$a_r = 12.7$ *mm*	flat
case 7	(7.07, 50) *mm*	$a_t = 3$ *mm*	$a_r = 6$ *mm*	curved

Table 4.4: Mean square error of the spectra of the received signals obtained by center summation Huygens method for different simulation scenarios. The unit of MSE is "%".

	5*mm*	10*mm*	20*mm*	50*mm*	100*mm*	200*mm*	500*mm*
case 1	0	0	0.0001	0.0051	0.0929	2.974	403.5808
case 2	0	0	0	0.0003	0.0047	0.1879	21.8272
case 3	0	0	0	0	0.0004	0.0189	1.5636
case 4	0	0	0	0.0006	0.0115	0.507	42.1549
case 5	0	0	0	0.0017	0.0315	1.061	107.178
case 6	0	0	0	0.0006	0.0111	0.3969	39.7812
case 7	0	0	0.0001	0.0097	1.086	21.2744	127.8321
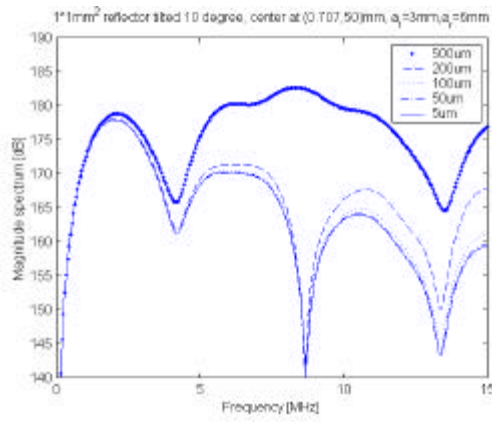
(a) Case 1
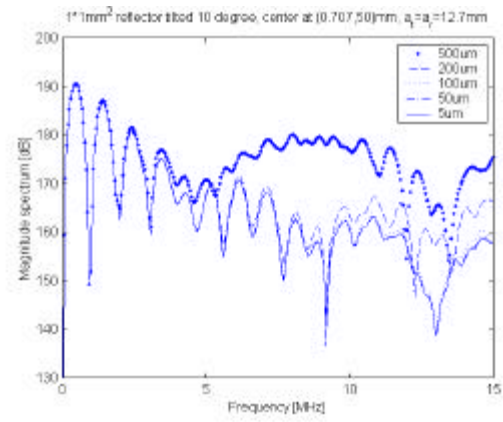
(b) Case 4
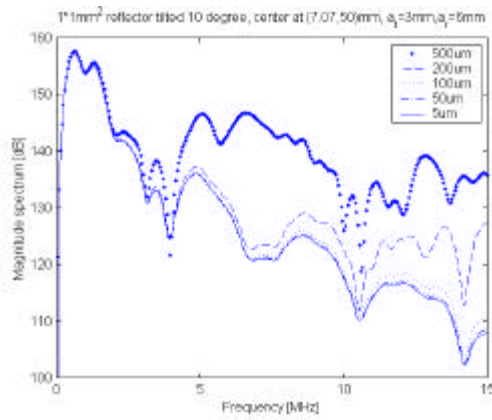
(c) Case 2
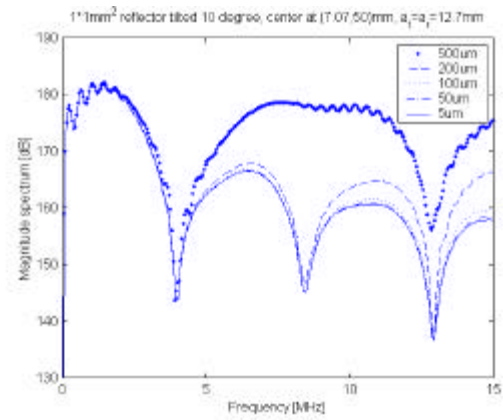
(d) Case 5
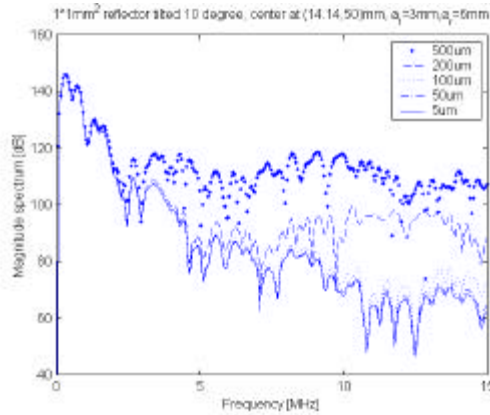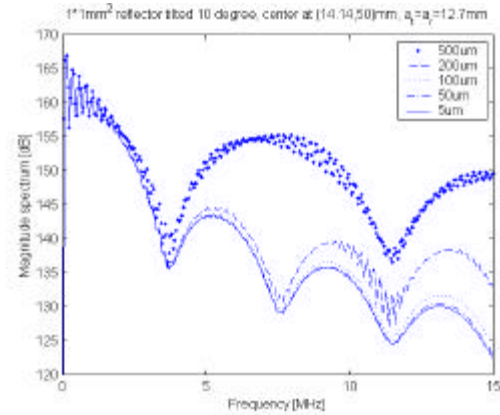
(e) Case 3   (f) Case 6

Figure 4.4 Spectra of the received signals obtained by center summation Huygens method for 6 different simulation scenarios: case 1 to case 6 as described above.
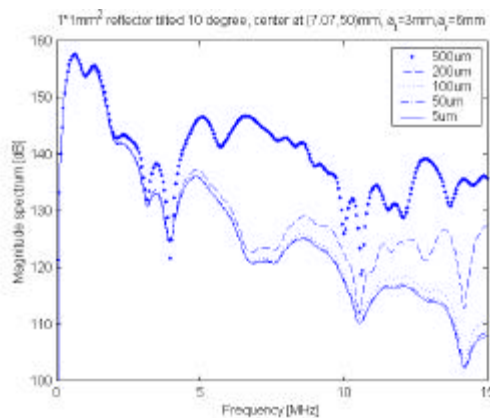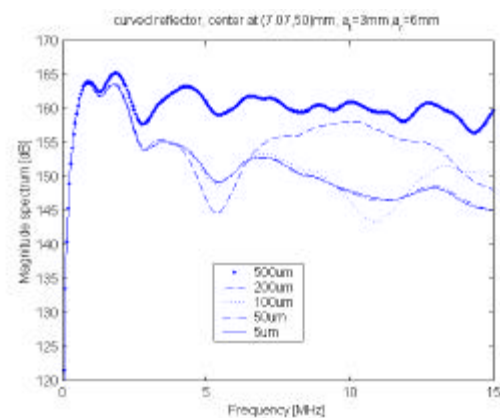
(a) Case 2   (b) Case 7

Figure 4.5 Spectra of the received signals obtained by center summation Huygens method for two different simulation scenarios: case 2 and case 7 as described above.

As can be observed from Table 4.4, when two planar circular piston transducers of radius 3*mm* and 6*mm* are used as transmitter and receiver, respectively, the error produced by a given tile size decreases when the radial distance of the reflector increases from 0.707*mm* to 7.07*mm* and then to 14.14*mm*; however, when a planar circular piston transducer of radius 12.7*mm* is used as both the transmitter and receiver,

75

the error produced by a given tile size increases and then decreases as the radial distance increases from 0.707*mm* to 7.07*mm* and then to 14.14*mm*. Such results are surprising because, normally, we think that the error should change in a similar way when the radial distance of the reflector changes.

We have calculated the spectra of the received signals from the 1*mm*1mm* square flat reflector, tilted 10° relative to the transducer surface, for a number of simulation scenarios by changing the size of the transmitter and receiver as well as changing the radial position of the reflector. For all these simulation scenarios, the axial distance of the center of the reflector is $z = 50mm$ and the radial distance of the center of the reflector is r = 0*mm, 0.707mm, 1.414mm, 2.828mm, 4.243mm, 5.657mm, 7.07mm, 8.485mm, 9.899mm, 11.31mm, 12.73mm, 14.14mm, 15.56mm, 16.97mm,* respectively. Figure 4.6 illustrates the relationship between the radial distance and the Mean Square Error (MSE), obtained with the 100***mm*** tile size for different simulation scenarios. It is another form of evidence that the accuracy of the received signals obtained with given tile size is quite dependent on the position of the reflector as well as the size of the transmitting and receiving transducer. More discussion about Figure 4.6 will be presented in section 5.2 in chapter 5.
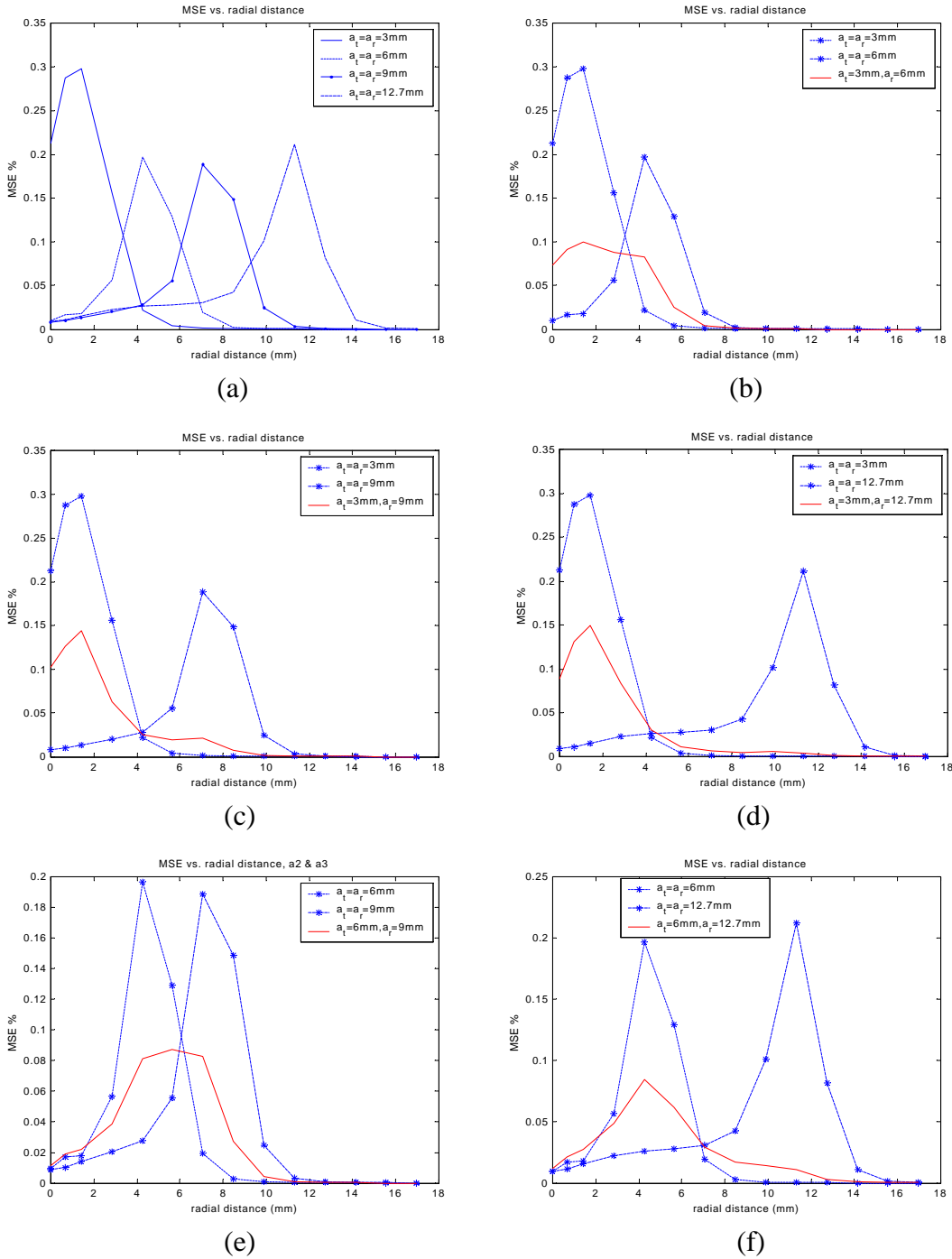
Figure 4.6 The relationship between the radial distance and the Mean Square Error of the spectra of the received signals obtained with the 100*mm* **tile size, from a 1***mm*** *** 1***mm*** square flat reflector, which is tilted 10° relative to the transducer surface. Part (a): The MSE produced when same size planar circular piston transducer is used as both the transmitter and receiver, the radius is 3***mm,*** 6***mm,*** 9***mm*** and 12.7***mm,*** respectively; Part (b) (c) (d) (e) and (f): The comparison between the MSE produced when two different size planar circular piston transducers are used as the transmitter and receiver, and the MSE produced when same size planar circular piston transducer is used as both the transmitter and receiver.**

From above examples, we conclude that the accuracy of the received signals obtained with a specified tile size is quite dependent on the parameters of the specific simulation scenario, such as the tilt angle of the reflector surface, the location, shape and size of reflector, the size of the transducers, etc. Therefore, the "optimal micro-tile size" needs to be found empirically by "trial and error" method.

Chapter 5

Evaluation of DREAM Method

In chapter 4, the simple, but computationally more demanding Huygens method was evaluated based on the received signals obtained from a $1mm*1mm$ square reflector under different simulation scenarios. In this chapter, the DREAM method will be used for calculating the received signal due to reflectors with different size, shape and position in different simulation scenarios. As described earlier in this thesis, the DREAM method tessellates the reflector into tiles of moderate size. To consider the trade-off between the computation time and accuracy for DREAM method, we need to find the optimal tile size for DREAM method. We have carried out a detailed investigation, and in this chapter we try to develop a set of rules that may help to decide the optimal tile size efficiently. The two implementations of the DREAM method, based on both rectangular tile (R-DREAM) and triangular tile (T-DREAM), will be used. The results obtained by DREAM method using the optimal tile size are compared and evaluated with the results obtained by Huygens method.

In chapter 4, the results obtained by Huygens method with $5\boldsymbol{m}m$ micro-tile size were used as the reference signal to evaluate results obtained with larger tile size. However, when the reflector size becomes much larger, for example, $15mm*15mm$, the

computation time using Huygens method with 5mm micro-tile size becomes too long to be acceptable. More than 140 hours are required to calculate the received signal from 15mm*15mm square flat reflector for just one set of transmitting and receiving transducers. As we found in chapter 4, the results obtained by Huygens method using the optimal micro-tile size are very close to the "ideal" results obtained with 5mm micro-tile size. Therefore, in this chapter, the results obtained by Huygens method using the optimal micro-tile size are used to make comparison with the DREAM method.

As discussed in section 2.6, the DREAM method can be used to calculate the received signal from an annular array transducer, which is the basis for chapter 6, *The Optimal Design of Acoustic Field and Receiver Characteristics*. The received signal from an array is calculated based on the superposition of the received signals from different combinations of planar circular transducers. Therefore, in this chapter, planar circular piston transducers with four different radii are used as transmitter and receiver, and all combinations of transmitter radius and receiver radius are considered. The radii of the transducers are 3mm, 6.3mm, 9mm and 12.7mm.

In section 5.1, a brief introduction is given to the behavior of diffraction response versus the radial position of the field points for different transmitting and receiving transducers. In section 5.2, a new term "*DREAM Error*" is defined. Section 5.3 evaluates the energy of the received signal from a small reflector, and in section 5.4, the term "*Normalized DREAM Error*" is introduced, based on the information from section 5.3. The DREAM Error, the energy of the received signal, and the normalized DREAM Error for a small reflector are dependent on such factors as the radial position of the reflector, the tilt angle of the reflector, and the radii of the transmitting and

80

receiving transducers. The relationship between the DREAM Error, the energy, and the normalized DREAM Error and the above-mentioned factors are illustrated in section 5.2, 5.3 and 5.4, respectively. In section 5.5, the issue of the optimal tile size for DREAM method is discussed, based on the discussions in sections 5.2, 5.3 and 5.4. In section 5.6, 5.7 and 5.8, different simulation results are presented. In section 5.6, to give more illustration to the discussion in sections 5.2 and 5.5, the spectra of the received signal from $1mm*1mm$ square tilted flat reflectors with different radial locations are presented, for a specific transmitter and receiver combination. The results obtained by Huygens, R-DREAM and T-DREAM method are presented and compared. Section 5.7 is similar to section 5.6 except that the reflectors are $15mm*15mm$ square flat reflectors with different tilt angles. In section 5.8, the received signals from a large curved reflector are presented. By the comparison of the results in sections 5.2 and 5.4, it is concluded that the T-DREAM produces better results than the R-DREAM for the same tile area. In addition, we prefer to T-DREAM in the practical applications. Therefore, in the last part of section 5.7 and section 5.8, only the results obtained by T-DREAM are presented and compared with those obtained by Huygens method.

5.1 Introduction to the Behavior of Diffraction Response

When the DREAM method is applied, it is also necessary to consider the trade-off between the computation time and accuracy as was done for Huygens method. That is, we also need to find the optimal tile size for DREAM method. For the DREAM method to produce the received signal with a small error, the tile size should be chosen so that the diffraction responses from the corners of the tile do not differ too much.

81

Therefore, it is useful to first have some idea about the behavior of the diffraction response. The factors which may cause the change of the diffraction response in both waveform (shape) and amplitude include the radial position of the field point and the radii of the transmitting and receiving transducers.
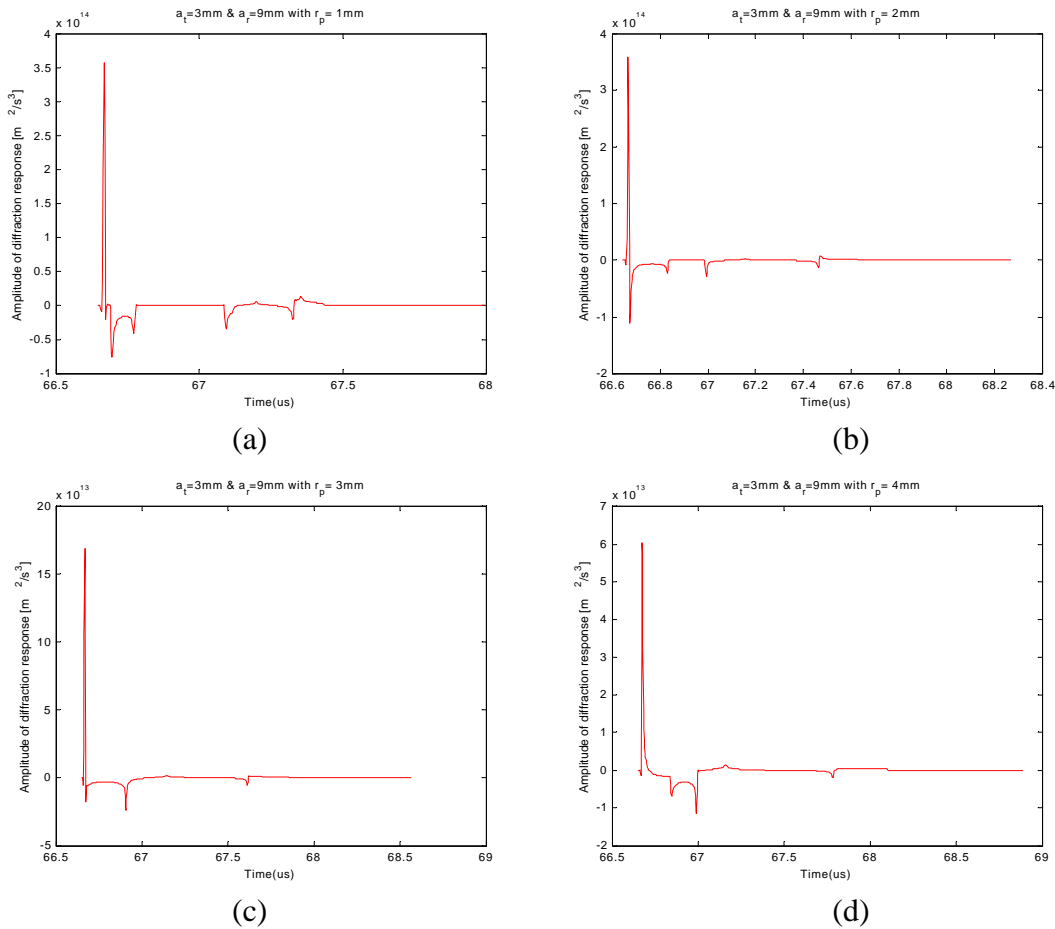
Figure 5.1 Illustration of the different diffraction responses when the radial position of the field points changes. Two planar circular pistons with radius 3*mm* and 9*mm* act as transmitter and receiver respectively. The axial position of the field points is 50*mm*. The radial positions are 1*mm*, 2 *mm*, 3*mm* and 4*mm* in part (a), (b), (c) and (d), respectively.

Figure 5.1 illustrates the different diffraction responses when the radial position of the field point changes from 1*mm* to 4*mm* with 1*mm* increment. The axial position of the field points is 50*mm* and the radii of the transmitter and receiver are 3*mm* and 9*mm,* respectively. By examining Figure 5.1, we can get some idea about the change of the

shape and amplitude of the diffraction responses when the radial position of the field point changes.

Figure 5.2 is similar to Figure 5.1, except that for Figure 5.2, the radii of the transmitter and receiver are 6.3*mm* and 9*mm,* respectively. By comparing corresponding parts in Figure 5.1 and Figure 5.2, we can observe that the shape and/or the amplitude of the diffraction response of a field point at a specific position change a lot when the radius of one transducer in the pulse-echo system differs.
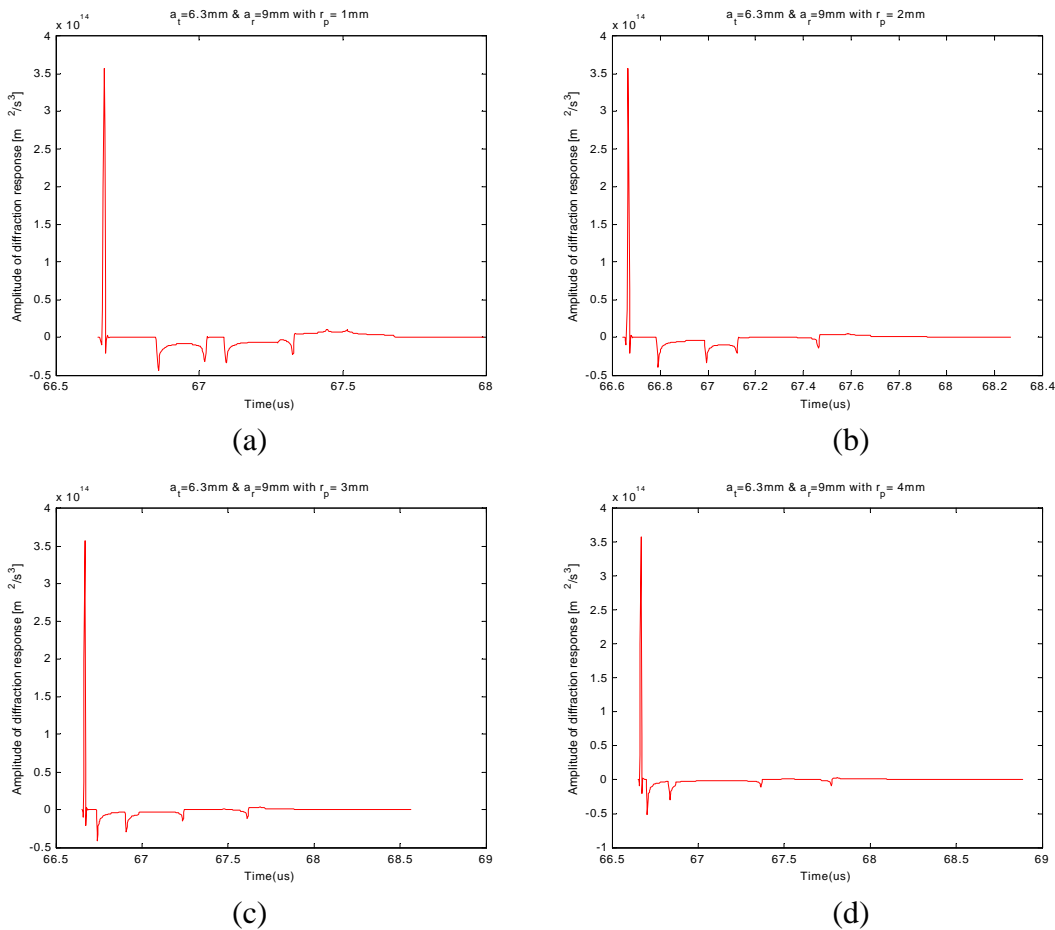
Figure 5.2 Illustration of the different diffraction responses when the radial position of the field points changes. Two planar circular pistons with radius 6.3*mm* and 9*mm* act as transmitter and receiver respectively. The axial position of the field points is 50*mm*. The radial positions are 1*mm*, 2 *mm*, 3*mm* and 4*mm* in part (a), (b), (c) and (d), respectively.

5.2 DREAM Error versus Radial Distance

As illustrated in section 5.1, the shape and amplitude of the diffraction responses change significantly when the radial position of the field points and/or the radii of the transducers change. However, it is hard to accurately/mathematically describe the *change* of the diffraction responses because it is difficult to define the measure for "change of the diffraction responses" precisely. The reason why we investigate the behavior of the diffraction response versus the radial position of the field points for different transmitting and receiving transducers is that we'd like to make use of such information to help us to determine the optimal tile size for DREAM method, and then to calculate the received signal for a pulse-echo system using DREAM method with the optimal tile size. Therefore, instead of investigating the "change of the diffraction responses", we calculate the error of the received signal obtained by DREAM method with a fixed tile size, using the received signal obtained by Huygens method as the reference signal. Large error (the numerical values will be discussed in section 5.5) means the tile size is too large for the delay linearization of DREAM method to produce good approximation. The larger the error when evaluated with a constant tile size, the smaller is the proper tile size that must be chosen for DREAM method.

To develop rules for the optimal tile size for a range of measurement situations, we investigate the relationship between the error and such factors as reflector position, the radii of the transmitting and receiving transducer, which are the factors closely related to the change of the diffraction responses. By doing this, we can get some idea about how those factors affect the choice of the tile size used by DREAM method. The

error is named "*DREAM Error*" and is calculated in the frequency domain, using the same MSE method as defined by equation (4.2) in Chapter 4. Equation (4.2) is repeated below for convenience:

$$\text{DREAM error} = \text{MSE} = \frac{\int_0^{15MHz} (|V_r(f)| - |V_{ref}(f)|)^2 \, df}{\int_0^{15MHz} |V_{ref}(f)|^2 \, df} * 100\% \qquad (5.1)$$

where $V_r(f)$ is the frequency spectrum of the received signal calculated with the DREAM method whose accuracy is to be evaluated. $V_{ref}(f)$ is the frequency spectrum of the *reference signal* calculated with the Huygens' method.

To illustrate the relationship between the DREAM Error and the radial location of the reflector, the received signal from a small square reflector (the size of the reflector will be presented later) is calculated by Huygens method as well as by both T-DREAM and R-DREAM method using equation (5.1). Next, the DREAM Error is calculated for both T-DREAM and R-DREAM method. The small square reflector is tilted 0.6° with respect to the transducer surface as shown in Figure 5.3 (a), followed by a set of measurements where the small reflector is tilted 6°. The center of the small square reflector moves in small steps along the dotted line shown in both Figure 5.3 (a) and (b). The center can be described in polar coordinates as

$$(r_p, z) = (r_p, 50 + \frac{r_p}{\sqrt{1 + (\cos 0.6°)^2}} \sin(0.6°))mm \qquad (5.2)$$

where $r_p = \sqrt{x^2 + y^2}$ is the radial position of the center of the small reflector and varies over the range of (0.35, 11.3)mm and z is the axial position of the center. The parameters r_p and z are shown in Figure 5.3 (b).

85

y

trajectory of the center
of the reflector

small square
reflector

0.6°

50*mm*

z

planar circular
transducers

(a)

y

center coordinate (r_p, z)

45°

x

(b)
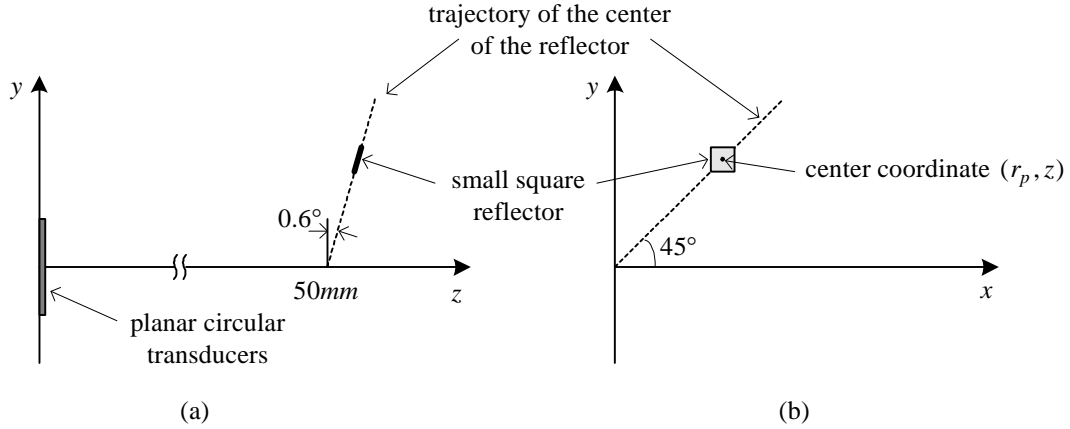
Figure 5.3 Illustration of the simulation scenarios used to illustrate the relationship between the DREAM Error and the radial location of the reflector.

When R-DREAM is applied, the size of the small reflectors is set to be 500*mm**500*mm*. The received signal from those small reflectors are calculated by Huygens method using 100*mm* point spacing and by R-DREAM using tile size of 500*mm**500*mm*. Then the DREAM Error is calculated for each small reflectors using equation (5.1), where $V_r(f)$ now is the frequency spectrum of the received signal from the 500*mm**500*mm* square reflectors obtained by R-DREAM method and $V_{ref}(f)$ is the frequency spectrum of the received signal obtained by Huygens method. When T-DREAM is applied, the size of the small tiles is set to 700*mm**700*mm* and the received signal from the tile is calculated by Hugyens method using 100*mm* point spacing. Each 700*mm**700*mm* tile is divided up into two equilateral right-triangles of same size along the diagonal line of the small square reflector and the received signal from the square tile is calculated by T-DREAM using the two equilateral right-triangles. Then the DREAM Error is calculated in the same way as that for the R-DREAM. The area of these triangular tiles used by T-DREAM is 0.7*mm**0.7*mm*/2 = 0.245*mm*^{2} which is about

86

the same as the area of those tiles used by R-DREAM, i.e., $0.5mm*0.5mm = 0.25mm^2$.

Therefore, the DREAM Error can also be used to compare the accuracy of the results obtained by T-DREAM and R-DREAM.

Our calculations have shown that the DREAM Error also depends strongly on the radii of the transmitting and receiving transducers. As described at the beginning of this chapter, we are considering four transducers of different sizes; therefore, there are ten simulation sets based on the different combination of these four transducers as transmitter and receiver. Table 5.1 shows those combinations. It should be noted that, due to reciprocity, we obtain the same received signal when the transmitter and receiver radii are a_1 and a_2, respectively, as when the transmitter and receiver radii are a_2 and a_1, respectively. The procedure described above to illustrate the relationship between the DREAM Error and radial position is applied to all these ten simulation sets.

Table 5.1 Summary of the simulation scenarios based on the different combination of the transducers as the transmitter and receiver.

	transmitter radius	receiver radius
simulation set 1	$a_t = 3\ mm$	$a_r = 3\ mm$
simulation set 2	$a_t = 3\ mm$	$a_r = 6.3\ mm$
simulation set 3	$a_t = 3\ mm$	$a_r = 9\ mm$
simulation set 4	$a_t = 3\ mm$	$a_r = 12.7\ mm$
simulation set 5	$a_t = 6.3\ mm$	$a_r = 6.3\ mm$
simulation set 6	$a_t = 6.3\ mm$	$a_r = 9\ mm$
simulation set 7	$a_t = 6.3\ mm$	$a_r = 12.7\ mm$
simulation set 8	$a_t = 9\ mm$	$a_r = 9\ mm$
simulation set 9	$a_t = 9\ mm$	$a_r = 12.7\ mm$
simulation set 10	$a_t = 12.7\ mm$	$a_r = 12.7\ mm$

Part (a) and (b) in Figure 5.4 illustrate the relationship between the DREAM Error and the radial position when the radii of the transmitter and receiver are both $6.3mm$. Part (a) is for T-DREAM and part (b) is for R-DREAM. Part (c) and (d) in

87

Figure 5.4 illustrate the relationship between the DREAM Error and the radial position when the radii of the transmitter and receiver are 3*mm* and 6.3*mm*, respectively. Part (c) is for T-DREAM and part (d) is for R-DREAM.The results for all the ten sets of simulation scenarios, listed in Table 5.1, are included in Appendix A.2.

(a) (b) (c) (d)
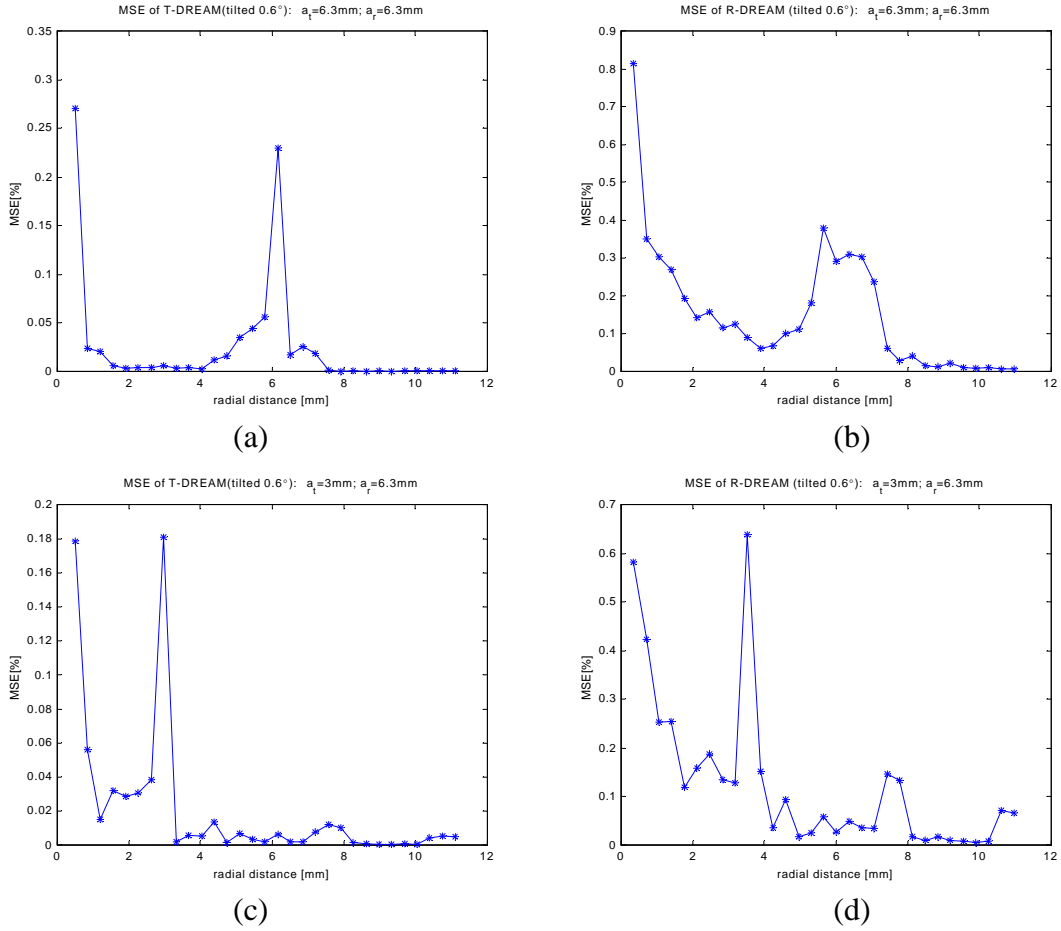
Figure 5.4 Illustration of the relationship between the DREAM Error (=MSE) and the radial position, basing on the MSE of the received signal obtained by DREAM method from small square reflectors. The results obtained by Huygens method with 100mm point spacing are used as reference signal. The reflectors are tilted 0.6° with respect to the surface of the transducer. The radii of the transmitter and receiver are: in part (a) and part (b): both 6.3mm; in part (c) and part (d): 3mm and 6.3mm. Part (a) and part (c) are for T-DREAM and part (b) and part (d) are for R-DREAM.

It is found from Figure 5.4 that, when the radii of the transmitter and receiver are both 6.3*mm*, the DREAM Error is relative large in both the region near the transducer axis and the region whose radial position is about the radius of the

transducer. The same conclusion holds for the other situations when the size of the transmitter and receiver are the same. When the size of the transmitter and receiver are different, the DREAM Error is also large in the near-axis region. And in most cases, the DREAM Error is also large in the region whose radial position is about the radius of the smaller transducer.

Recall that in section 4.2 of chapter 4, we investigated the relationship between the radial distance and the Mean Square Error (MSE) of the spectra of the received signals obtained by Huygens method (for the convenience of discussion, we will refer to the MSE as Huygens Error). By comparing Figure 5.4 and Figure 4.6, we can observe that the DREAM Error and the Huygens Error are both large in the region whose radial position is about the radius of the transducer.

During our investigation, we found that the DREAM Error also depends on the tilt angle of the reflector with respect to the surface of the transducer. Therefore, we have repeated the same simulations described above, except that the tilt angle of the small square reflector with respect to the transducer surface is now increased to 6°, instead of 0.6°. The trajectory of the center of the reflector is described as:

$$(r_p, z) = (r_p, 50 + \frac{r_p}{\sqrt{1 + (\cos 6°)^2}} \sin(6°)) mm \qquad (5.3)$$
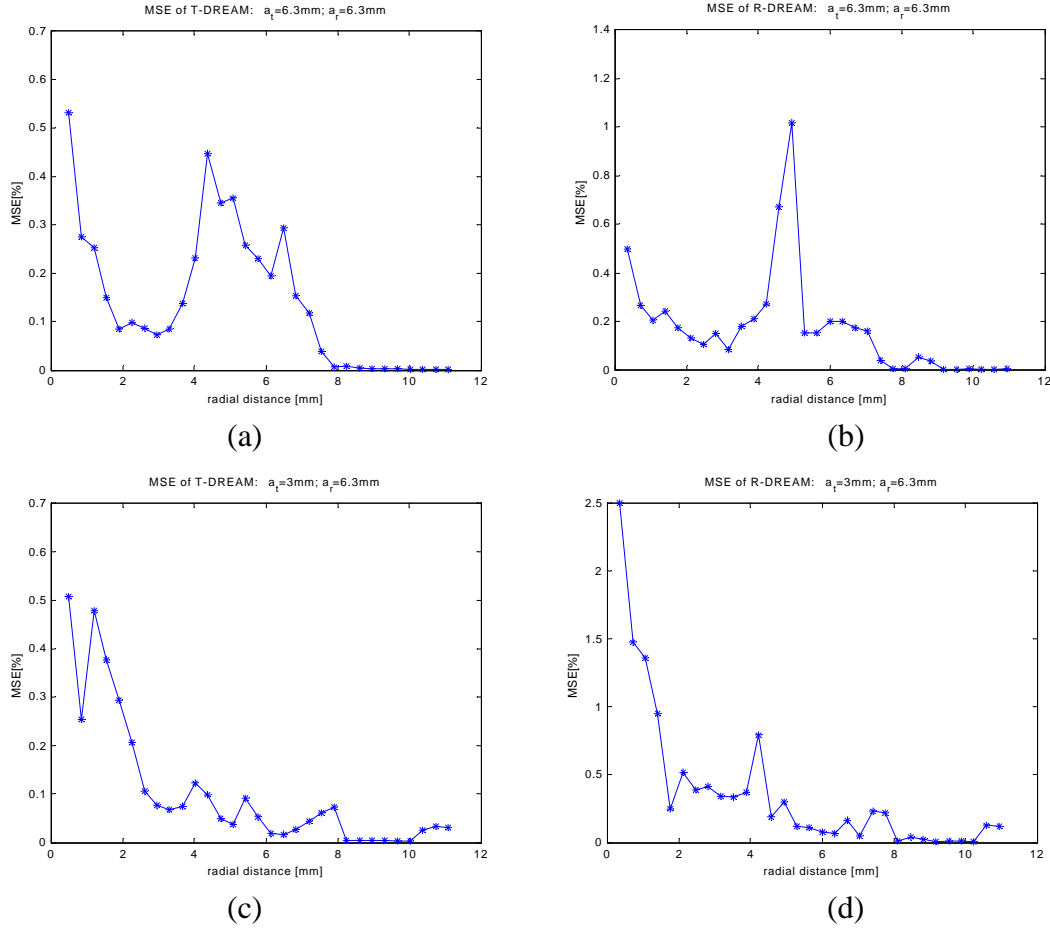
Figure 5.5 Illustration of the relationship between the DREAM Error (=MSE) and the radial position, basing on the MSE of the received signal obtained by DREAM method from small square reflectors. The results obtained by Huygens method with 50mm point spacing are used as reference signal. The reflectors are tilted 6° with respect to the surface of the transducer. The radii of the transmitter and receiver are: in part (a) and part (b): both 6.3mm; in part (c) and part (d): 3mm and 6.3mm. Part (a) and part (c) are for T-DREAM and part (b) and part (d) are for R-DREAM.

Figure 5.5 shows the relationship between the DREAM Error and the radial position when the reflector is tilted 6° with respect to the surface of the transducer, for the same cases as shown in Figure 5.4. Please refer to Appendix A.5, for the DREAM Error of all the ten sets of different combination of transducers.

By comparing Figure 5.4 and Figure 5.5, we can observe that the DREAM Error in 6° case is larger than that in corresponding 0.6° case. However, similar to the cases

with 0.6° tilted angle, for most cases with 6° tilted angle, the DREAM Error is relative large both in the region near the axis and the region where the radial position is about the same as the radius of the transducer. In general, larger DREAM Error means that smaller tile size should be used by DREAM method. Therefore, we can conclude that the optimal tile size for a specific set of transmitting and receiving transducers varies with the radial position of the reflector. More illustration will be presented in section 5.6, after we discuss the optimal tile size for DREAM method in section 5.5.

By comparing the DREAM Error for both T-DREAM and R-DREAM in Figure 5.4 and Figure 5.5, we can tell that T-DREAM produces better results than R-DREAM does for the same simulation scenario with same tile area.

5.3 Energy of the Received Signal from Small Reflector versus Radial Distance

The information given in section 5.2 is quite important if we are interested in the received signal from small reflector with a size such as $0.5mm*0.5mm$ or $1mm*1mm$. When we try to calculate the received signal from a much larger reflector, for example, 15mm*15mm flat reflector, other considerations should be made when it comes to finding the optimal tile size. One thing to be noted is that the energy of the received signal from the small reflector, which was described in section 5.2, differs a lot when its radial position changes. The energy distribution along the radial distance is also a function of the radii of the transmitter and receiver. The energy is defined as:

$$E_{ref}(r_p) = \int_0^{15MHz} |V_{ref}(f,r_p)|^2 \, df \tag{5.4}$$

where $V_{ref}(f,r_p)$ is the spectrum of the received signal from the 0.5*mm**0.5*mm* reflector,

as a function of the radial position r_p.
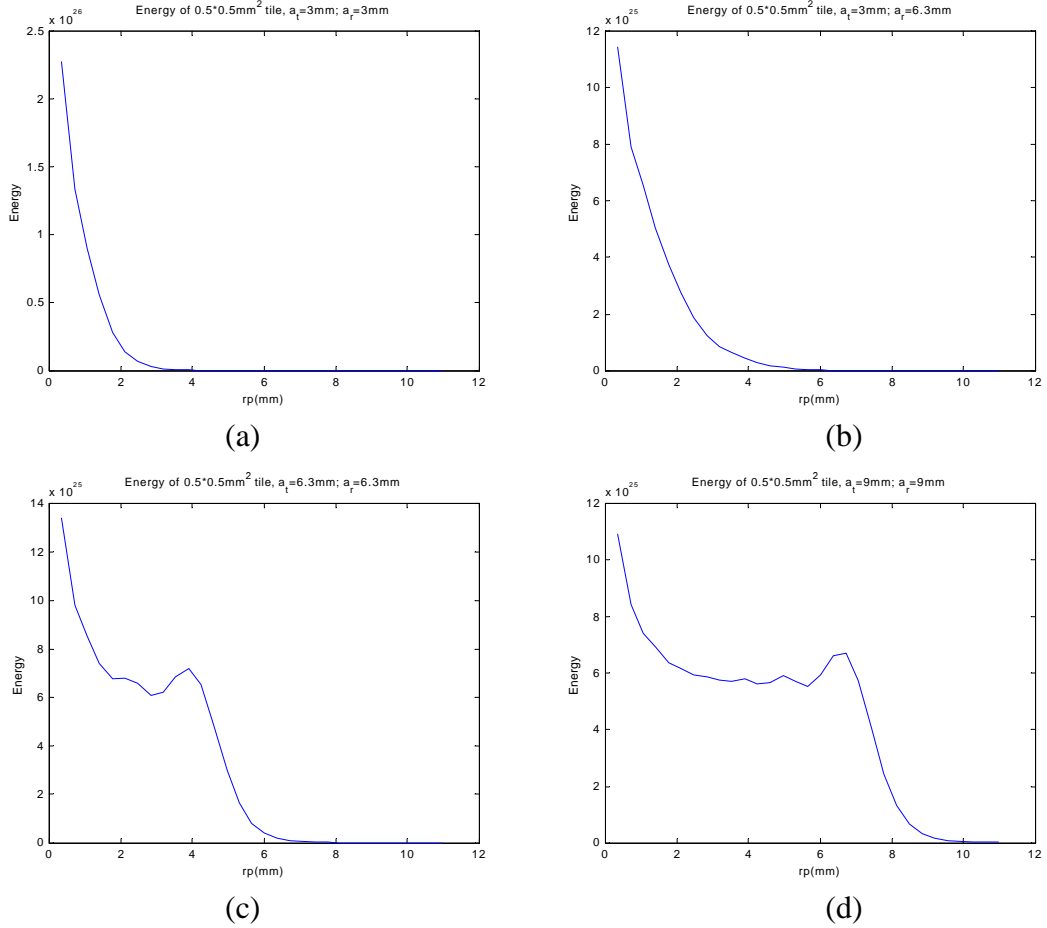
Figure 5.6 Illustration of the energy of the received signal from a 0.5*mm**0.5*mm* tile as a function of the radial position of the center of the tile. The reflector is tilted 0.6° with respect to the transducer surface. The radii of the transmitter and receiver are: in part (a) both 3*mm*; in part (b): 3*mm* and 6.3*mm*; in part (c): 6.3*mm* and 6.3*mm*; in part (d): 9*mm* and 9*mm*.

Figure 5.6 illustrates the energy of the received signal from a 0.5*mm**0.5*mm* tile

as a function of the radial position of the center of the tile. The reflector is tilted 0.6°

with respect to the transducer surface, and the trajectory of its center is described by

equation (5.2) in section 5.2. In part (a), the radii of the transmitter and receiver, are

both 3*mm*; in part (b): 3*mm* and 6.3*mm*; in part (c): 6.3*mm* and 6.3*mm*; in part (d): 9*mm* and 9*mm*. Please refer to Appendix A.1, for the energy distribution for all the ten situations with different combination of transducers.

(a)

(b)

(c)

(d)
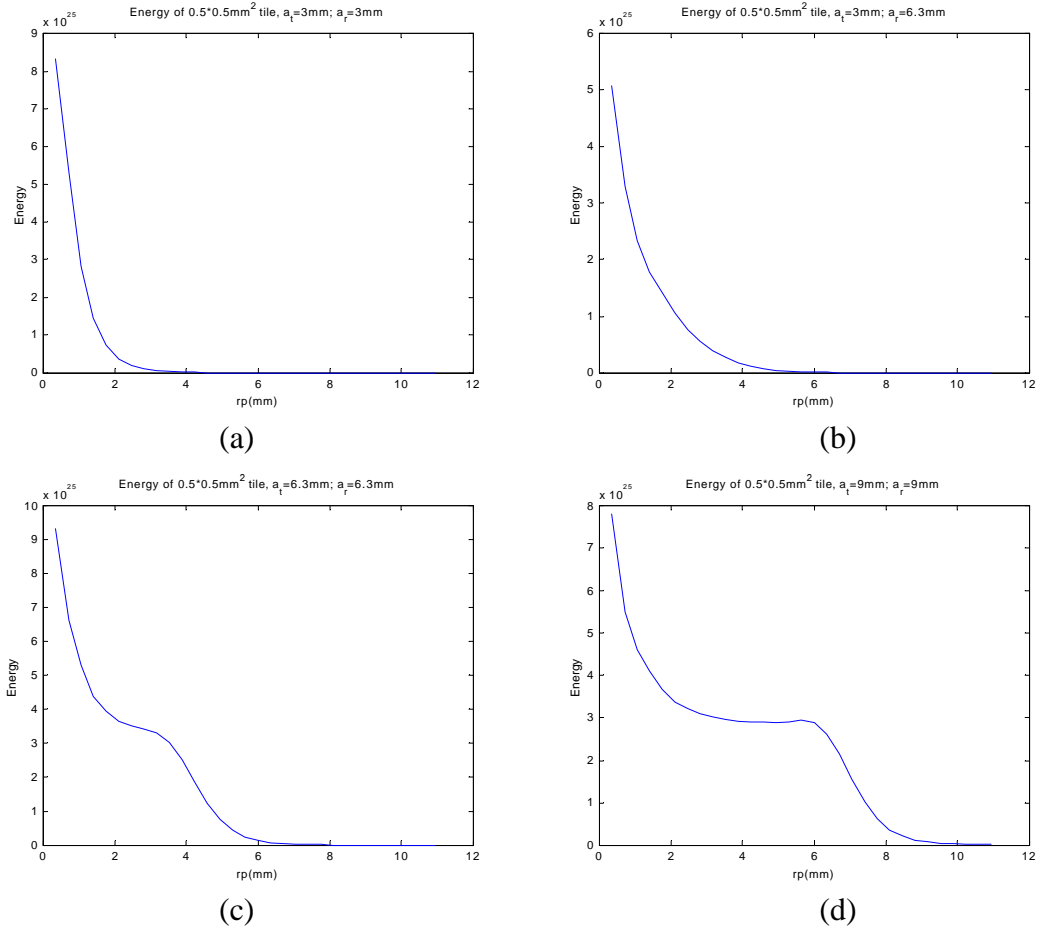
Figure 5.7 Illustration of the energy of the received signal from a 0.5*mm**0.5*mm* tile as a function of the radial position of the center of the tile. The reflector is tilted 6° with respect to the transducer surface. The radii of the transmitter and receiver are: in part (a) both 3*mm*; in part (b): 3*mm* and 6.3*mm*; in part (c): 6.3*mm* and 6.3*mm*; in part (d): 9*mm* and 9*mm*.

As we did in section 5.2, we repeat the energy calculations for the small reflector which now is tilted 6° with respect to the transducer surface, and the trajectory of its corner is described by equation (5.3) in section 5.2. Figure 5.7 illustrate the relationship between the energy of the received signal from a 0.5*mm**0.5*mm* tile as a

function of the radial position of the center of the tile for the same cases as shown in Figure 5.6. Please refer to Appendix A.4, for the energy distribution for all the ten situations with different combination of transducers.

By observing Figure 5.6 and Figure 5.7, we find that the received signal from a small reflector near the axis contains much more energy than the received signal from a reflector far away from the axis. The smaller the size of the transmitter and receiver, the more energy is concentrated in the received signal from the small reflectors near the axis. The energy distribution curves for the 0.6° case are similar to those for the 6° case, while the overall energy level is much higher when the reflector tilted 0.6° than when it is tilted 6°.

5.4 Normalized DREAM Error versus Radial Distance

In section 5.3, we calculated the energy of the received signal from a small tile as a function of the radial position of the center of the tile. As most modeling situations involve the received signal from an extended reflector, it is appropriate to define a normalized DREAM Error (or MSE) in which the mean square error of a small tile is normalized by the energy of the received signal from a large reflector. Such a normalized DREAM Error is defined as

$$\text{Normalized DREAM Error} = \frac{\int_0^{15MHz} (|V_{r\_tile}(f,r_p)| - |V_{ref\_tile}(f,r_p)|)^2 df}{\int_0^{15MHz} |V_{ref\_reflector}(f)|^2 \, df} * 100\% \quad (5.4)$$

where $V_{r\_tile}(f,r_p)$ is the frequency spectrum of received signal from the small reflector obtained by DREAM method. The reflector is tilted either 0.6° or 6° with respect to the transducer surface, and the trajectory of its corner is described by either equation (5.2)

94

or (5.3) in section 5.2. For R-DREAM, the size of the small reflector is 0.5*mm**0.5*mm*, and the received signal is calculated by R-DREAM using one square tile with area of 0.5*mm**0.5*mm*. For T-DREAM, the size of the small reflector is 0.7*mm**0.7*mm* and the received signal is calculated by T-DREAM using two equilateral right-triangles with area of 0.7*mm**0.7*mm*/2. The function $V_{ref\_tile}(f, r_p)$ is similar to $V_{r\_tile}(f, r_p)$ except that it is obtained by Huygens method. $V_{ref\_reflector}(f)$ is the frequency spectrum of the received signal from a 8*mm**8*mm* flat reflector, which is placed in the first quadrant of the *x-y* plane with one of its corner on the *z*-axis. It is tilted by the same angle as the small reflector with respect to the transducer surface. Thus, the small square reflector moves along the diagonal of the large reflector.

Figure 5.8 illustrates the relationship between the normalized DREAM Error and the radial position when the reflectors are tilted 0.6°. Part (a) and (b) are for T-DREAM and R-DREAM, respectively, when the radii of the transmitter and receiver are both 6.3*mm*. Part (c) and (d) present the relationship between the normalized DREAM Error and the radial position when the radii of the transmitter and receiver are 3*mm* and 6.3*mm*, respectively. Please refer to Appendix A.3 for the results for all ten combinations of the transmitter and receiver.

(a)

(b)

(c)

(d)
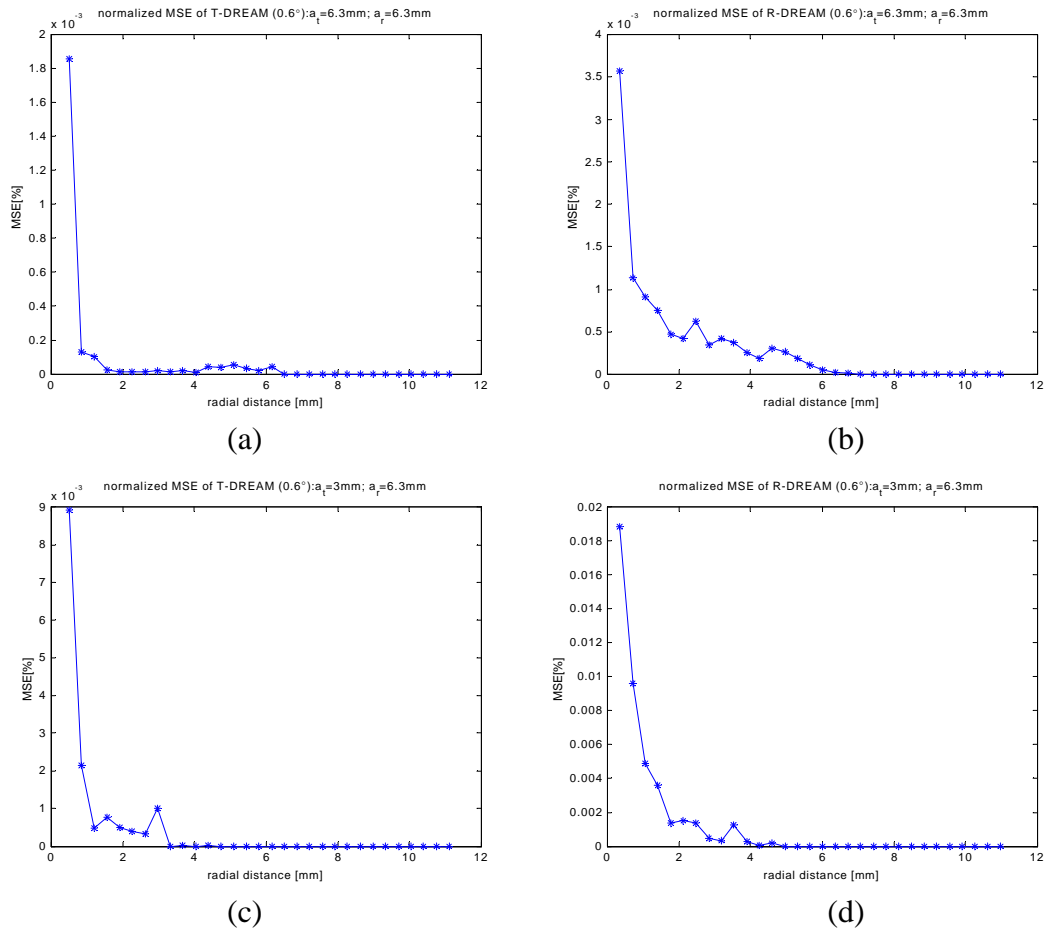
Figure 5.8 Illustration of the relationship between the radial position and the Normalized DREAM Error of the received signal from small square reflector. The results obtained by Huygens method with 100mm point spacing are used as reference signal. The reflector is tilted 0.6° with respect to the transducer surface. The radii of the transmitter and receiver are: in part (a) and part (b): both 6.3mm; in part (c) and part (d): 3mm and 6.3mm. Part (a) and part (c) are for T-DREAM and part (b) and part (d) are for R-DREAM.

Figure 5.9 illustrates the relationship between the normalized DREAM Error and the radial position when the reflectors are tilted 6° for the same cases as shown in Figure 5.8. Please refer to Appendix A.6 for the results for all ten combinations of the transmitter and receiver.
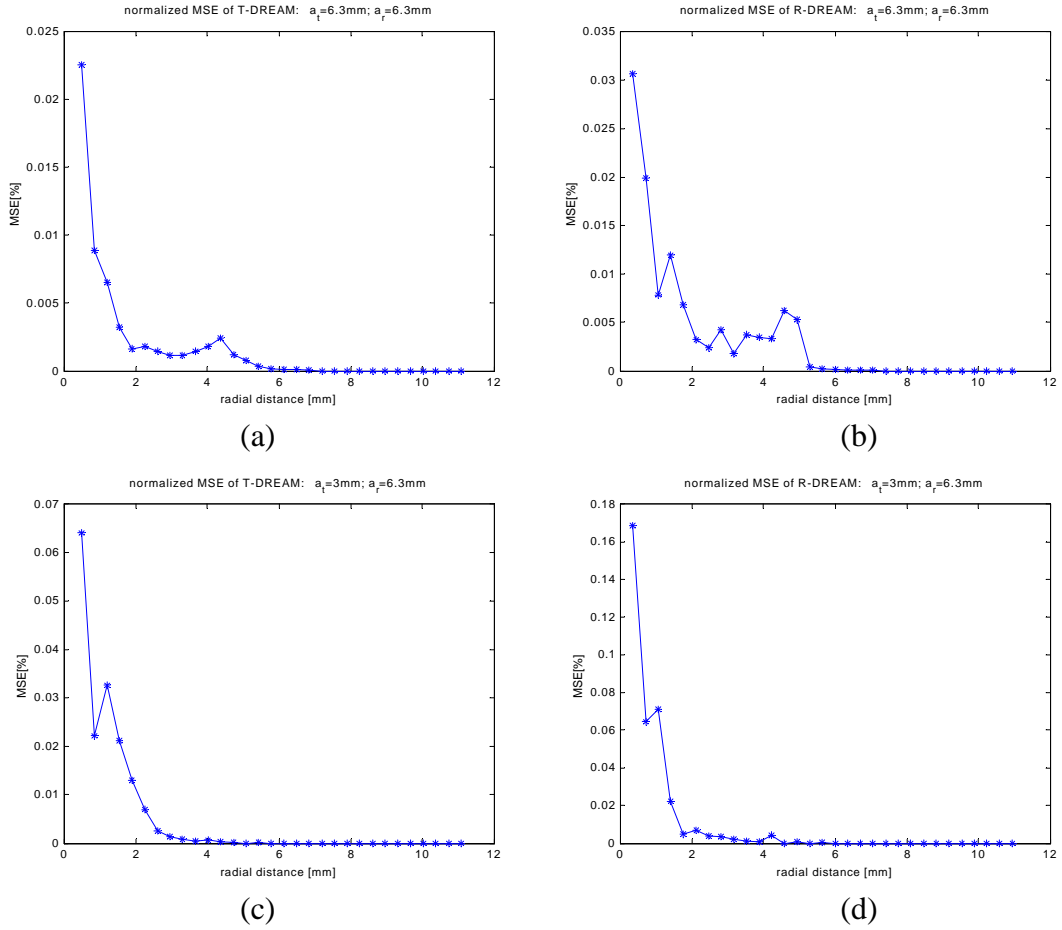
Figure 5.9 Illustration of the relationship between the radial position and the Normalized DREAM Error of the received signal from small square reflector. The results obtained by Huygens method with 50*mm* point spacing are used as reference signal. The reflector is tilted 6° with respect to the transducer surface. The radii of the transmitter and receiver are: in part (a) and part (b): both 6.3*mm*; in part (c) and part (d): 3*mm* and 6.3*mm*. Part (a) and part (c) are for T-DREAM and part (b) and part (d) are for R-DREAM.

It can be observed from Figure 5.8 and Figure 5.9 that the normalized DREAM Error is quite large in the region near the transducer axis. However, when the radial distance increases, the normalized DREAM Error becomes much smaller which means that this region contributes only a small fraction to the overall error. Consequently, larger tile size may be used in this region. It can also be found that the normalized DREAM Error largely depends on the sizes of the transducers, especially the size of the smaller of the transmitter and receiver. Generally, the smaller the size of the transducer,

97

the larger is the normalized DREAM Error and the smaller is the optimal tile-size. The observation holds true when the received signal is calculated for an extended reflector covering both near-axis region and the far-axis region. Figure 5.8 and Figure 5.9 also shows that the normalized DREAM Error is smaller in 0.6° case than that in 6° case and that T-DREAM produces better results than R-DREAM does in the same simulation scenario with same tile area, as we also found in section 5.2.

5.5 The Optimal Tile Size for DREAM Method

So far, we have calculated and analyzed several factors that may affect the error of the results obtained by DREAM method. The error magnitude in turn affects the optimal tile size that can be used by DREAM method to calculate the received signal in a pulse-echo system. The specific optimal tile size being chosen is also dependent on the allowable error level of the results in a specific application. In the work of this thesis, we define the optimal tile size in the DREAM method as the size which gives the shortest computation time and which at the same time keeps the error of the result obtained by DREAM less than 0.2%, compared with the result obtained by Huygens method, using equation (5.1).

One thing that should always be kept in mind is that the optimal tile size also depends on the shape of the reflector surface. The tile size must be chosen so that the tessellated tiles can approximate the surface sufficiently accurate. The more complicated the shape of the reflector surface is, the smaller the tile size should be chosen. How to optimally approximate a specific reflector surface with flat rectangular

or triangular tiles is an important topic closely related to DREAM method. Unfortunately, because of the limit of time, it is beyond the scope of this thesis. We will just try to keep the size of the tile moderate for the purpose of the optimal surface approximation. Although it is possible that, for some simulation scenarios, the DREAM method may produce good results with larger tile size, for all the following simulations, we limit the largest possible side length of the rectangular tile of R-DREAM method to 1*mm* and limit the largest possible side length of the triangular tile of T-DREAM method to 1.414*mm* which corresponding to the length of the diagonal line of the rectangular tile. For the ease of tessellation, the tessellated triangular tiles in the following parts are all right triangles generated by splitting a rectangular tile along the diagonal line. However, the T-DREAM is equally applicable to arbitrary-shaped triangular tiles. Furthermore, tessellation using arbitrary triangular tiles might be able to produce better results because the arbitrary-shaped triangular tiles can approximate the complex reflector surface more effectively. That is also one of the reasons that we prefer the T-DREAM to the R-DREAM.

For the convenience of tessellation, if a tile of specific size does not produce the results with required accuracy, it is tessellated into four smaller tiles with the same area. In most cases presented in the following part of this thesis, the R-DREAM uses square tiles and the T-DREAM uses equilateral right-triangular tiles. Note that we will use the side length of the square tile or the length of the hypotenuse of the equilateral right-triangular tile to describe the tile size used by R-DREAM or T-DREAM. Additional explanation will be given when the tile is not a square tile or an equilateral right-triangular tile for some cases. For the R-DREAM, the tile side length is set to be either

99

1000mm, 500mm, 250mm or 125mm. For the T-DREAM, the hypotenuse is set to be either 1414mm, 707mm, 354mm or 174mm. Of course, these values may be adjusted slightly for the convenience of the tessellation for a specific reflector surface.

Based on the discussion in previous sections, we try to develop several rules that may help to decide the optimal tile size efficiently. However, similar to what we found for Huygens method, the optimal tile size for DREAM method is quite dependent on specific simulation scenario and the allowable error level of the results. It is impossible to tell which tile size to be used in a specific situation without actual numerical experiments, and the basic way to decide the optimal tile size is "trial and error" method. Based on the discussion in previous sections and "trial and error method", we find that, in general, when the tilt angle of the reflector is small, for example, less than 2° or 3°, 1000mm or 500mm tile size can be used by R-DREAM and 1414mm can be used by T-DREAM.

When the tilt angle of the reflector becomes larger, the optimal tile size is dependent on factors such as the radial position of the tile, the size of the transducer and receiver. For the purpose of clarity, we use tables to summarize the optimal tile size for different situations. Based on the relationship between the DREAM Error and the radial position illustrated in Figure 5.5 and Appendix A.5, Table 5.2 and Table 5.3 summarize the optimal tile sizes when the reflector is small (dimensions in the order of 1mm*1mm) and tilted around 6° with respect to the transducer surface. Table 5.2 is for T-DREAM method and Table 5.3 is for R-DREAM method. Results based on the optimal tile size

will be presented in section 5.6 for small reflectors. More explanation will be presented

in section 5.6.

Table 5.2 Summary of the optimal tile size for T-DREAM when the reflector is small (with the dimension of 1*mm**1*mm*) and tilted around 6° with respect to the transducer surface.

radii of transducers		reflector radial position r	T-DREAM optimal tile size
3*mm*	3*mm*	$r < 3.5mm$	354***mm***
		$3.5mm \leq r < 4.5mm; 8mm \leq r <$	707***mm***
		$4.5mm \leq r < 8mm; 10mm \leq r < 11mm$	1414***mm***
3*mm*	6.3*mm*	$r < 3mm$	354***mm***
		$3mm \leq r < 8mm; 10mm \leq r < 11mm$	707***mm***
		$8mm \leq r < 10mm$	1414***mm***
3*mm*	9*mm*	$r < 3mm$	354***mm***
		$3mm \leq r < 11mm$	707***mm***
3*mm*	12.7*mm*	$r < 2mm$	354***mm***
		$2mm \leq r < 11mm$	707***mm***
6.3*mm*	6.3*mm*	$r < 1.5mm; 4mm \leq r < 7mm$	354***mm***
		$1.5mm \leq r < 4mm; 7mm \leq r < 8mm$	707***mm***
		$8mm \leq r < 11mm$	1414***mm***
6.3*mm*	9*mm*	$r < 2mm; 3.5mm \leq r < 5.5mm$	354***mm***
		$2mm \leq r < 3.5mm; 5.5mm \leq r <$	707***mm***
6.3*mm*	12.7*mm*	$r < 1.5mm; 3.5mm \leq r < 5mm$	354***mm***
		$1.5mm \leq r < 3.5mm; 5mm \leq r <$	707***mm***
9*mm*	9*mm*	$r < 1.5mm; 7mm \leq r < 9mm$	354***mm***
		$1.5mm \leq r < 7mm; 9mm \leq r < 11mm$	707***mm***
9*mm*	12.7*mm*	$r < 1.5mm; 6mm \leq r < 8mm$	354***mm***
		$1.5mm \leq r < 6mm; 8mm \leq r < 11mm$	707***mm***
12.7*mm*	12.7*mm*	$r < 1.5mm$	354***mm***
		$1.5mm \leq r < 11mm$	707***mm***

Table 5.3 Summary of the optimal tile size for R-DREAM when the reflector is small (with the dimension of 1*mm1*mm*) and tilted around 6° with respect to the transducer surface.**

radii of transducers		reflector radial position *r*	R-DREAM optimal tile size
3*mm*	3*mm*	$r < 3.5mm$	125*mm*
		$3.5mm \le r < 5mm$	250*mm*
		$5mm \le r < 11mm$	500*mm*
3*mm*	6.3*mm*	$r < 1.5mm$	125*mm*
		$1.5mm \le r < 5mm$	250*mm*
		$5mm \le r < 11mm$	500*mm*
3*mm*	9*mm*	$r < 1.5mm$	125*mm*
		$1.5mm \le r < 5mm$	250*mm*
		$5mm \le r < 11mm$	500*mm*
3*mm*	12.7*mm*	$r < 1.5mm$	125*mm*
		$1.5mm \le r < 5mm$	250*mm*
		$5mm \le r < 11mm$	500*mm*
6.3*mm*	6.3*mm*	$r < 1.5mm; 4mm \le r < 7mm$	250*mm*
		$1.5mm \le r < 4mm; 7mm \le r < 9mm$	500*mm*
		$9mm \le r < 11mm$	1000*mm*
6.3*mm*	9*mm*	$r < 1.5mm$	125*mm*
		$1.5mm \le r < 9mm$	250*mm*
		$9mm \le r < 11mm$	500*mm*
6.3*mm*	12.7*mm*	$r < 1.5mm$	125*mm*
		$1.5mm \le r < 9mm$	250*mm*
		$9mm \le r < 11mm$	500*mm*
9*mm*	9*mm*	$r < 2mm$	125*mm*
		$2mm \le r < 11mm$	250*mm*
9*mm*	12.7*mm*	$r < 2mm$	125*mm*
		$2mm \le r < 11mm$	250*mm*
12.7*mm*	12.7*mm*	$r < 2mm$	125*mm*
		$2mm \le r < 11mm$	250*mm*

When the reflector is large and covers both regions near the transducer axis and the regions far from the transducer axis, the rules for the optimal tile size are a little different from that for the small reflectors. Based on the "trial and error" method and the relationship between the normalized DREAM Error and the radial position illustrated in Figure 5.9 and Appendix A.6, Table 5.4 summarizes the optimal tile size

when the reflector is large and tilted around 6° with respect to the transducer surface.

Results for large reflectors based on the optimal tile size will be presented in sections

5.7 and 5.8.

Table 5.4 Summary of the optimal tile size for both T-DREAM and R-DREAM when the reflector is large and tilted around 6° with respect to the transducer surface.

radii of transducers		tile radial position r	T-DREAM	R-DREAM
		$r < 4mm$	354 μm	125 μm
3mm	3mm	$4mm \le r < 11mm$	707 μm	500 μm
		$r < 3mm$	354 μm	125 μm
3mm	6.3mm	$3mm \le r < 11mm$	707 μm	500 μm
		$r < 3mm$	354 μm	125 μm
3mm	9mm	$3mm \le r < 11mm$	707 μm	500 μm
		$r < 3mm$	354 μm	250 μm
3mm	12.7mm	$3mm \le r < 11mm$	707 μm	500 μm
		$r < 2mm$	354 μm	250 μm
6.3mm	6.3mm	$2mm \le r < 6.3mm$	707 μm	500 μm
		$6.3mm \le r < 11mm$	1414 μm	1000 μm
		$r < 6.3mm$	707 μm	500 μm
6.3mm	9mm	$6.3mm \le r < 11mm$	1414 μm	1000 μm
		$r < 6.3mm$	707 μm	500 μm
6.3mm	12.7mm	$6.3mm \le r < 11mm$	1414 μm	1000 μm
		$r < 9mm$	707 μm	500 μm
9mm	9mm	$9mm \le r < 11mm$	1414 μm	1000 μm
9mm	12.7mm	$r < 11mm$	1414 μm	1000 μm
12.7mm	12.7mm	$r < 11mm$	1414 μm	1000 μm

5.6 Received Signal from Small Tilted Reflector

To validate the conclusion we drew in sections 5.2 and 5.5, the DREAM method is used to calculate the spectra of the received signals due to 1*mm**1*mm* square flat reflectors, using the optimal tile size. The reflector is tilted 6° with respect to the transducer surface and the radii of the transmitter and receiver are both 6.3*mm*. Table 5.5 summarizes the position of center of these small reflectors.

Table 5.5 Summary of the position of the 1*mm**1*mm* square flat reflectors. The radii of the transmitter and receiver are both 6.3mm and the reflector is tilted 6° with respect to the transducer surface.

	reflector center position
reflector 1 (R1)	(0.71, 50.05) *mm*
reflector 2 (R2)	(2.12,50.16) *mm*
reflector 3 (R3)	(3.53,50.26)*mm*
reflector 4 (R4)	(4.94, 50.37)*mm*
reflector 5 (R5)	(6.35, 50.47)*mm*
reflector 6 (R6)	(7.76, 50.57)*mm*
reflector 7 (R7)	(9.17, 50.68)*mm*
reflector 8 (R8)	(10.58, 50.78)*mm*

The optimal tile size is based on the values listed in Table 5.2 and Table 5.3 and is listed in Table 5.6 together with the MSE of the results obtained by R-DREAM and T-DREAM. The received signals obtained by Huygens method with 50$\boldsymbol{m}$m point spacing are used as reference for the calculation of MSE. It is noticed that for some cases, for example for reflector position R1, the MSE of the result obtained by T-DREAM with 354$\boldsymbol{m}$m is 0.0083%, which is much smaller than the MSE value we used to define the optimal tile size for DREAM, namely, 0.2%. However, if we were to use 707$\boldsymbol{m}$m tile size for T-DREAM in this case, the MSE becomes 0.3431%, which doesn't

satisfy our definition of the optimal tile size. Therefore, 354mm is the optimal tile size in this case.

Table 5.6: Optimal tile size, Mean Square Error (MSE) and the computational time for R-DREAM, T-DREAM method for a 1mm*1mm square tile at various radial position. The results obtained by Huygens method with 50mm point spacing are used as reference signal for each case.

	R-DREAM			T-DREAM			Huygens
	tile-size	MSE(%)	Time(s)	tile-size	MSE(%)	Time(s)	Time(s)
R1	250mm	0.0574	1.76	354mm	0.0083	2.74	13.02
R2	500mm	0.1409	0.6	707mm	0.0929	0.93	14.66
R3	500mm	0.126	0.66	707mm	0.1078	1.04	16.53
R4	250mm	0.0991	3.02	354mm	0.0127	4.4	18.68
R5	250mm	0.017	3.18	354mm	0.0265	4.89	21.09
R6	500mm	0.1103	1.04	707mm	0.0296	1.7	23.67
R7	1000mm	0.0926	0.33	1414mm	0.0653	0.49	26.09
R8	1000mm	0.0313	0.33	1414mm	0.0268	0.55	29.55

In Table 5.6, the computation time for each tile position is also included for the Huygens method, T-DREAM and R-DREAM. By comparing the computation time, we may easily determine how efficient the DREAM method is. One thing to note is that the "computation time" is NOT a formal and strict way to evaluate the efficiency of different algorithms, because the computation time depends not only on the algorithms, but also on such factors as the kind of operating system used, the current status of CPU usage and so on. But it does provide a straightforward and convenient measure to roughly compare the computational efficiency of different algorithms.

For the convenience of further discussion, Figure 5.5 (a) and (b) in section 5.2 are presented as Figure 5.10 again. The graph illustrates the relationship between the radial distance and the DREAM Error when the reflector is tilted 6° with respect to the transducer surface and the radii of the transmitter and receiver are 6.3mm. Recall that in section 5.2, we concluded that the larger the DREAM Error is, the smaller the tile size

must be chosen for DREAM method to obtain the results with good accuracy. By comparing the optimal tile size given in Table 5.6 and the DREAM Error curve given in Figure 5.10, we find that our conclusion really holds. Take the results for R-DREAM for example: when the tile center is at (0.71, 50.05) *mm*, which is very near the axis, the DREAM Error found in Figure 5.10 is relative large with the value at about 0.5%, therefore, the tile size must be chosen small to get good results, i.e., 250μ*m* in this case; when the tile center is at (2.12,50.16) *mm*, the DREAM Error found in Figure 5.10 is relative small with the value at about 0.15%, therefore, larger tile size may be used, i.e., 500μ*m*; when the tile center is at (4.94, 50.37)*mm*, the DREAM Error found in Figure 5.10 is large, then smaller tile size must be used. Similar analysis can be given to the results obtained for all the other reflectors listed in Table 5.5, as well as to the results obtained by T-DREAM.
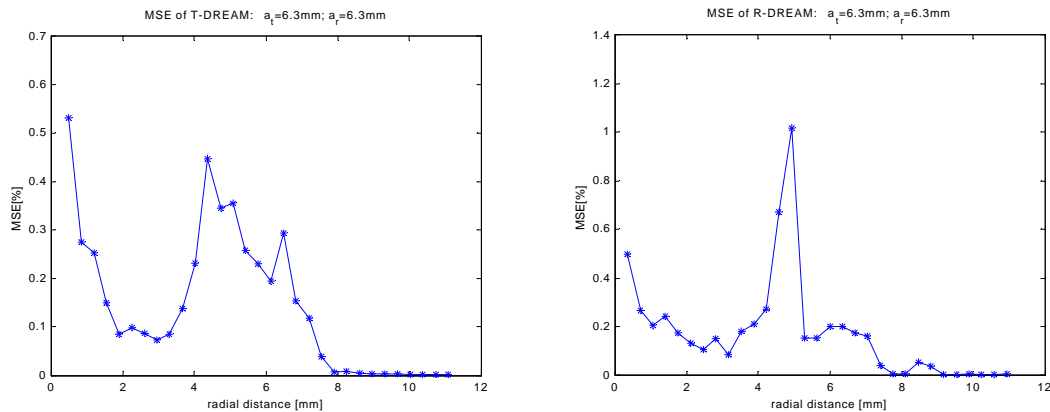
Figure 5.10 Illustration of the relationship between the DREAM Error and the radial position of a small square reflector. The results obtained by Huygens method with 50μ*m* point spacing are used as reference signal. The reflectors are tilted 6° with respect to the surface of the transducer. The radii of the transmitting and receiving transducers are both 6.3*mm*.

Figure 5.11 (a), (b), (c) and (d) illustrate the spectra of the received signals from four reflector positions defined in Table 5.5: R1, R2, R7 and R8. Please refer to Appendix B.1 for the spectra of the received signals from all the reflector positions.

(a)

(b)

(c)

(d)
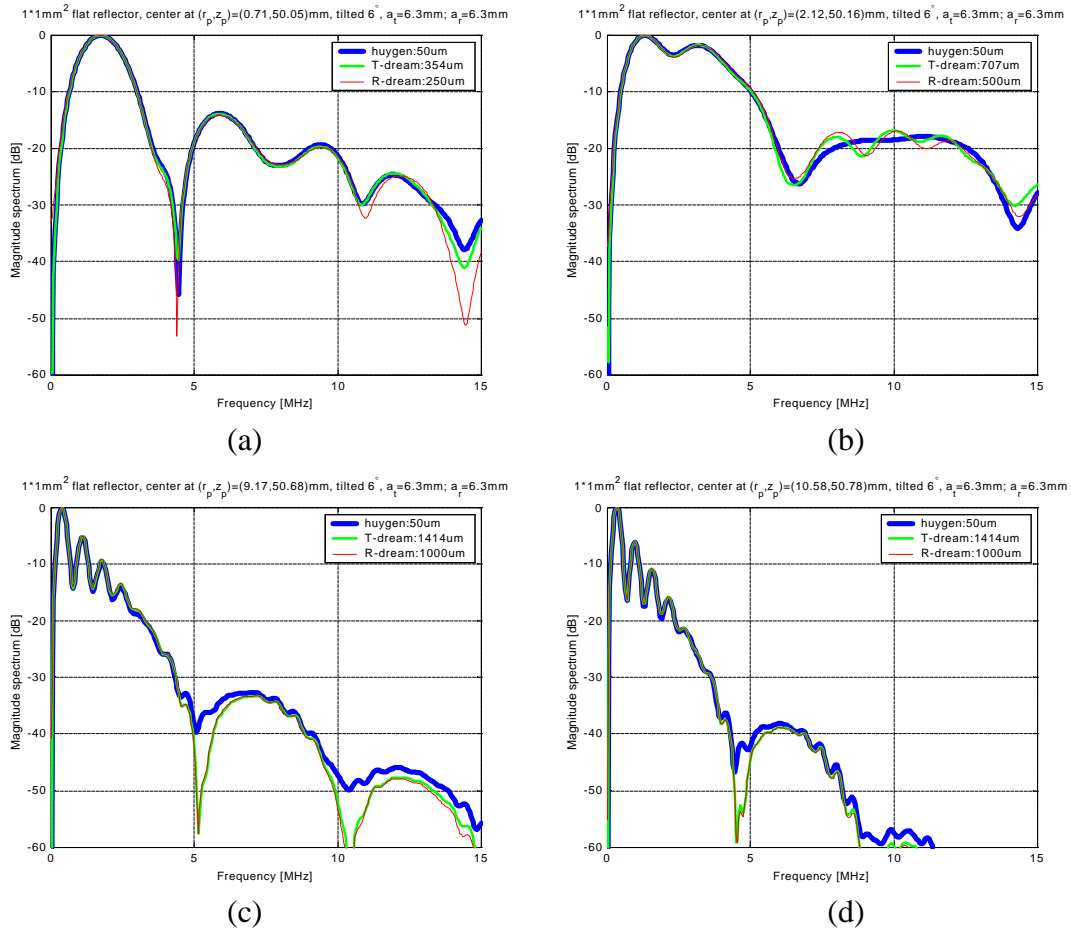
Figure 5.11 Spectra of received signal from a 1*mm**1*mm* square reflector to show the different results obtained by Huygens method, R-DREAM, T-DREAM. Part (a), (b), (c) and (d) correspond to the received signal from reflector positions R1, R2, R7 and R8, respectively.
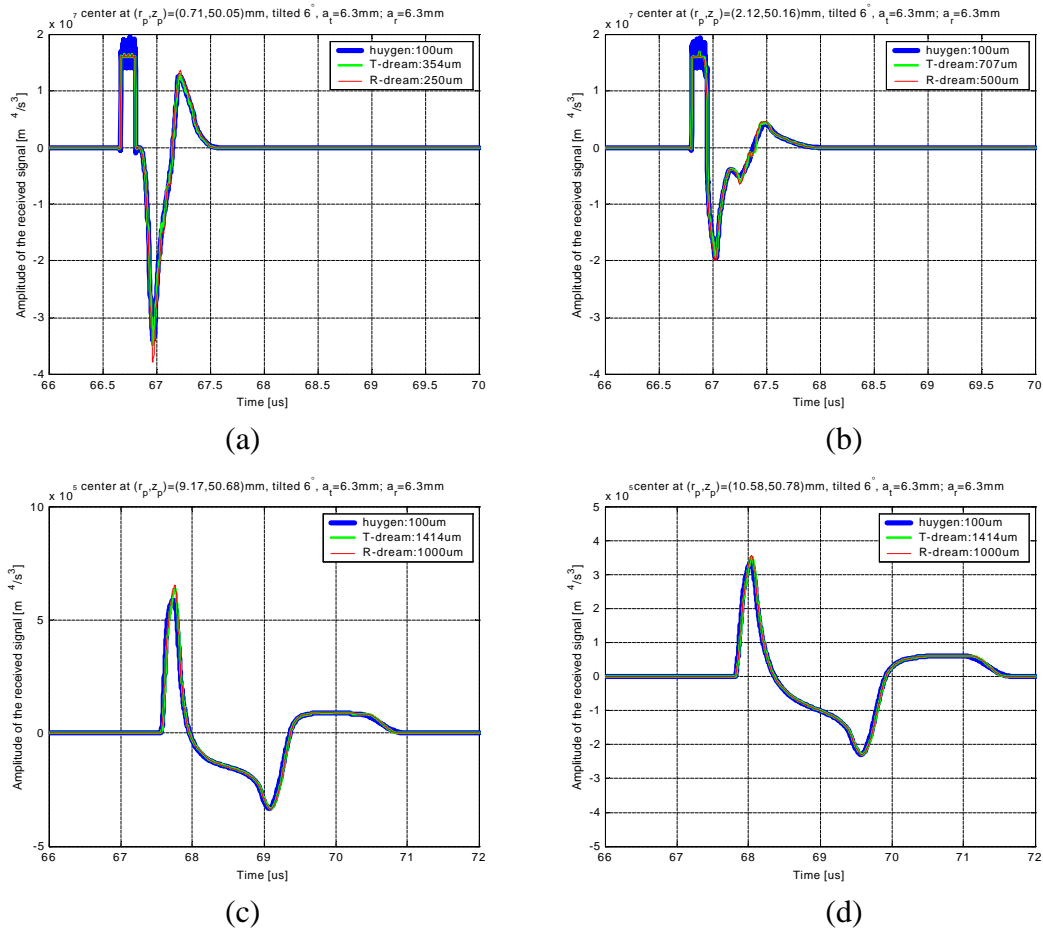
Figure 5.12 Time-domain received signal from a 1*mm**1*mm* square reflector to show the different results obtained by Huygens method, R-DREAM, T-DREAM. Part (a), (b), (c) and (d) correspond to the received signal from R1, R2, R7 and R8, respectively.

Figure 5.12 (a), (b), (c) and (d) illustrate the time-domain received signals from the same four reflector positions: R1, R2, R7 and R8. Please refer to Appendix B.5 for the time-domain received signals from all the reflectors. We find that the received signals obtained by different methods agree very well except that, in part (a) and (b), the signal obtained by Huygens method contains some very high frequency oscillations in the time range [66.5~ 67]*ms*. These oscillations appear because the Huygens method uses discrete summation instead of the continuous integration of the diffraction response over the reflector surface which is not able to smooth out the strong impulses

at the start of the diffraction response unless even smaller micro-tile size is used by Huygens method. However, the high frequency oscillations will not give error in the frequency range of interest. Based on the spectra of the received signal, we may investigate the system response only in the frequency range of interest. In general, the ultrasound transducers may be considered a bandpass filter with moderate bandwidth; therefore, only a certain frequency range of the received spectrum produces the output signal. In addition, we expect that more features identifying a given reflector can be found in the spectra. Therefore, for the simulations in later sections, only the spectra of the received signal will be included while the time-domain received signals may be found in corresponding Appendices.

5.7 Received Signal from Large Flat Reflector

In this section, the DREAM method is used to calculate the received signal due to $15mm*15mm$ square flat reflectors in different simulation scenarios. In section 5.7.1, the flat reflector is tilted 0.6° with respect to the transducer surface. Results obtained by both R-DREAM and T-DREAM are presented and compared with the corresponding results obtained by Huygens method for all ten sets of transmitter and receiver combinations. In section 5.7.2, the flat reflector is tilted 6° with respect to the transducer surface. Here, only the results obtained by T-DREAM are presented and compared with those obtained by Huygens method for all ten sets of transmitter and receiver combinations.

5.7.1 Received Signal from Large Flat Reflector Tilted 0.6°

To validate the conclusion drawn in section 5.5, that is, when the tilt angle of the reflector is small, large tile size can be used by DREAM to produce good results, the DREAM method is used to calculate the received signals from the flat reflector when it is tilted 0.6° with respect to the surface of the transducer. Table 5.7 summarizes the relevant parameters, and Table 5.8 presents the optimal tile size used as well as the MSE obtained for R-DREAM and T-DREAM. The results obtained by Huygens method with 100mm point spacing are used as reference signal. For the convenience of the comparison, the relative computation time of DREAM method to that of Huygens method is presented in the columns "Time" of Table 5.8.

Table 5.7 Summary of the parameters used for different simulation scenarios to calculate the diffraction response from 15mm*15mm square flat reflector.

	transmitter radius	receiver radius	tilted angle
case 1	$a_t = 3\ mm$	$a_r = 3\ mm$	0.6°
case 2	$a_t = 3\ mm$	$a_r = 6.3\ mm$	0.6°
case 3	$a_t = 3\ mm$	$a_r = 9\ mm$	0.6°
case 4	$a_t = 3\ mm$	$a_r = 12.7\ mm$	0.6°
case 5	$a_t = 6.3\ mm$	$a_r = 6.3\ mm$	0.6°
case 6	$a_t = 6.3\ mm$	$a_r = 9\ mm$	0.6°
case 7	$a_t = 6.3\ mm$	$a_r = 12.7\ mm$	0.6°
case 8	$a_t = 9\ mm$	$a_r = 9\ mm$	0.6°
case 9	$a_t = 9\ mm$	$a_r = 12.7\ mm$	0.6°
case 10	$a_t = 12.7\ mm$	$a_r = 12.7\ mm$	0.6°

Table 5.8 Optimal tile size, Mean Square Error (MSE) of the results and the computation time obtained by R-DREAM, T-DREAM method. The results obtained by Huygens method with 100mm tiles are used as reference signal for each case.

	R-DREAM			T-DREAM		
	optimal size	MSE (%)	Time	optimal size	MSE (%)	Time
case 1	500mm	0.0244	14.1%	1414mm	0.0219	5.9%
case 2	500mm	0.0216	16.9%	1414mm	0.0601	6.6%
case 3	500mm	0.0151	17.5%	1414mm	0.0873	7.4%
case 4	500mm	0.0432	19%	1414mm	0.1232	8.2%
case 5	500mm	0.0342	16.6%	1414mm	0.0756	6.5%
case 6	1000mm	0.0559	4.2%	1414mm	0.0217	6.6%
case 7	1000mm	0.06	4.7%	1414mm	0.0234	7.3%
case 8	1000mm	0.0874	4.9%	1414mm	0.0556	7.1%
case 9	1000mm	0.048	4.7%	1414mm	0.0091	7.3%
case 10	1000mm	0.0636	4.8%	1414mm	0.0175	7.3%

Figure 5.13 illustrates the spectra of the received signal for cases 1, 2, 9 and 10 in Table 5.7. Please refer to Appendix B.2 for the spectra of the received signal and Appendix B.6 for the time-domain received signals for all the cases. It can be seen from the figures in Figure 5.13 and the numerical values in Table 5.8 that the results obtained by DREAM methods really match those obtained by Huygens method very well.
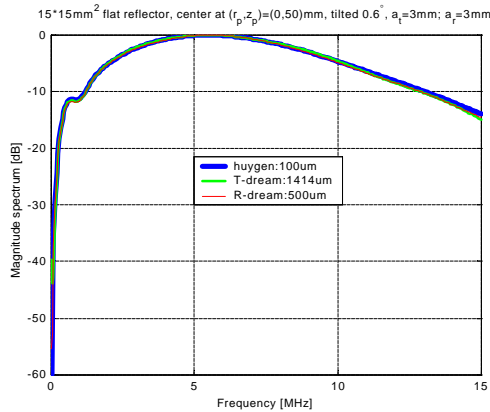
(a)
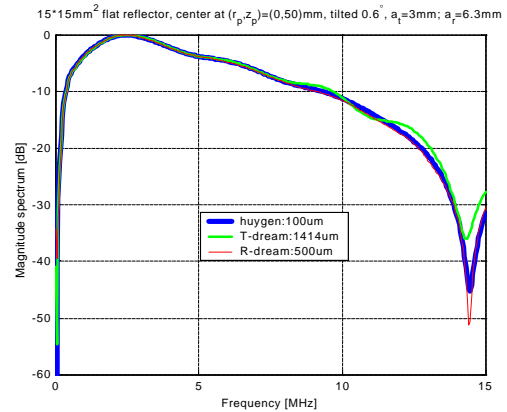
(b)
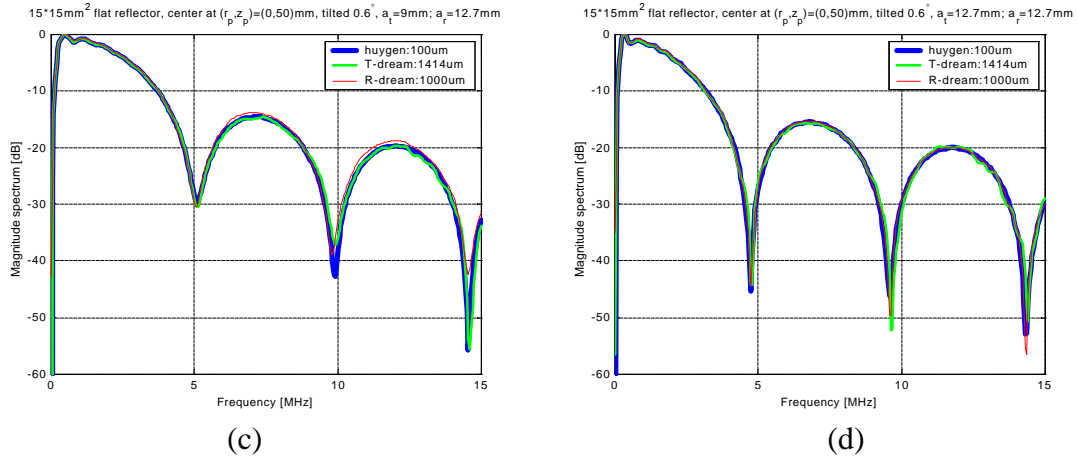
Figure 5.13 Spectra of the received signal from a 15*mm**15*mm* square reflector to show the different results obtained by Huygens method, R-DREAM, T-DREAM. The reflector is tilted 0.6° with respect to the transducer surface. Part (a), (b), (c) and (d) correspond to the received signal for case 1, 2, 9 and 10, respectively.

5.7.2 Received Signal from Large Flat Reflector Tilted 6°

Now, the DREAM method applying the optimal tile size in Table 5.4 is used to calculate the received signal due to 15*mm**15*mm* square flat reflector, which is tilted 6° with respect to the transducer surface. We found in sections 5.2 and 5.4 that the T-DREAM produces better results than the R-DREAM does. In addition, in practical applications, triangular tiles can approximate reflector surface better than rectangular tiles. Based on these reasons, only results obtained by T-DREAM will be presented from now on. Table 5.9 summarizes the different parameters for the simulation scenarios and presents the optimal tile size used as well as the MSE obtained for T-DREAM. The results obtained by Huygens method with 50μm point spacing are used as reference signal. In Table 5.9, the column "Time" gives the relative computation time of DREAM method to that of Huygens method for the convenience of the comparison. Figure 5.14 illustrates the spectra of the received signal for cases 11, 12, 19 and 20 in

Table 5.9. Please refer to Appendix B.3 for the spectra of the received signal and

Appendix B.7 for the time-domain received signals for all the cases.

Table 5.9 Summary of the parameters used for different simulation scenarios to calculate the received signal from 15*mm**15*mm* square flat reflector: The tile size used by T-DREAM method, Mean Square Error of the results and the computation time obtained by T-DREAM method. The results obtained by Huygens method with 50*mm* tiles are used as reference signal for each case. The reflector is tilted 6° with respect to the surface of the transducer.

	radii of transducers		T-DREAM		
			optimal size	MSE (%)	Time
case 11	3*mm*	3*mm*	if $r < 4$mm, 354*mm*; else 707*mm*	0.1981	9.2%
case 12	3*mm*	6.3*mm*	if $r < 3$mm, 354*mm*; else 707*mm*	0.0798	7.7%
case 13	3*mm*	9*mm*	if $r < 3$mm, 354*mm*; else 707*mm*	0.0923	8.8%
case 14	3*mm*	12.7*mm*	if $r < 3$mm, 354*mm*; else 707*mm*	0.0702	9.5%
case 15	6.3*mm*	6.3*mm*	if $r < 2$mm, 354*mm*; $2mm \leq r < 6.3mm$, 707*mm* else 1414*mm*	0.0928	5.2%
case 16	6.3*mm*	9*mm*	if $r < 6.3$mm, 707*mm*; else 1414*mm*	0.1238	4.4%
case 17	6.3*mm*	12.7*mm*	if $r < 6.3$mm, 707*mm*; else 1414*mm*	0.1467	4.7%
case 18	9*mm*	9*mm*	if $r < 9$mm, 707*mm*; else 1414*mm*	0.1467	4.5%
case 19	9*mm*	12.7*mm*	1414*mm*	0.1011	1.8%
case 20	12.7*mm*	12.7*mm*	1414*mm*	0.1333	1.8%
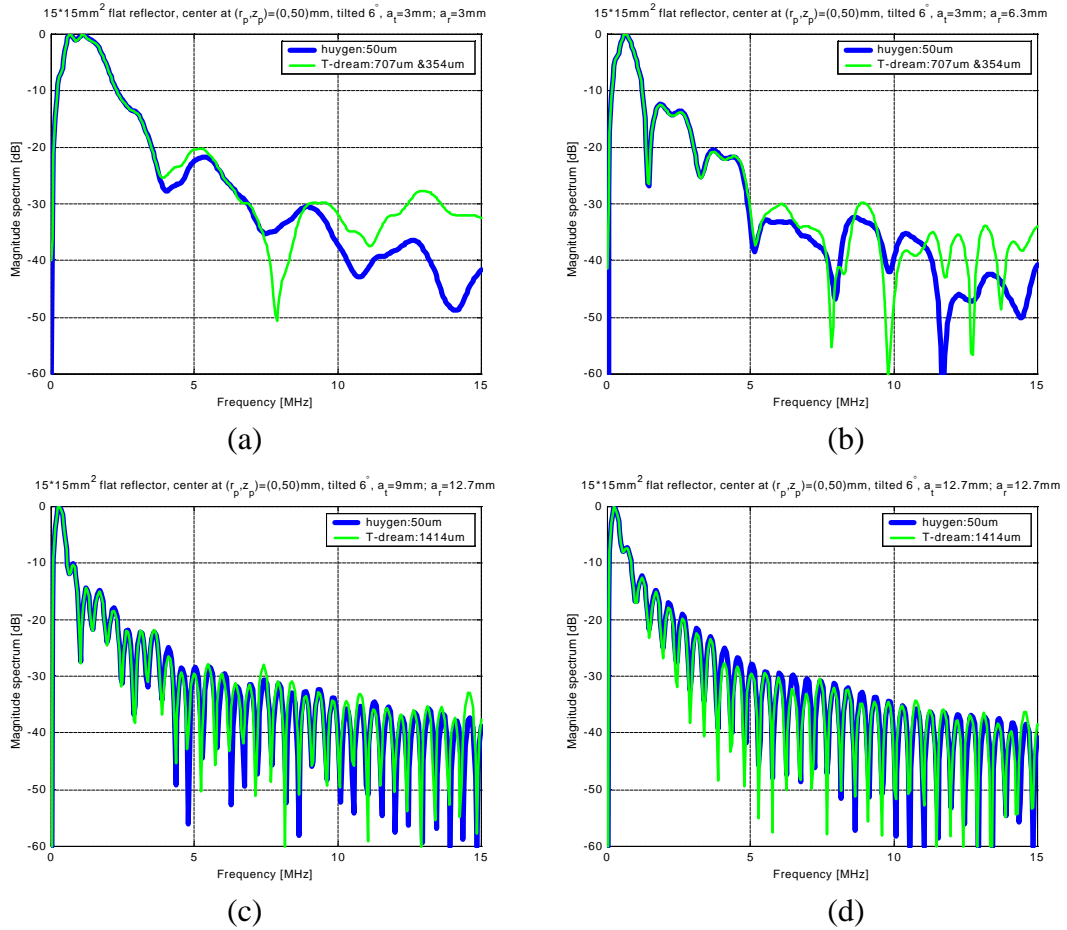
Figure 5.14 Spectra of the received signal from a 15*mm*** *15***mm** square reflector to show the different results obtained by Huygens method, T-DREAM. The reflector is tilted 6° with respect to the surface of the transducer. Part (a), (b), (c) and (d) correspond to the received signal for case 11, 12, 19 and 20, respectively.**

5.8 The Results Obtained for Curved Large Reflector

In this section, the DREAM method is used to calculate the received signal due to a large curved reflector for different simulation scenarios. The curved reflector is a 10° arc of a cylinder with radius = 86*mm* and length = 15*mm*, with the arc centered at $(r_p, z) = (0, 50)$ *mm*. The *x-y* cross-sectional area of the reflector is 15*mm* *15*mm*. Figure 5.15 illustrates the cross-sectional views of the curved reflector.

x-y cross-sectional view of the curved reflector

y-z cross-sectional view of the curved reflector
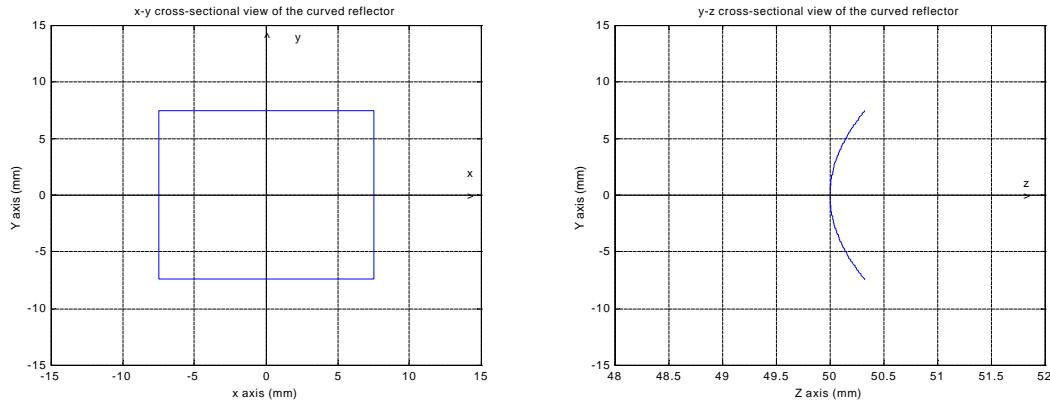
Figure 5.15 Cross-sectional views of the curved reflector.

For this case, it is hard to tessellate the reflector using equilateral right triangles. We tessellate it using right triangles with side length of 1000**mm**, 750**mm** and 1250**mm**, respectively. Table 5.10 summarizes the different parameters for the simulation scenarios and presents the optimal tile size used as well as the MSE of the received signal obtained for T-DREAM. The results obtained by Huygens method with 50**mm***37.5**mm** micro-tile size are used as reference signal.

Table 5.10 Summary of the parameters used for different simulation scenarios to calculate the received signal from the curved reflector: The tile size used by T-DREAM method, Mean Square Error of the results and the computationtime obtained by T-DREAM method. The results obtained by Huygens method with 50mm tiles are used as reference signal for each case. The curved reflector is a 10° arc of a cylinder with radius = 86mm and length = 15mm.

	radii of transducers		T-DREAM		
			optimal size	MSE (%)	Time
case 21	3*mm*	3*mm*	1000**mm***750**mm** /2	0.034	1.5%
case 22	3*mm*	6.3*mm*	1000**mm***750**mm** /2	0.064	1.7%
case 23	3*mm*	9*mm*	1000**mm***750**mm** /2	0.1439	1.8%
case 24	3*mm*	12.7*mm*	1000**mm***750**mm** /2	0.1928	2%
case 25	6.3*mm*	6.3*mm*	1000**mm***750**mm** /2	0.0886	1.6%
case 26	6.3*mm*	9*mm*	1000**mm***750**mm** /2	0.0511	1.6%
case 27	6.3*mm*	12.7*mm*	1000**mm***750**mm** /2	0.0744	1.8%
case 28	9*mm*	9*mm*	1000**mm***750**mm** /2	0.0932	1.8%
case 29	9*mm*	12.7*mm*	1000**mm***750**mm** /2	0.0914	1.8%
case 30	12.7*mm*	12.7*mm*	1000**mm***750**mm** /2	0.0916	1.9%

Figure 5.16 illustrates the spectra of the received signal for cases 21, 22, 29 and 30 in Table 5.10. Please refer to Appendix B.4 for the spectra of the received signal and Appendix B.8 for the time-domain received signals for all the cases. It can be seen from the figures in Figure 5.16 and the numerical values in Table 5.10 that the results obtained by T-DREAM methods with tile size of 1000mm*750mm/2 match those obtained by Huygens method very well.
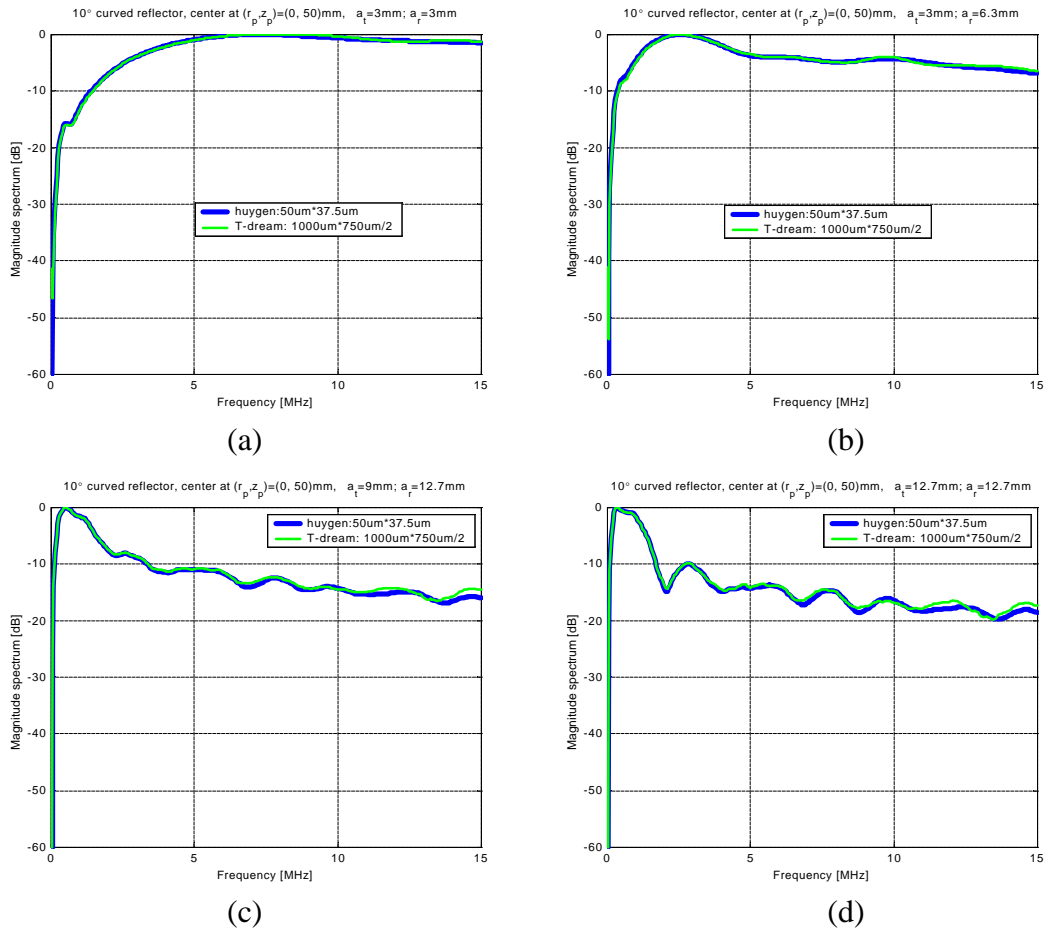
Figure 5.16 Spectra of the received signal from a curved reflector to show the different results obtained by Huygens method, T-DREAM. Part (a), (b), (c) and (d) correspond to the received signal for case 21, 22, 29 and 30, respectively.

Recall the results presented in Table 5.9 in section 5.7.2 for a flat reflector tilted 6° with respect to the transducer surface. When the radius of the smaller transducer is 3*mm*, a small tile area of 354***m****m**354***m****m*/2 must be used by T-DREAM in the region near the axis to produce good result. In this case, T-DREAM using large tile area of 1000***m****m**750***m****m*/2 produces good results even when the radius of the smaller transducer is 3*mm*. To approximate a 10° arc, the largest tilt angle of the flat triangular tiles is 5° at the edge of the reflector. For those tiles near the axis, the tilt angle is much smaller and large tile size may be used by T-DREAM, even when the radius of the smaller transducer is small. For the region far from the transducer axis with large tilt angle, as illustrated by the relationship between the normalized DREAM Error and the radial position in section 5.4, the normalized DREAM Error is very small, therefore, large tile size may also be used in this region to produce good results. Therefore, such large tile size as 1000***m****m**750***m****m*/2 may be used to generate good results for this curved reflector when the radius of the smaller transducer is 3*mm*. When the radius of the smaller transducer is large, as we can see in Table 5.9 in section 5.7.2, the T-DREAM is able to produce good results with large tile size when the entire reflector is tilted 6° with respect to the transducer surface. Therefore, it is not strange that T-DREAM is able to produce good results with large tile size for the curved reflector, for which the largest tilt angle of the reflector surface is only 5°.

Chapter 6

Optimal Design of Acoustic Fields and Receiver Characteristics

As discussed in section 2.6, the modeling concept of ultrasound pulse-echo system can be applied to an annular array transducer. The received signal from any array element due to transmission with any array element can be derived, based on the superposition of the received signal from planar circular transducers. With the annular array transducer, a large number of different acoustic fields can be produced, by varying the relative excitation delay and the amplitude scale factor for the individual transmitting elements. Similarly, a large number of receiver characteristics can be generated by varying the relative delay and gain factor for the individual receiving element. By customizing the acoustic field and receiver characteristics of an ultrasound pulse-echo system with annular array, the system can be optimized in the terms of identifying a given object or interface among a limited set of objects or interfaces.

To realize the optimal identification, a sequence of several numerical methods are required: 1) An effective means to determine the received signal from a given array element when transmitting with any given array element, based on the shape, location and orientation of the reflector; 2) a method for determining optimal acoustic field and

receiver characteristics for a specific application, by varying the relative delays and/or amplitude scale factors to the individual transmitting and receiving elements; 3) neural networks or self-organizing maps to achieve the most accurate classification of the actual reflector.

In previous chapters, we discussed the modeling of ultrasound pulse-echo system, as well as the implementation of the numerical modeling system, especially for a system with planar circular transmitter and receiver. Based on those discussions, the received signal from an array element or from an entire array can readily be derived. In this chapter, the optimal design of acoustic field and receiver characteristic will be explored which is carried out by varying the relative excitation delay of the individual transmitting and receiving elements. The last step in the sequence, "neural networks or self-organizing maps", will not be covered in the thesis.

In chapter 5, the DREAM method using optimal tile size was used to calculate the received signal from different reflectors for different sets of planar circular transducer combinations. All the results obtained by DREAM method were compared to those obtained by Huygens method. The results obtained by both methods match very well in both frequency-domain (0 to 15MHz) and in time-domain, while DREAM method is much more computationally efficient. It was also shown in chapter 5 that T-DREAM produces better results than the R-DREAM does when using the same tile area. In practical applications, triangular tiles can approximate reflector surface better than rectangular tiles. Therefore, in this chapter, only T-DREAM with optimal tile size will be used to determine the received signal in an annular array system.

In this chapter, both a 3-ring annual array system and a 6-ring annual array system are used. The radii of the rings are chosen so that the area of each ring is about the same. The radius of the whole annular array is 9*mm* for the 3-ring array and 12.7*mm* for the 6-ring array. Consequently, for the 3-ring array, the outer radii of each ring are 5.1*mm*, 7.3*mm* and 9*mm*, respectively; for the 6-ring array, the outer radii of each ring are 5.2*mm*, 7.3*mm*, 9*mm*, 10.4*mm*, 11.6*mm* and 12.7*mm,* respectively.

In section 6.1, a brief introduction is given to the concept of the optimization which will be used to find the set of delay values for an annular array system to optimally differentiate between two specific interfaces. Two methods are introduced: the *Global Search Method* and the *Waveform Alignment Method*. In section 6.2, both methods are applied to find the optimal set of delay values or the optimal delay matrix to best differentiate between a tilted flat surface and a convex curved surface.

The optimal delay matrix is the delay matrix which will maximize the energy of the difference signal between the received signals from two specified reflectors. As will be discussed later, the delay values contained in the optimal delay matrix need to be decomposed into separate transmit and receive delays; thus, the optimal delay matrix is an intermediate result from which the optimal set of delay values may be obtained. Because the Global Search Method is computationally infeasible when the number of elements in an array is large, it is only applied for a 3-ring annular array system. The Waveform Alignment Method is applied for given sets of two reflectors, using both 3-ring and 6-ring annular array systems. The actual output signals are presented as well. Specifically, in section 6.3, the Waveform Alignment Method is applied to obtain the optimal delay matrix which will best differentiate between a tilted flat surface and a

120

concave curved surface, using both 3-ring and 6-ring annular array systems. Section 6.4 is similar to section 6.3, except that the two reflector surfaces are a convex curved surface and a concave curved surface.

6.1 The Concept of Optimization

In section 2.6, the summed received signal (output voltage) from an annular array transducer due to an unspecified reflector is derived in equation (2.36), which is repeated below for convenience:

$$v_{total}^{REFL}(t) = \sum_{i=1}^{N} \sum_{j=1}^{N} A_i A_j' v_{i,j}^{REFL}(t) \otimes \boldsymbol{d}(t - (\boldsymbol{t}_i + \boldsymbol{t}_j')) \tag{6.1}$$

In equation (6.1), $v_{i,j}^{REFL}(t)$ refers to the received signal from a specific reflector, produced with the ith ring as transmitter and the jth ring as receiver. Due to reciprocity, $v_{i,j}^{REFL}(t) = v_{j,i}^{REFL}(t)$; A_i is an amplitude scale factor (excitation signal amplitude) assigned to the ith element in the array in transmitting mode; A_j' is an amplitude scale factor (gain value) assigned to the jth element in the array in receiving mode; $\boldsymbol{t}_i$ is the delay assigned to the ith element in the array in transmitting mode; $\boldsymbol{t}_j'$ is the delay assigned to the jth element in the array in receiving mode and $\otimes$ indicates convolution. As a first step to solve the optimization problem more generally, our objective in this thesis is to differentiate between only two specified interfaces at a time. In addition, we only consider the optimization of the delay assigned to the elements in the array and hence all A_i and A_j' values will be set equal to unity. Therefore, equation (6.1) is simplified to

$$v_{total}^{REFL}(t) = \sum_{i=1}^{N}\sum_{j=1}^{N} v_{i,j}^{REFL}(t) \otimes d(t-(t_i + t_j^{'})) \qquad (6.2)$$

Now, consider an N element annular array transducer and two reflectors with specified shape, location and orientation, namely, reflector A and reflector B. As discussed in section 2.6, an $N\acute{\ }N$ *signal matrix* of the form shown in equation (2.32) can be generated for the received signals from each reflector, namely $\mathbf{V^A}$(t) and $\mathbf{V^B}$(t). Therefore, an $N\acute{\ }N$ *difference signal matrix* $\mathbf{V^{A\text{-}B}}$(t) = $\mathbf{V^A}$(t) − $\mathbf{V^B}$(t) can readily be generated for the difference signal between the received signals from reflector A and reflector B. Figure 6.1 illustrates the calculation of the difference signal matrix for 3-ring annular array transducer. Equation (6.3) illustrates the general form of the difference signal matrix $\mathbf{V^{A\text{-}B}}$(t):

$$\mathbf{V^{A\text{-}B}}(t) = \begin{bmatrix} v_{1,1}^{A-B}(t) & . & . & v_{1,j}^{A-B}(t) & . & . & v_{1,N}^{A-B}(t) \\ . & . & . & . & . & . & . \\ v_{i,1}^{A-B}(t) & . & . & v_{i,j}^{A-B}(t) & . & . & v_{i,N}^{A-B}(t) \\ . & . & . & . & . & . & . \\ v_{N,1}^{A-B}(t) & . & . & v_{N,j}^{A-B}(t) & . & . & v_{N,N}^{A-B}(t) \end{bmatrix} \qquad (6.3)$$

In equation (6.3), each element of the matrix, $v_{i,j}^{A-B}(t)$, for $i, j \in [1, N]$, refers to the difference signal between the received signals from reflector A and reflector B, produced with the ith ring as transmitter and the jth ring as receiver, and

$$v_{i,j}^{A-B}(t) = v_{i,j}^{A}(t) - v_{i,j}^{B}(t) \qquad (6.4)$$

Obviously, $\mathbf{V^{A\text{-}B}}$(t) is symmetric due to reciprocity, as long as no time shifts have been introduced.
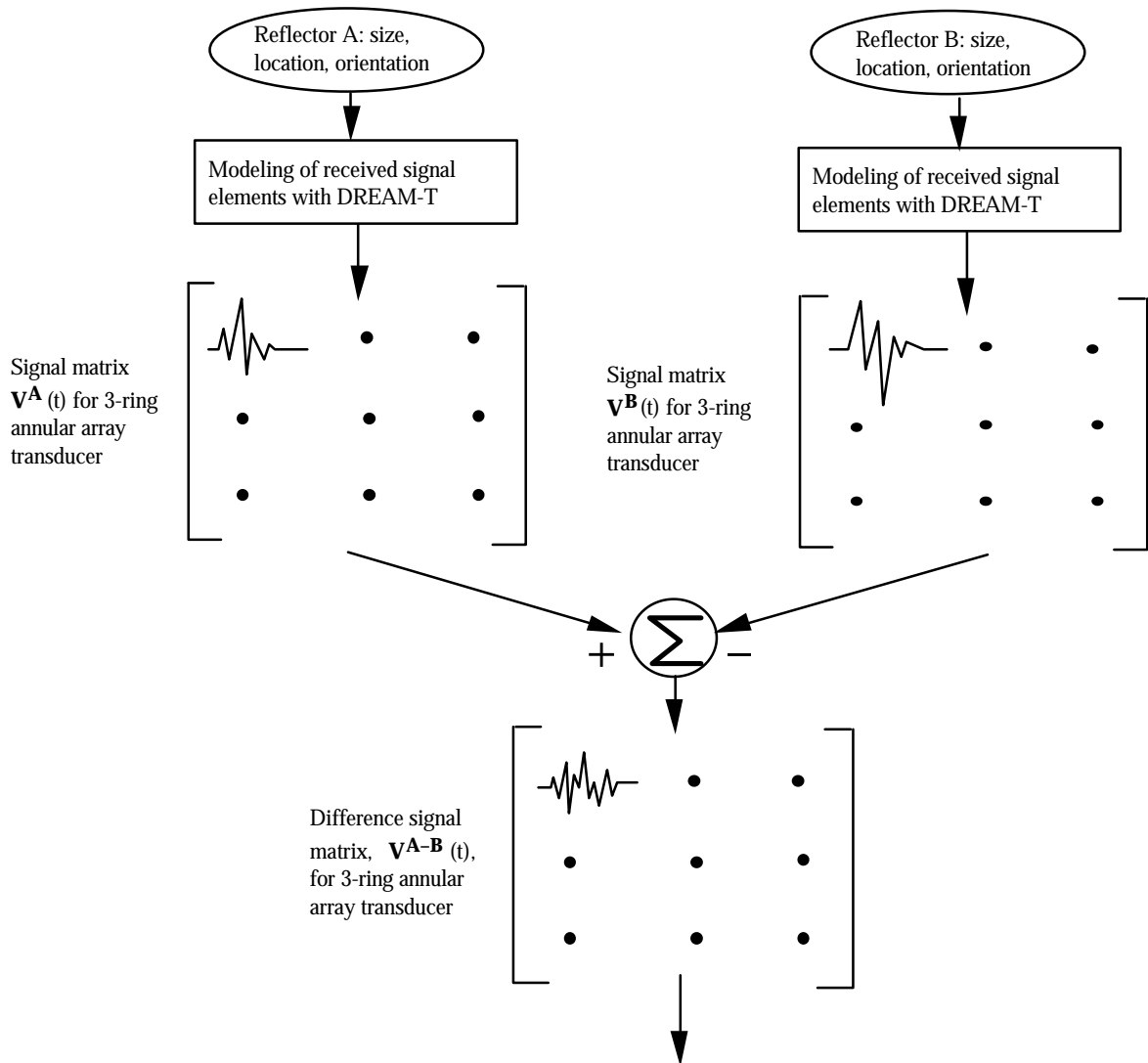
Figure 6.1 Calculation of the Difference Signal Matrix $V^{A-B}(t)$ for a 3-ring annular array transducer.

When separate transmit and receive delays are assigned to the individual components in the difference signal matrix, the summed output voltage of the difference signal from the two reflectors, $v_{total}^{A-B}(t)$, is:

$$v_{total}^{A-B}(t) = v_{total}^{A}(t) - v_{total}^{B}(t)$$

$$= \sum_{i=1}^{N}\sum_{j=1}^{N} v_{i,j}^{A}(t) \otimes \boldsymbol{d}(t - (\boldsymbol{t}_i + \boldsymbol{t}_j^{'})) - \sum_{i=1}^{N}\sum_{j=1}^{N} v_{i,j}^{B}(t) \otimes \boldsymbol{d}(t - (\boldsymbol{t}_i + \boldsymbol{t}_j^{'}))$$

$$= \sum_{i=1}^{N}\sum_{j=1}^{N} (v_{i,j}^{A}(t) - v_{i,j}^{B}(t)) \otimes \boldsymbol{d}(t - (\boldsymbol{t}_i + \boldsymbol{t}_j^{'})) \qquad (6.5)$$

$$= \sum_{i=1}^{N}\sum_{j=1}^{N} v_{i,j}^{A-B}(t) \otimes \boldsymbol{d}(t - (\boldsymbol{t}_i + \boldsymbol{t}_j^{'}))$$

In equation (6.5), $v_{total}^{A}(t)$ and $v_{total}^{B}(t)$ refer to the summed output voltage from reflector A and reflector B, respectively, produced by the entire annular array transducer. $v_{total}^{A}(t)$ and $v_{total}^{B}(t)$ are calculated using equation (6.2); $v_{i,j}^{A}(t)$ and $v_{i,j}^{B}(t)$ refer to the received signal from reflector A and reflector B, respectively, produced with the ith ring as transmitter and the jth ring as receiver; $v_{i,j}^{A-B}(t)$ is as defined in equation (6.4). Clearly, $v_{total}^{A-B}(t)$ can take on many forms, depending on the chosen set of $\boldsymbol{t}_i$, $\boldsymbol{t}_j^{'}$, i, $j \in [1, N]$. We define the *difference energy* between $v_{total}^{A}(t)$ and $v_{total}^{B}(t)$ as E_{total}^{A-B} which is formulated as

$$E_{total}^{A-B} = \int_{-\infty}^{\infty} v_{total}^{A-B}(t)^2 \, dt = \int_{-\infty}^{\infty} (\sum_{i=1}^{N}\sum_{j=1}^{N} v_{i,j}^{A-B}[t - (\boldsymbol{t}_i + \boldsymbol{t}_j^{'})])^2 \, dt \qquad (6.6)$$

If we can find a set of time delays, that is, a set of $\boldsymbol{t}_i$, $\boldsymbol{t}_j^{'}$, $i, j \in [1, N]$ which will maximize the difference energy E_{total}^{A-B}, then $v_{total}^{A}(t)$ and $v_{total}^{B}(t)$ will be considered optimally separated in terms of energy of the difference signal. Two different ways are implemented to find the optimal delay set to maximize the difference energy defined in equation (6.6): the *Global Search Method* and the *Waveform Alignment Method*.

6.1.1 The Global Search Method

The most straightforward method to find the optimal delay set is to search through all possible delay combinations for the elements of the annular array transducer in either transmitting or receiving mode. That is, apply all the possible combination of t_i and t_j', for i, $j \in [1, N]$, in equation (6.6) to calculate the corresponding difference energy. The set of t_i and t_j', which produces the largest difference energy, is then the optimal delay set.

Because the delays are relative delays and one delay can be set arbitrarily, there are N-1 transmit delays to be chosen independently for the N rings in transmitting mode. Similarly, there are N-1 independent receive delays. If there are m_1 possible transmit delay values and m_2 receive delay values, $m_1^{(N-1)} \times m_2^{(N-1)} = (m_1 \times m_2)^{(N-1)}$ calculations are needed to find the optimal delay set for a N-ring array with Global Search Method. As an example, a 3-ring annular array will be considered. We arbitrarily set $t_1 = t_1' = 0$ and assume that the transmitting delay values t_i can be set to be one of $-1\textit{ms}$, $0\textit{ms}$ and $1\textit{ms}$ for $i = 2, 3$; and the receiving delay values t_j' can be set to be one of $-2\textit{ms}$, $0\textit{ms}$ and $2\textit{ms}$ for $j = 2, 3$. Therefore, there are $3^{(3-1)} \times 3^{(3-1)} = 81$ possible combinations of (t_i, t_j'), for $i, j \in [1, 3]$, or, 81 sets of delay values $\{t_1, t_2, t_3, t_1', t_2', t_3'\}$. They are $\{0, -1, -1, 0, -2, -2\}$ $\textit{ms}$, $\{0, -1, -1, 0, -2, 0\}$ $\textit{ms}$, $\{0, -1, -1, 0, -2, 2\}$ $\textit{ms}$, $\{0, -1, -1, 0, 0, -2\}$ $\textit{ms}$, and so on. All the 81 sets of delay values are plugged into equation (6.6) to calculate the difference energy; the set which produce the largest energy in equation (6.6) is the optimal delay set.

Two major disadvantages of this method are: 1) The search can only be carried out over a limited delay range with discrete delay steps, which makes it probable that the optimal delay sets found is sub-optimal. 2) The computation time is so long that the Global Search Method is computational infeasible when the number of the elements in the array is large. For example, using just 41 discrete delay steps for both transmitting and receiving delays, which corresponds to $0.1ms$ step for a delay range of $-2ms$ to $2ms$, a 6-ring array transducer would require $41^{2(6-1)}$ calculations, i.e., 1.34×10^{16} calculations. For a fast calculation speed of one calculation per microsecond, about 426 years would be needed. An example with specified simulation scenario will be presented in section 6.2 to find the optimal delay set for a 3-ring array system with the Global Search Method.

6.1.2 The Waveform Alignment Method

For the convenience of following discussion, we define an N×N *delay matrix* **T** of the form shown in equation (6.7):

$$
\mathbf{T} = \begin{bmatrix} t_{1,1} & \cdot & \cdot & t_{1,j} & \cdot & \cdot & t_{1,N} \\ \cdot & \cdot & \cdot & \cdot & \cdot & \cdot & \cdot \\ t_{i,1} & \cdot & \cdot & t_{i,j} & \cdot & \cdot & t_{i,N} \\ \cdot & \cdot & \cdot & \cdot & \cdot & \cdot & \cdot \\ t_{N,1} & \cdot & \cdot & t_{N,j} & \cdot & \cdot & t_{N,N} \end{bmatrix} = \begin{bmatrix} \boldsymbol{t}_1 + \boldsymbol{t}_1^{'} & \cdot & \cdot & \boldsymbol{t}_1 + \boldsymbol{t}_j^{'} & \cdot & \cdot & \boldsymbol{t}_1 + \boldsymbol{t}_N^{'} \\ \cdot & \cdot & \cdot & \cdot & \cdot & \cdot & \cdot \\ \boldsymbol{t}_i + \boldsymbol{t}_1^{'} & \cdot & \cdot & \boldsymbol{t}_i + \boldsymbol{t}_j^{'} & \cdot & \cdot & \boldsymbol{t}_i + \boldsymbol{t}_N^{'} \\ \cdot & \cdot & \cdot & \cdot & \cdot & \cdot & \cdot \\ \boldsymbol{t}_N + \boldsymbol{t}_1^{'} & \cdot & \cdot & \boldsymbol{t}_N + \boldsymbol{t}_j^{'} & \cdot & \cdot & \boldsymbol{t}_N + \boldsymbol{t}_N^{'} \end{bmatrix} \quad (6.7)
$$

In equation (6.7), $\boldsymbol{t}_i$ and $\boldsymbol{t}_j$', for $i, j \in [1, N]$, have the same definition as in equation (6.1). Therefore, each element of the delay matrix **T**, $t_{i,j}$, is the combination of transmitting and receiving delays, which is exactly the delay values that should be assigned to the element of the difference signal matrix $\mathbf{V}^{\mathbf{A\text{-}B}}(t)$ to obtain the summed

126

output voltage of the difference signal, $v_{total}^{A-B}(t)$. By doing this, equation (6.6) is simplified as:

$$E_{total}^{A-B} = \int_{-\infty}^{\infty} v_{total}^{A-B}(t)^2 dt = \int_{-\infty}^{\infty} (\sum_{i=1}^{N} \sum_{j=1}^{N} v_{i,j}^{A-B}[t - (\mathbf{t}_i + \mathbf{t}_j^{'})])^2 dt$$

$$= \int_{-\infty}^{\infty} (\sum_{i=1}^{N} \sum_{j=1}^{N} v_{i,j}^{A-B}(t - t_{i,j}))^2 dt$$

(6.8)

and the delay matrix which maximize the E_{total}^{A-B} is the optimal delay matrix.

The concept behind the Waveform Alignment Method is to represent each element, or signal, $v_{i,j}^{A-B}(t)$, in the difference Signal Matrix $\mathbf{V^{A-B}}$(t) by a time shifted and amplitude scaled version of a specified waveform, termed *w(t)*, *solely for the purpose of establishing the optimal delay matrix*. The waveform *w(t)* is chosen to be a good approximation to the impulse response of the combined transmitting and receiving array transducer; it should be remembered that in actual experiments, the measured received signal is a convolution of this impulse response with the received signal as calculated under the assumption of frequency-independent transducers. Furthermore, the center frequency of the array transducer should be selected so that it will capture much of the energy of the difference signal; in other words, the mean (magnitude) spectrum of the difference signal should have a significant overlap with the (magnitude) spectrum of *w(t)*. The single waveform approximation is illustrated in the top part of Figure 6.2.

Difference signal matrix, $\mathbf{V}^{A-B}$(t), for 3-ring annular array transducer, from Figure 6.1

Single waveform matrix, providing best match between difference signal matrix, $\mathbf{V}^{A-B}$(t), and waveform $w(t)$

t^W_{11} t^W_{12} t^W_{13}
t^W_{21} t^W_{22} t^W_{23}
t^W_{31} t^W_{32} t^W_{33}

Delay matrix, $\mathbf{T}^{Wave}$, generated from positions of $w(t)$ in single waveform matrix

$$\begin{bmatrix} t^W_{11} & t^W_{12} & t^W_{13} \\ t^W_{21} & t^W_{22} & t^W_{23} \\ t^W_{31} & t^W_{32} & t^W_{33} \end{bmatrix}$$

Optimal delay matrix, $\mathbf{T}^{Opt}$, with time delay values to be applied to signals in matrix $\mathbf{V}^{A}$(t) and matrix $\mathbf{V}^{B}$(t)

$$\begin{bmatrix} t_{11} = t_{max} - t^W_{11} & t_{12} = t_{max} - t^W_{12} & t_{13} = t_{max} - t^W_{13} \\ t_{21} = t_{max} - t^W_{21} & t_{22} = t_{max} - t^W_{22} & t_{23} = t_{max} - t^W_{23} \\ t_{31} = t_{max} - t^W_{31} & t_{32} = t_{max} - t^W_{32} & t_{33} = t_{max} - t^W_{33} \end{bmatrix}$$

Figure 6.2 Calculation of the optimal delay matrix $\mathbf{T}^{Opt}$ using the Waveform Alignment Method. Note that in the lower part, the superscript "Opt" for $t_{i,j}$ has been left out for clarity.

As described earlier, we need to represent $v^{A-B}_{i,j}(t)$ by a time shifted and scaled

version of $w(t)$, in order to determine the optimal delay matrix. Thus, $v^{A-B}_{i,j}(t)$ and $w(t)$

are approximately matched as follows:

$$v^{A-B}_{i,j}(t) \approx A_{i,j} w(t) \otimes \boldsymbol{d}(t - t^w_{i,j}) = A_{i,j} w(t - t^w_{i,j}) \tag{6.9}$$

In equation (6.9), $A_{i,j}$ is the amplitude scale factor and $t_{i,j}^w$ is the time shift relative to some time reference. To determine $t_{i,j}^w$ and $A_{i,j}$, the cross-correlation function of $w(t)$ and $v_{i,j}^{A-B}(t)$ is calculated, and the location and amplitude of the cross-correlation peak is determined. This operation is performed separately on all the elements in the difference signal matrix $\mathbf{V^{A\text{-}B}}(t)$. The operation of representing $v_{i,j}^{A-B}(t)$ by $A_{i,j}w(t-t_{i,j}^w)$ may be viewed as a wavelet transform of $v_{i,j}^{A-B}(t)$ where only the first term is retained. Further description of the actual implementation of the Waveform Alignment Method is given in section 6.2.2.

The value of the scale factor, $A_{i,j}$, is not utilized in research presented here, but the time delay, $t_{i,j}^w$, is used to define a waveform alignment delay matrix, $\mathbf{T^{wave}}$ as follows:

$$\mathbf{T^{wave}} = \begin{bmatrix} t_{1,1}^w & \cdot & \cdot & t_{1,j}^w & \cdot & \cdot & t_{1,N}^w \\ \cdot & \cdot & \cdot & \cdot & \cdot & \cdot & \cdot \\ t_{i,1}^w & \cdot & \cdot & t_{i,j}^w & \cdot & \cdot & t_{i,N}^w \\ \cdot & \cdot & \cdot & \cdot & \cdot & \cdot & \cdot \\ t_{N,1}^w & \cdot & \cdot & t_{N,j}^w & \cdot & \cdot & t_{N,N}^w \end{bmatrix} \quad (6.10)$$

The top part of Figure 6.2 illustrates the "best match" locations of $w(t)$ for the signals in the difference signal matrix $\mathbf{V^{A\text{-}B}}(t)$, as determined by the cross-correlation function. The amplitude scale factor has been left out for clarity. The delay matrix, $\mathbf{T^{wave}}$ is then obtained from the "best match" locations, as also shown in Figure 6.2.

The difference between the summed output voltage from reflector A and the summed output voltage from reflector B is denoted $v_{total}^{A-B}(t)$ and was defined in equation

(6.5) where the delays $\boldsymbol{t}_I$, and $\boldsymbol{t}_j^{'}$ were left unspecified. In order to align the signal components in the difference signal matrix $\mathbf{V^{A\text{-}B}}(t)$, and thereby maximize the energy of $v_{total}^{A-B}(t)$, the signal components need to be individually time shifted.

Only the Global Search Method, performed with very small time steps, can identify the set of time shifts that maximizes the energy of $v_{total}^{A-B}(t)$. However, as has been shown, the computation time required to execute the Global Search Method makes this method impractical except for array transducers with only a few elements. The Waveform Alignment Method is based on the idea that the set of time shifts which aligns the waveforms in single waveform matrix also will align the signals in the difference signal matrix $\mathbf{V^{A\text{-}B}}(t)$ in such a way that, at least to a first approximation, the energy of $v_{total}^{A-B}(t)$ is maximized.

Equation (6.5) for calculating $v_{total}^{A-B}(t)$ was written for arbitrary transmit and receive delays, $\boldsymbol{t}_I$ and $\boldsymbol{t}_j^{'}$, respectively. In order to maximize the energy of $v_{total}^{A-B}(t)$, an additional delay, referred to as the optimal combined transmit and receive delay, $t_{i,j}^{OPT} = \boldsymbol{t}_i + \boldsymbol{t}_j^{'}$, is determined so that the waveforms, $w(t - t_{i,j}^{w})$, in the single waveform matrix will be aligned. Applying the approximation for $v_{i,j}^{A-B}(t)$ from equation (6.9) to equation (6.5) and substituting $t_{i,j}^{OPT}$ for $\boldsymbol{t}_i + \boldsymbol{t}_j^{'}$ gives:

$$
\begin{aligned}
v_{total}^{A-B}(t) &\approx \sum_{i=1}^{N}\sum_{j=1}^{N} A_{i,j}\, w(t)\otimes \boldsymbol{d}(t-t_{i,j}^{w})\otimes \boldsymbol{d}(t-t_{i,j}^{OPT}) \\
&= \sum_{i=1}^{N}\sum_{j=1}^{N} A_{i,j}\, w(t)\otimes \boldsymbol{d}(t-(t_{i,j}^{w}+t_{i,j}^{OPT}))
\end{aligned}
\tag{6.11}
$$

If we want to maximize the energy of $v_{total}^{A-B}(t)$, the $t_{i,j}^{w}+t_{i,j}^{OPT}$ should be the same for all I, $j \in [1, N]$. With the practical implementation of the Waveform Alignment Method in mind, only positive time shifts will be considered. For this purpose, we identify the maximum delay value in the delay matrix $\mathbf{T^{wave}}$ as $t_{\max}$ and set it to be $t_{i,j}^{w} + t_{i,j}^{OPT}$. For the case illustrated in Figure 6.2, $t_{\max} = t_{2,3}^{w}$. Therefore, the optimal combined delay values, $t_{i,j}^{OPT}$, necessary for the waveforms in single waveform matrix to be aligned are given as

$$t_{i,j}^{OPT} = t_{\max} - t_{i,j}^{w} \tag{6.12}$$

and the optimal delay matrix $\mathbf{T^{OPT}}$ is readily obtained as shown in the lower part of Figure 6.2. The summed difference signal $v_{total}^{A-B}(t)$, optimized to have the largest energy, can be calculated using equation (6.11). The corresponding difference energy can be calculated from equation (6.8).

To obtain the actual received signals from reflector A and reflector B, under the condition of optimized energy difference, the delay values in the optimal delay matrix $\mathbf{T^{OPT}}$ are applied to the corresponding signals in the signal matrices, $\mathbf{V^{A}}(t)$ and $\mathbf{V^{B}}(t)$, respectively. This is illustrated in the top part of Figure 6.3. Next, each signal in the signal matrices $\mathbf{V^{A}}(t)$ and $\mathbf{V^{B}}(t)$ are bandpass filtered with a filter with the impulse response *w(t)*. This operation emulates the filtering effect of the transmitting and receiving transducers, as discussed earlier in this section. Finally, the actual received signals from reflector A and reflector B are obtained by simply summing all the signals in the filtered signal matrices $\mathbf{V^{A}}(t)$ and $\mathbf{V^{B}}(t)$, respectively, as shown in Figure 6.3.

131

Signal matrix $\mathbf{V^A}$(t)
from Figure 6.1

Signal matrix $\mathbf{V^B}$(t)
from Figure 6.1

$$\begin{bmatrix} t_{11} & t_{12} & t_{13} \\ t_{21} & t_{22} & t_{23} \\ t_{31} & t_{32} & t_{33} \end{bmatrix}$$

Optimal delay
matrix, $\mathbf{T}^{\text{Opt}}$,
from Figure 6.2

$$\begin{bmatrix} t_{11} & t_{12} & t_{13} \\ t_{21} & t_{22} & t_{23} \\ t_{31} & t_{32} & t_{33} \end{bmatrix}$$

Signal matrix
$\mathbf{V^A}$(t), with time
shifts applied
according to delay
matrix, $\mathbf{T}^{\text{Opt}}$

Signal matrix
$\mathbf{V^B}$(t), with time
shifts applied
according to delay
matrix, $\mathbf{T}^{\text{Opt}}$

Bandpass filtering of each
signal in signal matrix $\mathbf{V^A}$(t),
using a filter with impulse
response, *w(t)*

Bandpass filtering of each
signal in signal matrix $\mathbf{V^B}$(t),
using a filter with impulse
response, *w(t)*

Filtered signal
matrix $\mathbf{V^A}$(t),
with time
shifts applied
according to
delay matrix,
$\mathbf{T}^{\text{Opt}}$

Filtered signal
matrix $\mathbf{V^B}$(t),
with time shifts
applied
according to
delay matrix,
$\mathbf{T}^{\text{Opt}}$

Summation of all signals in
filtered signal matrix $\mathbf{V^A}$(t)

Summation of all signals in
filtered signal matrix $\mathbf{V^B}$(t)

Received signal from array
transducer due to reflector A,
optimally reparated from
received signal from reflector B

Received signal from array
transducer due to reflector B,
optimally reparated from
received signal from reflector A

Figure 6.3 The calculation of the actual received signals from individual reflector A and reflector B, under the condition of optimized energy difference, using the Waveform Alignment Method: Alignment of array signal components; bandpass filtering and summation of signal components. Note that in the top part, the superscript "Opt" for $t_{i,j}$ has been left out for clarity.

6.1.3   Comparison of Two Optimization Methods

In the previous sections, two optimization methods are introduced, i.e., the Global Search Method and the Waveform Alignment Method. It is important to note that the results produced by the two methods differ in some important ways.

The result obtained by the Global Search Method is the optimal set of separate transmit and receive delay values. The delay values can be used directly to implement an actual experiment. In general, the optimal transmit delay values are different from the optimal receive delay values, which means that the array transducer will have different transmit and receive characteristics and the corresponding optimal delay matrix is not symmetric.

In contrast, the result produced by the Waveform Alignment Method is the optimal delay matrix, whose terms are a combination of the transmit and receive delays. We need to decompose the delay matrix into separate transmitting and receiving delay matrices before the optimal system can be implemented for an actual experiment. More discussion about the decomposition of the delay matrix will be presented in subsection 6.1.4 "Separating delay matrix into transmit and receive delay sets". Further, the optimal delay matrix obtained by the Waveform Alignment Method is symmetric. Based on the modeling results given later in this chapter, this aspect does not seem to have a seriously negative effect on the performance.

6.1.4   Separating Delay Matrix into Transmit and Receive Delay Sets

As mentioned in subsection 6.1.3, we need to decompose the delay matrix into separate transmit and receive delay matrices before the optimal system can be

implemented for an actual experiment, based on the results obtained by the Waveform Alignment Method. It can be done using the relationship between $\boldsymbol{t}_i$, $\boldsymbol{t}_j{}'$ and $t_{i,j}$, for $i, j \in [1, N]$, as presented in equation (6.7). This task is far from trivial. We will discuss it in this section without providing an actual solutions. For this reason, in section 6.2, 6.3 and 6.4, the delay values will be presented in the form of optimal delay matrix $\mathbf{T^{OPT}}$ instead of separated transmit and receive delay sets, and the received signals will be calculated based on $\mathbf{T^{OPT}}$.

We know that the difference signal matrix $\mathbf{V^{A\text{-}B}}(t)$ is symmetric, i.e., $v_{i,j}^{A-B}(t) = v_{j,i}^{A-B}(t)$, as long as no time shifts have been introduced. Except for this symmetry relationship, no other relationship between the terms in the matrix has been determined and hence, the number of independent terms is $(N+1)N/2$ for a N×N matrix. Therefore, for a N-ring array system, there are $(N+1)N/2$ independent terms in the optimal delay matrix $\mathbf{T^{OPT}}$ obtained by the Waveform Alignment Method. However, as we discussed in section 6.1.1, in an actual physical system, there are N-1 independent transmitting delays and N-1 independent receiving delays. Therefore, there are only 2(N-1) independent terms in the delay matrix for a real system, which means that the optimal delay matrix obtained by Waveform Alignment Method is over-determined.

The easiest way to solve this problem is to formulate 2(N-1) equations using only 2(N-1) independent terms in the optimal delay matrix and solve for the transmitting and receiving delays. However, this means that the remaining $[(N+1)N/2]$ – $[2(N-1)]$ delay values are not considered for the optimization.

For the convenience of the following discussion, equation (6.7) is rewritten as follows in equation (6.13),

$$
\mathbf{T} =
\begin{bmatrix}
\cdot & \cdot & \cdot & & \cdot & & \cdot & \cdot \\
\cdot & \cdot & \cdot & & \cdot & & \cdot & \cdot \\
\cdot & \cdot & t_{i,j} & t_{i,j+1} & \cdot & & \cdot \\
\cdot & \cdot & t_{i+1,j} & t_{i+1,j+1} & \cdot & & \cdot \\
\cdot & \cdot & \cdot & & \cdot & & \cdot & \cdot \\
\cdot & \cdot & \cdot & & \cdot & & \cdot & \cdot
\end{bmatrix}
=
\begin{bmatrix}
\cdot & \cdot & \cdot & & \cdot & & \cdot & \cdot \\
\cdot & \cdot & \cdot & & \cdot & & \cdot & \cdot \\
\cdot & \cdot & \boldsymbol{t}_i + \boldsymbol{t}_j^{'} & \boldsymbol{t}_i + \boldsymbol{t}_{j+1}^{'} & \cdot & \cdot \\
\cdot & \cdot & \boldsymbol{t}_{i+1} + \boldsymbol{t}_j^{'} & \boldsymbol{t}_{i+1} + \boldsymbol{t}_{j+1}^{'} & \cdot & \cdot \\
\cdot & \cdot & \cdot & & \cdot & & \cdot & \cdot \\
\cdot & \cdot & \cdot & & \cdot & & \cdot & \cdot
\end{bmatrix}
\tag{6.13}
$$

It is easily seen that, if we want to separate $t_{i,j}$ into $\boldsymbol{t}_i + \boldsymbol{t}_j^{'}$, any element in the delay matrix must satisfy

$$
\begin{aligned}
t_{i+1,j} &= \boldsymbol{t}_{i+1} + \boldsymbol{t}_j^{'} = \boldsymbol{t}_i + \boldsymbol{t}_j^{'} + \boldsymbol{t}_{i+1} + \boldsymbol{t}_{j+1}^{'} - (\boldsymbol{t}_i + \boldsymbol{t}_{j+1}^{'}) \\
&= t_{i,j} + t_{i+1,j+1} - t_{i,j+1}
\end{aligned}
\tag{6.14}
$$

An appropriate way is to modify the optimal delay matrix $\mathbf{T^{OPT}}$ obtained by Waveform Alignment Method, so that the rule in equation (6.14) is fulfilled. Obviously, there are an infinite number of modified delay matrices $\mathbf{T^m}$ which can satisfy equation (6.14). However, the best $\mathbf{T^m}$ is a modified delay matrix which minimizes the difference between $\mathbf{T}$ and $\mathbf{T^m}$. In the other words, the strategy is to minimize the error defined in equation (6.15).

$$
\sum_{i=1}^{N} \sum_{j=1}^{N} (t_{i,j}^{OPT} - t_{i,j}^{m})^2
\tag{6.15}
$$

In equation (6.15), the term $t_{i,j}^{m}$ is the element of the modified delay matrix $\mathbf{T^m}$. It is an undesirable aspect of the Waveform Alignment Method that it produces a symmetrical delay matrix while not fulfilling the rule given in equation (6.14) which is required.

However, the modified delay matrix, $\mathbf{T^m}$, will in general only differ slightly from a symmetrical delay matrix.

6.2 Optimal Delay Matrix for Convex Reflector and Tilted Flat Reflector

In section 6.1, two different ways are introduced to find the optimal delay matrix which gives a maximum differentiation between two reflectors with respect to the energy of the received signal. In this section, both methods are applied to find the optimal delay matrix to differentiate between a convex reflector and a tilted flat reflector. Figure 6.4 illustrates the simulation scenario. The transducer is the 3-ring array or the 6-ring array as described at the beginning of this chapter. The convex reflector is a 10° arc of a cylinder with radius = 86*mm* and length = 15*mm*. The *x-y* cross-sectional area of the convex reflector is 15*mm*×15*mm*. The other one is a 15*mm*×15*mm* square flat reflector which is tilted 0.6° with respect to the transducer surface. The two reflectors are both centered on the acoustic axis of the transducer and the axial distance is 50*mm*.
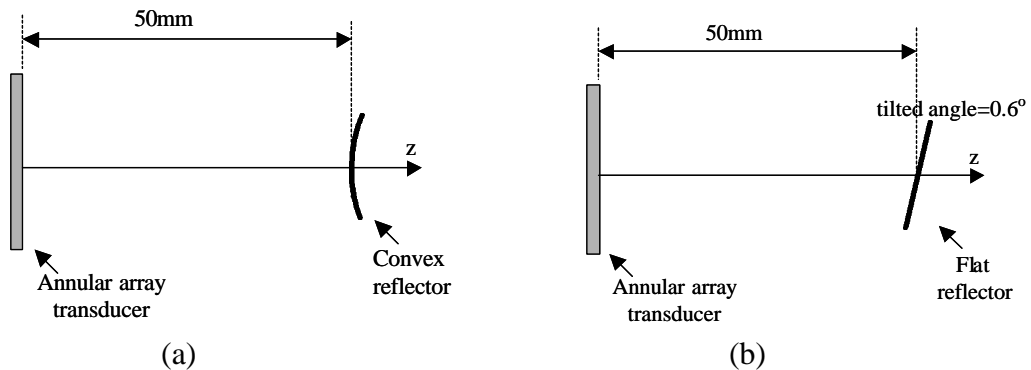
Figure 6.4 Cross-sectional view of the measurement scenarios with convex and tilted flat reflectors.

As we discussed in sections 2.6 and 6.1, using T-DREAM method, two *3´3 signal matrices* $\mathbf{V}^{convex}$(t) and $\mathbf{V}^{flat}$(t) can be generated for the received signals from the convex reflector and the tilted flat reflector for all the combinations of transmitting and receiving rings in a 3-ring annular array transducer. Figure 6.5 and Figure 6.6 illustrate the received signal matrices where Figure 6.5 is for the convex reflector and Figure 6.6 is for the tilted flat reflector.
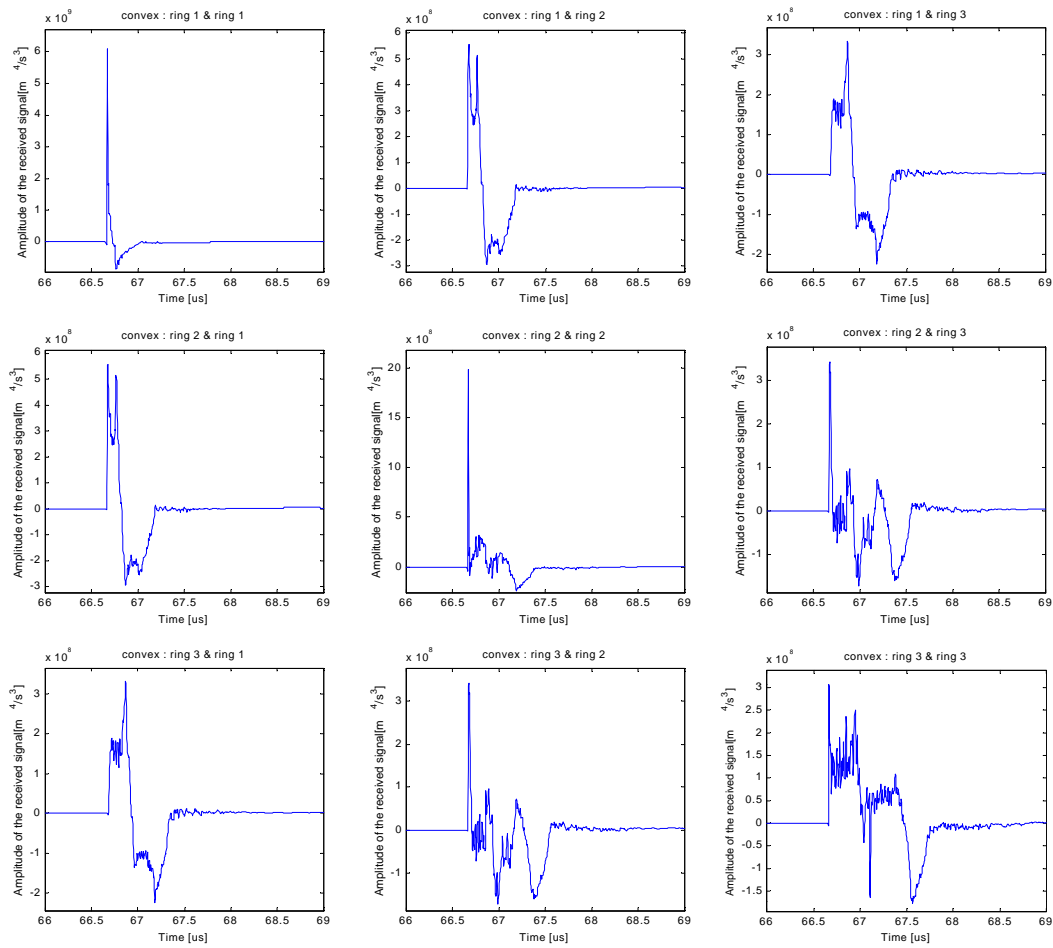
Figure 6.5 The received signal matrix $\mathbf{V}^{convex}$(t) for convex reflector.
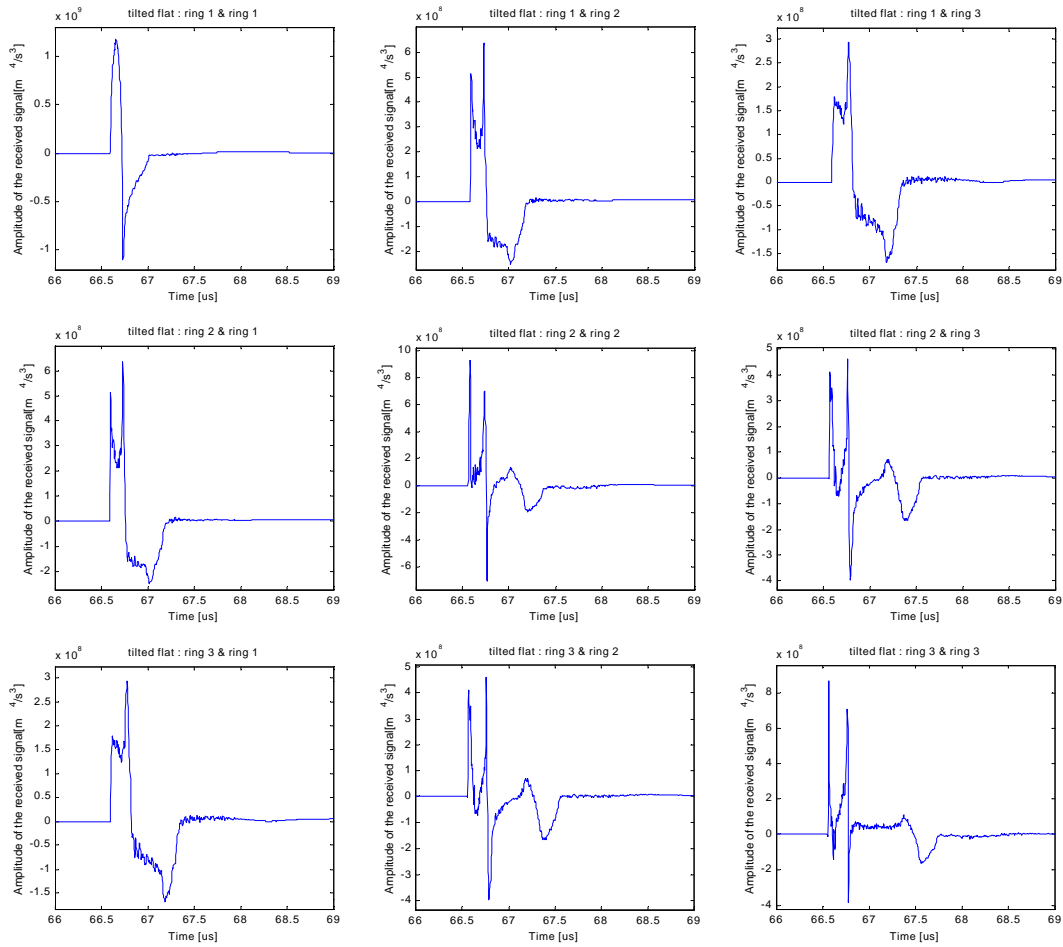
Figure 6.6 The received signal matrix V$^{\text{flat}}$(t) for tilted flat reflector.

By subtracting the received signal matrix in Figure 6.6 from that in Figure 6.5, we can obtain the difference signal matrix between the received signals from the convex reflector and the tilted flat reflector for the 3-ring annular array system. Figure 6.7 illustrates the difference signal matrix.
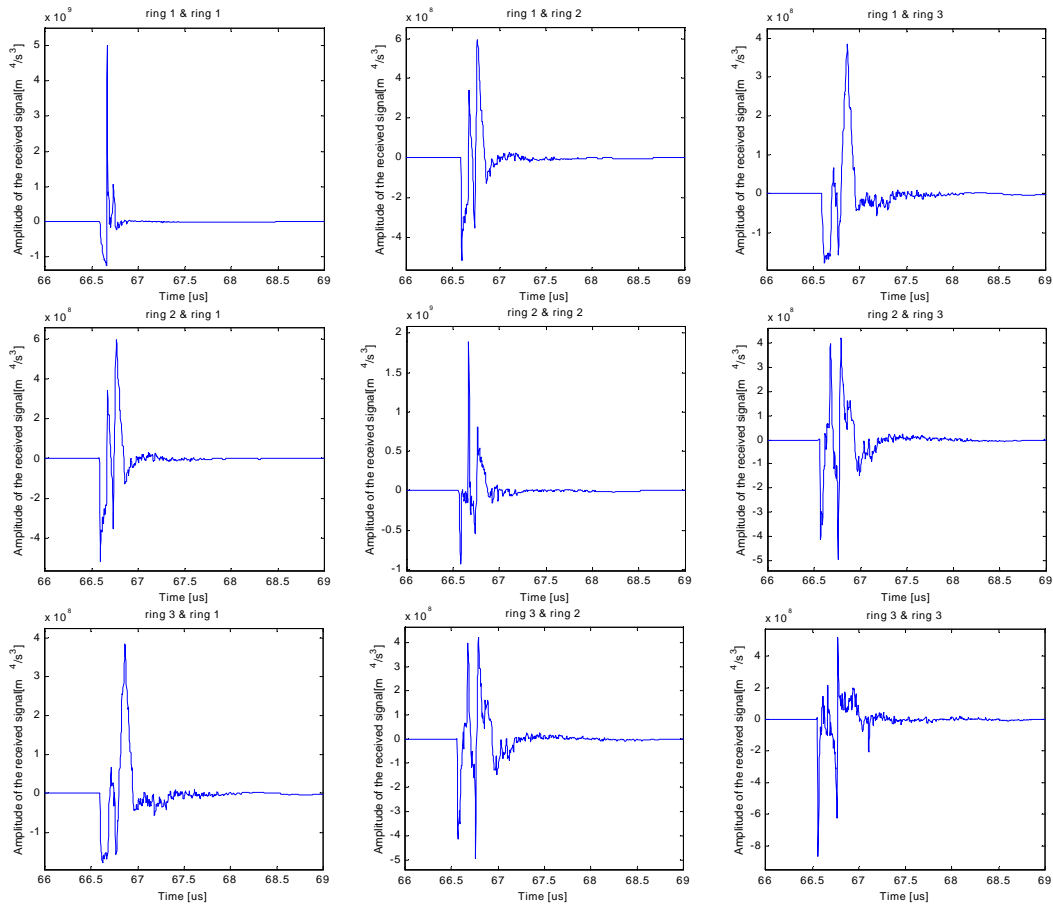
Figure 6.7 Difference signal matrix between the received signal from convex reflector and that from the tilted flat reflector.

Now the difference signal matrix is obtained as shown in Figure 6.7; both the Global Search Method and the Waveform Alignment Method use the difference signal matrix as input functions. In section 6.2.1, the *optimal set of delay values* is calculated by the Global Search Method, based on the 3-ring annular array described at the beginning of this chapter. In section 6.2.2, the *optimal delay matrix* is calculated by the Waveform Alignment Method, based on the same 3-ring annular array as in section 6.2.1. In section 6.2.3, the optimal delay matrix is calculated by the Waveform Alignment Method, based on the 6-ring annular array described at the beginning of this chapter.

6.2.1 Results Obtained by the Global Search Method, based on 3-Ring Array

Now, the Global Search Method is applied to find the optimal set of delay values. We arbitrarily choose $t_1 = 0$ and $t_1' = 0$. We also limit the possible transmitting and receiving delays t_i, t_j', $i, j \in [2, 3]$ to be the values in the range of $-2ms$ to $2ms$ with $0.1ms$ incremental step. Therefore, there are 41^4 possible combinations of (t_i, t_j'), for $i, j \in [1, 3]$, or 2,825,761 sets of possible delay values $\{t_1, t_2, t_3, t_1', t_2', t_3'\}$. The optimal delay set, which produces the largest difference energy in equation (6.6), is found to be: $\{0, -0.1, -0.1, 0, 0, 0\}$ ms; and the corresponding optimal delay matrix is:

$$
T_{global}^{OPT} = \begin{bmatrix} 0 & 0 & 0 \\ -0.1 & -0.1 & -0.1 \\ -0.1 & -0.1 & -0.1 \end{bmatrix} ms
$$

6.2.2 Results Obtained by the Waveform Alignment Method, based on 3-Ring Array

As discussed in section 6.1.2, all the difference signals in Figure 6.7 can be approximated by an amplitude scaled and time shifted version of a single waveform $w(t)$ as in equation (6.9). Recall that the measurements with transducer can be considered as filtering operations, and the spectrum of $w(t)$ should closely match the combined transmit-receive frequency response of the actual ultrasound array transducer. In this chapter, we assume that the annular array transducers acts like a bandpass filter with 7.5MHz central frequency and 7.5MHz bandwidth at the $-3dB$ level. Figure 6.8 illustrates the time-domain and frequency-domain impulse response of the annular arrays.
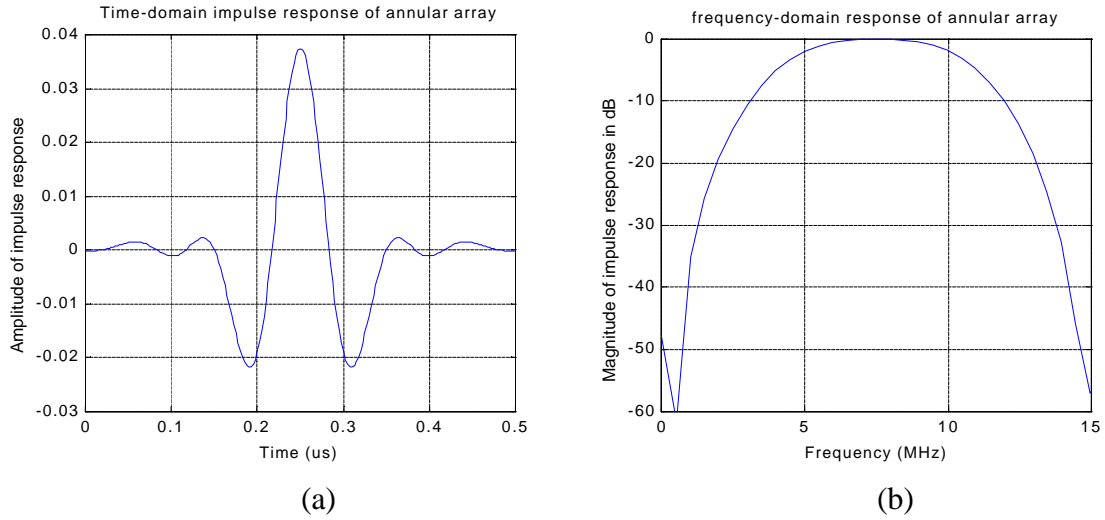
Figure 6.8 The time-domain and frequency-domain response of the annular array transducers.

The waveform $w(t)$ shown in Figure 6.8 (a) is cross-correlated with each difference signal shown in Figure 6.7 to obtain the time shift $t_{i,j}^{w}$ for $w(t)$ which will best approximate the difference signal. Then a scale factor is calculated to match the energy of the difference signal and the time shifted $w(t)$. Figure 6.9 illustrates the cross-correlation functions between $w(t)$ and the difference signal between the received signal from convex reflector and that from the tilted flat reflector shown in Figure 6.7.
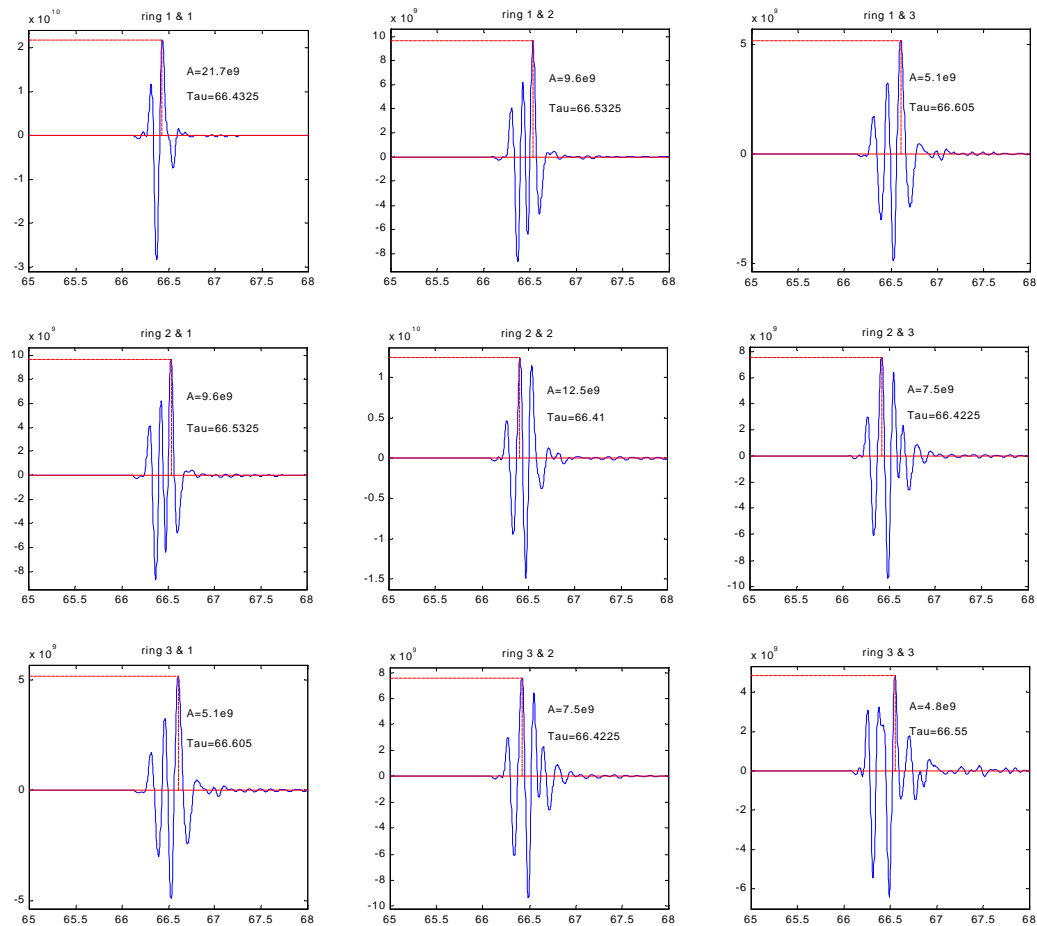
Figure 6.9 Illustration of the cross-correlation functions between $w(t)$ and the difference signal shown in Figure 6.7 of the received signal from convex reflector and that from the tilted flat reflector. The x-axis for all signals is in ms and the y-axis for all signals is in m^4/s^3.

Figure 6.10 illustrates the single waveform matrix obtained to approximate the difference signal matrix shown in Figure 6.7. The amplitude and the start time of the waveform $w(t)$ are indicated in Figure 6.10; the start time of the waveforms are the same as those shown in Figure 6.9. The amplitudes of the waveforms are the product of scale factors shown in Figure 6.9 and the amplitude of the waveform shown in Figure 6.8 (a).
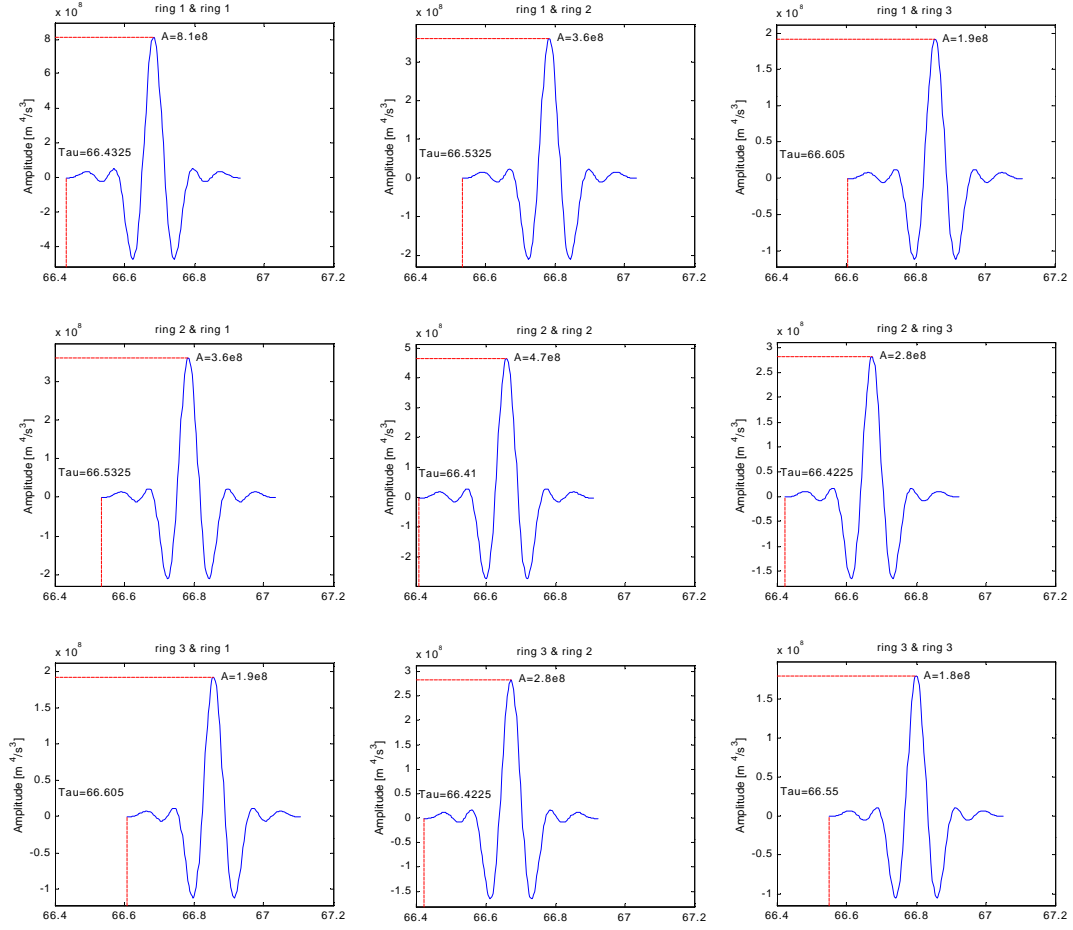
Figure 6.10 The single waveform matrix used to approximate the difference signal matrix of the received signal from convex reflector and that from the tilted flat reflector shown in Figure 6.7. The x-axis for all signals is in _ms_.

In Figure 6.10, we observe that the waveform with the largest shift, i.e., 66.605 _ms_, is found when the received signal is due to ring 1 and ring 3. As was discussed in section 6.1.2, this value is set to be t_{max}, and using equation (6.12), we can obtain the optimal delay matrix as:

$$T_{align\_3}^{OPT} = \begin{bmatrix} 0.1725 & 0.0725 & 0 \\ 0.0725 & 0.195 & 0.1825 \\ 0 & 0.1825 & 0.055 \end{bmatrix} ms$$

143

6.2.3 Results Obtained by the Waveform Alignment Method, based on 6-Ring Array

In this section, the optimal delay matrix is calculated for the 6-ring array system. The waveform $w(t)$ is the same as that in section 6.2.2. Using similar steps to those in section 6.2.2, we can obtain the optimal delay matrix as:

$$
T_{align\_6}^{OPT} = \begin{bmatrix}
0.855 & 0.7525 & 0.6825 & 0.5725 & 0.47 & 0.3675 \\
0.7525 & 0.8775 & 0.8675 & 0.7 & 0.6525 & 0.385 \\
0.6825 & 0.8675 & 0.7375 & 0.7375 & 0.44 & 0.6775 \\
0.5725 & 0.7 & 0.7375 & 0.465 & 0.7225 & 0.68 \\
0.47 & 0.6525 & 0.44 & 0.7225 & 0.815 & 0.07 \\
0.3675 & 0.385 & 0.6775 & 0.68 & 0.07 & 0
\end{bmatrix} ms
$$

Now, the optimal delay matrix has been obtained by three ways: the Global Search Method based on the 3-ring array; the Waveform Alignment Method based on the 3-ring array; the Waveform Alignment Method based on the 6-ring array. Using equation (6.8), with $t_{i,j} = t_{i,j}^{OPT}$, the energy of the summed difference signal from the two reflectors can readily be calculated. Table 6.1 gives the energy of the summed difference signal as well as the energy of the summed received signal from individual convex reflector and tilted flat reflector. All the signals are filtered using the band-pass filter with the frequency response of the array transducer, shown in Figure 6.8 because we assume that the annular array transducers act like a bandpass filter.

144

Table 6.1 Energy of the summed difference signal, summed received signal from individual convex and tilted flat reflector.

	Convex reflector	Tilted flat reflector	Difference signal
Global search optimal delay matrix in 3-ring array system	1.1656e+011	1.6329e+011	3.5207e+011
Waveform alignment optimal delay matrix in 3-ring array system	2.4786e+011	8.3998e+010	4.5159e+011
Waveform alignment optimal delay matrix in 6-ring array system	4.7206e+011	2.5082e+011	1.0992e+012

From Table 6.1, we can find that the difference energy obtained with the optimal delay matrix obtained by the Waveform Alignment Method is larger than that obtained with Global Search Method, for the 3-ring array system. The possible reasons for this result are that: 1) The global search can only be carried out in a limited delay range with discrete delay steps which makes it most probably that the optimal delay sets found is sub-optimal. The smaller the delay steps, the better the sub-optimal results should be. 2) The waveform alignment calculates the combined delay for the transmitter and receiver ring pair directly, which in general cannot be directly decomposed into separate delays for individual transmitter and receiver rings. If we have to modify the delay matrix to decompose it into separate transmit and receive delays, the energy of the difference signal obtained by the modified delay matrix must be become less.

We can also find from Table 6.1 that the difference energy obtained with the optimal delay matrix obtained by Waveform Alignment Method for the 6-ring array system is larger than that for the 3-ring array system. It also agrees with our expectation

because the 6-ring array presents more flexibility in varying the relative delay for individual array elements.
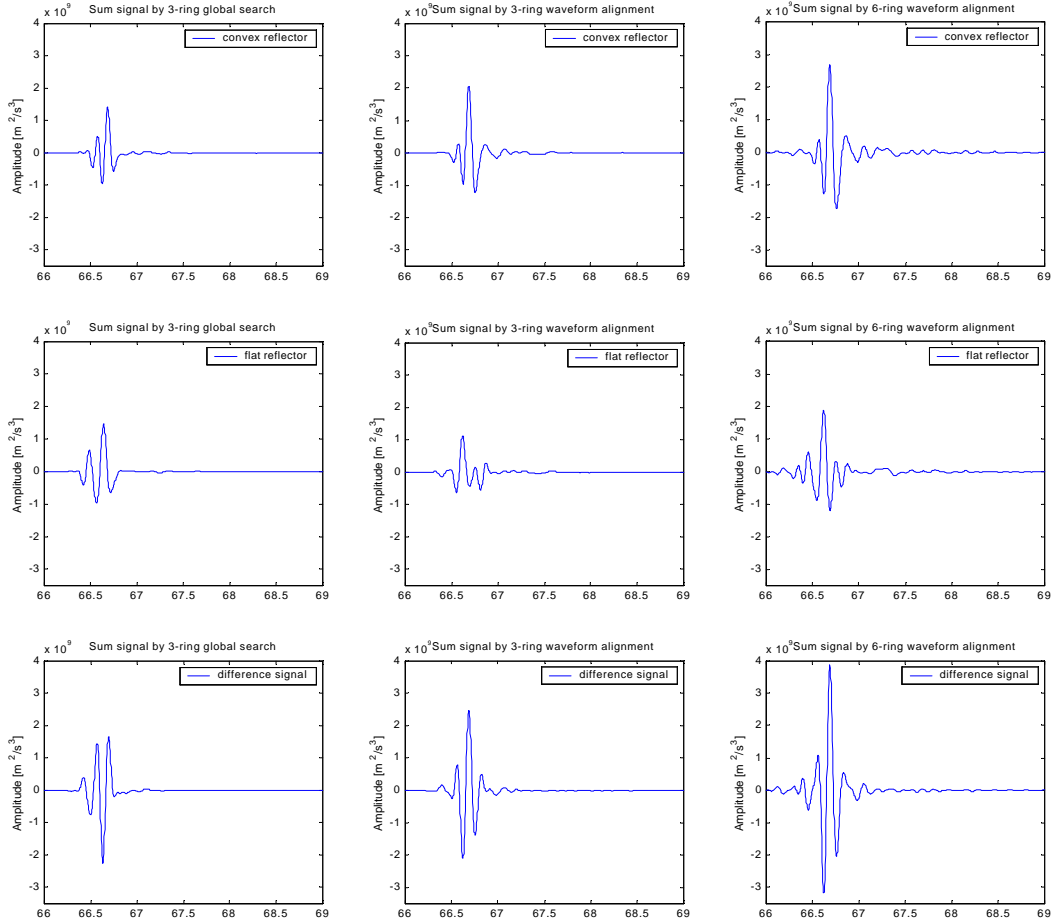
Figure 6.11 The sum received signal from convex reflector, flat reflector and the difference signal from those two reflectors. The first column is based on the optimal delay matrix obtained by the Global Search Method and the 3-ring array; the second column is based on Waveform Alignment Method and the 3-ring array and the third column is based on the Waveform Alignment Method and the 6-ring array. The x-axis for all signals is in *ms*.

Figure 6.11 illustrates the time-domain summed signals after the bandpass filtering. The three signals in first column are the summed received signal from convex reflector, the summed received signal from the tilted flat reflector, and the difference signal, respectively, based on the optimal delay matrix obtained by the Global Search

Method and the 3-ring array. The signals in second column are those based on the optimal delay matrix obtained by the Waveform Alignment Method and the 3-ring array. The signals in third column are those based on the optimal delay matrix obtained by the Waveform Alignment Method and the 6-ring array.

6.3 Optimal Delay Matrix for Concave Reflector and Tilted Flat Reflector

In this section, the Waveform Alignment Method is applied to find the optimal delay matrix to differentiate between a concave reflector and a tilted flat reflector. Both the 3-ring array and the 6-ring array transducer are used. The concave reflector is a square 10 arc of a cylinder with radius = 86*mm* and side length = 15*mm*. The *x-y* cross-sectional area of the reflector is 15*mm*×15*mm.* The concave reflector is centered on the acoustic axis of the transducer and the axial distance is 50*mm*. Figure 6.12 illustrates the cross-sectional view of the concave reflector. The tilted flat reflector is same as described in section 6.2.
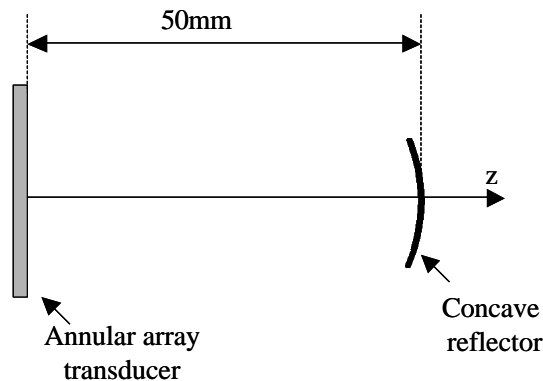
Figure 6.12 Cross-sectional view of the measurement scenario with concave reflector.

147

Figure 6.13 illustrates the *3´3 difference signal matrix* $\mathbf{V^{A\text{-}B}}$(t) generated for the difference signal between the received signals from the concave reflector and the tilted flat reflector for a 3-ring annular array system.
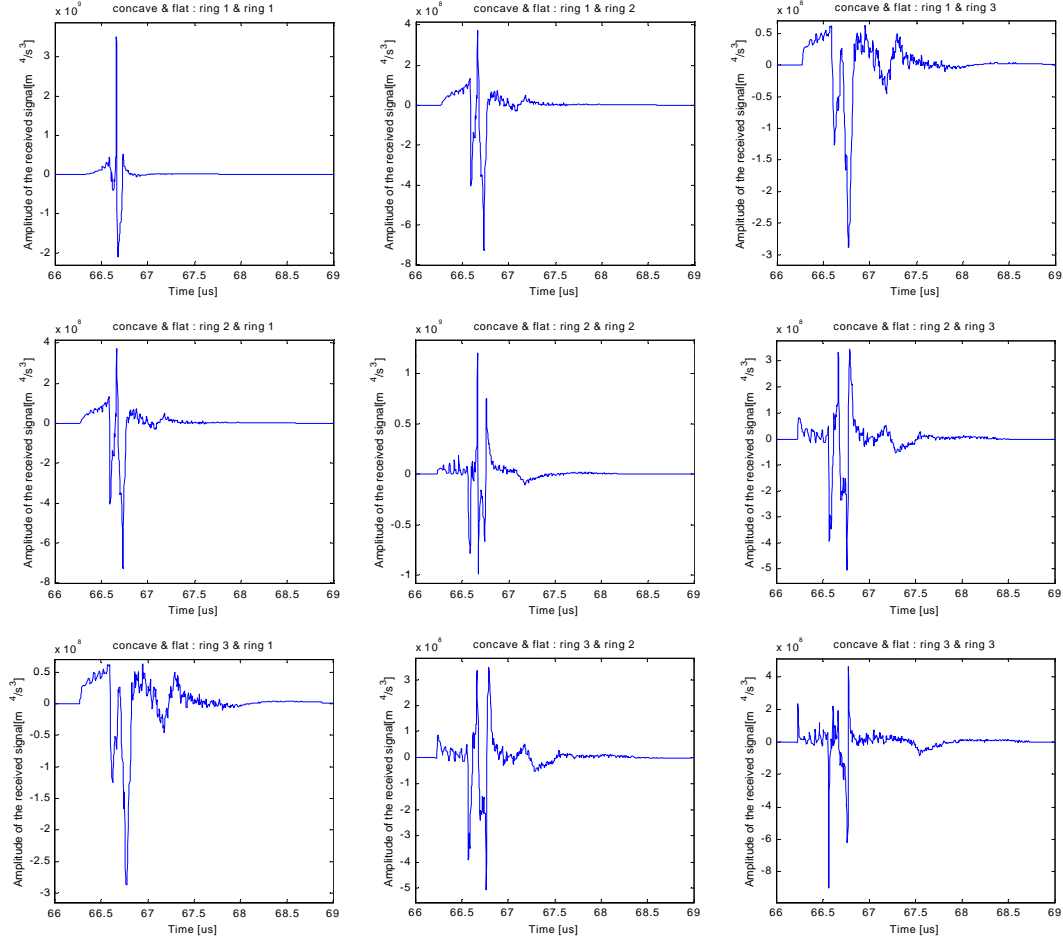
Figure 6.13 Difference signal matrix between the received signal from concave reflector and that from the tilted flat reflector.

Using similar steps and the same waveform *w(t)* used in sections 6.2.2 and section 6.2.3, we can obtain the optimal delay matrix to optimally differentiate between the concave reflector and the titled flat reflector as:

$$
T_{align\_3}^{OPT} = \begin{bmatrix} 0 & 0.0925 & 0.0575 \\ 0.0925 & 0.115 & 0.105 \\ 0.0575 & 0.105 & 0.1275 \end{bmatrix} \mathit{m}s
$$

$$T_{align\_6}^{OPT} = \begin{bmatrix} 1.3025 & 1.3975 & 1.3625 & 1.32 & 1.275 & 1.205 \\ 1.3975 & 1.4175 & 1.4075 & 1.22 & 1.3375 & 1.2825 \\ 1.3625 & 1.4075 & 1.43 & 1.2575 & 1.3525 & 1.31 \\ 1.32 & 1.22 & 1.2575 & 1.365 & 1.2425 & 0 \\ 1.275 & 1.3375 & 1.3525 & 1.2425 & 1.335 & 0.5875 \\ 1.205 & 1.2825 & 1.31 & 0 & 0.5875 & 1.3225 \end{bmatrix} ms$$

Table 6.2 illustrates the energy of the summed difference signal, as well as the energy of the summed received signal from the concave reflector and the tilted flat reflector. As in section 6.2, all the signals are filtered using the bandpass filter shown in Figure 6.8 before the energy is calculated.

Table 6.2 Energy of the summed difference signal, summed received signal from individual concave and tilted flat reflector.

	Concave reflector	Tilted flat reflector	Difference signal
Waveform alignment optimal delay matrix in 3-ring array system	9.2091e+010	2.5164e+011	5.0486e+011
Waveform alignment optimal delay matrix in 6-ring array system	1.2581e+011	7.0590e+011	1.1585e+012

Figure 6.14 illustrates the time-domain summed signals after band-pass filtering. The summed signals are received from the concave reflector, the tilted flat reflector and the difference signal between these two reflectors. The signals in the first column are those based on the optimal delay matrix obtained by the Waveform Alignment Method and the 3-ring array. The signals in the second column are those based on the optimal delay matrix obtained by the Waveform Alignment Method and the 6-ring array.
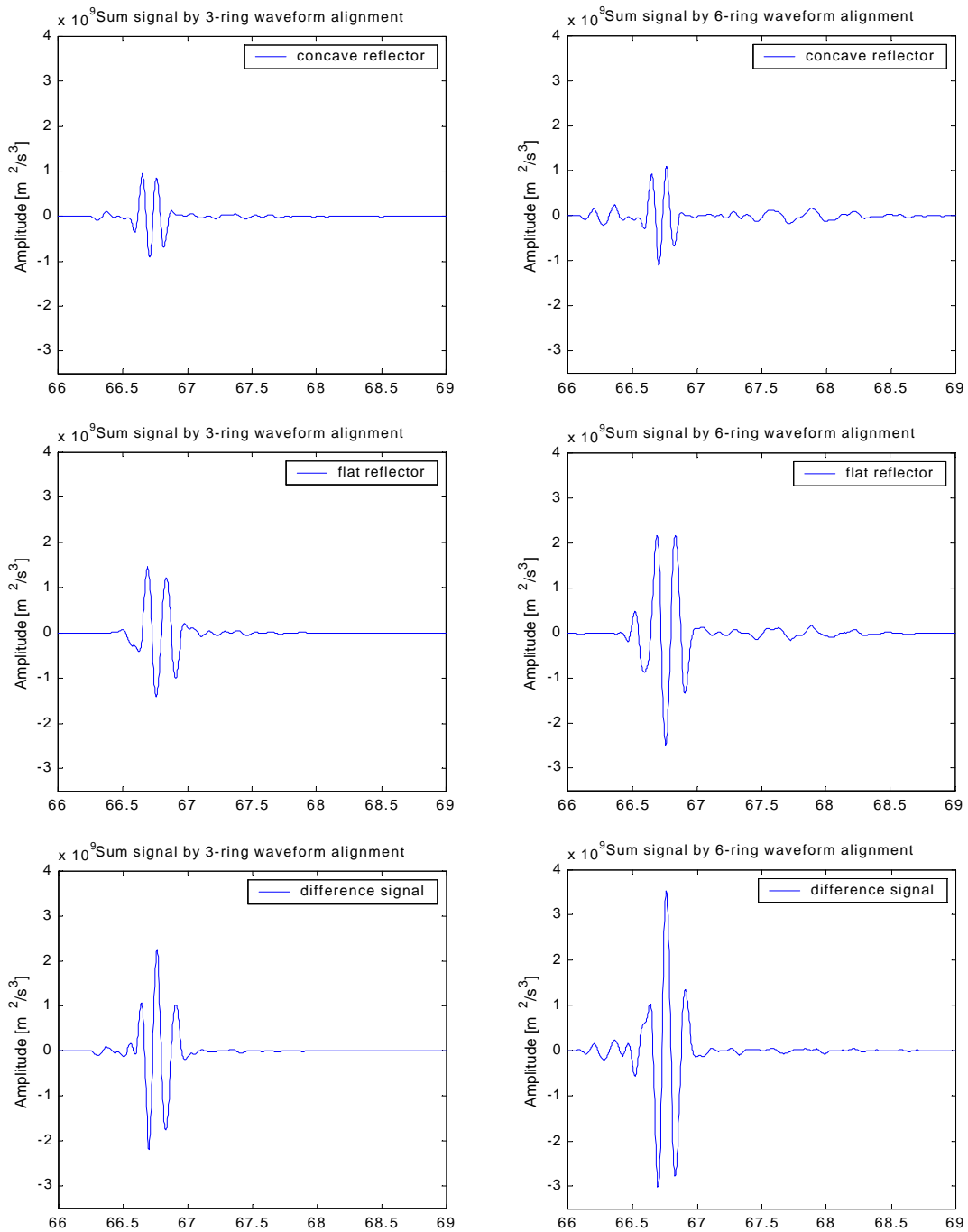
Figure 6.14 The summed received signal from the concave reflector, flat reflector and the difference signal from those two reflectors. The first column is obtained with the optimal delay matrix using the Waveform Alignment Method and the 3-ring array and the second column is obtained with the 6-ring array. The x-axis for all signals is in _ms_.

6.4 Optimal Delay Matrix for Convex Reflector and Concave Reflector

Figure 6.15 illustrates the *3´3 difference signal matrix* $\mathbf{V^{A\text{-}B}}$(t) which contains the difference signals between the received signals from the convex reflector and the concave reflector for the 3-ring annular array system. The convex reflector and the concave reflector are the same as were described previously.
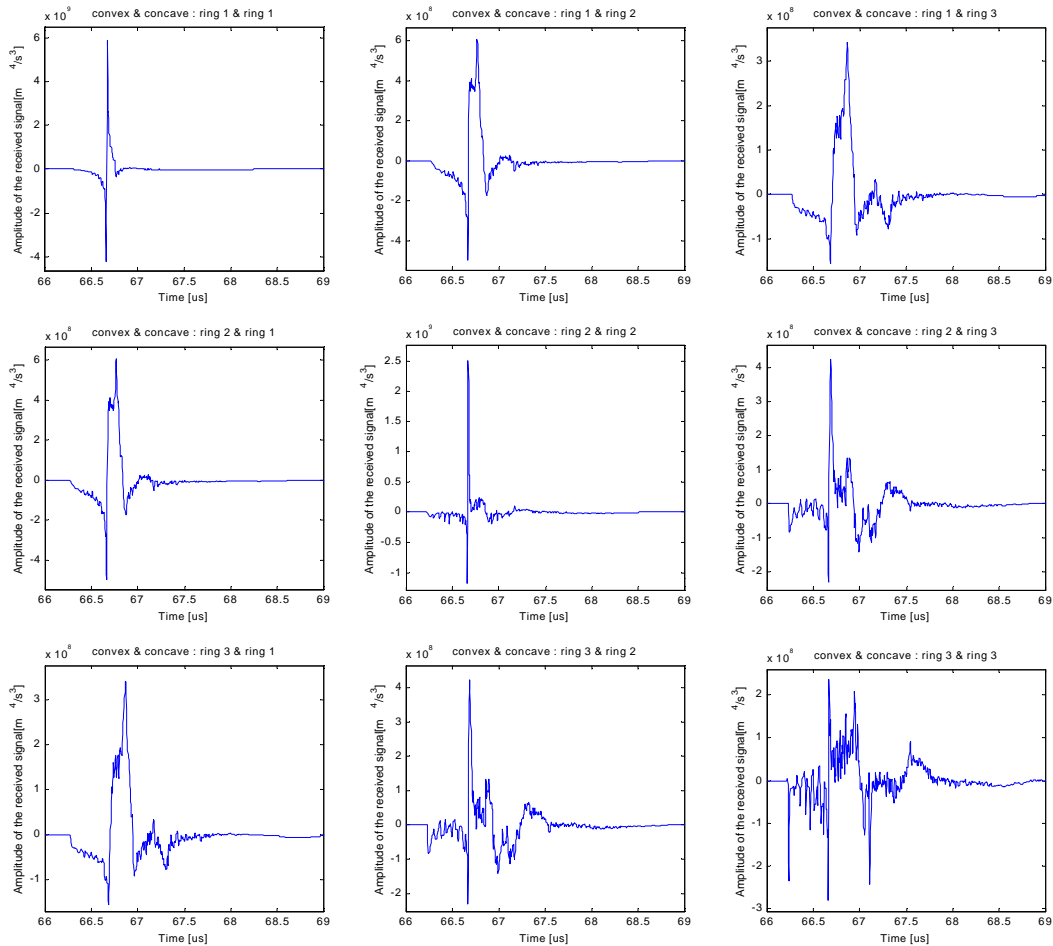
Figure 6.15 Difference signal matrix of the received signal from convex reflector and that from concave reflector.

Using similar steps and the same waveform used in sections 6.2 and section 6.3, we can obtain the optimal delay matrix to optimally differentiate between the convex and concave reflector as:

$$
T_{\text{align\_3}}^{\text{OPT}} = \begin{bmatrix} 0.2575 & 0.2425 & 0.085 \\ 0.2425 & 0.27 & 0.2575 \\ 0.085 & 0.2575 & 0 \end{bmatrix} ms
$$

$$
T_{\text{align\_6}}^{\text{OPT}} = \begin{bmatrix} 1.915 & 1.8275 & 1.7425 & 1.6425 & 1.535 & 1.4325 \\ 1.8275 & 1.9275 & 1.915 & 1.875 & 1.54 & 1.455 \\ 1.7425 & 1.915 & 1.6575 & 1.5725 & 1.51 & 1.43 \\ 1.6425 & 1.875 & 1.5725 & 1.5375 & 1.46 & 1.3875 \\ 1.535 & 1.54 & 1.51 & 1.46 & 1.4025 & 1.3275 \\ 1.4325 & 1.455 & 1.43 & 1.3875 & 1.3275 & 0 \end{bmatrix} ms
$$

Table 6.3 illustrates the energy of the summed difference signal as well as the energy of the summed received signal from the individual convex and concave reflectors. As in sections 6.2 and 6.3, all the signals are filtered using the bandpass filter shown in Figure 6.8 before the energy is calculated.

Table 6.3 Energy of the summed difference signal, summed received signal from individual convex and concave reflector.

	Convex reflector	Concave reflector	Difference signal
Waveform alignment optimal delay matrix in 3-ring array system	2.3688e+011	1.8166e+011	4.2275e+011
Waveform alignment optimal delay matrix in 6-ring array system	6.2343e+011	1.1232e+011	8.0054e+011

Figure 6.16 illustrates the time-domain summed signals after the bandpass filtering. The summed signals are received from convex reflector, concave reflector and the difference signal between these two reflectors. The signals in the first column are those based on the optimal delay matrix obtained by Waveform Alignment Method applied to the 3-ring array. The signals in the second column are those based on the optimal delay matrix obtained by Waveform Alignment Method applied to the 6-ring array.
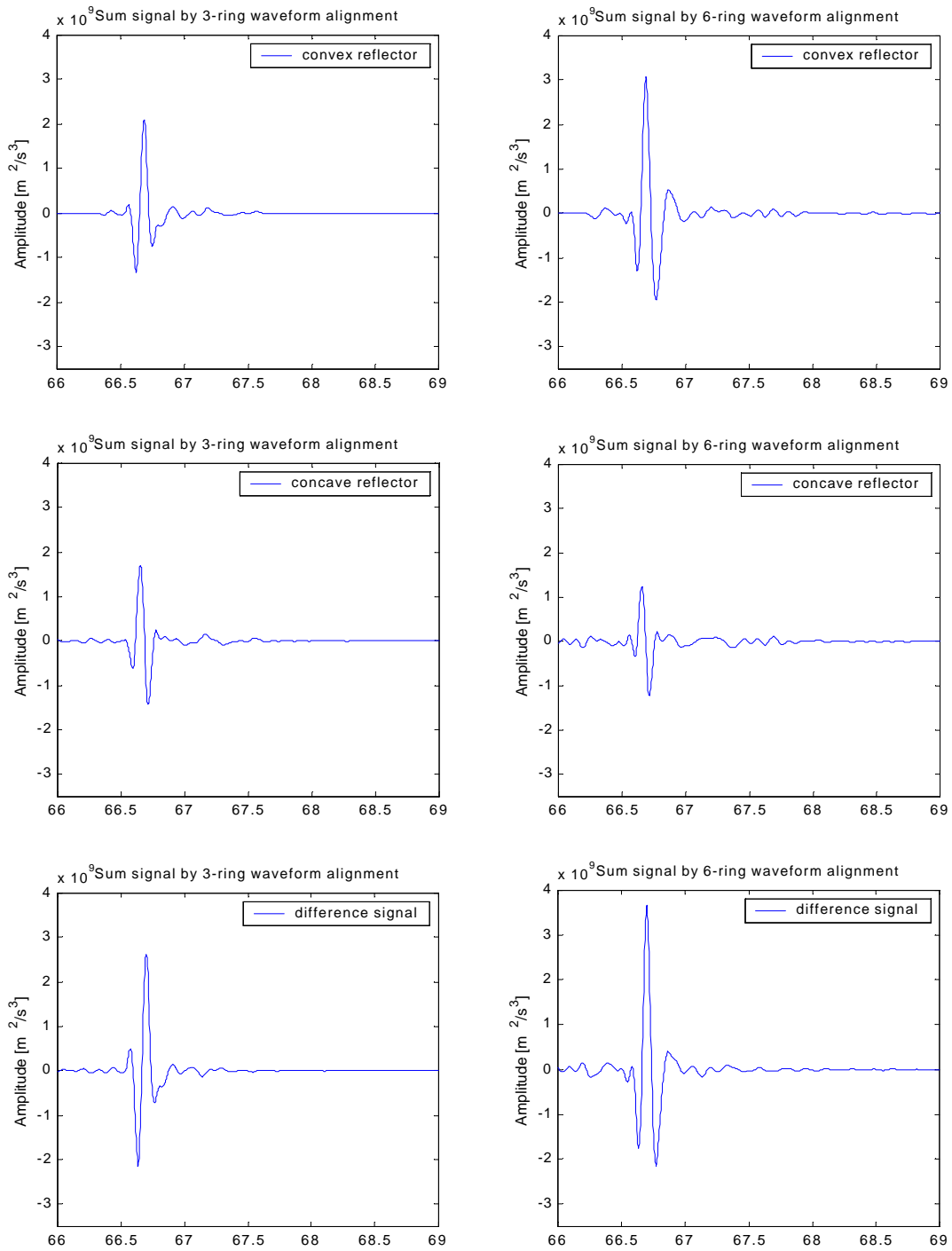
Figure 6.16 The summed received signal from the convex reflector, concave reflector and the difference signal from those two reflectors. The first column is obtained with the optimal delay matrix using the Waveform Alignment Method and the 3-ring array and the second column is obtained with the 6-ring array. The x-axis for all signals is in *ms*.

153

Chapter 7

Conclusions and Future Work

7.1 Conclusions

This thesis describes the implementation of a fast numerical modeling method, the *Diffraction Response from Extended Area Method* (DREAM), for calculation of the received signal from a transducer in a pulse-echo system. The modeling concept has been extended to calculate the received signal from individual elements in an annual array transducer, in which case the received signal is based on the superposition of the received signals from planar circular transducers. Then, based on the modeling of annular array system, we investigated the optimal design of ultrasound pulse-echo system for tasks such as identifying objects of specified shapes, determining surface topology or alignment of surfaces.

The DREAM method operates by dividing the surface of the reflector into a relatively small number (say, a few hundred) of rectangular or triangular "tiles" and performing the spatial integration of the *diffraction response* over each tile by an equivalent low pass filtering. The DREAM method has been implemented based on both rectangular tiles (R-DREAM) and triangular tiles (T-DREAM). Improvements have been made to the segmentation and the delay interpolation which are the two most important aspects in the practical implementation of DREAM. The results obtained by

154

both R-DREAM and T-DREAM are evaluated by comparing with the results obtained by the simpler, but slower method based on Huygens' Principle. The results from the two techniques match well. We have concluded that DREAM method is more computationally efficient than Huygens method. We have also found that T-DREAM performs better than R-DREAM in terms of accuracy and computation time. T-DREAM eliminates the small error introduced by the least squares approximation in the delay linearization for the rectangular tiles. In addition, in practical applications, triangular tiles can approximate reflector surface better than rectangular tiles do, and triangular tiles are standard elements used for surface tessellation. As a result, we decided to use T-DREAM as the modeling tool for our further research work.

The optimal design of the ultrasound pulse-echo system is based on annular array transducer which gives us the flexibility to create a wide variety of insonifying fields and receiver characteristics. As the first step to solve the optimization problem more generally, our objective is to differentiate between only two specified interfaces. We only consider the optimization of the delay values assigned to the elements in the array while the excitation amplitude and the receiver gain are kept constant for all the elements in the array. The optimization is realized by finding the optimal set of transmit and receive delay values, which will maximize the energy of difference signal between the array output signals from the two reflectors. Two optimization methods have been investigated for the optimal delay set: the *Global Search Method* and the *Waveform Alignment Method.*

The Global Search Method is searching through all possible delay combinations of the elements of the annular array transducer in either transmitting or receiving mode,

then calculating the difference signal between the received output signals from the two reflectors for each delay value combination. The set of delay values that produces the largest energy in difference signal is considered the optimal delay set. The disadvantage is that the search time increases even faster than exponentially with the number of array elements, and becomes computationally overwhelming even for a modest number of elements. In addition, the search can only be carried out in a limited delay range with discrete delay steps, which makes it probably that only a sub-optimal delay set is found.

The Waveform Alignment Method is using a time shifted and amplitude scaled version of a specified waveform to approximate the difference signal between two specified reflectors for each transmitting and receiving ring pair. Thus, each difference signal in the difference signal matrix can be represented by a delay value and amplitude scale factor. In our current research work, only the delay values are then used to align these waveforms to get the optimal delay matrix. The Waveform Alignment Method is very efficient. However, as it is currently implemented, the results obtained by the Waveform Alignment Method is the optimal delay matrix, whose items are combined transmit and receive delays. The optimal delay matrix is symmetrical and, in general, it cannot be decomposed into separate transmit and receive delays. This problem needs to be solved before the optimal system can be implemented for an actual experiment. In addition, as noted in the next section "future work", much more research work needs to be carried out with respect to the optimal design of ultrasound system.

7.2 Future Work

As part of the work of this thesis, we implemented and investigated the efficient modeling tool of ultrasound system: DREAM method. An important topic closely related to DREAM method, but not covered in this thesis, is how to optimally approximate a specific reflector surface with flat rectangular or triangular tiles. For future work, it is advantageous to merge the DREAM tools with optimal surface tessellation tools, in order to apply DREAM method to more complicated reflector surfaces.

Waveform Alignment Method is a promising method for the optimization of ultrasound pulse-echo system with respect to its ability to identify a given object or interface among a limited set of simple objects or interfaces. Future work on the Waveform Alignment Method may include: The optimal differentiation between two reflectors which includes: 1) developing the theory for separating the combined transmit-receive delays in the optimal delay matrix which is obtained by the Waveform Alignment Method into separate transmitting and receiving delays; 2) the optimization of the amplitude gain values assigned for each array element in transmitting and receiving modes; 3) exploring the effect of choosing different waveforms to represent the received signal for each transmitting and receiving ring pair; 4) using different criteria, for example, spectral features, for the optimization rather than maximizing the energy of the difference signal. After we accomplish the optimal differentiation between two reflectors, the next step is to exploring the optimal delay sets to identify a given reflector among more than two reflectors.

Another research topic closely related to the optimization of the ultrasound system is the development of the neural network or Self-Organizing Maps to achieve the most accurate classification of the actual reflectors. The inputs to the neural network are the received signals in the ultrasound pulse-echo system from the entire array transducer. The transmit and receive delays of each element in the array are adjusted according to the optimal delay sets obtained by the Waveform Alignment Method.

Experiments can be carried out as the verification of the numerical modeling results and the optimization techniques. The Tomoscan Focus (TF) instrument, manufactured by R/D Tech in Quebec City in Canada, can generate customized acoustic fields and receiver characteristics under software control. Therefore, by connecting the TF instrument and the computer to the array transducer in a real ultrasound pulse-echo system, the transmit and receive delays of each element in the array can be customized according to the optimal delay sets obtained by the Waveform Alignment Method. The received signals from the experiments can be used to verify the simulation results obtained by the DREAM modeling method. In addition, the experimental results can be used as the inputs to the neural network for the classification.

References

[1] R.K. Johnson and A.J. Devaney, "Transducer effects in acoustic scattering measurements", Appl., Phys., Lett., vol. 41, No. 7, pp. 622 – 624, 1982.

[2] R. Lerch, "Finite element analysis of piezoelectric transducers", *Proceedings of 1988 Ultrasonics Symposium*, pp. 643 – 654, Chicago, 1988.

[3] R. Lerch, H. Landes, and H.T. Kaarmann, "Finite element modeling of the pulse-echo behavior of ultrasound transducers", *Proceedings of 1994 Ultrasonics Symposium*, pp. 1021 – 1025, Cammes, France, 1994.

[4] D.P. Orofino and P.C. Pedersen, "Efficient angular spectrum decomposition of acoustic sources – Part I: Theory", *IEEE Transactions on Ultrasonic, Ferroelectrics and Frequency Control*, vol. 40, No. 3, pp. 238 – 249, May 1993.

[5] P.C. Pedersen and D.P. Orofino, "Modeling of received ultrasound signals from finite planar targets", *IEEE Transactions on Ultrasonic, Ferroelectrics and Frequency Control*, vol. 43, No. 2, pp. 303 – 311, March 1996.

[6] J.P. Weight and A.J. Hayman, "Observations of the propagation of very short ultrasonic pulses and their reflection by small targets", *The Journal of the Acoustical Society of America*, vol. 63, No. 2, pp. 396 – 404, February 1978.

[7] S. Mclaren, J.P. Weight, "Transmit-receive mode responses from finite-sized targets in fluid media", *The Journal of the Acoustical Society of America*, vol. 82, No. 6, pp. 2102 – 2112, December 1987.

[8] A. Lhemery, "Impulse-response method to predict echo-responses from targets of complex geometry. Part I: Theory", *The Journal of the Acoustical Society of America*, vol. 90, No. 5, pp. 2799 – 2807, November 1991

[9] S.K. Jespersen, P.C. Pedersen, and J.E. Wilhjelm, "The diffraction response interpolation method", *IEEE Transactions on Ultrasonics, Ferroelectrics and Frequency Control*, vol. 45, No. 6, pp. 1461 – 1475, November 1998.

[10] S.K. Jespersen, *Tools for Improving the Diagnosis of Atherosclerotic Plaque using Ultrasound*, PhD thesis, Technical University of Denmark, 1997.

[11] J.A. Zagzebski, *Essentials of Ultrasound Physics*, Mosby-Year Book, 1996.

[12] G.R. Harris, "Review of transient field theory for a baffled planar piston", *The Journal of the Acoustical Society of America*, vol. 70, No. 1, pp. 10 – 20, July 1981

[13] G. Scarano, N. Denisenko, M.Matteucci, and M. Pappalardo, "A new approach to the derivation of the impulse response of a rectangular piston", *The Journal of the Acoustical Society of America*, vol. 78, No. 3, pp. 1109 – 1113, September 1985

[14] P. Wu and T. Stepinski, "Spatial impulse response method for predicting pulse-echo fields from a linear array with cylindrically concave surface", *IEEE Transactions on Ultrasonics, Ferroelectrics and Frequency Control*, vol. 46, No. 5, pp. 1283 – 1297, September 1999.

[15] D.P. Orofino and P.C. Pedersen, "Multirate digital signal processing algorithm to calculate complex acoustic pressure field", *The Journal of the Acoustical Society of America*, vol. 92, No. 1, pp. 563 – 582, July 1992

[16] L.E. Kinsler, A.R. Frey, A.B. Coppens, and J.V. Sanders, *Fundamentals of Acoustics,* Fourth Edition, John Wiley & Sons, Inc., 2000.

[17] V.M. Ristic, *Principles of Acoustic Devices*, John Wiley & Sons, Inc., 1983.

[18] P.R. Stepanishen, "Transient radiation from pistons in an infinite planar baffle", *The Journal of the Acoustical Society of America*, vol. 49, No. 5, pp. 1629 – 1638, 1971.

[19] P. Kielczynski and W. Pajewski, "Acoustic field of gaussian and Bessel transducers", *The Journal of the Acoustical Society of America*, vol. 94, No. 3, pp. 1719 – 1721, 1993.

[20] J.L.S. Emeterio and L.G. Ullate, "Diffraction impulse response of rectangular transducer", *The Journal of the Acoustical Society of America*, vol. 92, No. 2, pp. 651 – 662, 1992.

[21] P. Faure, D. Cathignol, and J. Y. Chapelon, "On the pressure field of a transducer in the form of a curved strip", *The Journal of the Acoustical Society of America*, vol. 95, No. 2, pp. 628 – 637, 1994.

[22] A. Penttinen and M. Luukkala, "The impulse response and pressure nearfield of a curved ultrasonic radiator", *Phys. D: Appl. Phys*., 9:1547-1557,1976.

[23] J.A. Jensen, "Ultrasound fields from triangular apertures", *The Journal of the Acoustical Society of America*, vol. 100, No. 4, pp. 2049 – 2056, 1996.

[24] R.E. Crochiere and L.R. Rabiner, *Multirate Digital Signal Processing*, Prentice-Hall, Inc., 1983.

[25] B.B. Baker and E.T. Copson, *The Mathematical Theory of Huygens' Principle*, Second Edition, Oxford at the Clarendon Press, 1969.

Appendix A

Appendix A.1

The relationship between the radial distance and the energy of the received signal from a 0.5*mm**0.5*mm* square flat reflectors for the simulation scenarios given in section 5.3 when the reflector is tilted 0.6° relative to the transducer surface. Refer to section 5.3 for more details.
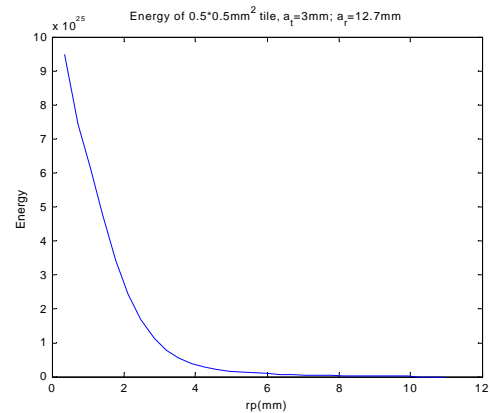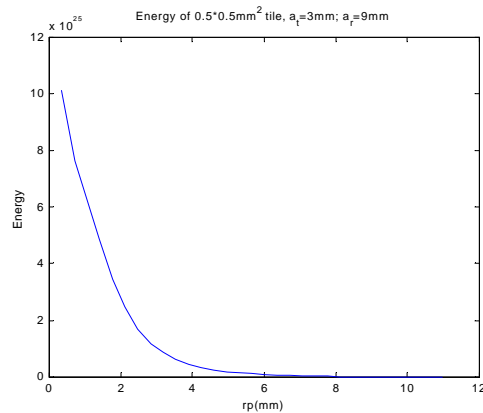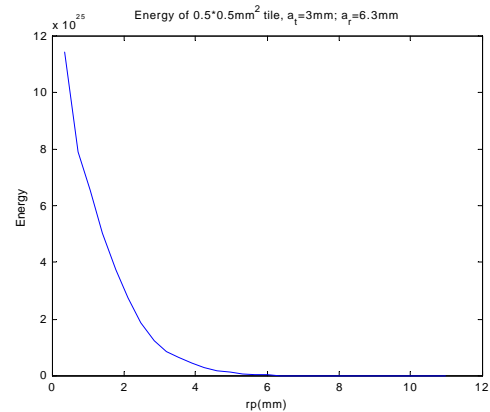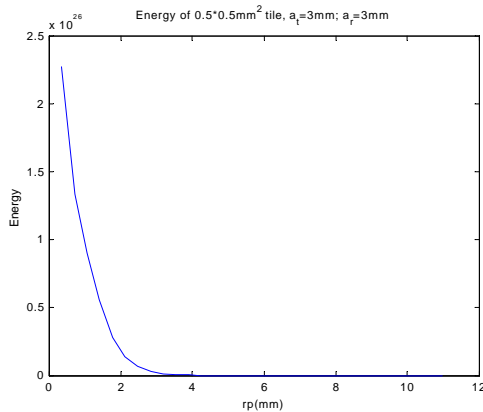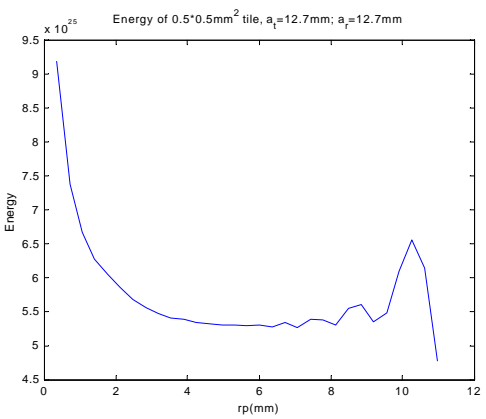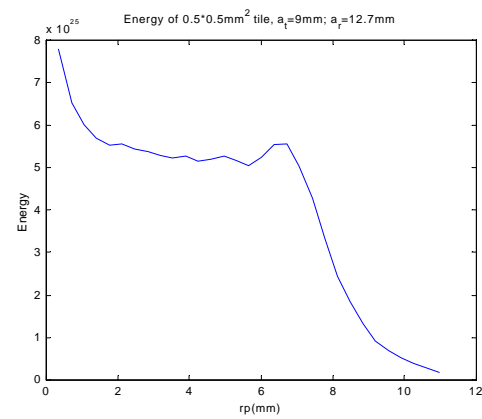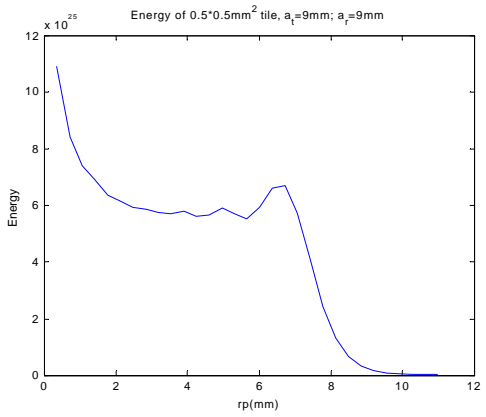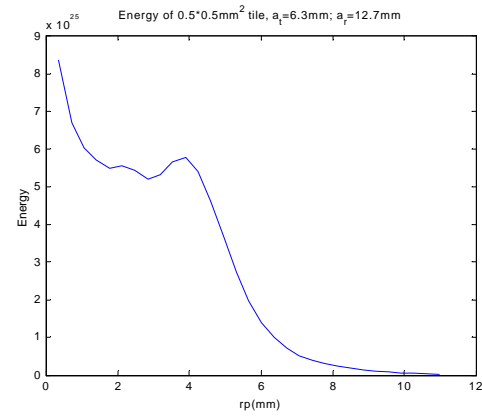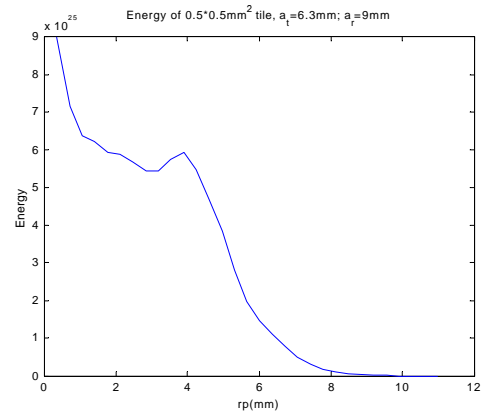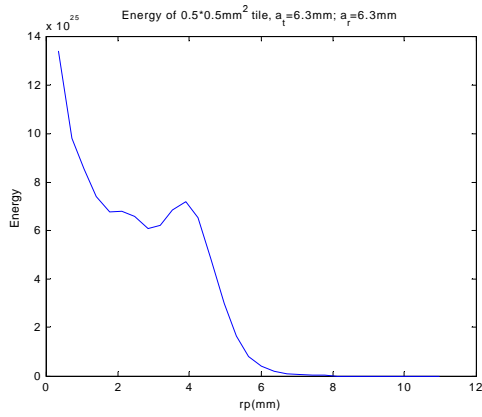
Appendix A.2

The relationship between the radial distance and the DREAM Error (=MSE) of the received signal from small square flat reflectors for the simulation scenarios given in section 5.2 when the reflector is tilted 0.6° relative to the transducer surface. Refer to section 5.2 for more details.

MSE of T-DREAM(tilted 0.6°): a_t=3mm; a_r=12.7mm

MSE of R-DREAM (tilted 0.6°): a_t=3mm; a_r=12.7mm

MSE of T-DREAM (tilted 0.6°): a_t=6.3mm; a_r=6.3mm

MSE of R-DREAM (tilted 0.6°): a_t=6.3mm; a_r=6.3mm

MSE of T-DREAM(tilted 0.6°): a_t=6.3mm; a_r=9mm

MSE of R-DREAM (tilted 0.6°): a_t=6.3mm; a_r=9mm
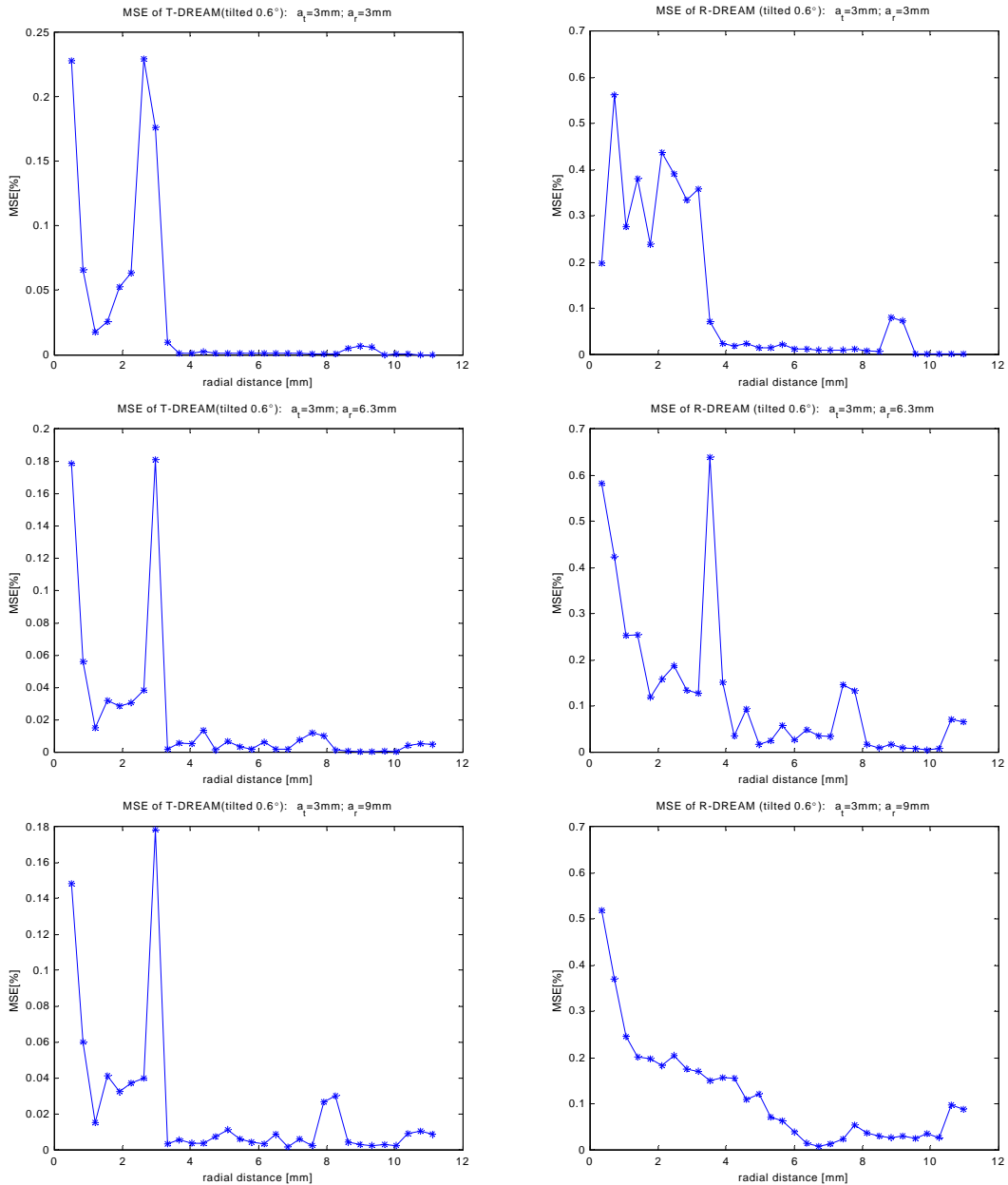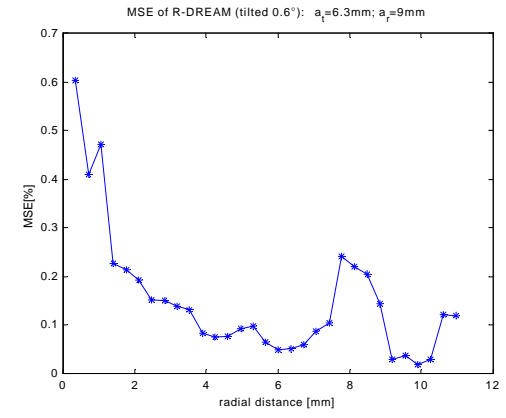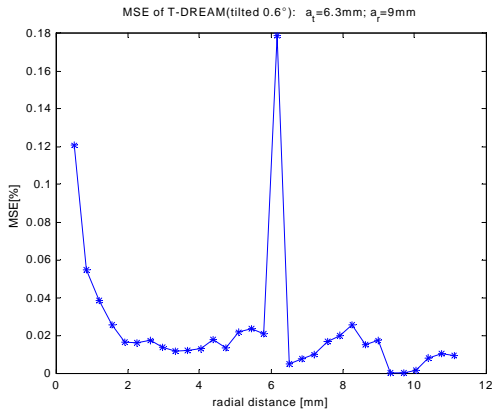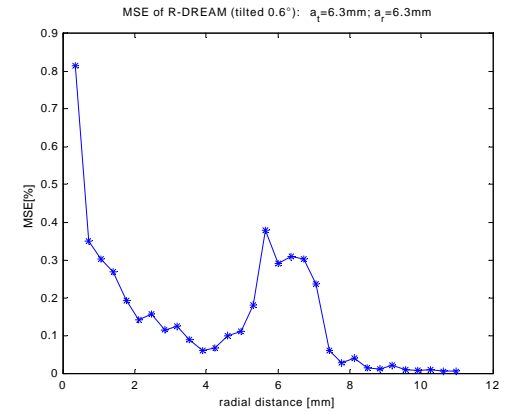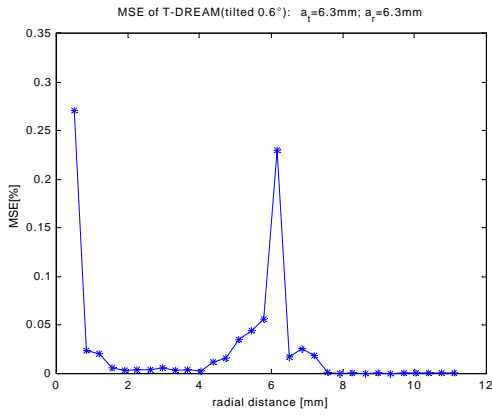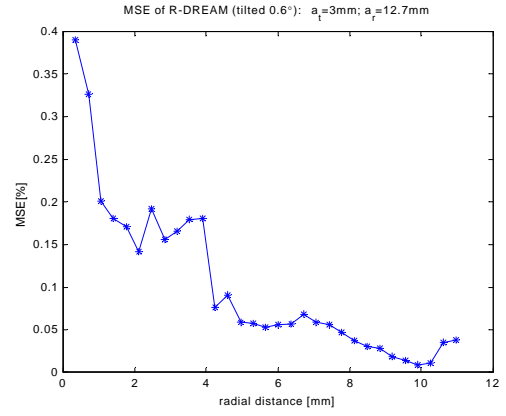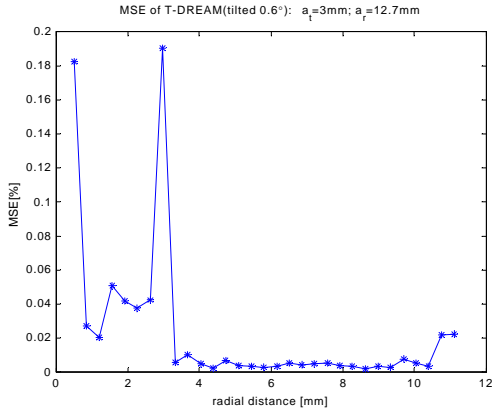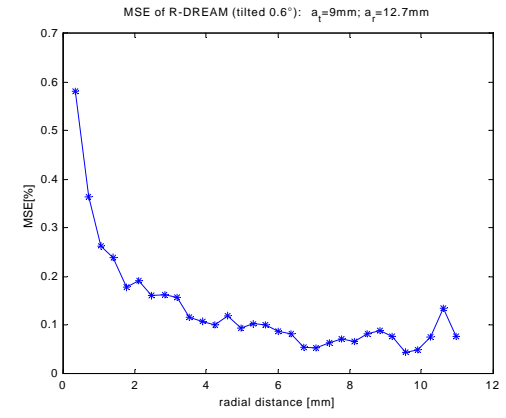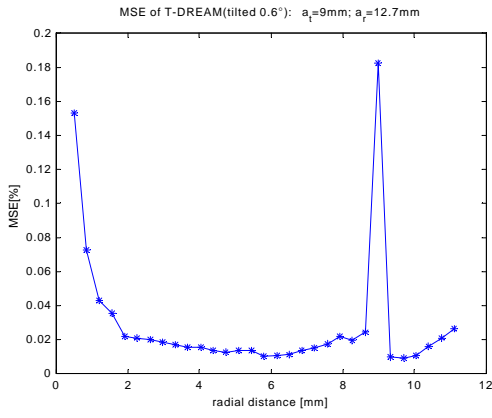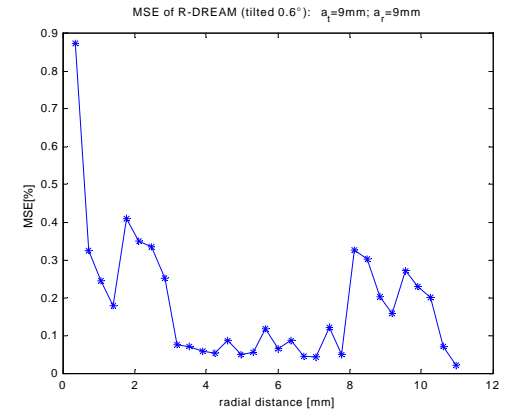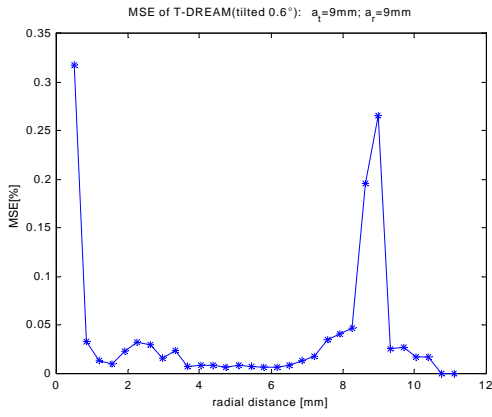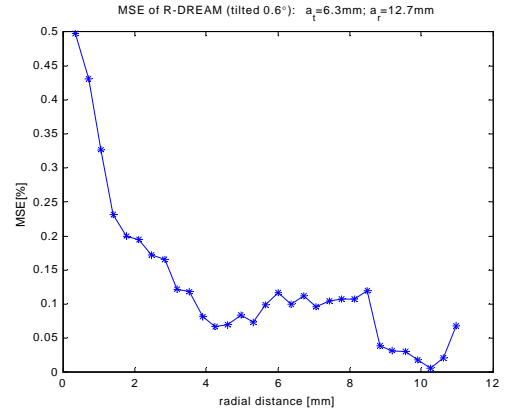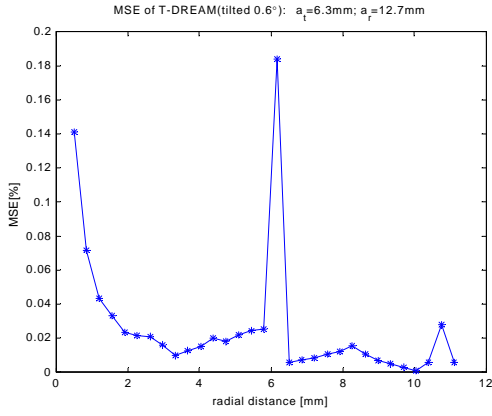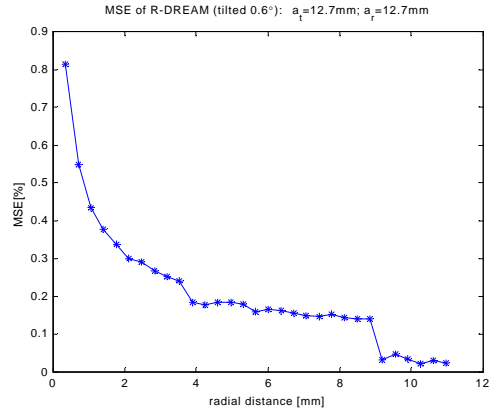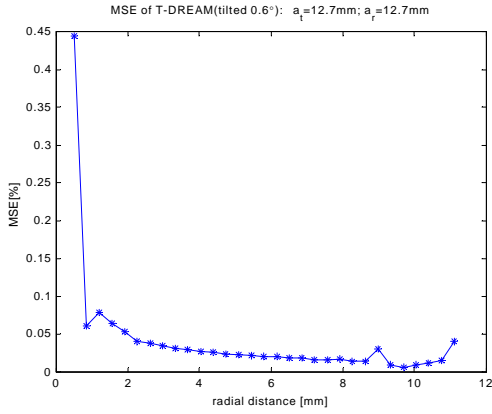
Appendix A.3

The relationship between the radial distance and the normalized DREAM Error (=MSE) of the received signal from small square flat reflectors for the simulation scenarios given in section 5.4 when the reflector is tilted 0.6° relative to the transducer surface. Refer to section 5.4 for more details.

normalized MSE of T-DREAM (0.6°):a_t=3mm; a_r=9mm

normalized MSE of R-DREAM (0.6°):a_t=3mm; a_r=9mm

normalized MSE of T-DREAM (0.6°):a_t=3mm; a_r=12.7mm

normalized MSE of R-DREAM (0.6°):a_t=3mm; a_r=12.7mm

normalized MSE of T-DREAM (0.6°):a_t=6.3mm; a_r=6.3mm

normalized MSE of R-DREAM (0.6°):a_t=6.3mm; a_r=6.3mm

normalized MSE of T-DREAM (0.6°):a_t=6.3mm; a_r=9mm

normalized MSE of R-DREAM (0.6°):a_t=6.3mm; a_r=9mm

169
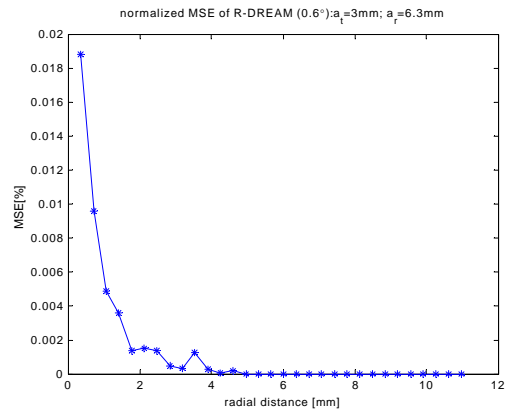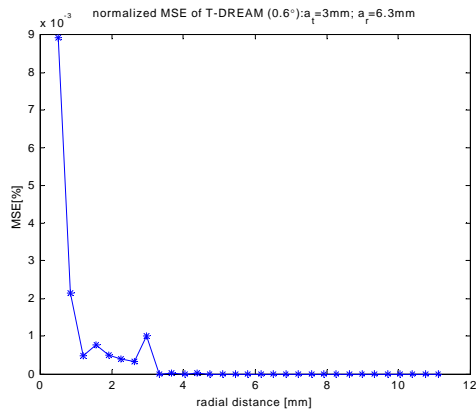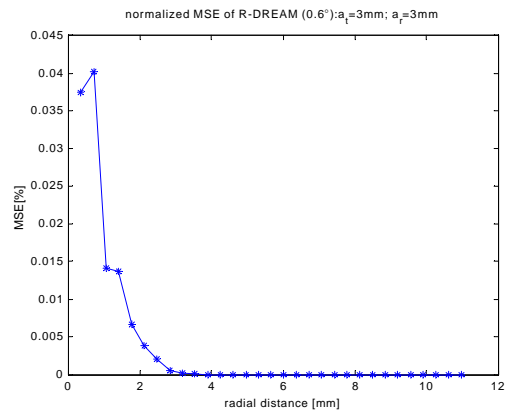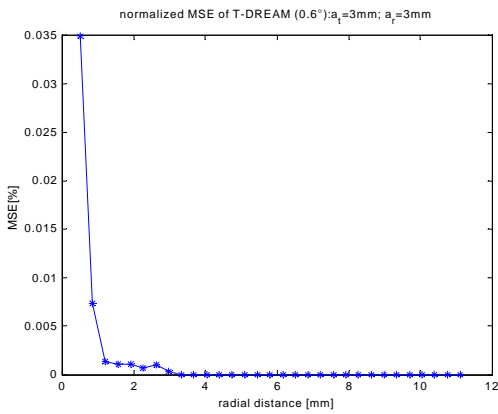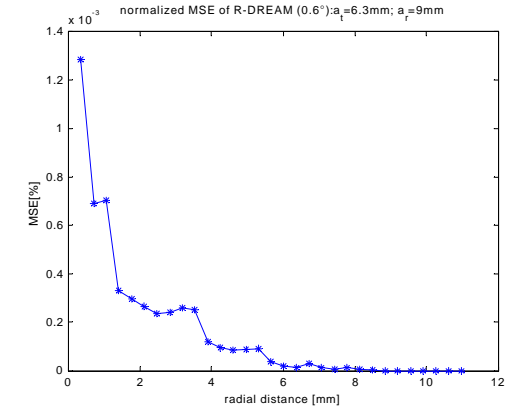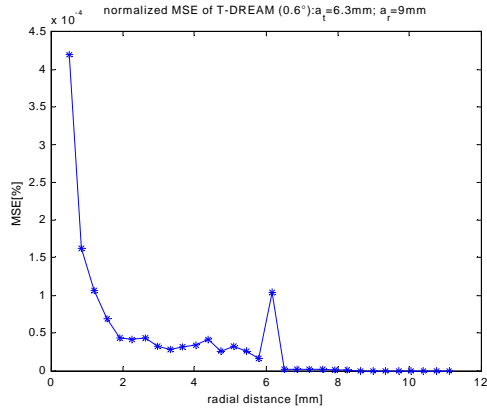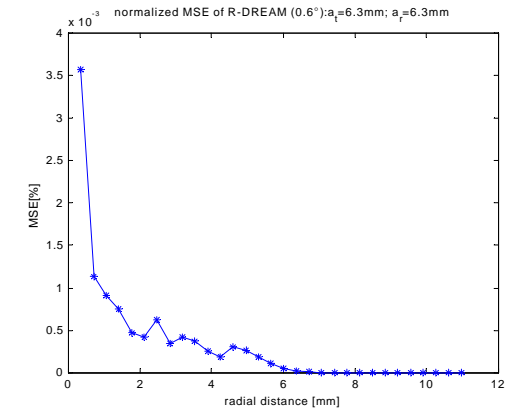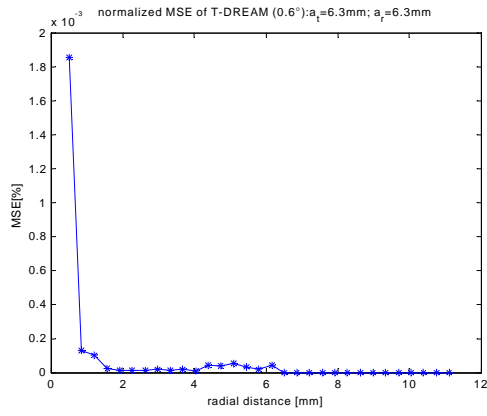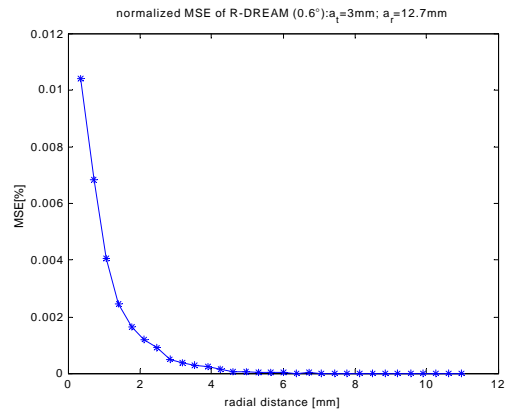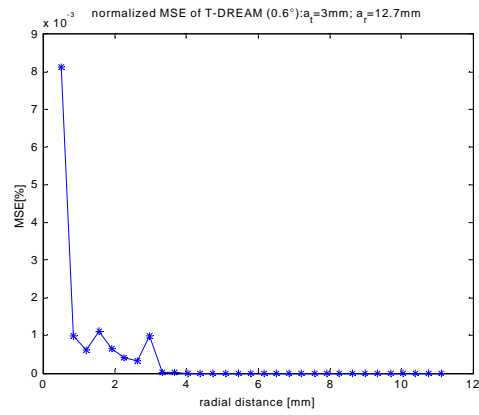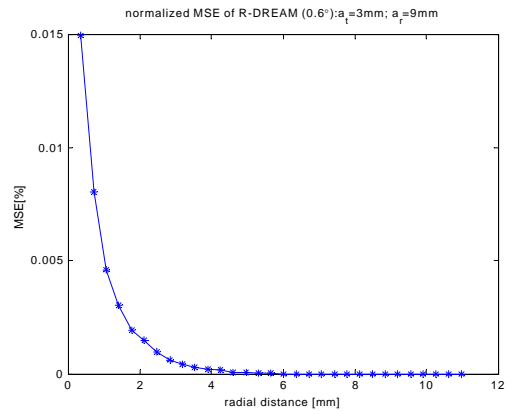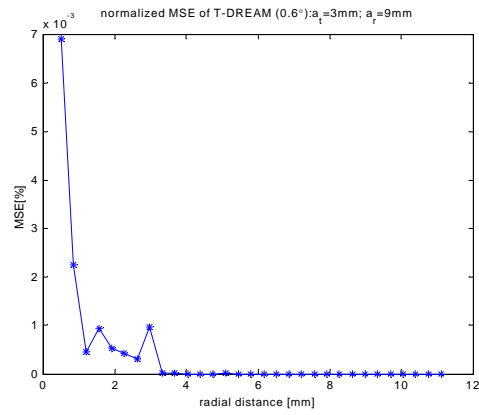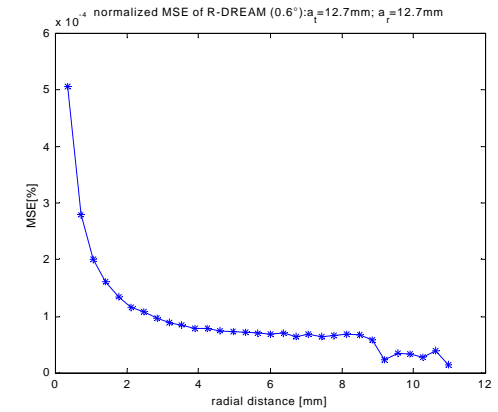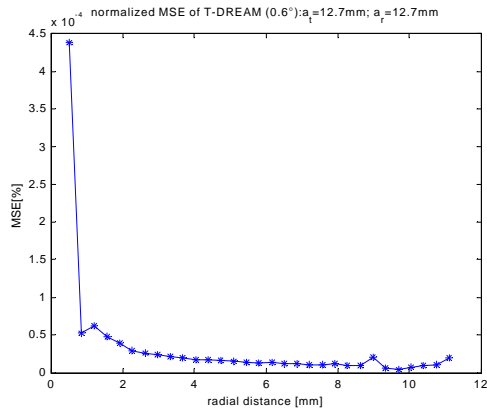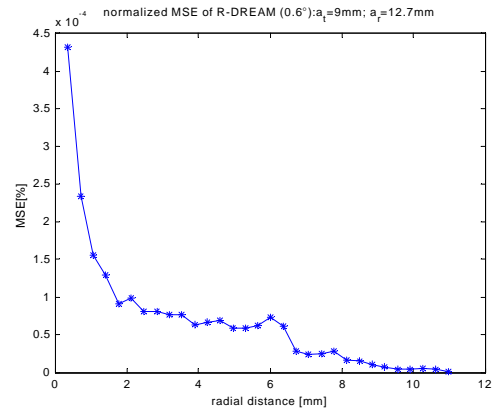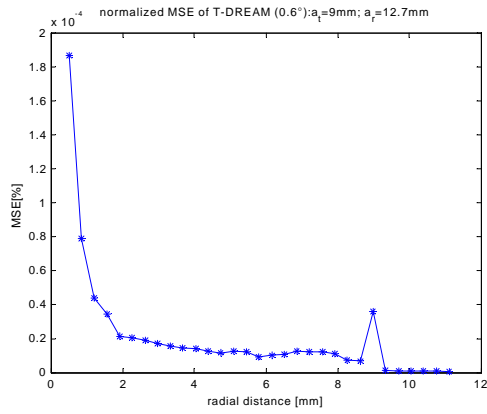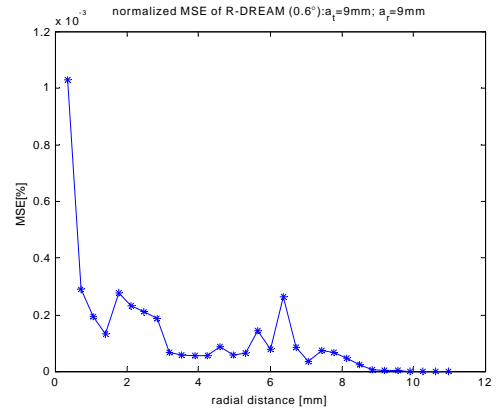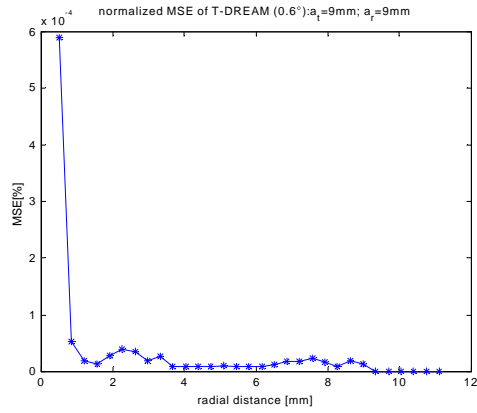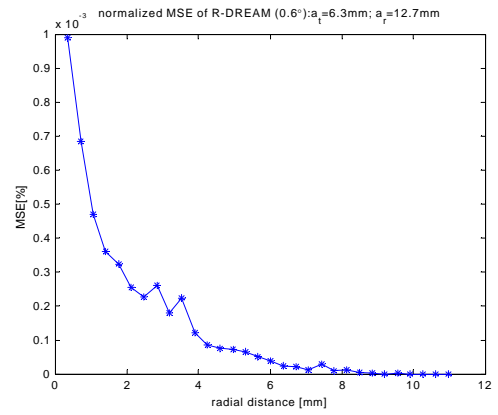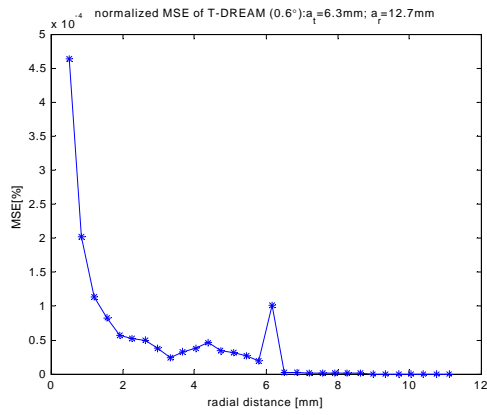
Appendix A.4

The relationship between the radial distance and the energy of the received signal from a $0.5mm*0.5mm$ square flat reflectors for the simulation scenarios given in section 5.3 when the reflector is tilted 6° relative to the transducer surface. Refer to section 5.3 for more details.

Energy of 0.5*0.5mm² tile, a_t=6.3mm; a_r=12.7mm

Energy of 0.5*0.5mm² tile, a_t=9mm; a_r=9mm

Energy of 0.5*0.5mm² tile, a_t=9mm; a_r=12.7mm

Energy of 0.5*0.5mm² tile, a_t=12.7mm; a_r=12.7mm
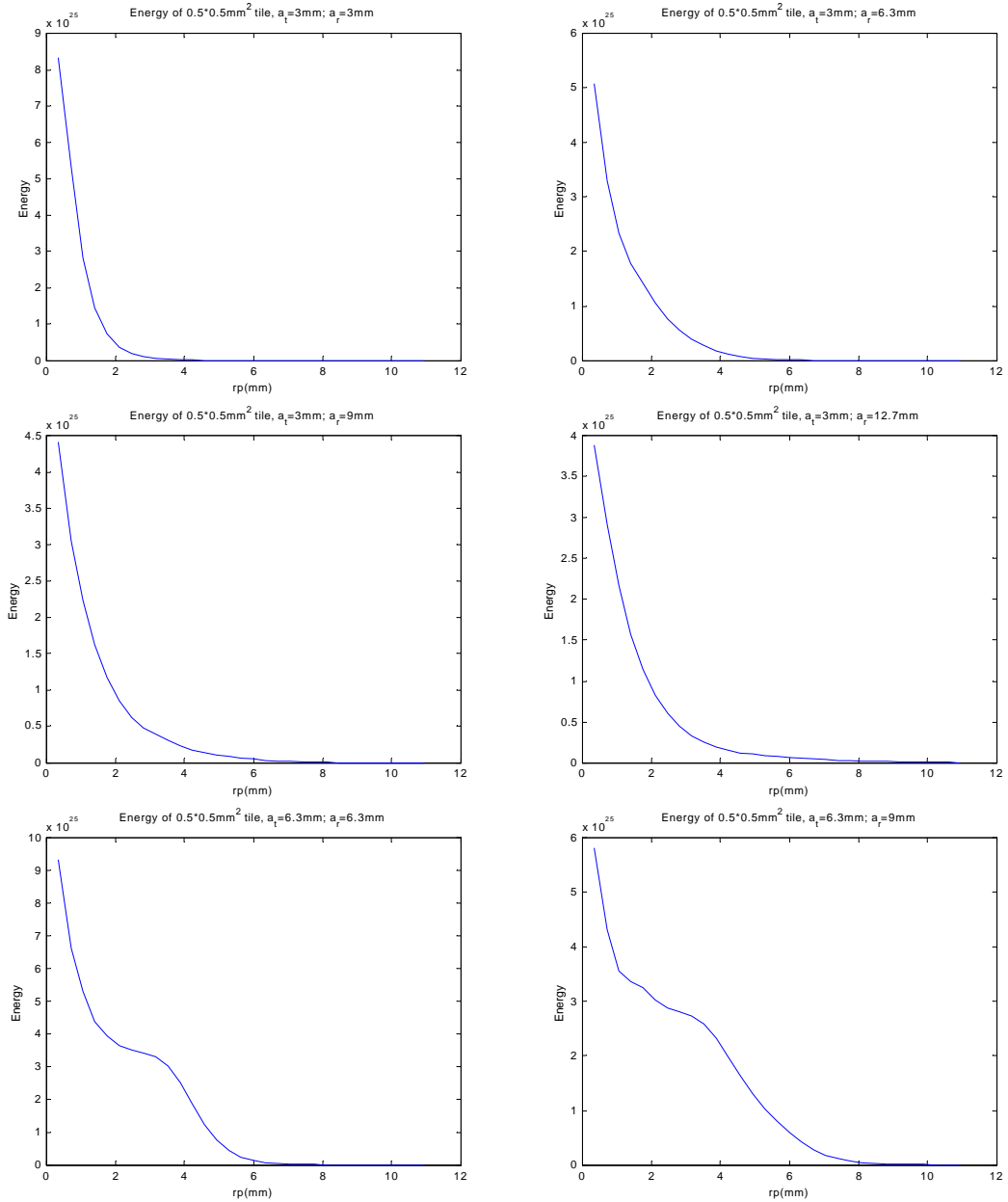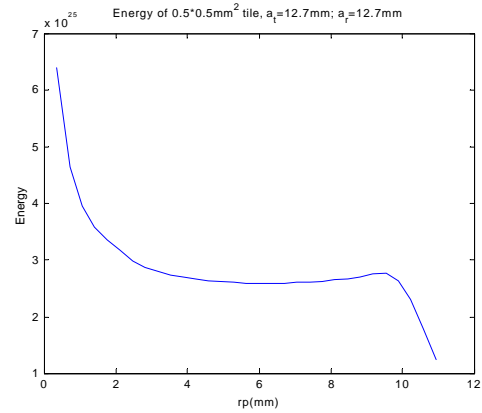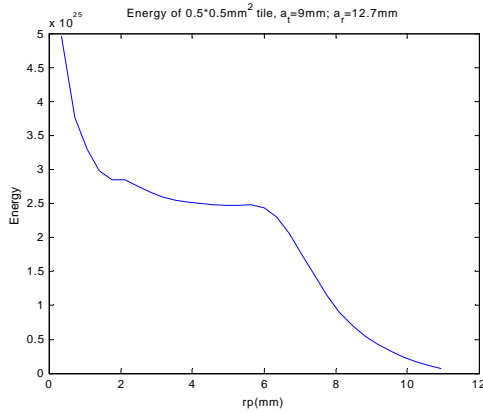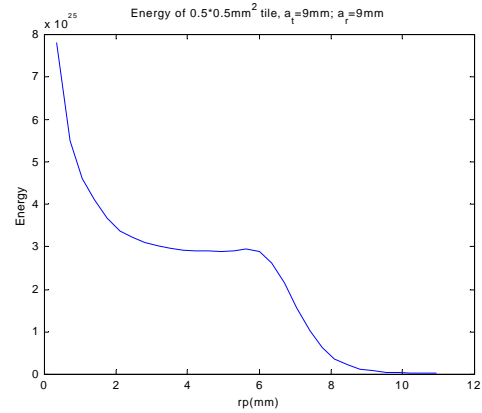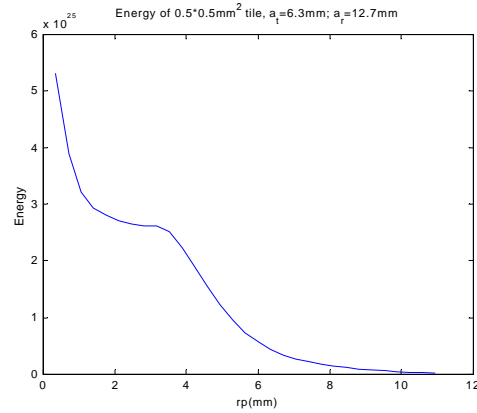
Appendix A.5

The relationship between the radial distance and the DREAM Error (=MSE) of the received signal from small square flat reflectors for the simulation scenarios given in section 5.2 when the reflector is tilted 6° relative to the transducer surface. Refer to section 5.2 for more details.

MSE of T-DREAM: a_t=3mm; a_r=3mm

MSE of R-DREAM: a_t=3mm; a_r=3mm

MSE of T-DREAM: a_t=3mm; a_r=6.3mm

MSE of R-DREAM: a_t=3mm; a_r=6.3mm

MSE of T-DREAM: a_t=3mm; a_r=9mm

MSE of R-DREAM: a_t=3mm; a_r=9mm

MSE of T-DREAM: a_t=3mm; a_r=12.7mm

MSE of R-DREAM: a_t=3mm; a_r=12.7mm

MSE of T-DREAM: a_t=6.3mm; a_r=6.3mm

MSE of R-DREAM: a_t=6.3mm; a_r=6.3mm

173

MSE of T-DREAM: a_t=12.7mm; a_r=12.7mm

MSE of R-DREAM: a_t=12.7mm; a_r=12.7mm
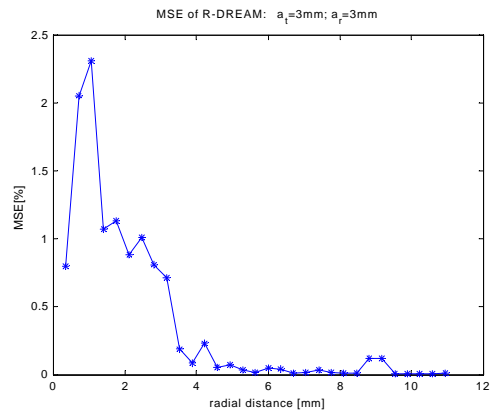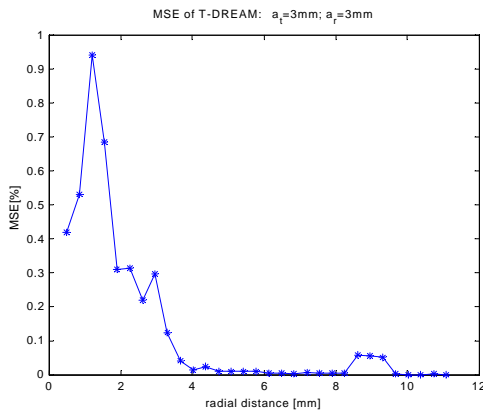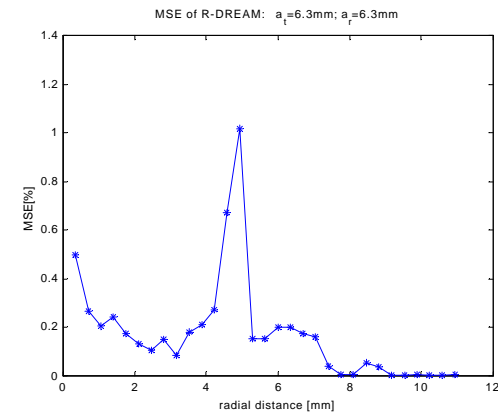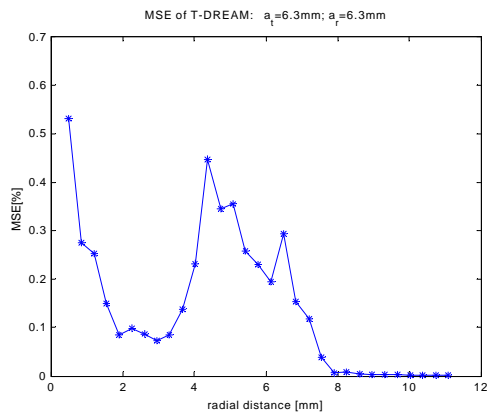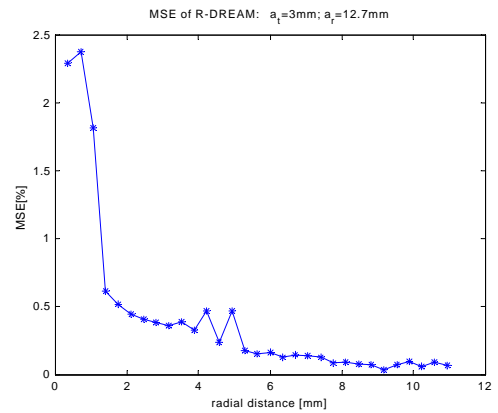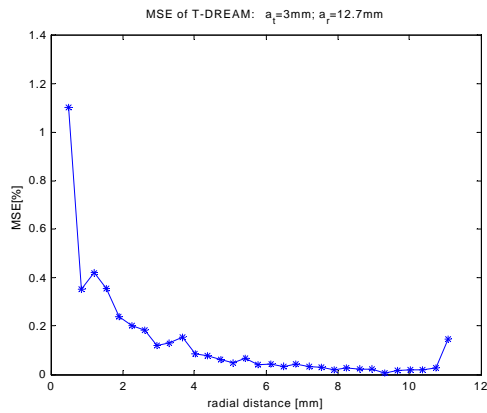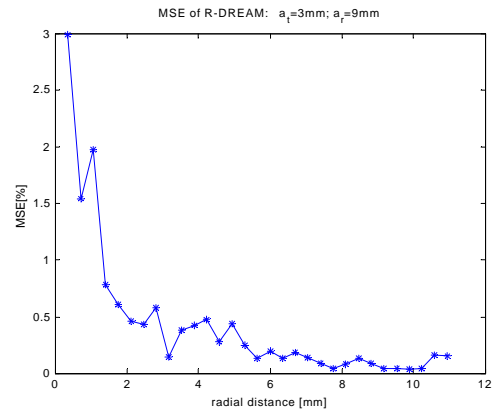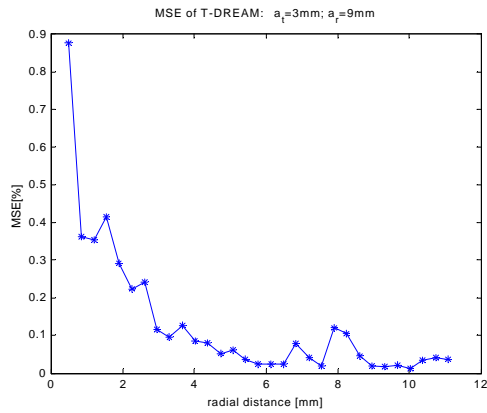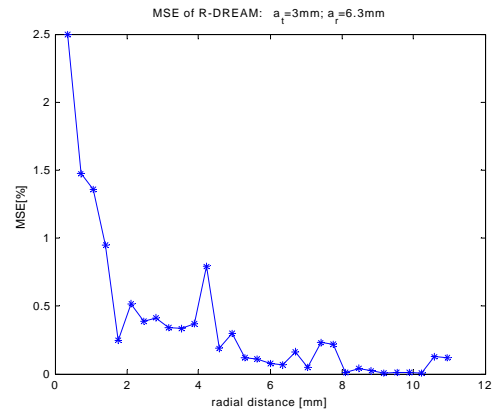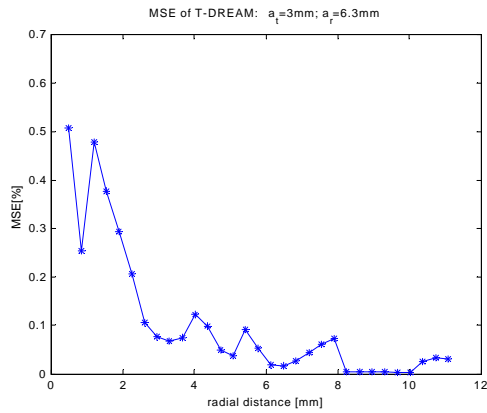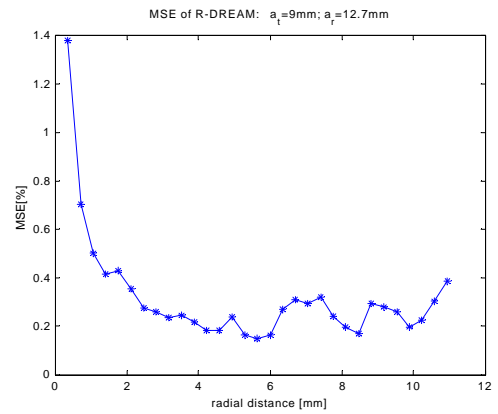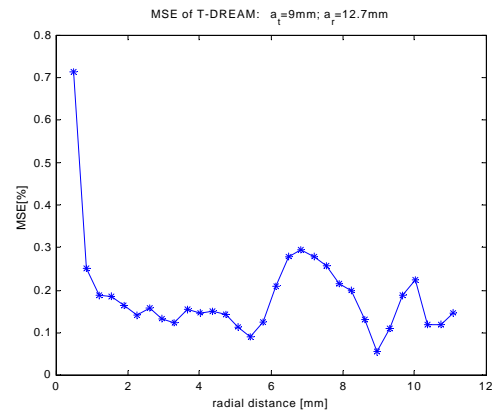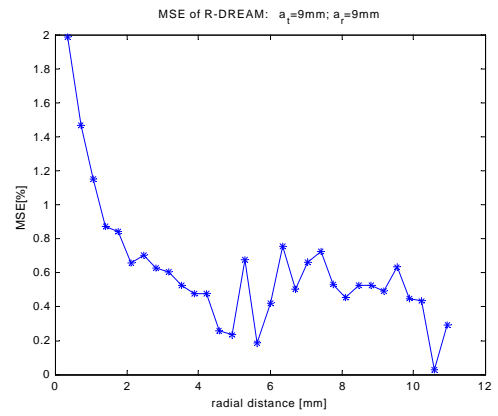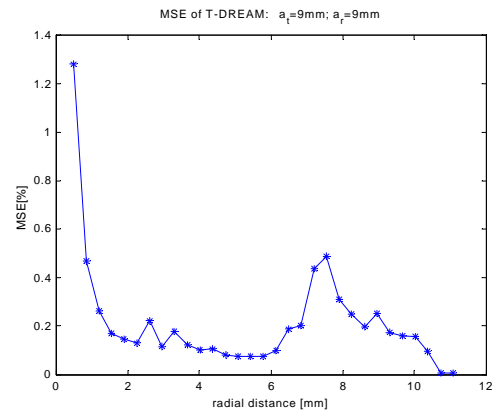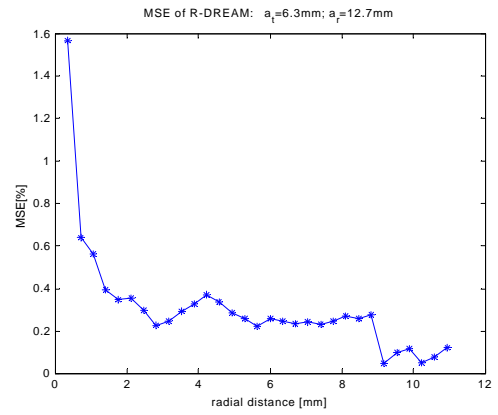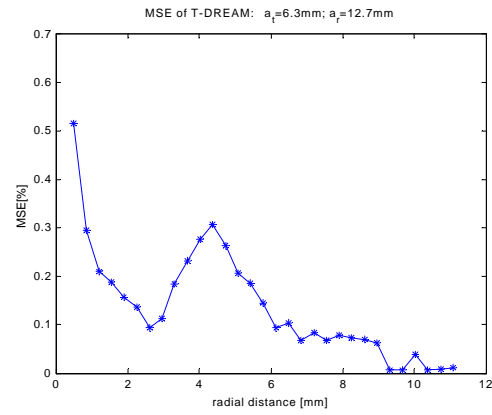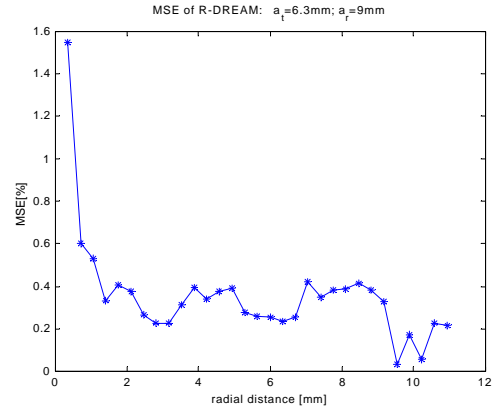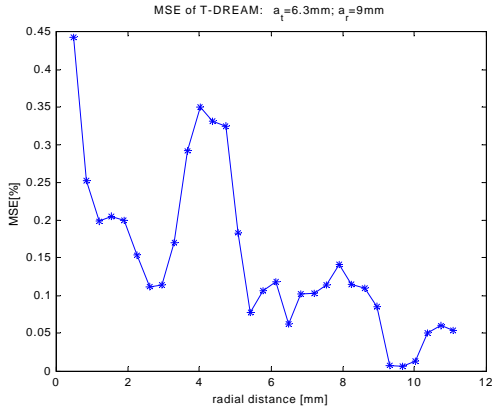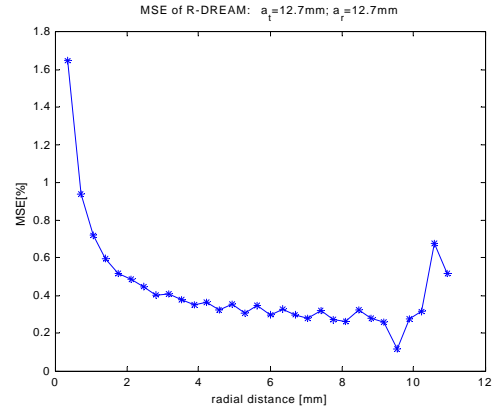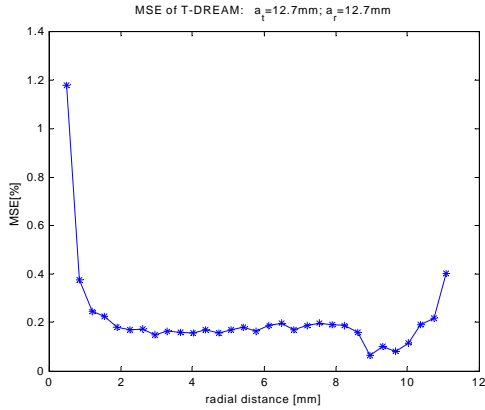
Appendix A.6

The relationship between the radial distance and the normalized DREAM Error (=MSE) of the received signal from small square flat reflectors for the simulation scenarios given in section 5.4 when the reflector is tilted 6° relative to the transducer surface. Refer to section 5.4 for more details.

normalized MSE of T-DREAM: a_t=3mm; a_r=3mm

normalized MSE of R-DREAM: a_t=3mm; a_r=3mm

normalized MSE of T-DREAM: a_t=3mm; a_r=6.3mm

normalized MSE of R-DREAM: a_t=3mm; a_r=6.3mm

175

normalized MSE of T-DREAM: a_t=3mm; a_r=9mm

normalized MSE of R-DREAM: a_t=3mm; a_r=9mm

normalized MSE of T-DREAM: a_t=3mm; a_r=12.7mm

normalized MSE of R-DREAM: a_t=3mm; a_r=12.7mm

normalized MSE of T-DREAM: a_t=6.3mm; a_r=6.3mm

normalized MSE of R-DREAM: a_t=6.3mm; a_r=6.3mm

normalized MSE of T-DREAM: a_t=6.3mm; a_r=9mm

normalized MSE of R-DREAM: a_t=6.3mm; a_r=9mm
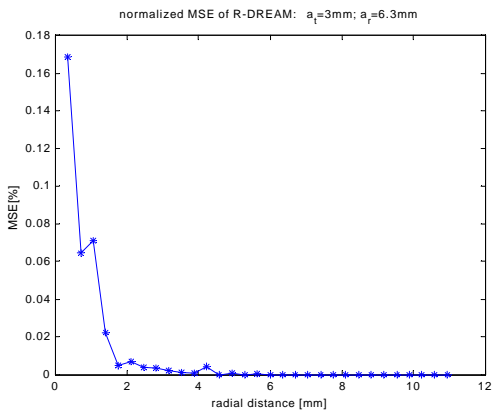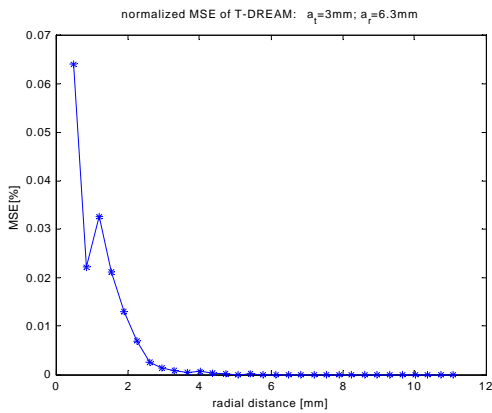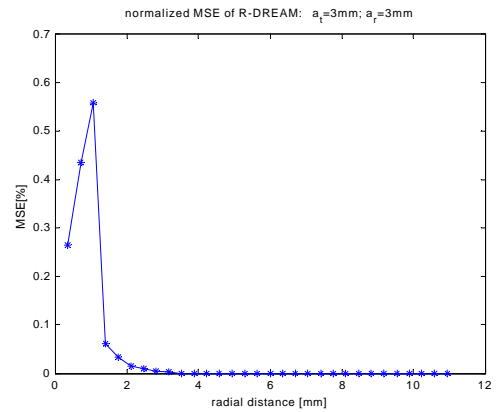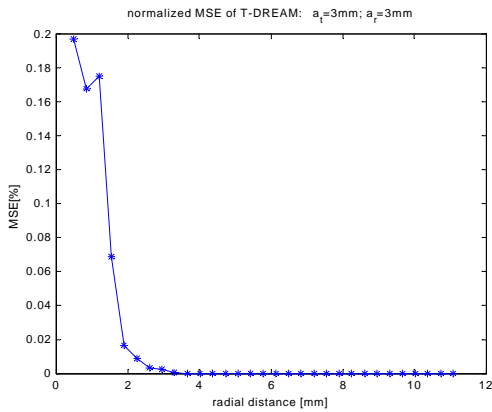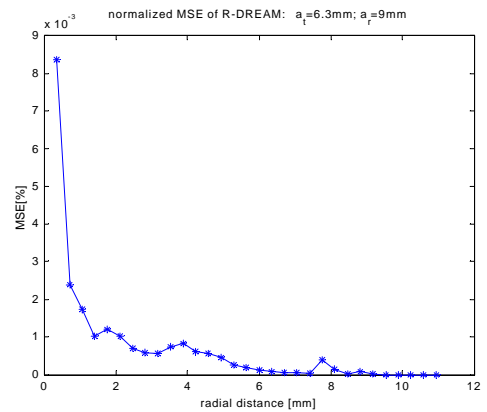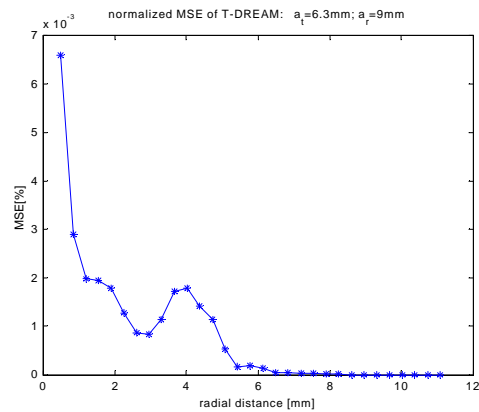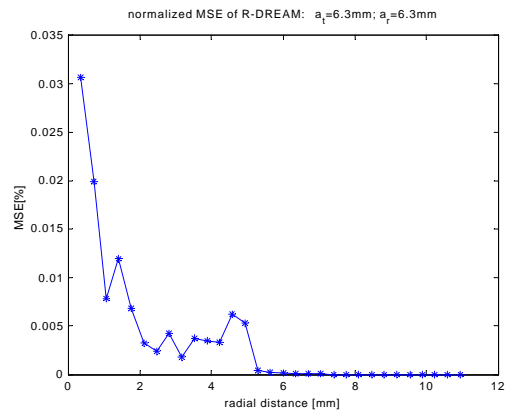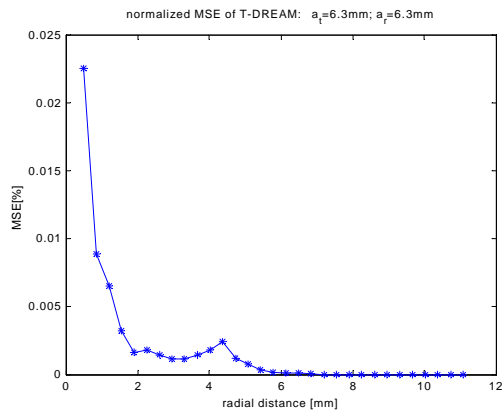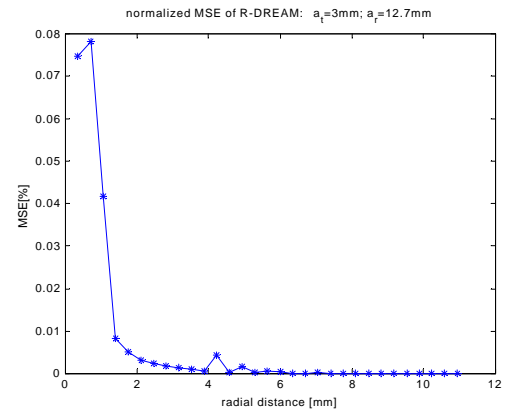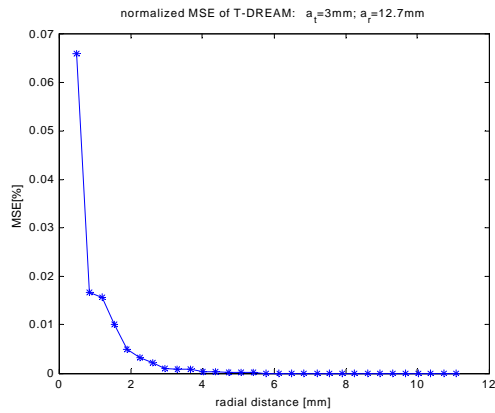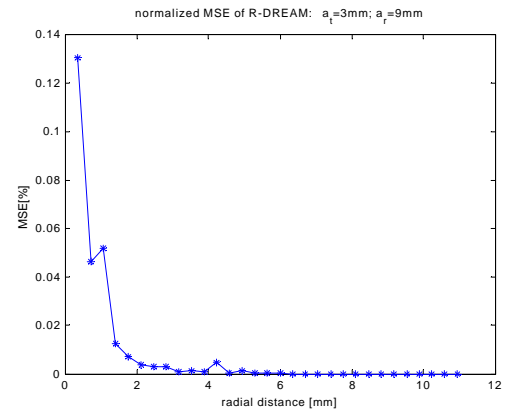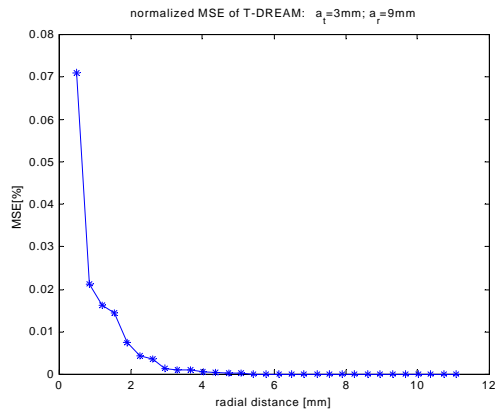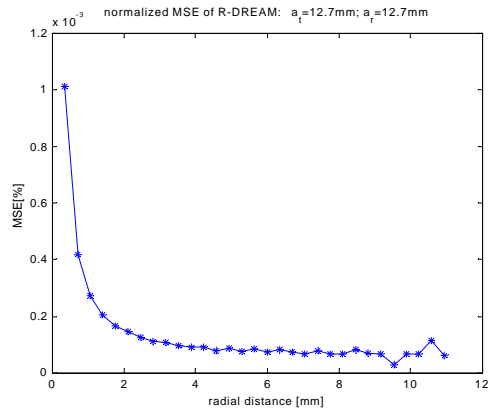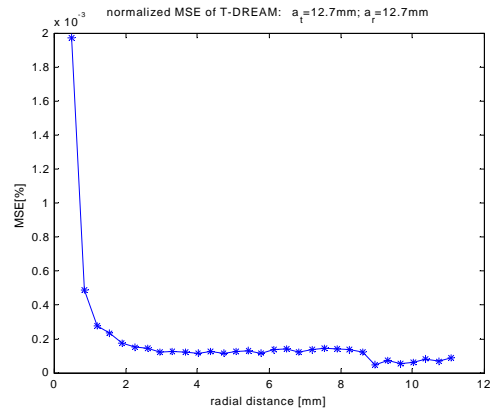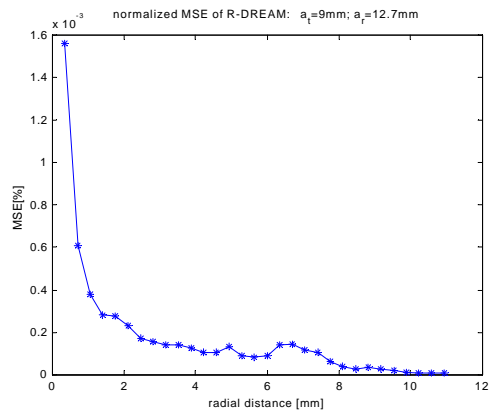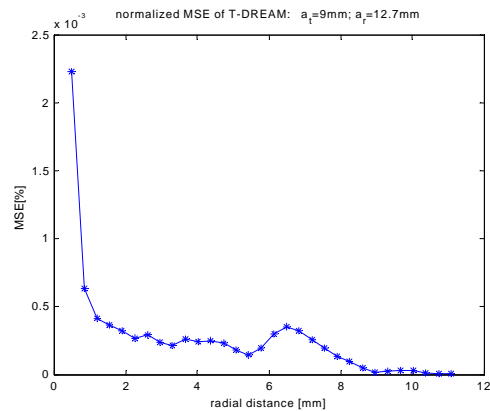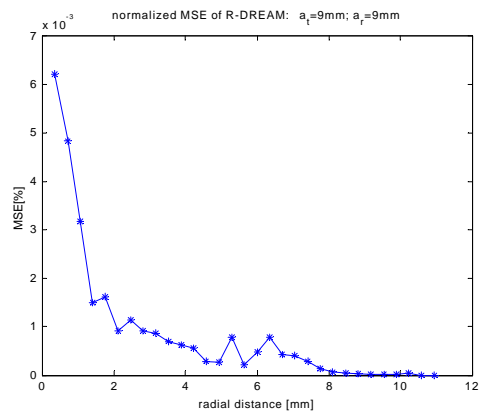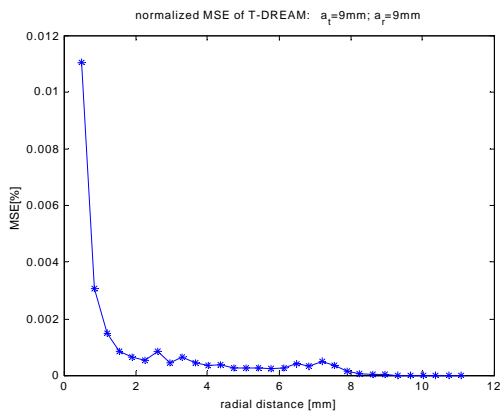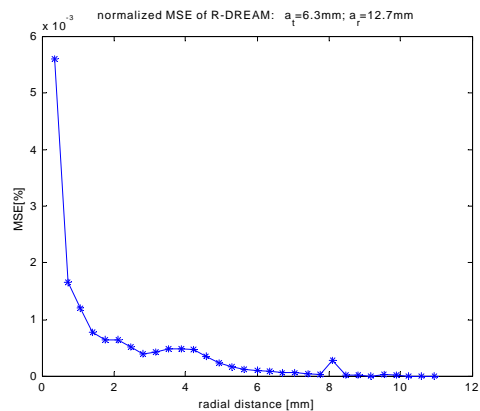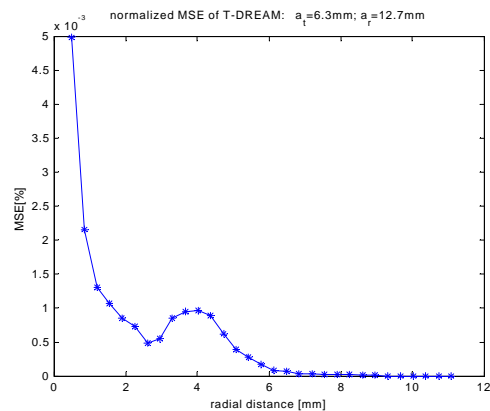
Appendix B

Appendix B.1

The spectra of the received signal from 1*mm**1*mm* square reflectors discussed in section 5.6. The parameters of the simulation scenarios are summarized in Table 5.5.

1*1mm² flat reflector, center at (r_p,z_p)=(6.35,50.47)mm, tilted 6°, a_t=6.3mm; a_r=6.3mm

1*1mm² flat reflector, center at (r_p,z_p)=(7.76,50.57)mm, tilted 6°, a_t=6.3mm; a_r=6.3mm

1*1mm² flat reflector, center at (r_p,z_p)=(9.17,50.68)mm, tilted 6°, a_t=6.3mm; a_r=6.3mm

1*1mm² flat reflector, center at (r_p,z_p)=(10.58,50.78)mm, tilted 6°, a_t=6.3mm; a_r=6.3mm
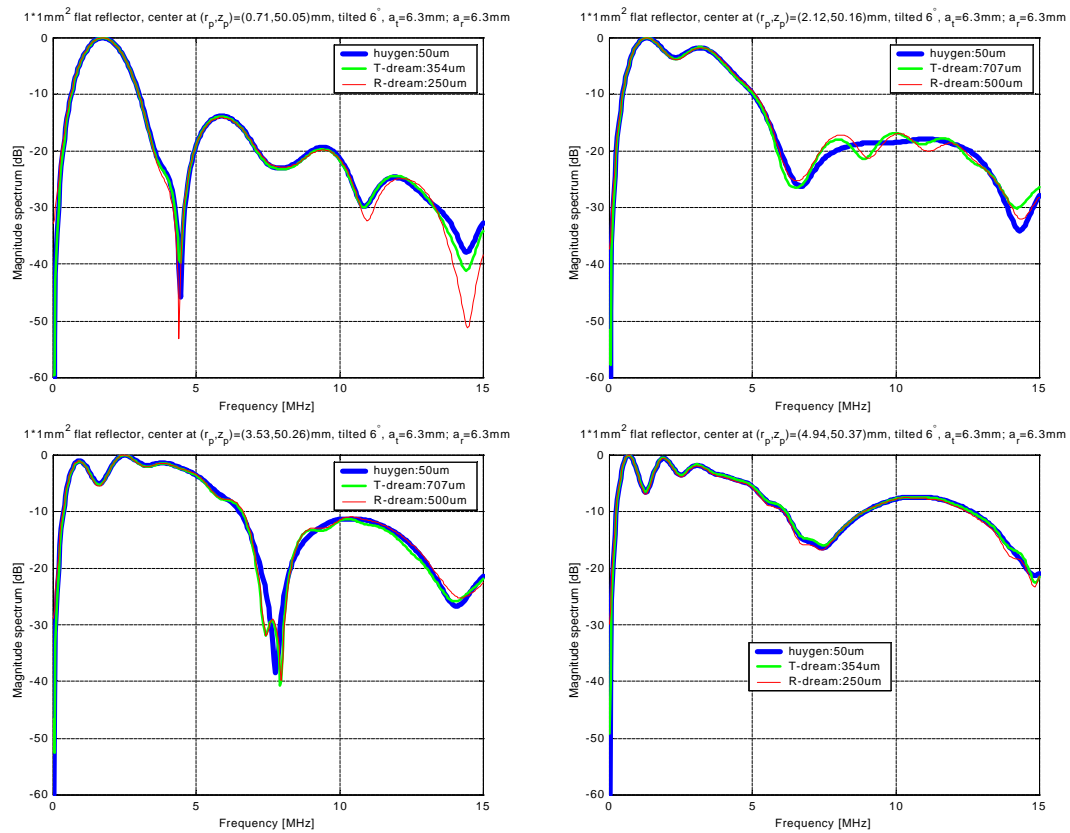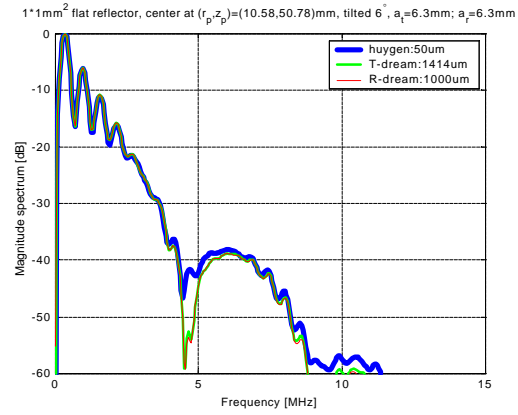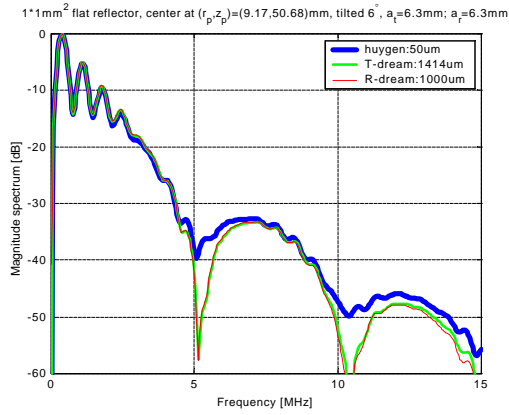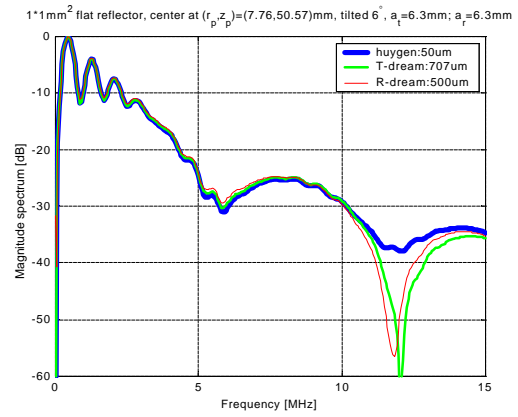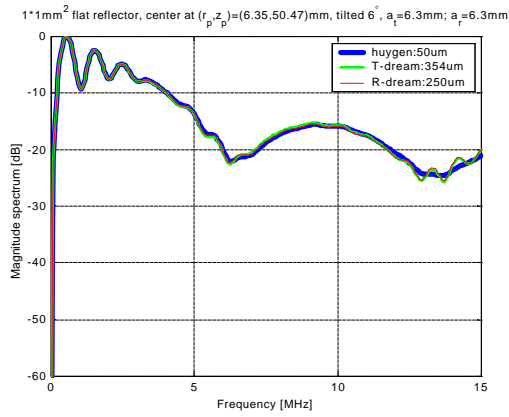
Appendix B.2

The spectra of the received signal from 15*mm**15*mm* square reflectors discussed in section 5.7.1. The reflector is tilted 0.6° relative to the surface of the transducer and the parameters of the simulation scenarios are summarized in Table 5.7.

15*15mm² flat reflector, center at (r_p,z_p)=(0,50)mm, tilted 0.6°, a_t=3mm; a_r=3mm

15*15mm² flat reflector, center at (r_p,z_p)=(0,50)mm, tilted 0.6°, a_t=3mm; a_r=6.3mm
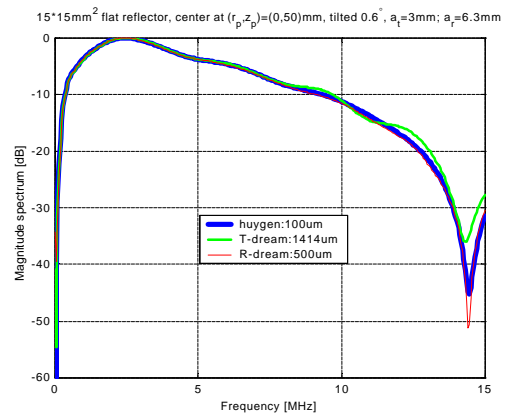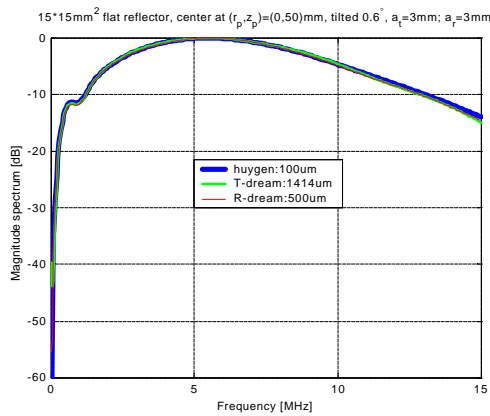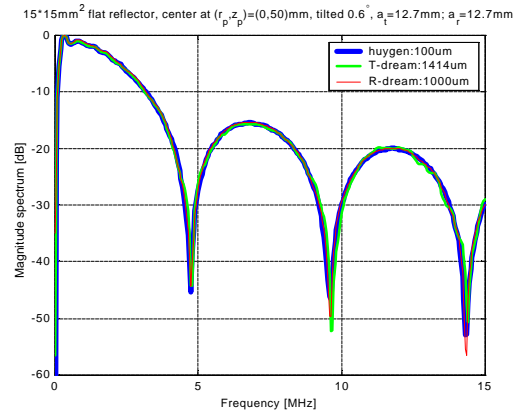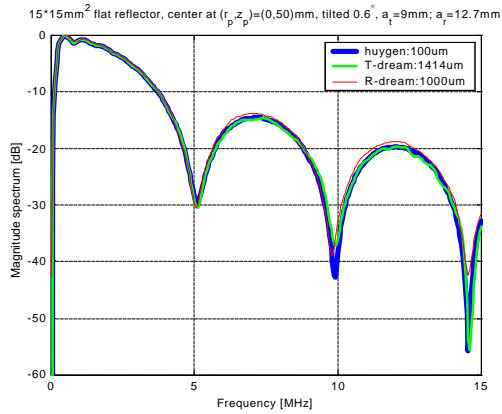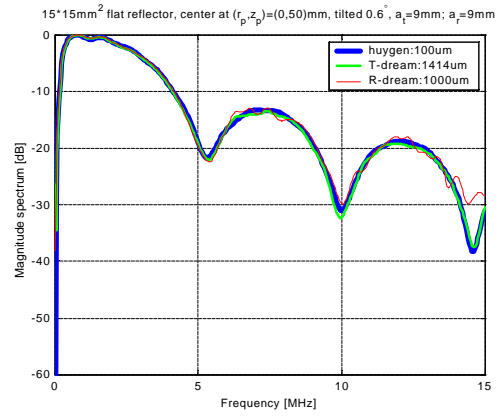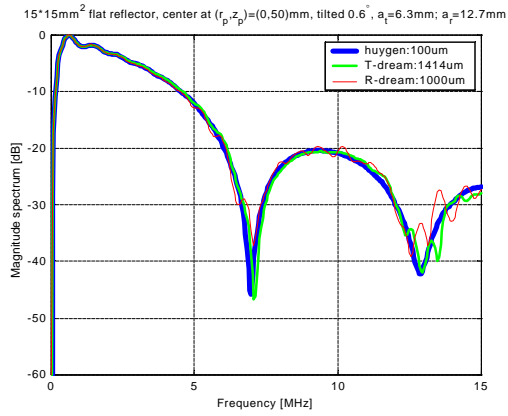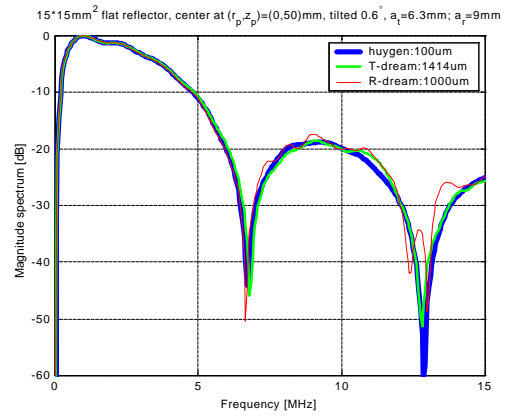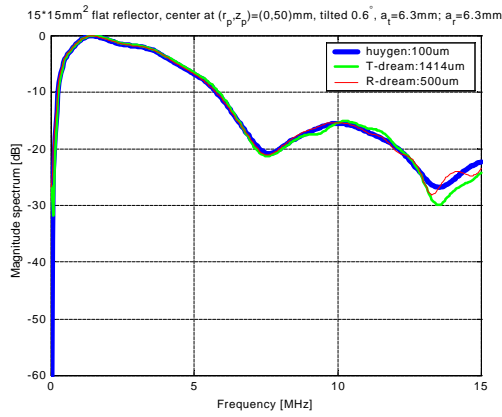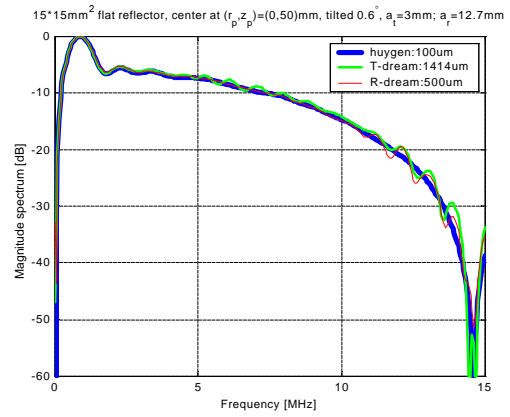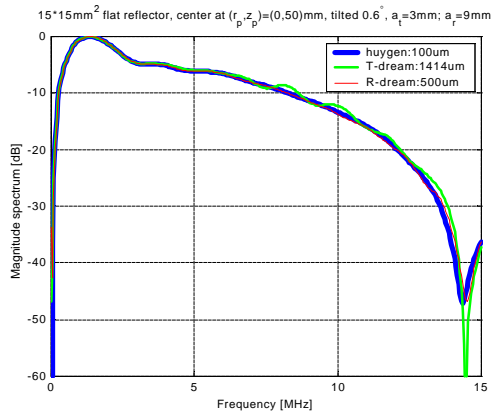
Appendix B.3

The spectra of the received signal from 15*mm**15*mm* square reflectors discussed in section 5.7.2. The reflector is tilted 6° relative to the surface of the transducer and the parameters of the simulation scenarios are summarized in Table 5.9. Refer to section 5.7.2 for more details.

15*15mm² flat reflector, center at $(r_p, z_p) = (0,50)$mm, tilted 6°, $a_t = 6.3$mm; $a_r = 12.7$mm

15*15mm² flat reflector, center at $(r_p, z_p) = (0,50)$mm, tilted 6°, $a_t = 9$mm; $a_r = 9$mm

15*15mm² flat reflector, center at $(r_p, z_p) = (0,50)$mm, tilted 6°, $a_t = 9$mm; $a_r = 12.7$mm

15*15mm² flat reflector, center at $(r_p, z_p) = (0,50)$mm, tilted 6°, $a_t = 12.7$mm; $a_r = 12.7$mm
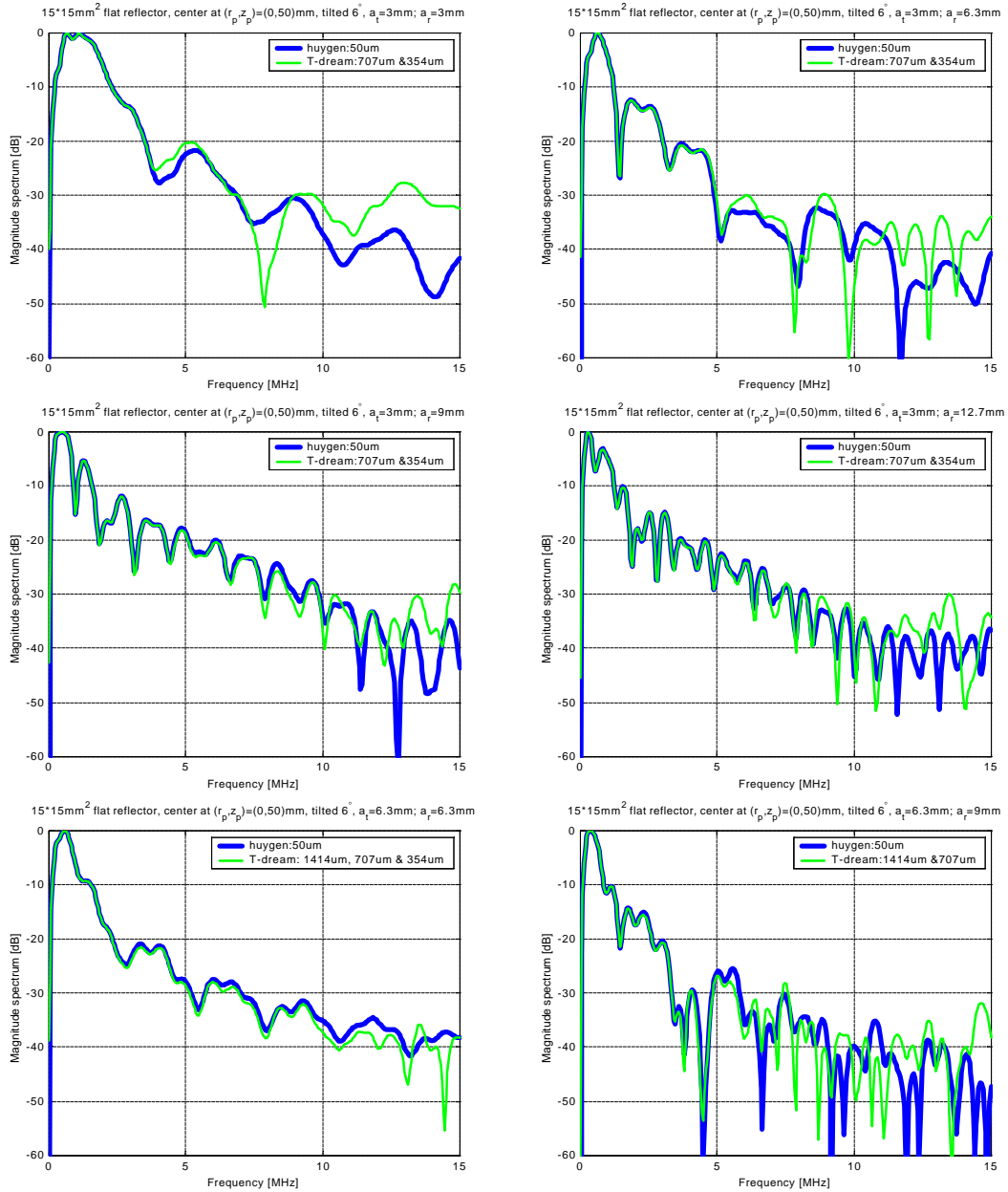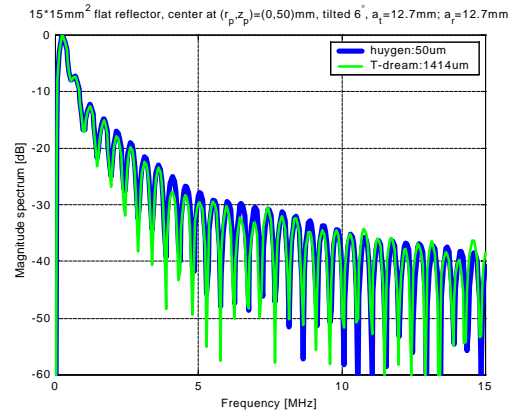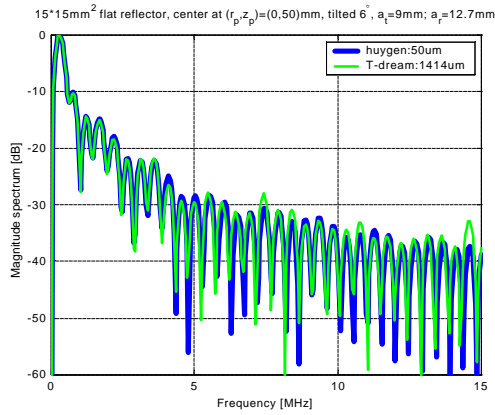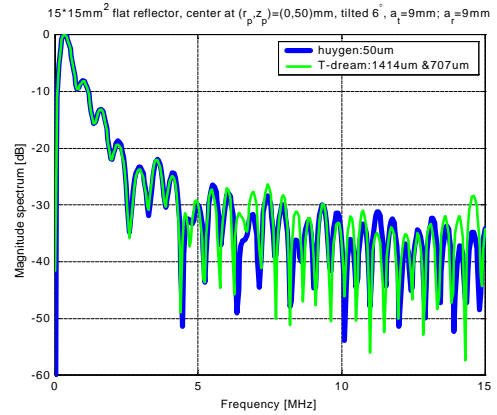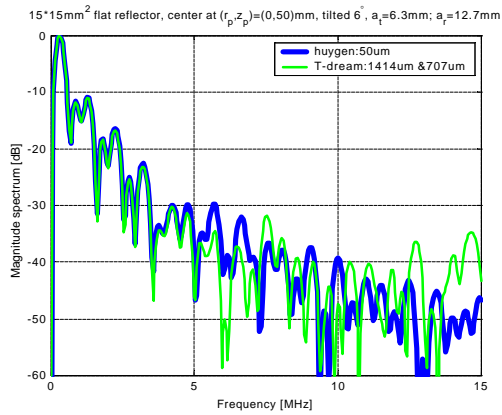
Appendix B.4

The spectra of the received signal from curved reflectors discussed in section 5.8. The parameters of the simulation scenarios are summarized in Table 5.10.

10° curved reflector, center at $(r_p, z_p) = (0, 50)$mm, $a_t = 3$mm; $a_r = 3$mm

10° curved reflector, center at $(r_p, z_p) = (0, 50)$mm, $a_t = 3$mm; $a_r = 6.3$mm
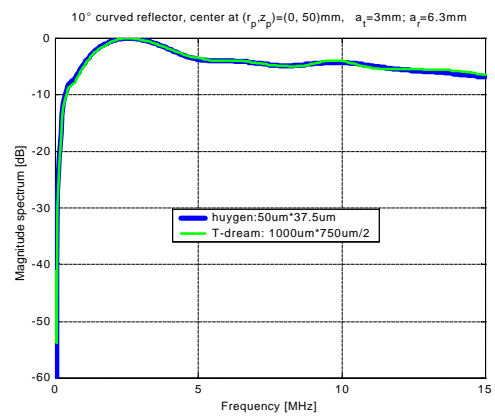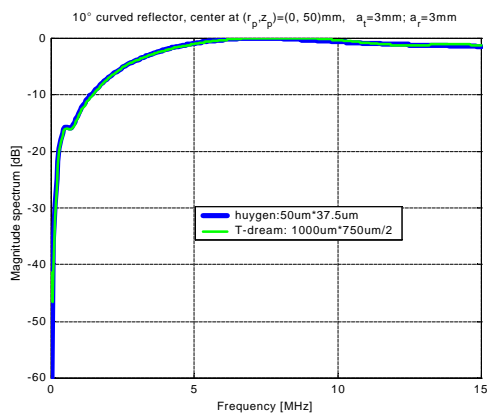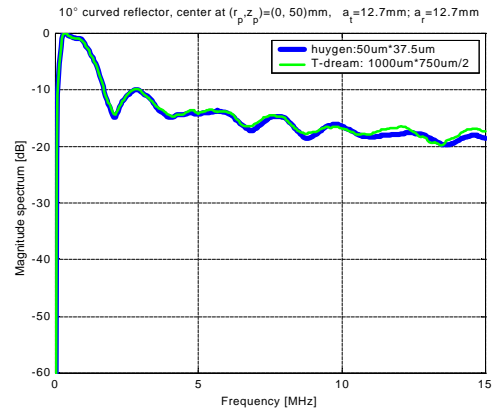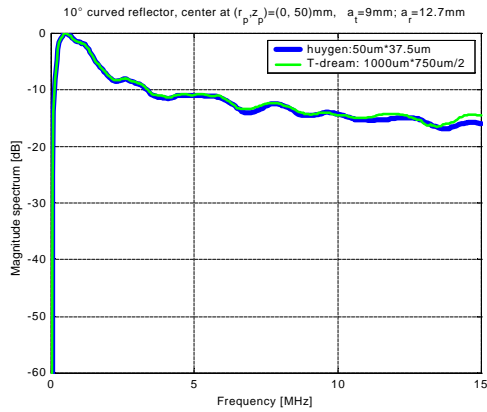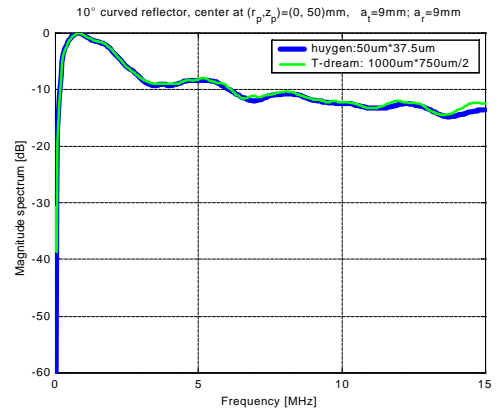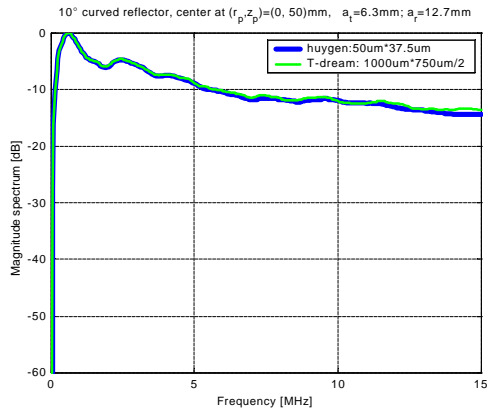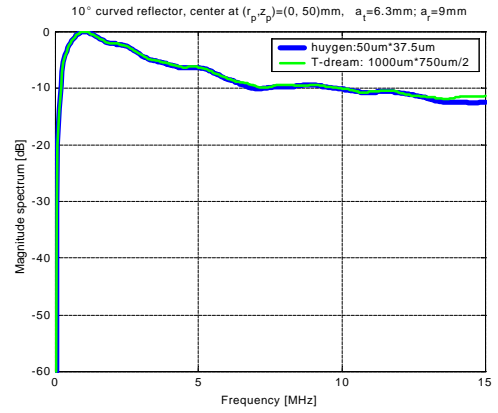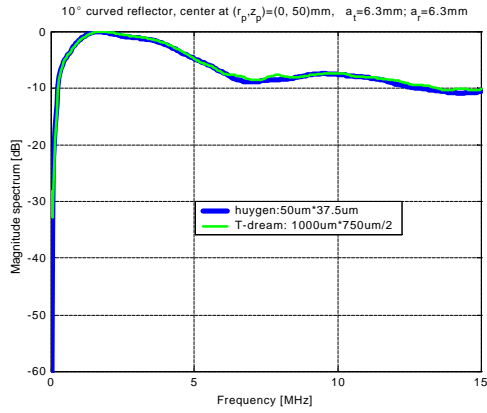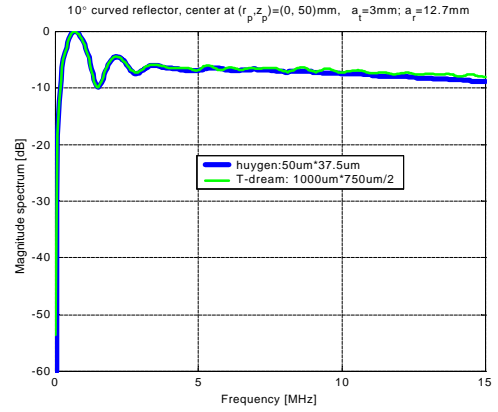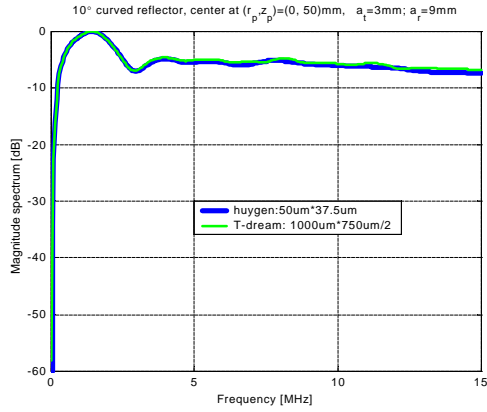
Appendix B.5

The time-domain received signal from 1*mm**1*mm* square reflectors discussed in section 5.6. The parameters of the simulation scenarios are summarized in Table 5.5.
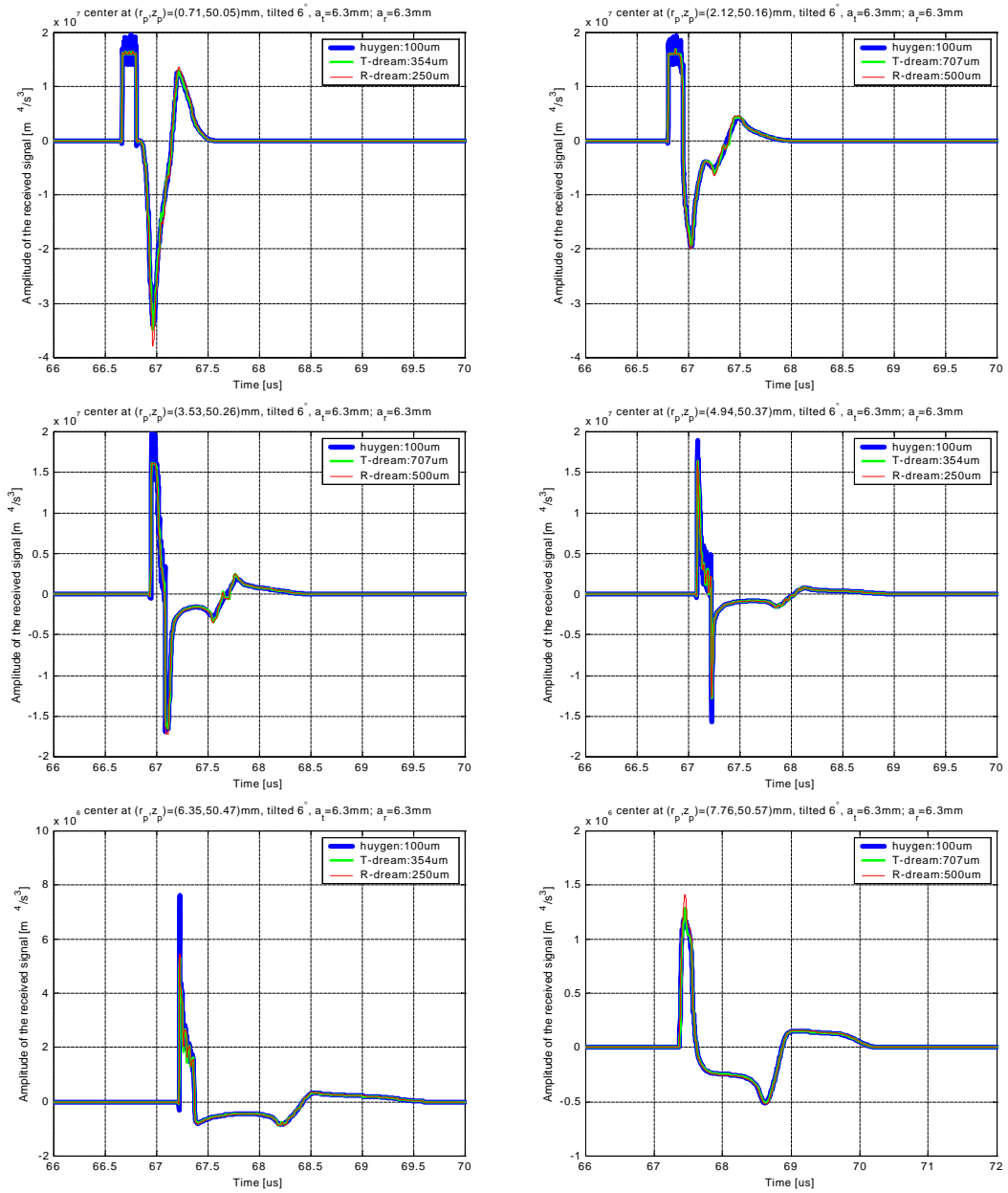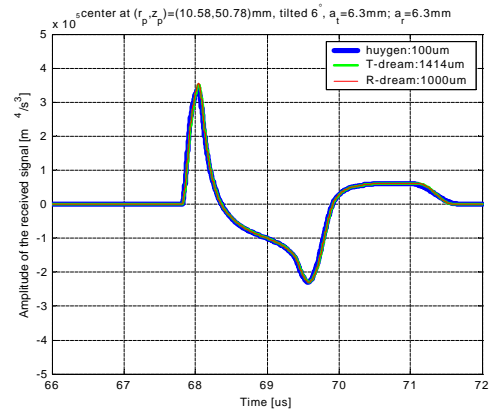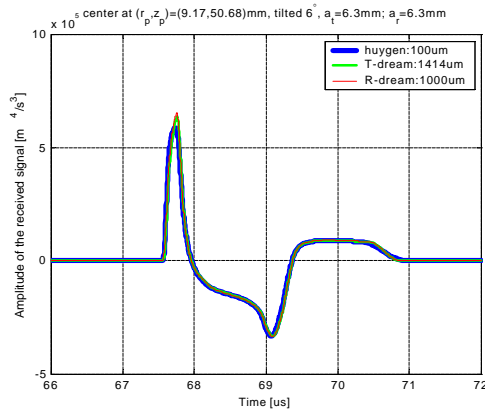
Appendix B.6

The time-domain received signal from 15*mm**15*mm* square reflectors discussed in section 5.7.1. The reflector is tilted 0.6° relative to the surface of the transducer and the parameters of the simulation scenarios are summarized in Table 5.7.
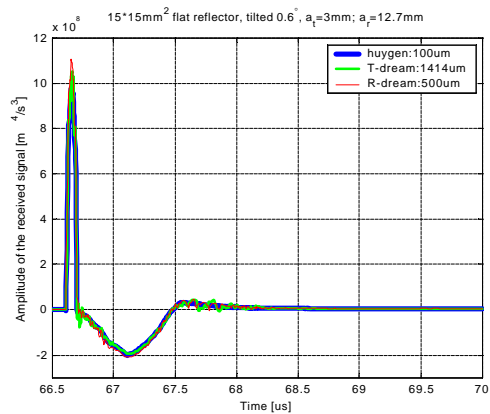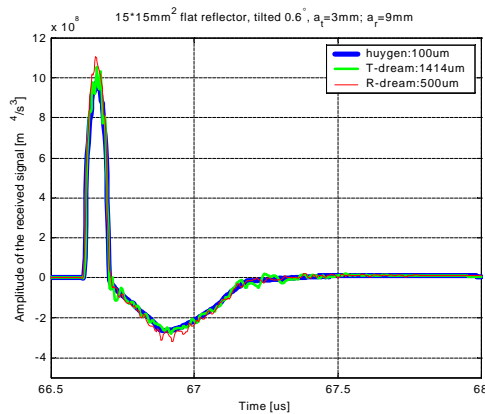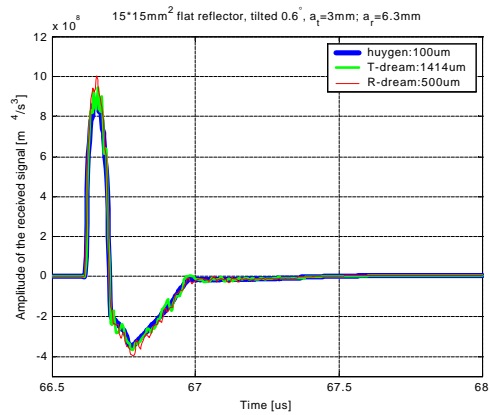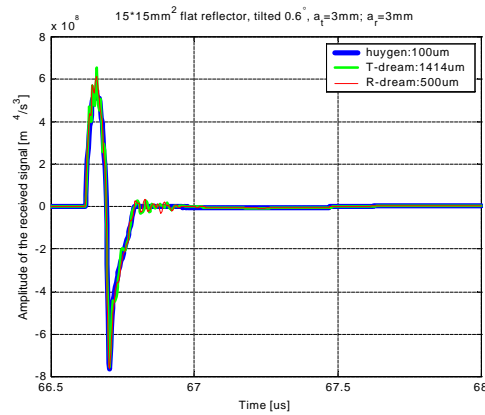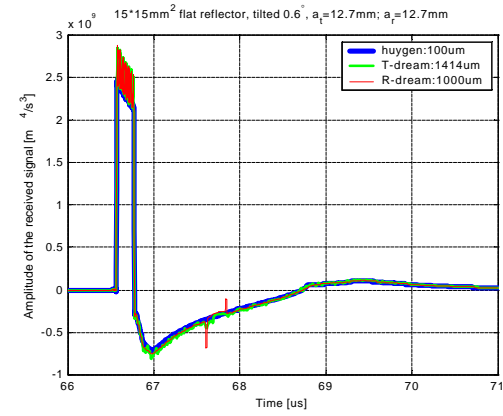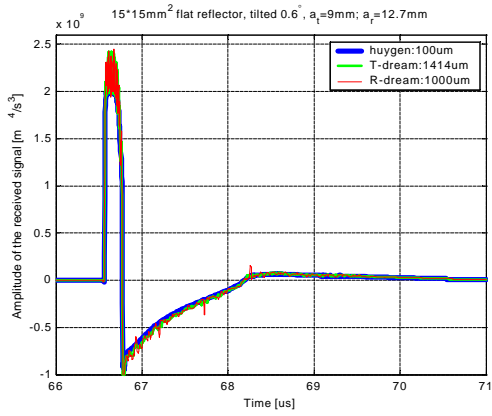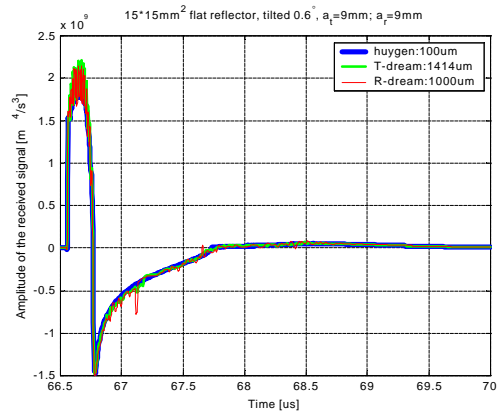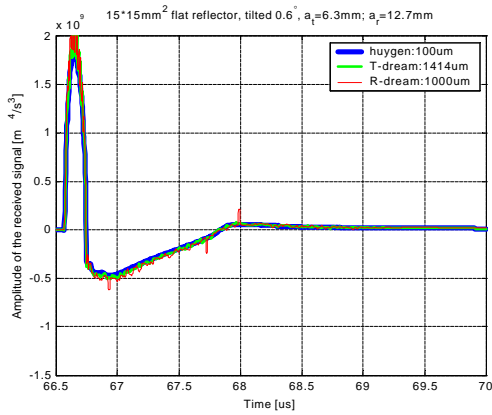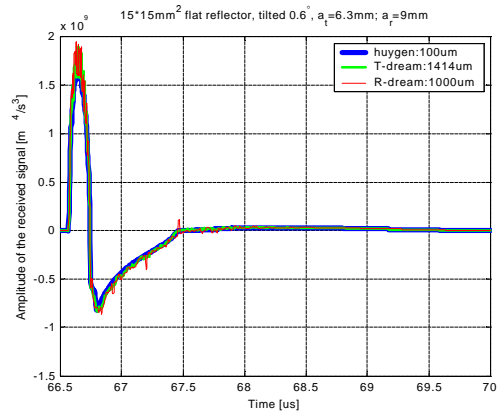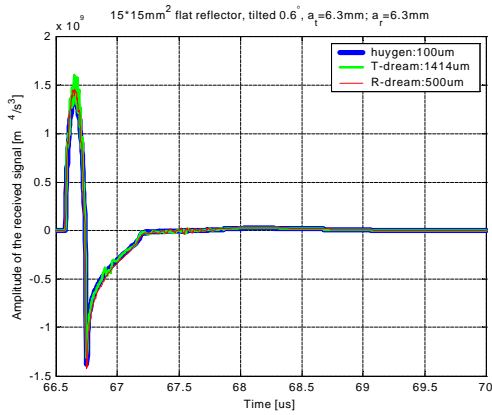
Appendix B.7

The time-domain received signal from 15*mm**15mm* square reflectors discussed in section 5.7.2. The reflector is tilted 6° relative to the surface of the transducer and the parameters of the simulation scenarios are summarized in Table 5.9.
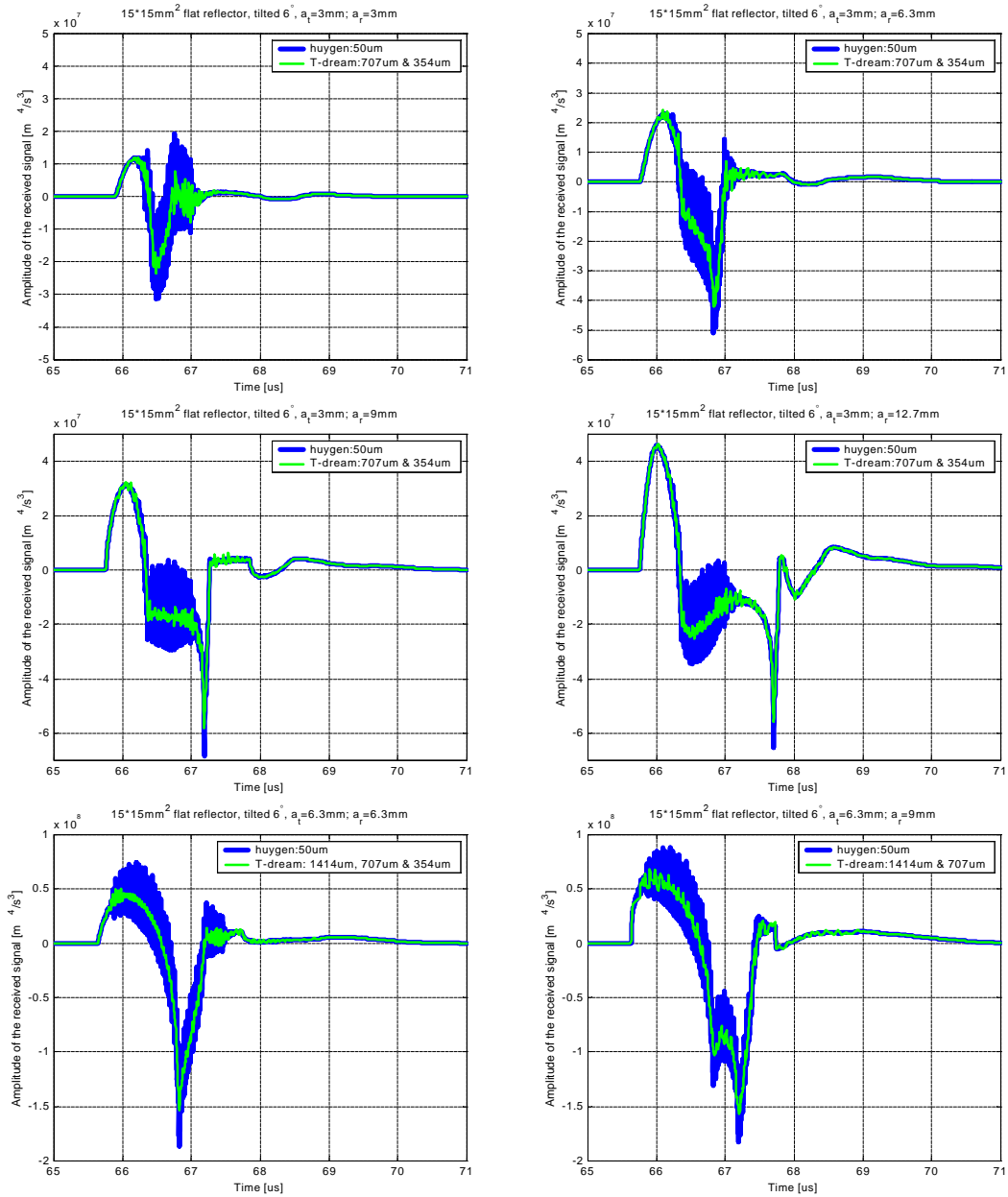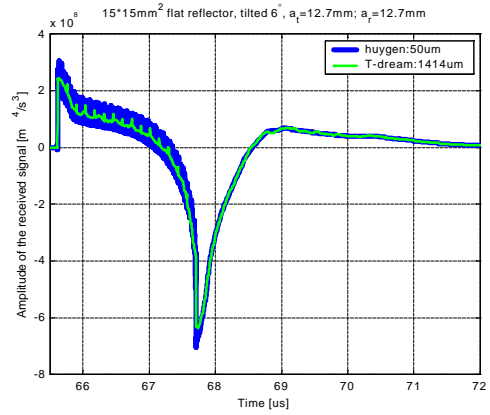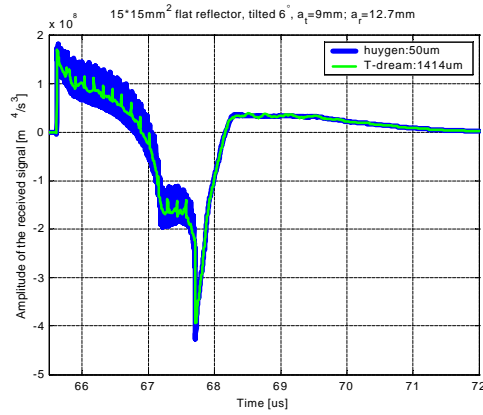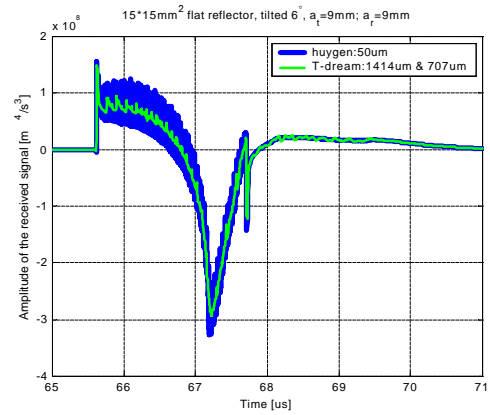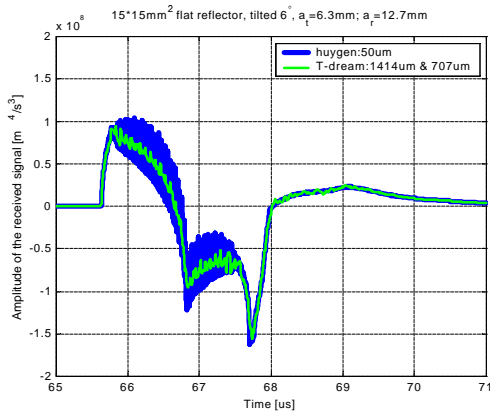
Appendix B.8

The time-domain received signal from curved reflector discussed in section 5.8. The parameters of the simulation scenarios are summarized in Table 5.10.

10° curved reflector, a_t=9mm; a_r=12.7mm

huygen:50um*37.5um
T-dream: 1000um*750um/2

Amplitude of the received signal [m ^{4}/s^3]

Time [us]

10° curved reflector, a_t=12.7mm; a_r=12.7mm

huygen:50um*37.5um
T-dream: 1000um*750um/2

Amplitude of the received signal [m ^{4}/s^3]

Time [us]